



**HAL**  
open science

# Surface Plasmon Polariton and Wave Guide Modes in a Six Layer Thin Film Stack

Moustafa Achlan

► **To cite this version:**

Moustafa Achlan. Surface Plasmon Polariton and Wave Guide Modes in a Six Layer Thin Film Stack. Optics [physics.optics]. Université Paris Saclay (COMUE), 2018. English. NNT: 2018SACLS109 . tel-02560547

**HAL Id: tel-02560547**

**<https://theses.hal.science/tel-02560547>**

Submitted on 2 May 2020

**HAL** is a multi-disciplinary open access archive for the deposit and dissemination of scientific research documents, whether they are published or not. The documents may come from teaching and research institutions in France or abroad, or from public or private research centers.

L'archive ouverte pluridisciplinaire **HAL**, est destinée au dépôt et à la diffusion de documents scientifiques de niveau recherche, publiés ou non, émanant des établissements d'enseignement et de recherche français ou étrangers, des laboratoires publics ou privés.

# Surface Plasmon Polariton and Wave Guide Modes in a Six Layer Thin Film Stack

Thèse de doctorat de l'Université Paris-Saclay

Préparée à l'Université Paris-Sud

École doctorale n°572 : Ondes et Matière (EDOM)

Spécialité de doctorat : Nanophysique

Thèse présentée et soutenue à Orsay, le 16 Mai 2018, par

**Moustafa Achlan**

## Composition du Jury :

**Dominique BARCHIESI**

Professeur, Institut Charles Delaunay (UTT)

Président

**Gérard COLAS DES FRANCS**

Professeur, Laboratoire interdisciplinaire  
Carnot de Bourgogne (UB)

Rapporteur

**Antoine MOREAU**

Maître de conférences, Institut Pascal (UCA)

Rapporteur

**Xavier QUELIN**

Maître de conférences, Laboratoire Groupe d'Etude  
de la matière condensée (UVSQ)

Examineur

**Elizabeth BOER-DUCHEMIN**

Maître de conférences, Institut des Sciences  
Moléculaires d'Orsay (UPS)

Directrice de thèse

**Georges RASEEV**

Directeur de Recherche, Institut des Sciences  
Moléculaires d'Orsay (UPS)

Co-Directeur de thèse

**Eric LE MOAL**

Chargé de recherche, Institut des Sciences

Invité



# Acknowledgments

*The work presented in this thesis would not be possible without my close association with many people. I take this opportunity to extend my sincere gratitude and appreciation to all those who made my Ph.D thesis possible.*

*There are no proper words to convey my deep gratitude and respect for my supervisors, Dr, Georges Raseev for his dedicated help, advice, inspiration, encouragement and continuous support throughout my Ph.D. He offered me a lot of help both on scientific subjects and daily life. I will never forget the day that he picked up me from the Airport when I first came to France. I also would like to thank Dr. Elizabeth Boer Duchemin for her enthusiasm, and integral view on research. Her mission for providing high-quality work has made a deep impression on me. Working with both of them has not only broadened my knowledge but also helped me to know how to do research because each one gave me a different experience.*

*I would also like to thank Dr. Eric LE Moal with whom I discussed a lot during my Ph.D. and who advised me a lot. I am very lucky to have been able to learn from his extensive knowledge in science. I also would like to thank the other members of the Nanoscience Group Dr. Andrew Mayne, Prof. Hamid Oughaddou, Dr. Gérald Dujardin, Dr. Hanna Enriquez, Dr. Séverine Le Moal, Dr. Jean-Louis Lemaire and Dr. Damien Riedel for the free atmosphere and for their kindness. Especially Dr. Andrew Mayne who helped me with my thesis and with whom I had many discussions about science and daily life.*

*I want to express my gratitude to all the jury members present at my PhD defense: Prof. Dominique Barchiesi, Prof. Gérard Colas des Francs, Dr. Antoine Moreau, and Dr. Xavier Quelin. They generously gave their time to offer me valuable comments toward improving my work. The discussion with them really inspired me a lot and broadened my knowledge.*

*Moreover, I would like to extend my sincerest thanks to my fellow office-mates Ala Hussein, Khalid Quertite, Shuiyan Cao, Wei Zhang, Delphine Pommier, Laury Martins-Lopès, Nicolas Lamarre, Viet Tiep Phung, Mali Zhao, Thi Kim Cuong Le, Tianzhen Zhang and Luqiong Zhang for all the fun we had together, I really enjoyed being with you, and you gave me a family atmosphere. Especially Ala Hussein and Khalid Quertite with whom I spent very good time and they were with me in happiness and sadness. I really gained a brother and sister.*

*My gratitude to all my friends who were with me during my Ph.D in France. I will not*

---

*forget the time that I spent with Abdel Majid Kassir, Bachar Mallat and Mouhamad Tlais who were with me from the beginning until now. After two days of my arriving to France, I met My friend Abdel Majid who gave me self-confidence and always pushed me for the best. Meeting with him was great support for me. I will not forget the road trip on bikes with Ivan Alata and Ali AlDhaybi, it was a good adventure for me. Thanks to them for the very good time that we spent together and thanks to Ivan for his advice. Last but not the least, my gratitude to Sara Alhomsy , Walid Tarraf and Mostafa Dennaoui whom I met in the last year of my Ph. D.*

*As always it is impossible to mention everybody who had an impact on this work, however, there are those whose spiritual support is even more important. I feel a deep sense of gratitude for my grand parents, parents, and brothers who taught me good things that really matter in life. Their infallible love and support have always been my strength. Their patience and sacrifice will remain my inspiration throughout my life. I am also very much grateful to all my family members for their constant inspiration and encouragement.*

# Contents

<b>Abstract</b>	<b>6</b>
<b>1 Introduction</b>	<b>7</b>
<b>2 Electronic and photonic modes of a thin film stack: quantum well and wave guide modes</b>	<b>14</b>
2.1 Surface and thin film electronic states . . . . .	15
2.1.1 A solid bordered by a surface: surface and image states . . . . .	15
2.1.2 Electronic states associated to a single thin film: Quantum well states . .	16
2.2 Photonic wave guide (WG) mode . . . . .	17
2.2.1 Model . . . . .	17
2.2.2 Thin films and the WG modes penetration depth . . . . .	18
2.3 Conclusion . . . . .	18
<b>3 Plasmon properties and their dispersion</b>	<b>20</b>
3.1 Bulk and surface plasmon polaritons . . . . .	20
3.1.1 Drude permittivity . . . . .	21
3.1.2 Electromagnetic waves in metals: bulk plasmons (BP) . . . . .	23
3.1.3 Polaritons, surface plasmons polariton (SPP) and surface plasmons (SP) .	25
3.2 Continuity of the wave vectors and fields at an interface. Descartes-Snell law .	27
3.2.1 Descartes-Snell law at a dielectric-dielectric interface . . . . .	27
3.2.2 Propagating and evanescent fields at a dielectric-dielectric interface . . .	28
3.2.3 Descartes-Snell law at a dielectric-metal interface . . . . .	30
3.3 Dispersion of surface plasmon polaritons . . . . .	31
3.3.1 One interface . . . . .	32
3.3.1.1 Transverse magnetic (TM) polarization . . . . .	33
3.3.1.2 Transverse electric (TE) polarization . . . . .	38
3.3.2 Dispersion of surface plasmons polaritons (SPP) for a three layer (two	
interface) thin film structure . . . . .	38
3.3.3 Dispersion of surface plasmons polaritons (SPP) for an n layer geometry .	42
3.4 Conclusion . . . . .	42
<b>4 Experimental set-ups for measuring plasmon properties</b>	<b>43</b>
4.1 Measuring the reflected light . . . . .	44
4.1.1 Plane wave source using a prism . . . . .	44
4.1.2 Focused laser beam . . . . .	45
4.2 Measuring the transmitted light. Leakage radiation microscopy . . . . .	46
4.2.1 Near field scanning optical microscope (NSOM) . . . . .	46

4.2.2	Rough thin films and illumination of a defect . . . . .	47
4.3	Excitation by electrons . . . . .	49
4.3.1	Scanning tunneling microscope (STM) . . . . .	49
4.3.2	Scanning electron microscope . . . . .	50
4.4	Conclusion . . . . .	51
<b>5</b>	<b>Modeling: source at infinity and local source of excitation</b>	<b>52</b>
5.1	Excitation source at infinity (ESI) . . . . .	52
5.1.1	Fresnel coefficients in a one interface system . . . . .	52
5.1.2	Fresnel coefficients in a thin film stack . . . . .	55
5.2	Excitation by a local source . . . . .	59
5.2.1	From tunneling electrons of an STM to the oscillating dipole (OD) model	60
5.3	Oscillating dipole model (OD) in the momentum space . . . . .	61
5.3.1	Oscillating dipole (OD) transmitted flux in coordinate space . . . . .	67
5.4	Conclusion . . . . .	67
<b>6</b>	<b>Comparative study of the SPP-like and of the wave guide like (WG-like) modes of the three and six-layer thin film stacks</b>	<b>68</b>
6.1	Material functions . . . . .	68
6.2	Excitation by a source at infinity (ESI): Reflectance and transmittance . . . .	69
6.2.1	Au thickness variation . . . . .	70
6.2.2	SiO <sub>2</sub> thickness variation in a six-layer stack . . . . .	72
6.2.3	Reflectance of three and six-layer thin film stacks as a function of $\lambda$ and $k_\rho/k_0$ . . . . .	75
6.2.4	Dispersion of the reflectance for $s$ and $p$ polarizations . . . . .	78
6.2.5	Reflectance: comparison with the experiment . . . . .	79
6.2.6	Transmittance . . . . .	81
6.3	Conclusion for the excitation by a source at infinity (ESI) calculations . . . . .	84
6.4	Local source excitation using the oscillating dipole model (OD): Transmitted flux intensity in momentum space . . . . .	85
6.4.1	Transmitted flux intensity as a function of layer thickness in the three and six-layer thin film stacks . . . . .	85
6.4.2	Comparison between the transmitted flux for the light sources located at infinity and close to the surface. . . . .	88
6.4.3	Dispersion of the transmitted flux intensity . . . . .	90
6.4.4	Model and experimental dispersion of a six-layer thin film stack . . . . .	92
6.5	Local excitation: transmitted flux intensity in coordinate space . . . . .	98
6.5.1	Transmitted flux intensity in the coordinate space from the inverse Fourier transform of the fields. Padding the Fourier space . . . . .	98
6.5.2	Comparison and interpretation of three and six layers stack in the coordinate space at a single wavelength . . . . .	100
6.5.3	3D-coordinate space transmitted flux of the stacks function of the wavelength and the in-plane coordinate . . . . .	101
6.5.4	Comparison of the coordinate-space experimental results with the model calculation for dipole-illuminated stacks . . . . .	107
6.6	Conclusion of the local excitation OD model calculations . . . . .	108

<b>7</b>	<b>Characterization of the SPP and WG modes of the three and six-layer thin film stacks</b>	<b>111</b>
7.1	Electric field profile mode assignment . . . . .	111
7.1.1	Electric field as a function of the penetration coordinate . . . . .	112
7.1.2	Characterization of the modes . . . . .	113
7.1.3	Validation of the E(z) algorithm . . . . .	113
7.1.4	Modulus of the total electric field as a function of the penetration coordinate (z), $d_{Au}$ and $d_{SiO_2}$ . . . . .	115
7.1.5	Total electric field modulus as a function of the wavelength $\lambda$ and the penetration coordinate z . . . . .	118
7.2	Conclusion . . . . .	123
<b>8</b>	<b>Conclusion</b>	<b>124</b>
<b>A</b>	<b>Electric field profile</b>	<b>136</b>

# Abstract

In this thesis, we investigate the optical properties of a six-layer stack (air-Au- $SiO_2$ -Au-Ti-glass). The interfaces are flat and the modeling is performed using elementary Fresnel expressions at the interface and plane wave propagation in the layers. Two models are used where the sample is: i) excited by a source at infinity (excitation by source at infinity (ESI)); ii) excited by a local source. In the experiments we are modeling this source consists of the inelastic tunneling electrons from a scanning tunneling microscope (STM). In our modeling this source is replaced by a vertical oscillating dipole. Using these two models one calculates the reflected (reflectance) and the transmitted (transmittance) flux from a source at infinity and the transmitted flux of a local source. Surface plasmon polariton (SPP) and wave guide (WG) modes may be identified in the reflectance, transmittance and transmitted flux. In a particular wavelength domain the SPP and WG repel each other giving rise to an avoided crossing.

The choice of the gold (Au) and silica ( $SiO_2$ ) thicknesses of the six-layer stack is guided by two requirements: high amplitude of the observable and wide wavelength dependence of the in-plane wave vector  $k_\rho$ . We also study the influence of the gold and silica thicknesses on the observables. We find that the observables are significant for  $d_{Au}^{three} \in [10, 90]$  for the three and  $d_{Au}^{six} \in [10, 50]$  nm for six layer stacks and this predictive study guided the choice of the experimental sample thicknesses. The wave guide mode appears for  $d_{SiO_2} > 190$  nm.

The electric field as a function of the penetration coordinate  $z$  is calculated in order to characterize the location of the field in the stack and to assign the nature of the modes. We observe that for the SPP the electric field is confined at the Au-air interface whereas, the electric fields corresponding to the WG mode are confined inside  $SiO_2$  layer.

Our calculations presented in this work are in good agreement with the experimental measurements performed in our group.

# Chapter 1

## Introduction

This work is devoted to a theoretical study of the surface plasmon polariton (SPP) and wave guide (WG) modes of a stack of thin films composed of dielectrics and plasmonic metals (gold in the present case). The idea is to have a versatile material system with few geometrical parameters permitting the enhancement of a particular property or observable to be used in applications. For example the SPP and/or WG modes are widely used in applications in physics, chemistry and especially in biology.

There are bulk and surface plasmons, the latter appearing at the surface. Energetically the surface plasmons located below the bulk plasmon, the three words defining a surface plasmon polariton (SPP) mean:

- **surface** corresponds to the solid state periodicity breaking permitting the appearance of these modes only at an interface;
- **plasmon** is a quasiparticle corresponding to collective quantum oscillations of the free electron gas density or plasma;
- **polariton** is a quasiparticle resulting from strong coupling of electromagnetic waves with the plasmons.

In summary the SPP are coherent longitudinal surface fluctuations of an electron plasma at the interface between two media usually a metal and a dielectric and interacting with an electromagnetic wave.

In this work we also encounter wave guide (WG) modes which are well characterized in a dielectric. They are related to the propagation of the electromagnetic field in a layer and their properties can be obtained as standing wave solutions of Maxwell's equations in a box. Through the use of the material equations, our model, based on electromagnetic theory, takes into account the material system. In a dielectric medium bordered by metals the electrons are trapped in a quantum well and will give rise to quantum well states of the electrons (see chapter

---

2). Since this work concentrates on the behavior of light, in the following we will concentrate on the WG states and the question of its relation to quantum well states remains open.

Next let us discuss the material systems sustaining SPP and WG modes. These systems can have diverse geometries. In the literature different geometrical forms have been studied:

- 2D samples with flat interfaces, the simplest being a three layer two interface stack. The first and the last layer are semi infinite and are called the cladding: symmetric for identical first and last layers and asymmetric otherwise. The middle layer is usually a thin film of a thickness smaller than the penetration/skin depth. One also studies n layer stacks so that one may increase the SPP intensity by tuning of n-2 thicknesses. These thicknesses are tuned to allow the penetration of the evanescent waves perpendicular to the interfaces through the thin films producing a non zero amplitude at the bottom interface. Parallel to the interfaces the SPP can be propagating or if the excitation is localized then the SPP can or can not be localized;
- 1D sample as for example wires and 2D systems periodic only in one direction, e.g. 2D samples having surface strips or stepped surfaces. Also one can have planar wave guides with a narrow region located in a wider wave guide;
- 0D samples including 2D samples with randomly oriented adsorbate or island-populated metal films (see Berini [1, sec 2.7]) and objects of nanometric size of any form including antennas.

The above classification neglects the interaction between the SPPs located in the different regions of the geometric space:

the SPP located at different interfaces of the 2D thin film stack can interact with each other giving rise to **composite SPP modes** having new physical properties. An example are the long and short range SPP (LRSPP and SRSPP, see e.g. Berini [1, sec. 2.2]) of the 3 layer thin film stack;

In the present study our sample permits the appearance of the composite SPP modes.

In the first half of the 20th century several theoretical attempts have been made to identify plasmons (Sommerfeld quoted by Economou [2]). In the 1950s, the pioneering work of Pines and Bohm [3; 4] solves for the first time the problem of the dense electron plasma quantum mechanically. The single electron Hamiltonian is re-expressed in such a way that the long-range part of the Coulomb interactions between the electrons is described in terms of collective fields, representing an organized "plasma" oscillation of the system as a whole. The obtained Hamiltonian describes these collective fields plus a set of individual electrons which interact with the collective fields and with one another via short-range screened Coulomb interactions.

Ritchie [5; 6] and Ferrell [7] solve the problem of a fast incident electron interacting with a plasma of free electrons. The dense electron plasma of Pines and Bohm, treated as a continuous

---

homogeneous medium, can be characterized by a dielectric function  $\varepsilon = f(\vec{k}, \omega)$  where  $\vec{k}$  is the wave vector of the electromagnetic disturbance in the metal. This is true if one considers the inter-electronic action over distances that are large compared to the inter-electronic spacing. In the Ritchie model [5] one solves the Poisson equation obtaining the absorption energy in relation to the surface plasmon excitation.

To our knowledge Ritchie [8] was the first to study the excitation of surface plasmons using light but he was interested in the observables related to the electrons. Later Economou [2] used the Pines and Bohm [3; 4] formulation of the problem in terms of plasma of electrons discussed above to solve the Maxwell and material equations simultaneously. The Drude permittivity is reduced to a simplified real form ( $\varepsilon = 1 - (\omega/\omega_p)^2$ , the exact real part of the permittivity is given in eq. (3.9)), and an analysis of the transverse and longitudinal components of Maxwell equations concluded that only transverse magnetic or "p" polarized light can excite surface plasmons. With his model, Economou studied thin film stacks made of consecutive dielectric and metallic layers (up to 7). A clear and detailed analysis of the dispersion performed by Franzen [9] (see chapter 3). He showed that the damping constant contributes to the real part of the wave vector and to the dispersion with the consequence that the surface-bulk plasmon gap disappears.

An extended discussion of the recent developments in the field of surface plasmons is given in a review paper by Pitarke *et al.* [10]. Pitarke *et al.* detail the experimental and theoretical work related to the identification and the characterization of the monopole  $\omega_s$  surface plasmon polariton (SPP) mode. They explain that the present models give good qualitative results for the free electron metals (Li, Na, K, Cs, Al and Mg) using the jellium (fixed uniform positive background occupying a half space plus a neutralizing cloud of electrons). For transition metals (Ag, Au and Hg) one must further add some screening or perform calculations using more involved models as for example the density functional theory.

In a review on nanometal plasmon polaritons, Akjouj *et al.* [11, section 5] have studied planar plasmonic wave guides. In particular, they have studied Ag-SiO<sub>2</sub>-Ag stacks of the metal insulator metal (MIM) type with an inserted cavity using a Finite Difference Time Domain (FDTD) algorithm with perfectly matched layer (PML) boundary conditions. As expected the cavity gives rise to a significant photon flux in the reflection and transmission but this result is due to the cavity not to the intrinsic properties of the thin film stack. Since the FDTD algorithm is general it permits any geometrical form of the sample, and in particular the studied cavity in a thin film stack.

Today a simple theoretical approach for studying an interface or the thin film stacks of interest in the present work, can be found in many books e.g. Born and Wolf [12, section 1.6], Potter [13], Raether [14, particularly the appendix], Maier [15, chapter 2], Sarid and Challener [16], Baltar *et al.* [17] and many others. There are also many semi-analytic and numerical approaches which solve implicitly or explicitly Maxwell equations:

- **plane wave electromagnetic fields and Fresnel model** of continuity at the interfaces of a thin film stack. These methods use the continuity of the fields at abrupt interfaces but do not solve the Maxwell or Helmholtz wave equations explicitly. Between the interfaces

---

one assumes a plane wave form of the field (see e.g. Lukosz and Kunz [18; 19], Novotny and Hecht [20; 21], Arnoldus and Foley [22] and Drezet and Genet [23] and many others);

- **explicit numerical calculations of the electromagnetic fields using** existing software, some of them open source:
  - **the integral Maxwell equations.** this software either effectively solves the integral form of Maxwell equations. Two examples of available software of this type are: DDSCAT: Discrete-dipole approximation (DDA) [24] and Draine and Flatau (2012) [25; 26], GranFilm: Optical Properties of Granular Thin Films, Ingve Simonsen and Rémi Lazzari, (2002-2012) [27], <http://web.phys.ntnu.no/~ingves/Software/GranFilm/Current/> and Generalized Field Propagator for electromagnetic scattering);
  - **the differential Maxwell equations in coordinate and time domains.** This software is mainly based on Finite Difference Time Domain (FDTD) methods initiated by a paper by Yee [28]. Following the book of Taflove and Hagness [29] one propagates the differential Maxwell equations simultaneously in the coordinate and the time domains. An example of FDTD software is MIT Electromagnetic Equation propagation (MEEP) software by Oskooi *et al.* (2010) [30];
  - **the differential Maxwell equations in the harmonic approximation and one numerical coordinate perpendicular on interfaces.** An example is the vector potential from the electron density (VPED) [31] but there are many other non-commercial and non-distributed softwares of this type.

How can SPP modes be excited in an experiment? Since the wave vector of light at the air-solid interface is smaller than the wave vector of the SPP mode, the SPP bound mode can not be excited without using special experimental set-ups. Otto [32; 33] and Kretschmann and Raether [34; 35] excited the SPP mode using light incident on a prism measuring the SPP dispersion of the reflectance (see chapter 4). Recently Barchiesi and Otto [36] revisited these two experimental configurations explaining that the Kretschmann configuration is easy to implement in a standard experiment whereas the Otto configuration can be used in the study of rough surfaces.

To permit the simultaneous measurement at all incident angles Kano *et al.* [37] excited surface plasmon polaritons (SPP) using a focused light. Other experiments use local sources of excitation: a near field scanning optical microscope (NSOM) [38] and its variants or a local source of electrons of low (STM) [39] or high energy (SEM) (see e.g. ref. [40; 41]).

Above we have seen that the sample can be excited by electrons or photons. The interaction of the source with matter can generate either photons or electrons measured by different experimental methodologies: when measuring the reflected (attenuated total reflection/reflectance (ATR), see e.g. Fahrenfort [42] or the transmitted photons (leakage radiation (LR) spectroscopy or microscopy, see e.g. Drezet *et al.* [43]) one uses continuous lasers of moderate intensity at definite angular frequencies (harmonic approximation). The spectra are analyzed as a function of the emission angle or in-plane wave vector  $k_p$  and the angular frequency. One is interested

---

in the nature and the interaction of the SPP modes, in the experimental conditions of their exaltation and the length of their propagation mean free path parallel to the interfaces;

In this work we investigate the optical properties of stacks made of metal-insulator-metal (MIM) thin films on a glass substrate. An SPP can be used to increase the interaction of light with matter due to their capacity to confine light at one or several interfaces. But the propagation length of SPPs is rather short and it is not useful for macroscopic transport of the light. Below we present some examples of this wide domain of study.

Berini [1] presented a well documented review of SPPs appearing in metal slabs and metal stripes. He discussed in detail the excitation conditions of these bound modes, the characterization of the long and short range SPPs and the main applications. Smith *et al.* [44] carefully studied three layers IMI and MIM thick film stacks and the coupling between the SPPs at the two interfaces. To characterize the nature of the SPP mode, namely its long or short range propagation character parallel to the interface Smith *et al.* calculate the electric field modulus perpendicular to the interfaces as a function of the penetration coordinate (see chapter 7). Relative to the interfaces, these fields can be symmetric or anti-symmetric and this symmetry may be used to characterize the nature of the SPP mode. Using angle-resolved electron energy-loss spectroscopy (AREELS) Saito *et al.* [45] have studied a seven-layer system air-Al<sub>2</sub>O<sub>3</sub>-Al-SiO<sub>2</sub>-Al-Al<sub>2</sub>O<sub>3</sub>-air. The agreement between the theoretical results, calculated using a model similar to the one of the present work, and the experiment is obtained only if one includes in the simulation the aluminum oxide. This indicates that the dispersion relations are sensitive to the presence of the very thin film insulators like Al<sub>2</sub>O<sub>3</sub>. To increase the SPP amplitude Yang *et al.* [46] use in a FDTD calculation a multilayer insulating structure cladded by a metal namely Au/SiO<sub>2</sub>/Al<sub>2</sub>O<sub>3</sub>/SiO<sub>2</sub>/Au. The excitation dipole source is in the first insulator at about 1 nm below the first interface. The total thickness of the dielectrics (Al<sub>2</sub>O<sub>3</sub> and SiO<sub>2</sub>) is about 100 nm, consequently the wave guide (WG) mode is absent. The presence of a composite dielectric layer modifies the effective refractive index of the dielectric and maximize the SPP mode by a significant factor (125%) compared to the three-layer (Au-SiO<sub>2</sub>-Au or Au-Al<sub>2</sub>O<sub>3</sub>-Au) .

Hayashi *et al.* [47] explore the photoluminescence (PL) properties of a dye layer embedded in an MIM structure. They clearly demonstrate the enhancement of PL intensities relative to those of the dye layer embedded in a reference sample without metal layers. Chance *et al.* [48] studied the fluorescence of molecules located above a metal surface or a insulator-metal surface. Choudhury *et al.* [49] focuses on tailoring fluorescence directionality using a planar metallic or dielectric and hybrid plasmonic-photonic structure.

SPR sensors employing conventional surface plasmons propagating along planar structures and their applications for detection of chemical and biological species are reviewed by Homola [50]. SPR sensors are thin-film refractometers that measure changes in the refractive index occurring at the surface of a metal film supporting a surface plasmon. These sensors are classified as sensors with angular [51], wavelength [52], intensity [53], or phase [54] modulation. White light excitation is often used in the analysis of the biological systems. For example Lan *et al.* [55] proposed a metal-insulator-metal (MIM) stack to simultaneously study the angular and spectral (white light) behavior of a surface plasmon resonance (SPR). Due to its rapidity and versatility this structure certainly has a promising impact on the development of SPR sensor

---

and biometric studies.

Before presenting our work let me discuss two papers related to the avoided crossing (anti-crossing) of interest in the present work. Ditlbacher *et al.* [56] discussed the coupling between the dielectric wave guide (called in this work simply wave guide (WG)) and surface plasmon polariton (SPP) modes. The system where these two modes are coupled is an air-SiO<sub>2</sub>(85 nm)-Ag (50nm)-SU8(700 nm)-glass substrate stack and it is analyzed by comparing it to two uncoupled systems: (A) air-SiO<sub>2</sub>(85 nm)-Ag (50nm)-SU8 substrate and (B) SiO<sub>2</sub>-Ag (50nm)-SU8(700 nm)-glass substrate. The uncoupled system (A) sustains the dielectric wave guide (WG) mode and the system (B) sustains the SPP mode. The uncoupled WG and SPP modes have the maximum of the magnetic field  $|H|^2$  in the dielectric layer and at the air-Ag interface respectively. Using these three systems Ditlbacher *et al.* [56] characterized the avoided crossing taking place at  $\lambda=500$  nm. Refki *et al.* [57] studied a BK7-Ag-PMMA-Ag-air five-layer stack and measured the attenuated total reflexion (ATR) and calculated the observables using a 2X2 transfer matrix algorithm to characterize the nature of the SPP modes and their coupling. The authors demonstrated the coupled-mode nature of the SPP modes in an MIM structure and demonstrated the avoided crossing (anticrossing) behavior of the dispersion curves (see figures 4 and 6 of the reference [57]).

The difference between the few examples presented above and the present work is that our study systematically varies the geometrical parameters of the thin film in a search for the appropriate geometrical parameters for the experimental measurements. Contrary to Ditlbacher *et al.* [56] we have studied the SPP-WG avoided crossing (anti-crossing) in less detail. In this work I present our simulations of a six-layer thin film stack of dielectrics and gold where the reflectance, the transmittance and the transmitted flux of a local source display surface plasmon polariton (SPP) and wave guide (WG) modes. The excitation is either from a source of light located at infinity (reflectance, transmittance) or a local source (transmitted flux) of inelastic tunneling electrons provided by an STM. The interfaces are flat and the modeling is performed, following Abèles-Bethune optical transfer matrix algorithm, using elementary Fresnel expressions at the interface and plane wave propagation in the layers. The reflected and the transmitted photon flux from a source at infinity and the transmitted flux of a local source are calculated and they are compared to the experiments performed in our group.

Chapter 2 presents the samples we will study, namely the thin film stacks, from the point of view of electronic theory. Our interest is in the consequences of the appearance of interfaces on the band structure. Due to this symmetry breaking we will see that surface and quantum well states appear. As discussed in the conclusion (section 2.3) the surface or Tamm states can interact with surface plasmon polaritons.

Chapter 3 reviews the elementary theory of plasmons at single and multiple flat interfaces. We were interested in a study where the stack is a combination of insulating and metallic thin films. In such a case one must extend the Descartes-Snell relations to absorbing media.

In a short chapter 4 we discuss the experimental set-ups permitting the excitation of the SPP modes of a thin film stack. The understanding of the experiment is important for us since it permits a better exchange with the experimentalists with whom we are collaborating.

Chapter 5 presents our models for the excitation with the source at infinity (ESI) and the oscillating dipole (OD) model. We do not solve Maxwell equations explicitly but instead take into account the tangential continuity of the fields at the interface. In both the ESI and the OD models the Fresnel coefficients of the multilayer thin film stack are calculated using the transfer matrix algorithm initiated by Abelès in the implementation of Bethune [58]. For the OD model we use the papers of Lukosz and Kunz [18; 19], Novotny [20], Bharadwaj *et al.* [59], Drezet and Genet [23], Marty *et al.* [60] and Arnoldus and Foley [22; 61].

Chapter 6 presents the main results of the present work. It shows the modeling of the excitation of the three and six layer thin film stacks. We restrict the geometrical parameters of the six-layer stack to two thicknesses,  $d_{\text{SiO}_2}$  for the dielectric and  $d_{\text{Au}}$ , identical for the two layers of the gold (see figure 1.1). The first part of this chapter discusses the reflectance and transmittance obtained from the excitation of a laser source located at infinity of the six-layer stack. The second part of this chapter presents the calculation of the transmitted flux corresponding to the leakage radiation microscopy of a stack excited by a local source of electrons or photons located a few nanometers above the surface. The last part of the chapter presents our results in coordinate space shining a different light on our modeling. For a six layers stack we find two modes: a surface plasmon polariton mode (SPP) and a wave guide mode (WG). The WG mode appears when the dielectric SiO<sub>2</sub> layer is greater than 190 nm and we identify an avoided crossing (anti-crossing) between these two modes.

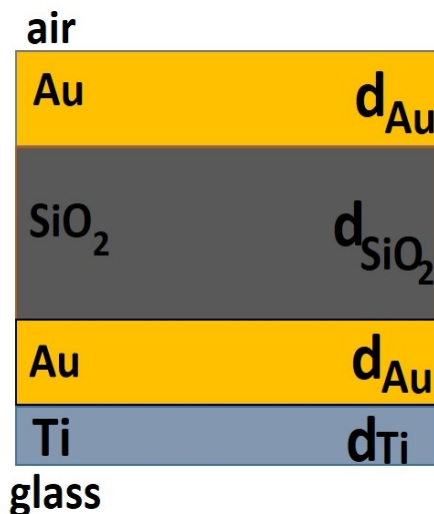


Figure 1.1: Six-layer thin film stack air-Au ( $d_{\text{Au}}$ )-SiO<sub>2</sub> ( $d_{\text{SiO}_2}$ )-Au ( $d_{\text{Au}}$ )-Ti ( $d_{\text{Ti}}$ )-glass.

Chapter 7 presents the behavior of the electric field as a function of the coordinate perpendicular to the interface. This behavior characterizes the location of the field in the stack permitting the assignment of the nature of the mode: SPP or WG.

The last chapter is a conclusion giving some ideas for future work.

## Chapter 2

# Electronic and photonic modes of a thin film stack: quantum well and wave guide modes

A crystal is periodic in the three dimensions. The electronic states of a solid are organized in bands, particularly valence and conduction bands. The 3D periodicity is broken in one direction by the presence of a surface or an interface, and its presence leads to a change of the electronic band structure. In this short chapter I discuss the electronic and photonic bound states or modes appearing in the many layers stacks with flat interfaces. In a stack the first and the last layer are semi-infinite, and will be called the cover layer and the substrate or cladding. For the electrons a thin film corresponds to a quantum well of width  $L$  and it can sustain quantum well states/modes (QWS) and surface states/modes. When a laser excites a thin film stack containing a dielectric layer cladded by other dielectrics or metals at particular wave length wave guide modes (WG) appear. Both QWS and WG are governed by a wave equation: (i) Schrödinger equation for the quantum mechanical description of the QWS of the electrons; (ii) photon wave equation of the classical wave description of the photons.

The above mentioned QWS and WG mode can be calculated for abrupt interfaces. A surface state appearing at a single or multiple interface is sustained by a shallower potential well compared to the bulk and can be calculated only if the corresponding potential and electron density change smoothly at the interface.

This chapter presents these states and their relation with the WG states we have calculate for our stacks in the rest of this work.

## 2.1 Surface and thin film electronic states

### 2.1.1 A solid bordered by a surface: surface and image states

It can be shown (see e.g. Zangwill [62, chap: 4]) that the presence of a surface gives rise to a supplementary boundary condition in the Schrödinger equation. Then an associated new single-particle localized bound electronic state, i.e. the surface state, appears usually in the valence-conduction band gap. The simplest model to discuss these states is the phase accumulation model (PAM) introduced among others by Echenique and Pendry [63] (see also Smith [64]). In this model a bound state appears if the sum of the phase of the system is an integer  $l$  of  $2\pi$  (Echenique and Pendry [63, eq. (5)])

$$\phi_C + \phi_B = 2\pi l, \quad (2.1)$$

where  $\phi_C$  is the phase shift of the periodic potential of the crystal (solid),  $\phi_B$  bound surface state phase shift towards the vacuum and  $l$  the quantum number of the state. The above expression imply viewing a surface state as being trapped between the bulk crystal and the surface barrier. The first member in the series with  $l = 1$  is the surface state the members with  $l > 1$  are called image states and they form a Rydberg like series. Precisely, this series is equivalent to a Rydberg series in atoms where the radial coordinate  $r$  is replaced by the  $z$  coordinate normal to the interface.

In the literature a surface state is calculated using two numerical models:

- **a nearly free electron model**, where the wave function is a product of a plane wave and a periodic function corresponding to a weak periodic perturbation. In this case the surface state is called a **Shockley state**;
- **a tight-binding model**, where the electronic wave functions are expressed as linear combinations of atomic orbitals (LCAO). In this case the surface state is called **Tamm state**. The Schrödinger equation is written in a matrix form and each element is an integral  $\langle \text{basis function} | \text{Hamilton operator} | \text{basis function} \rangle$  and the solid state bands are obtained by diagonalizing this matrix. The TB model is a simplification of the LCAO model where the integrals are not explicitly calculated but obtained from tables given in the literature.

Equation (2.1) gives the phase shift condition for the appearance of the surface and image states but the method of calculation of the phase shifts and its approximations are not specified. One can calculate the PAM phases for an abrupt surface/interface consequently no surface and image states will be present. Or, if the potential is continuous, then as it can be seen in figure 2.1 (left graph) the first well from left is shallow and can sustaining a surface and image states.

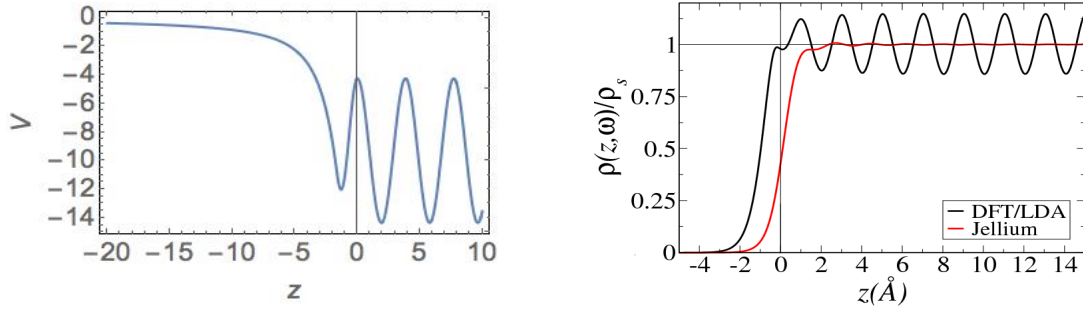


Figure 2.1: Potential and density of states at an interface. The solid is either jellium or Ag(001).

In summary following Echenique and Pendry [63] a surface state can be calculated using the PAM provided the surface phase shift  $\phi_B$  is obtained using a smooth and continuous potential and electron density.

### 2.1.2 Electronic states associated to a single thin film: Quantum well states

Consider now a single film with two interfaces consisting of a number of atomic layers. In quantum mechanics the obvious model of such a system is a one-dimensional box in the direction perpendicular to the interface. In this model the wave vector  $k$ , the energy  $E$  and the wave function  $\psi(z)$  read

$$k = \frac{l\pi}{d} \quad E = \frac{\hbar^2 k^2}{2m} = \frac{\hbar^2}{2m} \left( \frac{l\pi}{d} \right)^2 \quad \psi(z) = \sin(kz) = \sin\left(\frac{l\pi z}{d}\right)$$

where  $m$  is the electron mass,  $d$  is the film thickness and  $l$  is the number of the quantum well state. The quantization conditions given in the above equation are valid for an infinite potential barrier. Parallel to the interfaces the solid state periodicity is conserved. But in the present model these interfaces are structureless since in our range of wavelengths, i.e.  $\lambda(nm) \in [500, 1100]$  the atomic structure is not visible.

Consider now a thin film with a metallic and a dielectric claddings. Following Forster *et al.* [65] the PAM, giving the appearance condition for the surface state in eq. (2.1) above can be extended for a thin film stack with two interfaces

$$\phi_C + \phi_B + 2k_{\perp}d = 2\pi l, \quad (2.2)$$

where the surface barrier phase shift  $\phi_B$  is calculated using an abrupt or a smooth interface,  $k_{\perp}$  is the wave vector perpendicular to the surface and  $d$  is the depth of the thin film. Again here  $l$  is the number of the quantum well state.

## 2.2 Photonic wave guide (WG) mode

### 2.2.1 Model

Let us consider a simplified WG model corresponding to a stationary photonic wave equation solution of the electric field in a box (see e.g. Saleh and Teich [66, section 7.2]). The planar wave guide Au-SiO<sub>2</sub>-Au is presented in left graph of figure 2.2. The stationary waves are defined by a zero amplitude of the fields at the boundaries of the square well

$$\frac{2\pi}{\lambda} 2n_{SiO_2} d \cos \theta - 2\varphi_z = 2\pi l \quad m = 0, 1, 2, \dots \quad (2.3)$$

where  $\lambda$  is vacuum wavelength,  $n_{SiO_2}$  and  $d$  are the refractive index and the thickness of SiO<sub>2</sub> layer,  $\theta$  the angle relative to the normal of the wave guide boundary and  $\varphi_z$  the phase change at the boundary of the square well. This phase  $\varphi_z$  is obtained from the reflection coefficient of the SiO<sub>2</sub>/Au interface as the argument of the refraction coefficient

$$r_p = \frac{n_{Au} \cos \theta_{SiO_2} - n_{SiO_2} \cos \theta_{Au}}{n_{Au} \cos \theta_{SiO_2} + n_{SiO_2} \cos \theta_{Au}} \quad \tan \varphi_z = \frac{\text{Im}(r_p)}{\text{Re}(r_p)}$$

The above coefficient are valid for complex refractive indexes.

Manipulating eq. (2.3) one obtains the incident angle  $\theta^l$

$$\theta^l = \cos^{-1} \left( \frac{\pi l + \varphi_z}{2\pi d n_{SiO_2}} \lambda \right).$$

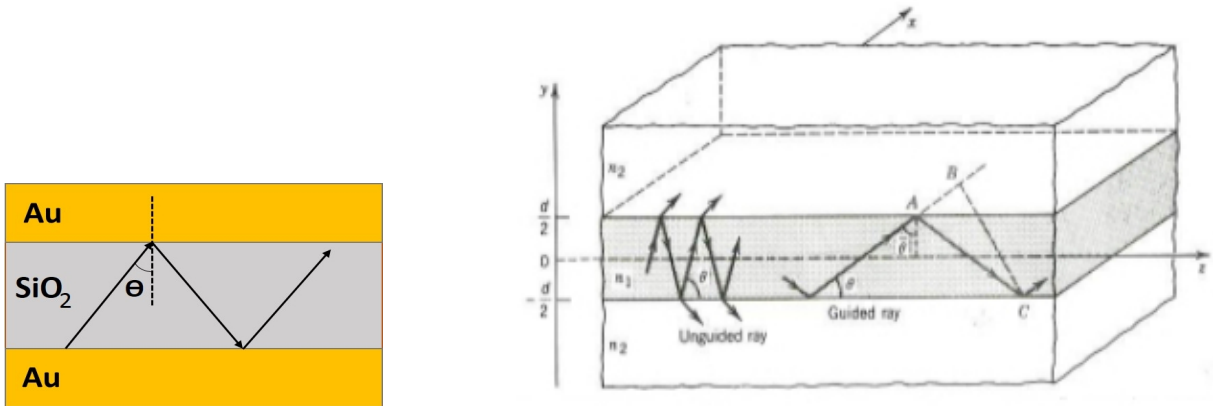


Figure 2.2: **Left graph:** Au-SiO<sub>2</sub>-Au planar wave guide; **Right graph:** Planar dielectric wave guide. Rays making an angle  $\theta < \theta_c = \cos^{-1}(n_2/n_1)$  are guided by the total internal reflection. Here  $\bar{\theta} = \pi/2 - \theta$ ,  $d$  is the depth of the planar wave guide and  $n_1 > n_2$  permitting the appearance of the wave guide modes. Figure 7.2-1 of Saleh and Teich [66]).

The normalized in-plane wave vector  $k_\rho^l/k_0$  is calculated using this angle

$$k_\rho^l/k_0 = n_{SiO_2} \sin \theta_1^l.$$

### 2.2.2 Thin films and the WG modes penetration depth

In the present work we are interested in the propagation of light through a thin film stack of three or six layers. The layers must be thin enough to permit the light to propagate through the stack and not be completely absorbed at the last interface. In a plane wave formulation of light propagation the attenuation is proportional to the imaginary part of the plane wave vector. The penetration depth (derived in detail in chapter 3) is the distance from the interface where the power has decayed by a factor of  $1/e$ . The origin of the attenuation is two fold:

- **penetration depth of an evanescent wave:** consider the simplest case of an interface between two dielectric media of different refractive indices. If the light is incident from the material with the high refractive index, then there exist a critical angle  $\theta_c$  at which the light is totally reflected and no transmission occurs. The corresponding field is evanescent and the wave vector becomes purely imaginary. The penetration depth reads

$$\delta \approx \frac{1}{2 \operatorname{Im}(k_z)} \quad \theta \geq \theta_c$$

where  $\operatorname{Im}(k_z)$  is the imaginary part of the perpendicular component of the wave vector.

- **skin depth of a metal:** The skin depth is related to the imaginary part  $\kappa$  of the refractive index  $\tilde{n} = n + i\kappa$  which is significant in metals. Correspondingly the wave vector is also complex. The skin depth is given by an approximate expression

$$\delta \approx \frac{c}{\kappa \omega} \approx \frac{1}{\operatorname{Im}(k)}$$

In summary, in the present work we consider that a film is thin enough such that the light reaches the second interface. For a stack of thin films their thickness is such that the light reaches the last interface and one can measure a non zero transmitted flux intensity. The two definitions above imply that if one of the media is a metal, the penetration depth and the skin depth must be summed up giving rise to a larger absorption in the material.

## 2.3 Conclusion

In this chapter we used the boundary condition of two second order differential equations respectively of the motion of electrons or photons to discuss the QWS, WG modes and surface states. For both differential equations one uses the boundary conditions at the limit of the

potential well to obtain the position of the states/modes. What approximations are effectively included in a model depends on how the phase shifts are calculated:

- for QWS one solves the Schrödinger equation usually excluding the laser-matter interaction considered to be a weak interaction. But at interfaces the potential well and the associated electron densities are continuous allowing the calculation of the surface states;
- for WG modes the material system is introduced through the material functions but, since one is using Fresnel theory at abrupt interfaces, one is unable to take into account surface states.

In fact, as for the surface plasmon polaritons (SPP) discussed in the next chapter, in a perfect model the QWS and WG mode will interact with each other giving rise to a composite electron-photon mode related to the potential well of the thin film. In the conclusion of this work I will mention papers showing the interaction between the SPP and WG modes and the surface states.

The rest of the thesis uses models based on the Fresnel theory at abrupt interface and therefore we will be unable to include surface states in our modeling. In chapter 6 section 6.4.4 we will use the results of the WG mode section 2.2 above to analyze the nature of the modes found in the experiment and in our model.

# Chapter 3

## Plasmon properties and their dispersion

In this chapter I will first introduce bulk and surface plasmons and explain the conditions of their appearance. Then I will present Snell's law at dielectric-dielectric and dielectric-metal interfaces. Further, I will derive an analytical expression for dispersion in the case of one interface systems where one of the media is metallic. I will discuss qualitatively two interface systems including the coupling between the SPP modes. Finally, I will introduce the dispersion relation for n interface systems.

### 3.1 Bulk and surface plasmon polaritons

The introduction of the present work detailed the historical development of the field of plasmons. Briefly in the 1950s the pioneering work of Pines and Bohm [3; 4] solves for the first time the problem of the dense electron plasma quantum mechanically. The single electron Hamiltonian is re-expressed in such a way that the long-range part of the Coulomb interactions between the electrons is described in terms of collective fields, representing organized "plasma" oscillations of the system as a whole. The Hamiltonian describes these collective fields plus a set of individual electrons which interact with the collective fields and with one another via short-range screened Coulomb interactions.

Ritchie [5] and Economou [2] used the Pines and Bohm [3; 4] formulation of the problem in terms of plasma of electrons discussed above solving the Maxwell and material equations simultaneously. The Drude permittivity is reduced to a real form ( $\varepsilon = 1 - (\omega/\omega_p)^2$ ) and an analysis of the transverse and longitudinal components of Maxwell equations concludes that only transverse magnetic or "p" polarized light can excite surface plasmons. A clear and detailed analysis of the dispersion using a Drude dielectric function including damping is due to Franzen [9], analysis which is at least partly reproduced in this chapter.

Instead of following the quantum mechanic description of matter coupled with to the classi-

cal description of light using Maxwell equation, in the following we will derive the bulk plasmon polarization using the simplest possible approach based on the Newton equation, approach which can be found in many textbooks (see e.g. Born and Wolf [12], Kittel [67], Jackson [68]).

### 3.1.1 Drude permittivity

The permittivity  $\varepsilon$  or dielectric function describes the behaviour of matter in interaction with an electric or electromagnetic field. To a first approximation the electrons of a metal can be described as an electron gas. The associated dielectric function depends on the angular frequency  $\omega$  and on the wave vector  $\vec{k}$ , i.e.  $\varepsilon(\omega, \vec{k})$ .

Many books discussing the behavior of the electrons in a solid present the Lorentz and Drude models of the material function (see e.g. Wooten [69], Ashcroft and Mermin [70], Born and Wolf [12], Jackson [68], [67] and Maier [15]). The derivations of the macroscopic polarization  $\vec{P}$  are based on the Newton (see e.g. Wooten [69]) or microscopic Boltzman equations (see e.g. refs.[71; 72]).

The Newton equation of motion of the electrons reads

$$m^* \frac{d^2 \vec{r}}{dt^2} + m^* \Gamma \frac{d\vec{r}}{dt} + m^* \omega_0^2 \vec{r} = e \vec{E}_{loc}. \quad (3.1)$$

where  $m^*$  is the effective electron mass. The term containing the first derivative is a damping force  $\vec{F}_{damping} = m^* \Gamma \frac{d\vec{r}}{dt}$  with the damping constant  $\Gamma$  corresponding to the various inelastic scattering mechanisms in the solid. The electron is bounded by a harmonic oscillator force  $\vec{F}_{binding} = m^* \omega_0^2 \vec{r}$  of frequency  $\omega_0$ . The external  $\vec{E}_{loc}$  field is a local, microscopic electric field. If the local field oscillates in time (i.e.  $E \sim e^{-i\omega t}$ ), the solution of the Newton equation reads

$$\vec{r} = \frac{e \vec{E}_{loc}}{m^* (\omega^2 - \omega_0^2 + i \Gamma \omega)}. \quad (3.2)$$

Now one can define the induced dipole moment  $\vec{p}$

$$\vec{p} = -e \vec{r} = -\frac{e^2 \vec{E}_{loc}}{m^* (\omega^2 - \omega_0^2 + i \Gamma \omega)} = \alpha \vec{E}_{loc}, \quad (3.3)$$

where  $\alpha$  is the frequency dependent atomic polarizability. The macroscopic polarization  $\vec{P}$  reads

$$\vec{P} = \rho_s \langle \vec{p} \rangle = \rho_s \alpha \langle \vec{E}_{loc} \rangle = \varepsilon_0 \chi \vec{E}, \quad (3.4)$$

where  $\rho_s$  is the electron density per unit volume of the solid,  $\langle \vec{E}_{loc} \rangle$  is the average of the

microscopic field  $\vec{E}_{loc}$ . In general  $\langle \vec{E}_{loc} \rangle \neq \langle \vec{E} \rangle$  but since the conduction electrons are not bound, the field experienced by the conduction electrons is on average simply the macroscopic field  $E$  [69], and finally  $\chi$  is the macroscopic electron susceptibility. The electron density  $\rho_s$ , is expressed in terms of the volume occupied by an electron

$$\rho_s^{-1} = (4\pi/3)[r_s]^3, \quad (3.5)$$

where  $r_s$  is the Wigner Seitz radius. The average induced dipole moment  $\langle \vec{p} \rangle$  and the polarization  $\vec{P}$  now read

$$\begin{aligned} \rho_s \frac{d^2}{dt^2} \langle \vec{p} \rangle + \rho_s \Gamma \frac{d}{dt} \langle \vec{p} \rangle + \rho_s \omega_0^2 \langle \vec{p} \rangle &= \rho_s \frac{e^2}{m^*} \langle \vec{E}_{loc} \rangle && \text{microscopic} \\ \frac{d^2}{dt^2} \vec{P} + \Gamma \frac{d}{dt} \vec{P} + \omega_0^2 \vec{P} &= \varepsilon_0 \omega_p^2 \vec{E} && \text{macroscopic.} \end{aligned}$$

Comparing the above equations, one can define the bulk plasmon frequency  $\omega_p$

$$\omega_p^2 = \frac{e^2 \rho_s}{m^* \varepsilon_0}, \quad (3.6)$$

Note that the link between the microscopic and macroscopic descriptions is  $\rho_s$  the electron density per unit volume. Using eqs (3.3) and (3.4) we obtain the relative susceptibility of the electron  $\chi$  and the permittivity or dielectric function  $\varepsilon$ <sup>1</sup>

$$\chi = - \frac{\omega_p^2}{\omega(\omega + i\Gamma) - \omega_0^2} \quad (3.7)$$

$$\varepsilon = 1 + \chi = 1 - \frac{\omega_p^2}{\omega(\omega + i\Gamma) - \omega_0^2} = \varepsilon^r + i\varepsilon^i \quad (3.8)$$

---

<sup>1</sup> In the SI system of units used in this text  $\bar{\varepsilon} = \varepsilon_0 \varepsilon$  where  $\bar{\varepsilon}$ ,  $\varepsilon_0$  and  $\varepsilon$  are the absolute, vacuum and relative permittivities. The sign of the imaginary part of the relative permittivity  $\varepsilon = \varepsilon^r \pm i\varepsilon^i$  and of the refractive index  $\bar{n} = \sqrt{\bar{\varepsilon}} = n \pm i\kappa$  is in principle arbitrary but should correspond to an absorption in the solid. A given sign convention of the imaginary part of the refractive index fixes the sign of the imaginary part of the permittivity. Two conventions are used:

- "spectroscopic" convention  $\bar{n} = n - i\kappa$  corresponding to  $\varepsilon = \varepsilon^r - i\varepsilon^i$ . For  $z > 0$  one uses  $k_z = (\omega/c)(n - i\kappa) \cos \theta$ , where  $\theta$  is the light incident angle, giving the plane wave form

$$\exp[-i k_z z] = \exp[-i(\omega/c)(n - i\kappa) \cos(\theta) z] = \exp[-i(\omega/c)n \cos(\theta) z] \exp[-(\omega/c) \kappa \cos \theta z]$$

- "plasmonic" convention  $\bar{n} = n + i\kappa$  corresponding to  $\varepsilon = \varepsilon^r + i\varepsilon^i$ . For  $z > 0$  one uses  $k_z = (\omega/c)(n + i\kappa) \cos(\theta)$ , giving the plane wave form

$$\exp[i k_z z] = \exp[i(\omega/c)(n + i\kappa) \cos \theta z] = \exp[i(\omega/c)n \cos(\theta) z] \exp[-(\omega/c) \kappa \cos \theta z]$$

In the present formulation I am using the "plasmonic" convention.

The real and imaginary parts of the Drude permittivity equation (3.8) are

$$\varepsilon^r = 1 - \frac{\omega_p^2(\omega^2 - \omega_0^2)}{(\omega^2 - \omega_0^2)^2 + \omega^2\Gamma^2} \quad \varepsilon^i = \frac{\omega\Gamma\omega_p^2}{(\omega^2 - \omega_0^2)^2 + \omega^2\Gamma^2} \quad (3.9)$$

### 3.1.2 Electromagnetic waves in metals: bulk plasmons (BP)

A bulk plasmon is a collective oscillation of the free electron gas of a metal. The right hand side inhomogeneous term of the Newton equation (3.1) corresponds to an external electric field. Therefore the BP appears when an external electric field is present and its wave vector  $k_p$  reads

$$k_p = \frac{\omega_p}{c} = \sqrt{\rho_s \frac{e^2}{\varepsilon_0 m^*}} \sqrt{\varepsilon_0 \mu_0} = \sqrt{\rho_s \frac{e^2 \mu_0}{m^*}}. \quad (3.10)$$

where  $\omega_p$  is given in eq. (3.6) above. Being dependent on  $\rho_s$ , the BP frequency  $\omega_p$  measures the system electronic density (see also Kittel [67, p.273] and Ritchie [6]). The bulk plasmon can be considered as a quasiparticle since it arises from the quantization of plasma oscillations. For conduction electrons  $\omega_0 = 0$  and  $\Gamma=0$  (eq. 3.7), the real part of the metal dielectric function presented in figure 3.1 reads:

$$\varepsilon^r = 1 - \frac{\omega_p^2}{\omega^2} \quad (3.11)$$

The Helmholtz wave equation for homogeneous media in the time harmonic approximation

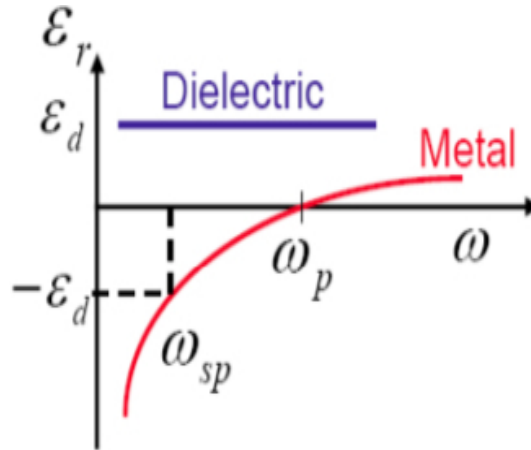


Figure 3.1: Real part of the metal permittivity function of  $\omega$  in the attenuation ( $\omega < \omega_p$ ) and propagation ( $\omega > \omega_p$ ) regions [73]

and plan wave electric field (no charge nor current) read as

$$-\vec{\nabla}(\vec{\nabla} \cdot \vec{E}) + \nabla^2 \vec{E} = \frac{\varepsilon(\vec{k}, \omega)}{c^2} \frac{\partial^2 \vec{E}}{\partial t^2} \quad (3.12)$$

$$\vec{k}(\vec{k} \cdot \vec{E}) - k^2 \vec{E} = -\varepsilon(\vec{k}, \omega) \frac{\omega^2}{c^2} \vec{E} \quad (3.13)$$

Depending on the polarization of the electric field vector, two cases can be distinguished:

1. **Transverse waves**  $\vec{k} \cdot \vec{E} = 0$  yielding the dispersion relation

$$k^2 = \varepsilon(\vec{k}, \omega) \frac{\omega^2}{c^2} \quad (3.14)$$

Using eqs. (3.11) and (3.14) one obtains the dispersion relation of propagating transverse waves of bulk plasmons (see figure 3.2)

$$\frac{\omega^2}{\omega_p^2} = 1 + \frac{k^2 c^2}{\omega_p^2}. \quad (3.15)$$

Eq. (3.15) is plotted in figure 3.2 for a generic free electron metal. Two regimes can be

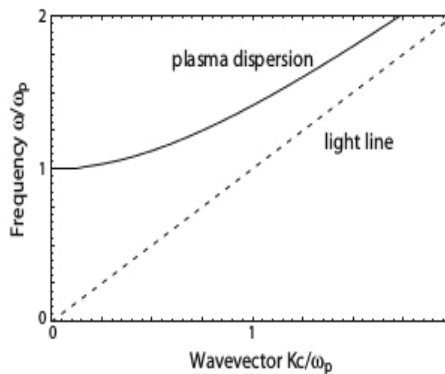


Figure 3.2: The dispersion relation of the bulk plasmons for a free electron gas. The transverse electromagnetic wave is only allowed for  $\omega > \omega_p$  (following Maier [15, figure 1.3]).

distinguished (see Figures 3.1 and 3.2):

- (i)  $\omega < \omega_p$ , **forbidden, attenuation or no penetration**, the propagation of transverse electromagnetic waves is forbidden inside the solid (see e.g. ref [15, chap. 1]);
- (ii)  $\omega \geq \omega_p$ , **allowed propagation, penetration** in the solid or **transparent** solid region. The bulk plasmon appears in this regime. In figure 3.2, the curve above the light line corresponds to the dispersion of the bulk plasmon. The dispersion of the bulk plasmon will be discussed below together with surface plasmons.

2. **Longitudinal waves** described in eq. (3.13) satisfy the relation

$$\varepsilon(\vec{k}, \omega) = 0 \quad (3.16)$$

In a solid the bulk (volume) plasmon appears in the transparency regime when the permittivity changes sign at frequencies equal or larger than the bulk plasmon frequency  $\varepsilon(\vec{k}, \omega)_{\omega \geq \omega_p}$ . Precisely, as in figure 3.2, above  $\omega_p$  a dispersion curve of the bulk plasmon can be plotted. For more details see section 3.3.1.1 and Kittel [67], Sarid and Challener [16] and Maier [15, chap. 1]. The longitudinal oscillations of the electric field in a solid can appear only for  $\varepsilon(\omega) = 0$ . This is because the Gauss-Maxwell law in the absence of charges reads

$$\begin{array}{ll} \text{coordinate} & \vec{\nabla} \cdot \vec{D} = 0 \\ & \vec{D} = \varepsilon(\omega) \vec{E} \end{array} \quad \begin{array}{ll} \text{momentum} & \vec{k} \cdot \vec{D} = 0 \end{array}$$

The scalar product between  $\vec{k}$  and  $\vec{D}$  above shows that the displacement must be perpendicular on the propagation direction, i.e. transverse. Except if the displacement itself is zero which is true only if the permittivity  $\varepsilon(\omega)$  is zero. The zero displacement gives

$$\vec{D} = \varepsilon_0 \vec{E} + \vec{P} = 0 \quad \varepsilon_0 \vec{E} = -\vec{P} \quad (3.17)$$

where  $\vec{P}$  is the longitudinal polarization and  $\vec{E}$  is the depolarization field. The phenomenological build up of the electric field is very well explained in Kittel [67, p. 277, figs. 4 and 5] in relation with the plasma oscillations.

### 3.1.3 Polaritons, surface plasmons polariton (SPP) and surface plasmons (SP)

1. A **Polariton** is a boson quasiparticle resulting from the strong coupling of electromagnetic waves with an electric or magnetic dipole-carrying excitation. Figure 3.3 presents the uncoupled (red lines) and coupled (black line) dispersion curves of a polariton. As in other avoided crossings in physics, this one has a frequency band gap (see between the horizontal lines in figure 3.3).
2. **Surface plasmon polaritons (SPP)** are coherent longitudinal surface fluctuations of an electron plasma at the interface between two media usually a metal and a dielectric that is coupled to an electromagnetic wave. It can also be seen as an electrical polarization wave at the interface between two media (see figure 3.4).
  - The SPP are particular solutions of the Faraday and Ampère-Maxwell equations in each region of the permittivity  $\varepsilon$ . At the interface the obtained solutions are matched using appropriate boundary conditions. Perpendicular to the interface the SPP are bound. Parallel to a flat infinite interface the SPP are propagating, and in a nanostructure they are localized.

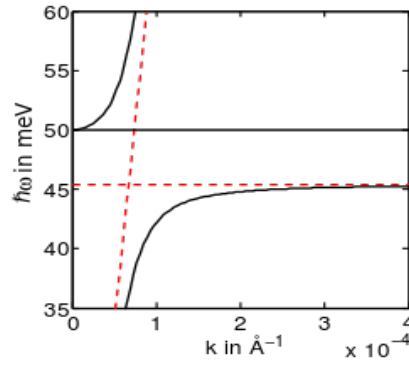


Figure 3.3: Dispersion relation of polaritons in GaP. The red curves are the uncoupled phonon and photon dispersion relation, and the black curves are the result of coupling (from top to bottom: upper polariton, lower polariton). (From wikipedia polariton definition).

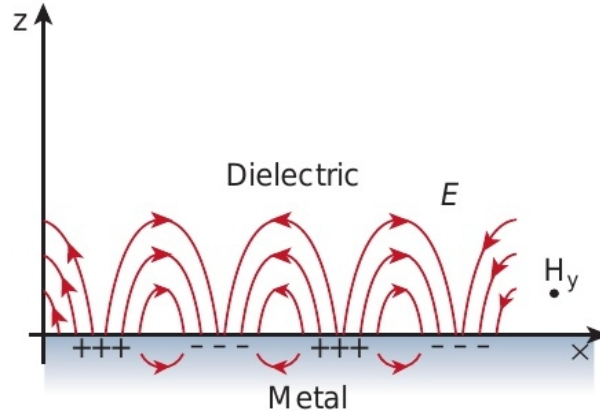


Figure 3.4: At an interface between a metal and a dielectric material the surface plasmon polaritons (SPP) have a combined electromagnetic wave and surface charge (alternatively positive and negative) character. The electromagnetic wave is transverse magnetic (TM) or  $p$  linearly polarized, i.e.  $\vec{H}$  is in the  $y$  direction and  $\vec{E}$  is in a plane normal to the interface [74].

The frequency dependent SPP wave vector reads (see eq. (3.53) below)

$$k_{SPP} = \frac{\omega}{c} \sqrt{\frac{\varepsilon_d \varepsilon_m}{\varepsilon_d + \varepsilon_m}} \quad (3.18)$$

where  $\varepsilon_m$  and  $\varepsilon_d$  are the permittivities of the absorbing/metallic and dielectric media. Using the Drude expression of  $\varepsilon_m$  given in eq. (3.11), the above SPP wave vector reads

$$k_{SPP} = \frac{\omega}{c} \sqrt{\frac{\varepsilon_d \left(1 - \frac{\omega_p^2}{\omega^2}\right)}{\varepsilon_d + 1 - \frac{\omega_p^2}{\omega^2}}} \quad (3.19)$$

3. **Surface plasmon (SP) resonance:** The SP appears at an interface between two materials with the real part of their permittivity having opposite signs. At the dielectric-metal interface this gives  $\varepsilon_m^r = -\varepsilon_d$ , where  $\varepsilon_m^r$  and  $\varepsilon_d$  are the dielectric functions of the metal and dielectric, respectively (see figure 3.1).

$$k_x = \lim_{\omega \rightarrow \omega_{sp}} \frac{\omega}{c} \sqrt{\frac{\varepsilon_d(\omega^2 - \omega_p^2)}{(1 + \varepsilon_d)\omega^2 - \omega_p^2}} \rightarrow \infty \quad \text{for} \quad \omega_{sp} = \frac{\omega_p}{\sqrt{1 + \varepsilon_d}} = \frac{\omega_p}{\sqrt{2}}, \quad (3.20)$$

where in the last equality  $\varepsilon_d = 1$ . The wave vector projection  $k_x \rightarrow \infty$  corresponds to the position of the surface plasmon resonance

$$\boxed{\text{SP} = \lim_{k_x \rightarrow \infty} [\text{SPP}]}$$

## 3.2 Continuity of the wave vectors and fields at an interface. Descartes-Snell law

This section defines the Descartes-Snell law at an interface that will be used later in this chapter in the study of the SPP in thin film stacks.

### 3.2.1 Descartes-Snell law at a dielectric-dielectric interface

Consider light of frequency  $\omega$  and wave vector  $\vec{k}$  incident on a flat boundary between two dielectric homogeneous isotropic media. Figure 3.5 presents the geometry of the problem for  $s$  or transverse electric (TE, left graph) and  $p$  or transverse magnetic (TM, right graph) polarizations. This plane wave is split into a transmitted wave with wave vector  $\vec{k}^{(t)}$  propagating into the second medium and a reflected wave with wave vector  $\vec{k}^{(r)}$  propagating back into the first medium. The plane of incidence is defined by  $\vec{k}$  and the normal  $\vec{n}$  to the boundary. The permittivities of the media above and below the plane  $z=0$  are respectively  $\varepsilon_s \equiv \varepsilon_t$  and  $\varepsilon \equiv \varepsilon_i$ .

The electric fields of the incident, reflected and refracted wave read

$$E^{(i)} = E_0^{(i)} e^{(i\vec{k}^{(i)} \cdot \vec{r} - i\omega t)} \quad E^{(r)} = E_0^{(r)} e^{(i\vec{k}^{(r)} \cdot \vec{r} - i\omega t)} \quad E^{(t)} = E_0^{(t)} e^{(i\vec{k}^{(t)} \cdot \vec{r} - i\omega t)} \quad (3.21)$$

The wave vectors have the magnitudes :

$$\begin{aligned} |\vec{k}^{(i)}| &= |\vec{k}^{(r)}| = k = \frac{\omega}{c} \sqrt{\varepsilon_i} \\ |\vec{k}^{(t)}| &= k^{(t)} = \frac{\omega}{c} \sqrt{\varepsilon_t} \end{aligned} \quad (3.22)$$

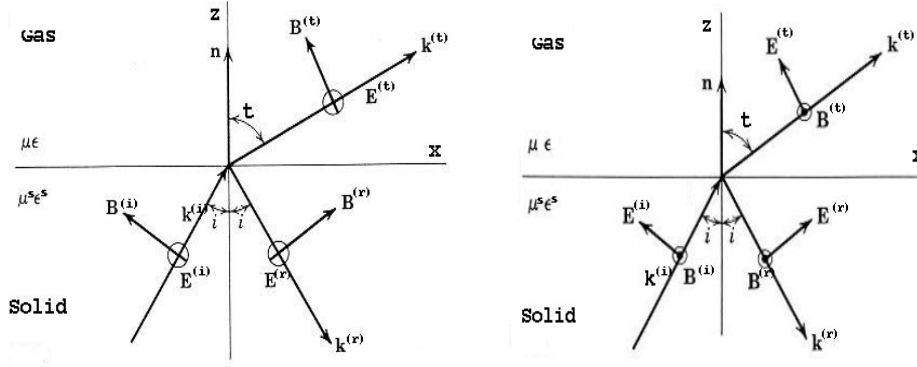


Figure 3.5: Reflexion and refraction of a light plane wave. Left figure *s* or transverse electric (TE) polarization with the electric field vector  $\vec{E}$  perpendicular to the plane of incidence (POI) defined by  $\vec{n}$  and  $\vec{k}$ . Right figure *p* or transverse magnetic (TM) polarization with the electric field vector  $\vec{E}$  in the POI. Here  $E^{(i)} \equiv E^{(incident)}$ ,  $E^{(r)} \equiv E^{(reflected)}$  and  $E^{(t)} \equiv E^{(transmitted)}$ , are the incident (angle  $i \equiv \theta_i$ ), reflected (angle  $r \equiv \theta_r$ ) and transmitted/refracted (angle  $t \equiv \theta_t$ ) electric fields. The electric permittivity and permeability are respectively  $\epsilon$  and  $\mu$ ,  $\epsilon \equiv \epsilon_i$  and  $\mu \equiv \mu_i$  and  $\epsilon_s \equiv \epsilon_t$  and  $\mu_s \equiv \mu_t$  in the text. Following Jackson [68, figs. 7.6 and 7.7, p.280].

At the boundary between the two media ( $z=0$ ), the time variation of the secondary fields will be the same as that of the incident primary field. Consequently at  $z=0$  all the phase factors are equal

$$\begin{aligned}
 (\vec{k}^{(i)} \cdot \vec{r})_{z=0} &= (\vec{k}^{(t)} \cdot \vec{r})_{z=0} = (\vec{k}^{(r)} \cdot \vec{r})_{z=0} \\
 (k_x^{(i)} x + k_z^{(i)} z)_{z=0} &= (k_x^{(t)} x + k_z^{(t)} z)_{z=0} = (k_x^{(r)} x + k_z^{(r)} z)_{z=0} \\
 k_x^{(i)} &= k_x^{(t)} = k_x^{(r)} \\
 k^{(i)} \sin \theta_i &= k^{(t)} \sin \theta_t = k^{(r)} \sin \theta_r
 \end{aligned} \tag{3.23}$$

Since the scalar product above reduces to the  $k_x$  projection, the three wave vectors lie in the same plane. Now since  $k^{(r)} = k^{(i)}$ ,  $\theta_i = \theta_r$  i.e. the angle of incidence equals the angle of reflection (reflection law). Eq. (3.23) now reads:

$$\begin{aligned}
 k^{(i)} \sin \theta_i &= k^{(t)} \sin \theta_t \\
 n_i \sin \theta_i &= n_t \sin \theta_t
 \end{aligned} \tag{3.24}$$

Eq. (3.24) gives Snell's law at a dielectric-dielectric interface.

### 3.2.2 Propagating and evanescent fields at a dielectric-dielectric interface

Depending on the material functions of the two media, the reflected and transmitted fields of an interface behave differently:

- $n_t > n_i$ , the second medium is optically denser. In this case there is a real angle of refraction  $\theta_t$  for every angle of incidence  $\theta_i \in [0, 90^\circ]$ . At any incident angle the incident electromagnetic plane waves will generate a **propagating** wave into the second medium;
- $n_t < n_i$ , here one can introduce a critical angle  $\theta_c < 90^\circ$ :

$$\theta_c = \arcsin \frac{n_t}{n_i} \quad (3.25)$$

defining two regions:

1.  $\theta_i < \theta_c$ : the angle of refraction  $\theta_t$  is real, the light is transmitted in the second medium.

$$\sin \theta_t = \frac{n_i \sin \theta_i}{n_t}, \quad \cos \theta_t = \sqrt{1 - \frac{n_i^2 \sin^2 \theta_i}{n_t^2}}, \quad (3.26)$$

2.  $\theta_i \geq \theta_c$ : no transmitted wave in the second medium, the waves are **evanescent**. Total internal reflection takes place if  $\theta_i > \theta_c$ , and the transmitted light propagates along the interface when  $\theta_i = \theta_c$ . The angle of refraction  $\theta_t$  reads

$$\sin \theta_t = \frac{n_i \sin \theta_i}{n_t}, \quad \cos \theta_t = \pm i \sqrt{\frac{n_i^2 \sin^2 \theta_i}{n_t^2} - 1}, \quad (3.27)$$

The transmitted electric field eq. (3.21) now reads

$$\begin{aligned} E^{(t)} &= E_0^{(t)} \exp(i(k_x^{(t)} x + k_z^{(t)} z) - i\omega t) \\ &= E_0^{(t)} \exp(i(k_0 n_t \sin \theta_t x) - i\omega t) \exp\left(\mp k_0 n_t \sqrt{\frac{n_i^2 \sin^2 \theta_i}{n_t^2} - 1} z\right) \end{aligned} \quad (3.28)$$

Following eq (3.27), at and above the critical angle  $\theta_c$ ,  $k_z = n_t \cos \theta_t$  is purely imaginary, so the negative sign in front of the square root in eq. (3.28) is selected since it corresponds to the absorption in the solid, otherwise the amplitude tends to infinity with increasing distance. The propagation in the  $z$  direction decays exponentially while parallel to the surface the plane waves propagate along the interface. The penetration depth  $\delta$  of the evanescent waves (see also the definition of  $\delta$  for SPP eq (3.60)) is

$$\delta = \frac{1}{2k_0 \sqrt{n_i^2 \sin^2 \theta_i - n_t^2}} = \frac{\lambda_0}{4\pi \sqrt{n_i^2 \sin^2 \theta_i - n_t^2}}. \quad (3.29)$$

where  $\lambda_0$  is the wavelength of the incident light. The penetration depth  $\delta$  is independent of the polarization of the incident light and decreases with increasing  $\theta_i$

$$\delta \in \left] \frac{\lambda_0}{4\pi \sqrt{n_i^2 \sin^2 \theta_c - n_t^2}}, \frac{\lambda_0}{4\pi \sqrt{n_i^2 - n_t^2}} \right] \quad \text{for} \quad \theta_i \in ]\theta_c, \pi/2].$$

For visible and near ultraviolet light the penetration depth is between 10 and 1000

nm (see de Fornel [75, table I-1,p.14]). If the thickness of the second medium is smaller than the penetration depth, adding an interface with  $n_3 \geq n_1$  will convert the evanescent wave into a propagating one. For a two-interface system, if  $n_3 < n_1$  and for  $\theta_i > \theta_c = \arcsin(n_3/n_1)$ , the transmitted wave will be evanescent no matter the value of the refractive index  $n_2$ .

### 3.2.3 Descartes-Snell law at a dielectric-metal interface

Since the metal refractive index  $\tilde{n}$  is complex  $\tilde{n}_t = n_t + i \kappa_t$ , the transmission angle  $\theta_t$  no longer has a simple relation with the angle of refraction. So how does the Descartes-Snell law change if some material functions are complex? There is an abundant literature on the subject: Born and Wolf [12, chap. 13, p.616], Nicols *et al.* [76] and Proctor *et al.* [77; 78] and the revues of Kovalenko [79] and Hopcraft *et al.* [80]. To derive the law of refraction at a dielectric-metallic interface the procedure of Born and Wolf [12] is followed. Consider the propagation of a plane wave from a dielectric into a metal, both media being assumed to be of infinite extent. By analogy with eq. (3.24) the law of refraction is

$$n_i \sin \theta_i = \tilde{n}_t \sin \theta_t \quad (3.30)$$

$$\sin \theta_t = \frac{n_i \sin \theta_i}{n_t + i \kappa_t} = \frac{n_i (n_t - i \kappa_t) \sin \theta_i}{n_t^2 + \kappa_t^2} \quad (3.31)$$

$$\cos \theta_t = \sqrt{1 - \sin^2 \theta_t} = \sqrt{1 - \frac{n_i^2 (n_t^2 - \kappa_t^2) \sin^2 \theta_i}{(n_t^2 + \kappa_t^2)^2} + \frac{(2 i n_i^2 n_t \kappa_t) \sin^2 \theta_i}{(n_t^2 + \kappa_t^2)^2}} \quad (3.32)$$

$\cos \theta_t$  can be expressed in polar form

$$\cos \theta_t = q \exp(i\gamma) \quad (3.33)$$

where the amplitude  $q$  and the phase  $\gamma$  are real. Expressions for  $q$  and  $\gamma$  in terms of  $n_t$  and  $\kappa_t$  and  $\sin \theta_i$  are obtained by first squaring eqs. (3.32) and (3.33) then equating the real and imaginary parts. This gives

$$q^2 \cos 2\gamma = 1 - \frac{n_i^2 (n_t^2 - \kappa_t^2) \sin^2 \theta_i}{(n_t^2 + \kappa_t^2)^2} \quad (3.34)$$

$$q^2 \sin 2\gamma = \frac{(2 n_i^2 n_t \kappa_t) \sin^2 \theta_i}{(n_t^2 + \kappa_t^2)^2}$$

$q$  and  $\gamma$  are obtained by solving eq.(3.34)

$$q^2 = \sqrt{\left[1 - \frac{n_i^2 (n_t^2 - \kappa_t^2) \sin^2 \theta_i}{(n_t^2 + \kappa_t^2)^2}\right]^2 + \left[\frac{(2 n_i^2 n_t \kappa_t) \sin^2 \theta_i}{(n_t^2 + \kappa_t^2)^2}\right]^2} \quad (3.35)$$

$$\gamma = \frac{1}{2} \arctan \left\{ 2 \sin^2 \theta_i n_i^2 \frac{n_t \kappa_t}{[n_t^2 + \kappa_t^2]^2} / \left( 1 - \sin^2 \theta_i n_i^2 \frac{n_t^2 - \kappa_t^2}{[n_t^2 + \kappa_t^2]^2} \right) \right\} \quad (3.36)$$

The scalar product  $\vec{k}^{(t)} \cdot \vec{r}$  reads

$$\vec{k}^{(t)} \cdot \vec{r} = k_x^{(t)} x + k_z^{(t)} z \quad (3.37)$$

where  $k_0 = \omega/c$  and

$$k_x^{(t)}/k_0 = \tilde{n}_t \sin \theta_t = n_i \sin \theta_i \quad k_z^{(t)}/k_0 = \tilde{n}_t \cos \theta_t = \tilde{n}_t q (\cos \gamma + i \sin \gamma).$$

The refractive index  $\tilde{n}_t$  reads

$$\begin{aligned} \tilde{n}_t &= \frac{1}{k_0} \sqrt{(k_x^{(t)})^2 + (k_z^{(t)})^2} \\ &= \frac{1}{k_0} \left\{ n_i^2 \sin^2 \theta_i + q^2 [(n_t \cos \gamma - \kappa_t \sin \gamma)^2 - (\kappa_t \cos \gamma + n_t \sin \gamma)^2 \right. \\ &\quad \left. + 2i(n_t \cos \gamma - \kappa_t \sin \gamma)(\kappa_t \cos \gamma + n_t \sin \gamma)] \right\}^{1/2} = \sqrt{a + ib} = n_t^{Snell} + i \kappa_t^{Snell} \end{aligned} \quad (3.38)$$

The real and imaginary parts of  $\tilde{n}_t^{Snell}$  are

$$n_t^{Snell} = \frac{1}{\sqrt{2}} \sqrt{\sqrt{a^2 + b^2} + a} \quad \kappa_t^{Snell} = \frac{\text{sign}(b)}{\sqrt{2}} \sqrt{\sqrt{a^2 + b^2} - a}. \quad (3.39)$$

Where  $\text{sign}(b)$  is the sign of the imaginary part  $b$ . Finally the extension of Snell's law for complex refractive indices reads

$$n_i \sin \theta_i = \text{Re}[\tilde{n}_t^{Snell} \sin \theta_t] \quad n_i \sin \theta_i = \text{Re}[\tilde{n}_t^{Snell}] \text{Re}[\sin \theta_t] = n_t^{Snell} \text{Re}[\sin \theta_t], \quad (3.40)$$

and the refraction angle has a real value and is

$$\text{Re}[\sin \theta_t] = \sin \theta'_t = \frac{n_i \sin \theta_i}{n_t^{Snell}} \quad (3.41)$$

In conclusion above we have extended Snell's law for dielectric-absorbing interfaces. Below, this extended Snell's law will be used to calculate the dispersion at dielectric metallic interfaces.

### 3.3 Dispersion of surface plasmon polaritons

In this section I will give some elements for the derivation of the dispersion relationships for surface plasmon polaritons for one and two interface systems.

### 3.3.1 One interface

Consider a single dielectric-conducting interface as shown in figure 3.6. The two homogeneous media are non magnetic and there are no charges or current. Many authors (Maier [15, chapter 2], Sarid and Challener [16], Barnes [81] and [14, Appendix]) derived analytically the dispersion function of a surface plasmon polariton. Here I will follow the derivation based on standard plane waves and continuity of the field at the interface.

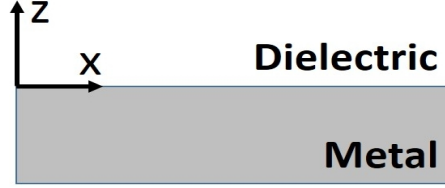


Figure 3.6: Single interface geometry and its coordinate system.

One starts from the Faraday and Ampère-Maxwell equations for non magnetic materials, without charges and current densities

$$\nabla \times \vec{E} = -\mu_0 \frac{\partial \vec{H}}{\partial t} \quad \nabla \times \vec{H} = \varepsilon \varepsilon_0 \frac{\partial \vec{E}}{\partial t} \quad (3.42)$$

In the time-harmonic approximation one explicit the curl and then separates the result into the x, y and z components

$$\begin{aligned} \frac{\partial E_z}{\partial y} - \frac{\partial E_y}{\partial z} &= i\omega\mu_0 H_x & \frac{\partial H_z}{\partial y} - \frac{\partial H_y}{\partial z} &= -i\omega\varepsilon\varepsilon_0 E_x \\ \frac{\partial E_x}{\partial z} - \frac{\partial E_z}{\partial x} &= i\omega\mu_0 H_y & \frac{\partial H_x}{\partial z} - \frac{\partial H_z}{\partial x} &= -i\omega\varepsilon\varepsilon_0 E_y \\ \frac{\partial E_y}{\partial x} - \frac{\partial E_x}{\partial y} &= i\omega\mu_0 H_z & \frac{\partial H_y}{\partial x} - \frac{\partial H_x}{\partial y} &= -i\omega\varepsilon\varepsilon_0 E_z. \end{aligned} \quad (3.43)$$

Since SPPs appear when the light is TM/ $p$  polarized I will deduce the dispersion for TM/ $p$  polarization only.

### 3.3.1.1 Transverse magnetic (TM) polarization

- In the two media and TM/ $p$  polarization with  $E_y = H_x = H_z = 0$  the fields read

$$\begin{aligned}
 z > 0 & & H_2 &= (0, H_{y2}, 0) \exp\{i(k_{x2}x - \omega t)\} \exp[-k_{z2}z] & (3.44) \\
 & & E_2 &= (E_{x2}, 0, E_{z2}) \exp\{i(k_{x2}x - \omega t)\} \exp[-k_{z2}z] \\
 z < 0 & & H_1 &= (0, H_{y1}, 0) \exp\{i(k_{x1}x - \omega t)\} \exp[+k_{z1}z] \\
 & & E_1 &= (E_{x1}, 0, E_{z1}) \exp\{i(k_{x1}x - \omega t)\} \exp[+k_{z1}z];
 \end{aligned}$$

where  $k_{zj}$  is the wave vector perpendicular to the interface.

- Rewriting eqs. (3.43) for TM/ $p$  polarization, one obtains

$$\begin{aligned}
 \text{Faraday} & & \frac{\partial E_x}{\partial z} - \frac{\partial E_z}{\partial x} &= i\omega\mu_0 H_y & (3.45) \\
 \text{Ampère} & & \frac{\partial H_y}{\partial z} = i\omega\varepsilon\varepsilon_0 E_x & & \frac{\partial H_y}{\partial x} = -i\omega\varepsilon\varepsilon_0 E_z;
 \end{aligned}$$

- At the interface there is continuity of the electric and magnetic fields parallel to the interface and of the displacement  $D$  perpendicular to the interface

$$E_{x1} = E_{x2} \qquad H_{y1} = H_{y2} \qquad \varepsilon_1 E_{z1} = \varepsilon_2 E_{z2} \qquad (3.46)$$

The continuity of the fields at the interface imply the continuity of the wave vector  $k_x$  given by Snell's law already discussed in detail in sections (3.2.1) and (3.2.3)

$$k_{x1} = k_{x2} = k_x \qquad n_1 \sin \theta_1 = n_2 \sin \theta_2. \qquad (3.47)$$

- Replacing eqs. (3.44) in (3.45) one obtains two Ampère equations in each medium

$$\begin{aligned}
 k_{z1} H_{y1} &= i\varepsilon_1 \varepsilon_0 \omega E_{x1} & k_x H_{y1} &= -\varepsilon_1 \varepsilon_0 \omega E_{z1} \\
 k_{z2} H_{y2} &= -i\varepsilon_2 \varepsilon_0 \omega E_{x2} & k_x H_{y2} &= -\varepsilon_2 \varepsilon_0 \omega E_{z2}.
 \end{aligned} \qquad (3.48)$$

Applying the same operation on the Faraday equation (3.45) one writes

$$\begin{aligned}
 i k_x E_{z1} - k_{z1} E_{x1} &= -i\mu_0 \omega H_{y1} \\
 i k_x E_{z2} + k_{z2} E_{x2} &= -i\mu_0 \omega H_{y2};
 \end{aligned} \qquad (3.49)$$

- Now a system of equations can be written, composed from the magnetic field continuity from the second equation (3.46) and the sum of the two left column equations (3.48)

$$\left\{ \begin{array}{l} H_{y1} - H_{y2} = 0 \\ \frac{k_{z1} H_{y1}}{\varepsilon_1} + \frac{k_{z2} H_{y2}}{\varepsilon_2} = i\omega\varepsilon_0 (E_{x1} - E_{x2}) = 0 \end{array} \right. , \qquad (3.50)$$

The solution of this homogeneous system corresponds to a zero determinant

$$\frac{k_{z1}}{\varepsilon_1} + \frac{k_{z2}}{\varepsilon_2} = 0; \quad (3.51)$$

- Eliminating  $H_{yi}$  in the Ampère-Maxwell equations (3.48) one has

$$E_{z1} = \frac{-i k_x}{k_{z1}} E_{x1} \quad E_{z2} = \frac{i k_x}{k_{z2}} E_{x2}.$$

Now perform two operations: i) start from the Faraday-Maxwell equations (3.49) where one replaces  $E_{zj}$  from the equations above and ii) in the resulting equations explicit  $H_{yi}$  in terms of  $E_{xj}$  using the left column of the Ampère-Maxwell equations (3.48)

$$\begin{aligned} \frac{k_x^2}{k_{z1}} E_{x1} - k_{z1} E_{x1} &= \frac{\omega^2}{c^2} \frac{\varepsilon_1}{k_{z1}} E_{x1} & k_{z1}^2 &= k_x^2 - \frac{\omega^2}{c^2} \varepsilon_1 \\ \frac{k_x^2}{k_{z2}} E_{x2} - k_{z2} E_{x2} &= \frac{\omega^2}{c^2} \frac{\varepsilon_2}{k_{z2}} E_{x2} & k_{z2}^2 &= k_x^2 - \frac{\omega^2}{c^2} \varepsilon_2 \end{aligned} \quad (3.52)$$

Dividing  $k_{z1}^2$  by  $k_{z2}^2$  and using eq. (3.51) one obtains

$$\frac{\varepsilon_1^2}{\varepsilon_2^2} = \frac{k_x^2 - (\omega^2/c^2) \varepsilon_1}{k_x^2 - (\omega^2/c^2) \varepsilon_2}$$

Manipulating the above equation leads to the final dispersion relation

$$k_x = \frac{\omega}{c} \sqrt{\frac{\varepsilon_1 \varepsilon_2^2 - \varepsilon_1^2 \varepsilon_2}{\varepsilon_2^2 - \varepsilon_1^2}} \quad \boxed{k_x = \frac{\omega}{c} \sqrt{\frac{\varepsilon_1 \varepsilon_2}{\varepsilon_1 + \varepsilon_2}}}. \quad (3.53)$$

There are two ways to plot the dispersion curve of the surface plasmon polariton.

### (A) Real permittivities for the two media defining the interface

This discussion concerning real permittivities can be found in many papers and textbooks. Figure 3.7 presents the plasmon dispersion, using real permittivities in eq. (3.53). Several features can be distinguished:

- $\omega < \omega_{sp}$  where  $\omega_{sp} = \omega_p / \sqrt{1 + \varepsilon_d}$ . In this region, called the absorption region, where the SPP can appear (see Sarid and Challener [16]), the real part of the permittivity of the metal is negative and the dielectric permittivity is positive. Two frequency regimes can be defined (see [15, chapter 2 p.27-28]):

1. for small wave vectors, corresponding to low frequency, the dispersion curve is close to the light line. The SPP acquire the nature of a grazing-incidence light field, also known as Sommerfeld-Zenneck waves;

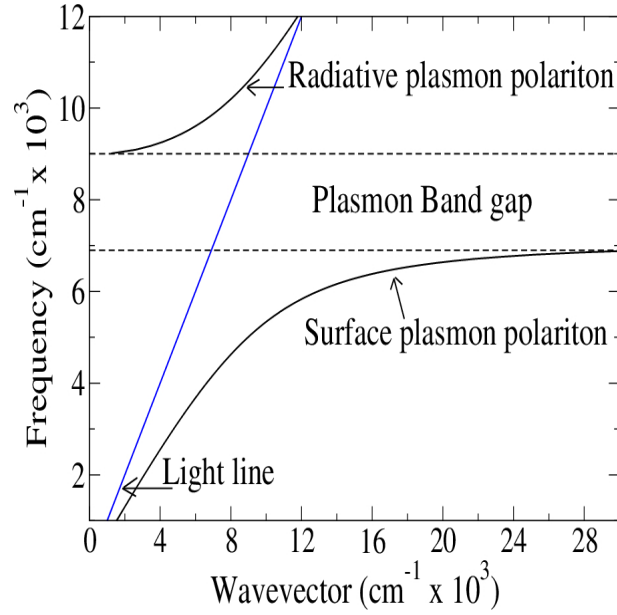


Figure 3.7: The dispersion curve, of an SPP on indium thin oxide (ITO) as a function of the wavenumber  $k_{ph}/(2\pi) = 1/\lambda$ .

2. at large wave vectors the SPP tend to the surface plasmon (SP) resonance with characteristic surface plasmon frequency  $\omega_{sp}$  (eq. (3.20))
- $\omega_{sp} < \omega < \omega_p$  Plasmon band gap separating the surface plasmon polaritons (SPP) and the bulk plasmon (BP). In this region the SPP wave vector  $k_x$ , calculated using Drude theory in eq. (3.20), is purely imaginary. The dispersion curve can not be plotted and the virtual or quasi bound plasmon modes (QBM) are present;
  - $\omega > \omega_p$  transparent region where the bulk plasmon (BP) appear when the permittivity change sign (see also section 3.1.2 above). The dispersion of the bulk plasmons alone is presented in figure 3.2 above;

### (B) One of the material functions is complex

Below I will consider the case when  $\varepsilon_m = \varepsilon_m^r + i\varepsilon_m^i$ . Following the analysis of Franzen [9], and using deduction of the same type as that given in section 3.2.3, the real  $\varepsilon_m^r$  and imaginary  $\varepsilon_m^i$  parts of the Drude permittivity read

$$\varepsilon_m^r = 1 - \frac{\omega_{mp}^2}{\omega^2 + \Gamma_m^2} \quad \varepsilon_m^i = \frac{\Gamma_m \omega_{mp}^2}{\omega(\omega^2 + \Gamma_m^2)}.$$

Using eq. (3.53), where  $1 \equiv d$  or dielectric and  $2 \equiv m$  or metal, one obtains

$$k_x = \frac{\omega}{c} \sqrt{\frac{\varepsilon_d(\varepsilon_m^r + i\varepsilon_m^i)}{\varepsilon_d + \varepsilon_m^r + i\varepsilon_m^i}} = \frac{\omega}{c} \sqrt{a' + ib'} = k_x^r(\omega) + ik_x^i(\omega) \quad (3.54)$$

where

$$k_x^r(\omega) = \frac{\omega}{c\sqrt{2}} \left[ \sqrt{\sqrt{a'^2 + b'^2} + a'} \right] \quad k_x^i(\omega) = \frac{\omega}{c\sqrt{2}} \left[ \text{sgn}(b') \sqrt{\sqrt{a'^2 + b'^2} - a'} \right]$$

$$F = \frac{\varepsilon_d}{[(\varepsilon_d + \varepsilon_m^r)^2 + (\varepsilon_m^i)^2]} \quad a = F [\varepsilon_m^r(\varepsilon_d + \varepsilon_m^r) + (\varepsilon_m^i)^2] \quad b = F \varepsilon_d \varepsilon_m^i$$

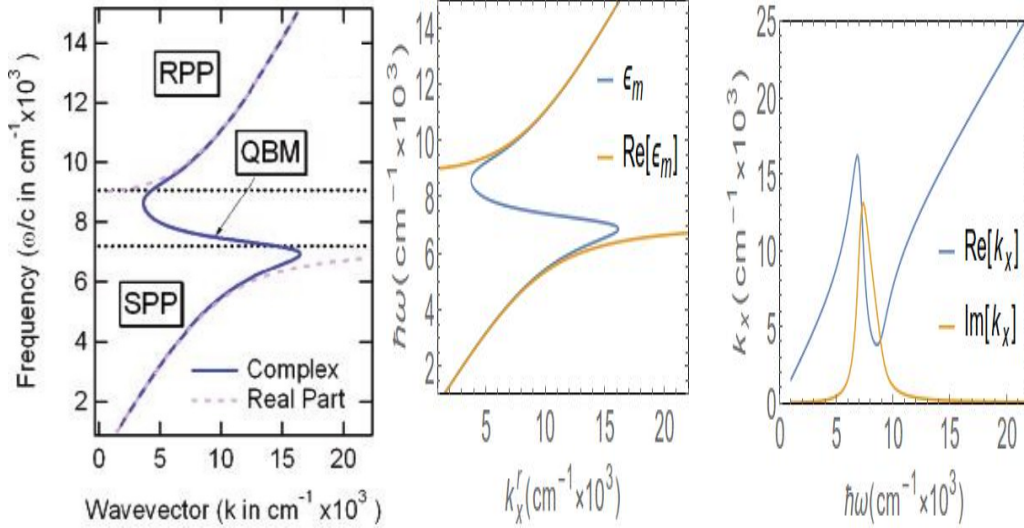


Figure 3.8: ITO dispersion curve using the complex dielectric function ( $k_x^r$  eq. (3.54) plain line, dashed line  $\varepsilon_m \equiv \varepsilon_m^r$ ), published by Franzen [9, figure 5] (left graph), in the middle graph the Franzen dispersion curve is reproduced (my blue line corresponds to his blue continuous line and the orange line corresponds to his dashed line), the right graph presents  $k_x^r$  eq. (3.54) blue line and  $k_x^i$  the orange one.

The above complex wave vector  $k_x(\omega)$  contains

- **real dispersive contribution  $k_x^r(\omega)$**  corresponding the propagation of the SPP along the interface. Except at and near the plasmon band gap, this contribution is very close to the case when the real part of the material functions case is used. Compared to figure 3.7, figure 3.8 shows that  $k_x^r(\omega)$  has a non zero contribution in the plasmon band gap known as the quasi-bound mode.
- **imaginary contribution  $k_x^i(\omega)$**  corresponding to the SPP absorption.

Figure 3.8 displays the ITO dispersion curve using the complex dielectric function published by Franzen [9, figure 5] (left graph). In the middle graph the Franzen dispersion curve is reproduced (where the blue line corresponds to his blue plain line and the orange line corresponds to his dashed line). This figure presents the comparison between the cases (A) when only real permittivity is used (orange line  $\varepsilon_m = \varepsilon_m^r$ ) and (B) when the complex permittivity is used (blue line  $\varepsilon_m = \varepsilon_m^r + i\varepsilon_m^i$ ). The dispersion obtained with the complex permittivity presents a quasi band mode (QBM), while the second case has no contribution in the gap. The right graph presents  $k_x^r$  eq. (3.54) (blue line) and  $k_x^i$  (orange line).

### (C) Qualitative discussion of the SPP when one medium is absorbing

Following Barnes [82] and Novotny and Hecht [21] I discuss some properties of SPPs occurring at the dielectric-metal interface where  $\varepsilon_m$  and  $k_{SPP}$  are complex quantities. The complex wave vector arises from the absorbing nature of the metal, SPPs are attenuated as they propagate and have a finite lifetime [82]. For  $|\varepsilon_m^i| \ll |\varepsilon_m^r|$  the real and imaginary parts of  $k_x$  are determined from eq. (3.54) :

$$k_{SPP}^{xr} \simeq k_0 \sqrt{\frac{\varepsilon_d \varepsilon_m^r}{\varepsilon_d + \varepsilon_m^r}} \quad k_{SPP}^{xi} \simeq k_0 \frac{\varepsilon_m^i}{2(\varepsilon_m^r)^2} \left( \frac{\varepsilon_d \varepsilon_m^r}{\varepsilon_d + \varepsilon_m^r} \right)^{3/2} \quad (3.55)$$

using these equations the characteristic properties at a dielectric-metal interface can be defined:

- **The SPP wavelength**

$$\lambda_{SPP} = \frac{2\pi}{k_{SPP}^{xr}} = \lambda_0 \sqrt{\frac{\varepsilon_d + \varepsilon_m^r}{\varepsilon_d \varepsilon_m^r}} \quad (3.56)$$

- **SPP propagation length parallel to the interface:** The propagation length is derived from the electric field and the energy density. The electric field associated with a SPP reads

$$\vec{E} = \vec{E}_0 e^{-\vec{k}_{SPP}^i \cdot \vec{r}} e^{i \vec{k}_{SPP}^r \cdot \vec{r} - i \omega t} \quad (3.57)$$

The energy density  $W$  is given by

$$W \propto \vec{E} \cdot \vec{E}^* = W_0 e^{-2\vec{k}_{SPP}^i \cdot \vec{r}} = W_0 e^{-2k_{SPP}^i \delta_{SPP}} \quad (3.58)$$

For a density energy  $W$  falling to  $e^{-1}$  of its initial value, we deduce from eq. (3.58) that the propagation length parallel to the interface  $\delta_{SPP}$  is proportional to the inverse of the imaginary part of the SPP wave vector eq. (3.55)

$$\delta_{SPP} = \frac{1}{2k_{SPP}^i} = \lambda_0 \frac{(\varepsilon_m^r)^2}{2\pi \varepsilon_m^i} \left( \frac{\varepsilon_d + \varepsilon_m^r}{\varepsilon_d \varepsilon_m^r} \right)^{3/2} \quad (3.59)$$

- **SPP penetration depth:** The total wave vector and the  $z$  component are

$$k_j^2 = (k_x^{SPP})^2 + k_{zj}^2$$

$$k_{zj}^2 = k_j^2 - (k_x^{SPP})^2 = k_0^2 \left( \varepsilon_j - \frac{\varepsilon_m \varepsilon_d}{\varepsilon_m + \varepsilon_d} \right) \begin{cases} j = d, & k_{zd}^2 = k_0^2 \varepsilon_d^2 / (\varepsilon_m + \varepsilon_d) \\ j = m, & k_{zm}^2 = k_0^2 \varepsilon_m^2 / (\varepsilon_m + \varepsilon_d). \end{cases}$$

For  $\varepsilon_m \approx \varepsilon_m^r < 0$  one finds  $(k_x^{SPP})^2 > \varepsilon_j k_0^2$ . Then, since  $\varepsilon_m^r + \varepsilon_d < 0$  and from eq. (3.52)  $k_{zj}$  is purely imaginary, so that extending away from the interface, the field decays exponentially. Applying  $\delta = 2\pi/k$  gives the penetration depth in the

dielectric and metal

$$\delta_d = \lambda_0 \operatorname{Im} \left| \frac{\varepsilon_m^r + \varepsilon_d}{\varepsilon_d^2} \right|^{1/2} \quad \delta_m = \lambda_0 \operatorname{Im} \left| \frac{\varepsilon_m^r + \varepsilon_d}{\varepsilon_m^2} \right|^{1/2}. \quad (3.60)$$

For a non negligible  $\varepsilon_m^i$  the expressions are more complicated.

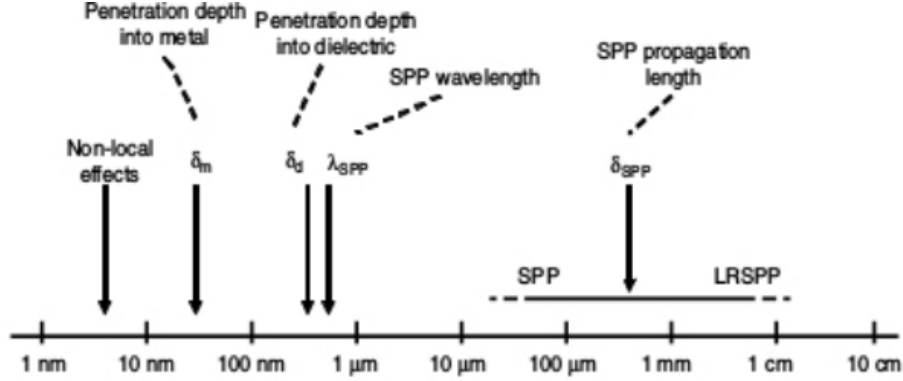


Figure 3.9: The different length scales of importance for surface plasmon polaritons in the visible and near infrared are indicated on a logarithmic scale (taken from Barnes [82, figure 1]).

Figure 3.9 (from Barnes [82, figure 1]) presents different length scales of importance for an SPP. At the single nanometer end the non-local (spatially dispersive) response of real metals provides a lower limit. At the other end, the propagation length of long-range surface plasmon–polaritons (LRSPPs) has so far reached centimetres. The penetration depth into the metal and the dielectric are around 50 and 150 nm respectively.

### 3.3.1.2 Transverse electric (TE) polarization

The p-polarization wave has a non zero perpendicular component of the electric field ( $E_z \neq 0$ ). As  $D_z$  is continuous,  $E_z$  changes [68], resulting in the creation of charge density at the interface. In an s-polarized wave, the electric field has a non zero component parallel to the surface  $E_y$  which is perpendicular to the plane of incidence. Since no density of charge is produced, one can not excite the SPP by a TE/s polarized light (see Lide *et al.* [83]).

## 3.3.2 Dispersion of surface plasmons polaritons (SPP) for a three layer (two interface) thin film structure

The subwavelength confinement near the SPP energy asymptote is an interesting property of the single interface SPP. But an SPP is also characterized by high attenuation especially near its energy asymptote, limiting the scope for applications. In this section I will derive the dispersion relation of a multilayer system consisting of alternating conducting and dielectric thin films. To derive the dispersion relation for the two-interface system I will follow Baltar[17]. The

complexity of such a system arises because each single interface can sustain a bound SPP. When the separation between adjacent interfaces is comparable to or smaller than the penetration depth eq. (3.60) the interaction between SPPs give rise to a coupled mode.

Consider a non-magnetic three layer (two interface) system as shown in figure 3.10 where the zero of the coordinate system is in the middle of the thin layer.

- **The first and last layer have different dielectric functions**

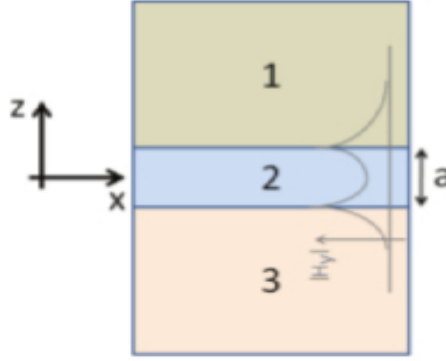


Figure 3.10: Three layer structure, the first and last layers have different dielectric functions (Baltar [17, figure 4]).

As previously discussed for the one-interface geometry, only a p-polarized wave can excite SPPs. The field components are

$$\begin{aligned}
 (1) \quad z \geq a/2 & \quad H_1 = (0, H_{y1}^+, 0) \exp\{i(k_{x1}x - \omega t)\} \exp[-k_{z1}z] \\
 & \quad E_1 = (E_{x1}^+, 0, E_{z1}^+) \exp\{i(k_{x1}x - \omega t)\} \exp[-k_{z1}z] \\
 (2) \quad a/2 \geq z \geq -a/2 & \quad H_2 = (0, H_{y2}^+, 0) \exp\{i(k_{x2}x - \omega t)\} \exp[-k_{z2}z] \\
 & \quad + (0, H_{y2}^-, 0) \exp\{i(k_{x2}x - \omega t)\} \exp[k_{z2}z] \\
 & \quad E_2 = (E_{x2}^+, 0, E_{z2}^+) \exp\{i(k_{x2}x - \omega t)\} \exp[-k_{z2}z] \quad (3.61) \\
 & \quad + (E_{x2}^-, 0, E_{z2}^-) \exp\{i(k_{x2}x - \omega t)\} \exp[k_{z2}z] \\
 (3) \quad -a/2 \geq z & \quad H_3 = (0, H_{y3}^-, 0) \exp\{i(k_{x3}x - \omega t)\} \exp[k_{z3}z] \\
 & \quad E_3 = (E_{x3}^-, 0, E_{z3}^-) \exp\{i(k_{x3}x - \omega t)\} \exp[k_{z3}z]
 \end{aligned}$$

where  $k_{zj}$  is the perpendicular wave vector projection. Since the magnetic field has only one component ( $H_y$ ) I will use this field in the derivation. The continuity of the tangential

fields

$$\begin{aligned}
 \text{at } z = a/2 \quad H_{y1}^+ \exp\left(-\frac{k_{z1} a}{2}\right) &= H_{y2}^- \exp\left(\frac{k_{z2} a}{2}\right) + H_{y2}^+ \exp\left(-\frac{k_{z2} a}{2}\right) \\
 E_{x1}^+ \exp\left(-\frac{k_{z1} a}{2}\right) &= E_{x2}^- \exp\left(\frac{k_{z2} a}{2}\right) + E_{x2}^+ \exp\left(-\frac{k_{z2} a}{2}\right) \\
 \text{at } z = -a/2 \quad H_{y3}^- \exp\left(-\frac{k_{z3} a}{2}\right) &= H_{y2}^- \exp\left(-\frac{k_{z2} a}{2}\right) + H_{y2}^+ \exp\left(\frac{k_{z2} a}{2}\right) \\
 E_{x3}^- \exp\left(-\frac{k_{z3} a}{2}\right) &= E_{x2}^- \exp\left(-\frac{k_{z2} a}{2}\right) + E_{x2}^+ \exp\left(\frac{k_{z2} a}{2}\right)
 \end{aligned} \tag{3.62}$$

eq. (3.62) with Ampère-Maxwell equation (3.45) leads to

$$\frac{1}{\varepsilon_1} \frac{\partial H_{y,1}}{\partial z} = \frac{1}{\varepsilon_2} \frac{\partial H_{y,2}}{\partial z} \tag{3.63}$$

At each boundary eq. (3.63) gives:

– Boundary 1-2 ( $z=a/2$ )

$$H_{y1}^+ \exp\left(-\frac{k_{z1} a}{2}\right) = H_{y2}^+ \exp\left(-\frac{k_{z2} a}{2}\right) + H_{y2}^- \exp\left(\frac{k_{z2} a}{2}\right) \tag{3.64}$$

$$\frac{1}{\varepsilon_1} k_{z1} H_{y1}^+ \exp\left(-\frac{k_{z1} a}{2}\right) = \frac{1}{\varepsilon_2} k_{z2} H_{y2}^+ \exp\left(-\frac{k_{z2} a}{2}\right) - \frac{1}{\varepsilon_2} k_{z2} H_{y2}^- \exp\left(\frac{k_{z2} a}{2}\right) \tag{3.65}$$

– Boundary 2-3 ( $z=-a/2$ )

$$H_{y3}^- \exp\left(-\frac{k_{z3} a}{2}\right) = H_{y2}^+ \exp\left(\frac{k_{z2} a}{2}\right) + H_{y2}^- \exp\left(-\frac{k_{z2} a}{2}\right) \tag{3.66}$$

$$\frac{1}{\varepsilon_3} k_{z3} H_{y3}^- \exp\left(-\frac{k_{z3} a}{2}\right) = -\frac{1}{\varepsilon_2} k_{z2} H_{y2}^+ \exp\left(\frac{k_{z2} a}{2}\right) + \frac{1}{\varepsilon_2} k_{z2} H_{y2}^- \exp\left(-\frac{k_{z2} a}{2}\right) \tag{3.67}$$

Substituting  $H_{y1}^+ \exp\left(-\frac{k_{z1} a}{2}\right)$  in eq. (3.65) by (3.64), and  $H_{y3}^- \exp\left(-\frac{k_{z3} a}{2}\right)$  in (3.67) by (3.66), and multiplying by  $\exp\left(-\frac{k_{z2} a}{2}\right)$  one obtains:

$$\left(\frac{k_{z1}}{\varepsilon_1} - \frac{k_{z2}}{\varepsilon_2}\right) H_{y2}^+ \exp\left(-k_{z2} a\right) + \left(\frac{k_{z1}}{\varepsilon_1} + \frac{k_{z2}}{\varepsilon_2}\right) H_{y2}^- = 0 \tag{3.68}$$

$$\left(\frac{k_{z3}}{\varepsilon_3} + \frac{k_{z2}}{\varepsilon_2}\right) H_{y2}^+ + \left(\frac{k_{z3}}{\varepsilon_3} - \frac{k_{z2}}{\varepsilon_2}\right) H_{y2}^- \exp\left(-k_{z2} a\right) = 0 \tag{3.69}$$

Re-arranging the terms, the following relationship is obtained in a matrix form:

$$\begin{pmatrix} e^{-k_{z2}a} \left[ \frac{k_{z1}}{\varepsilon_1} - \frac{k_{z2}}{\varepsilon_2} \right] & \left[ \frac{k_{z1}}{\varepsilon_1} + \frac{k_{z2}}{\varepsilon_2} \right] \\ \left[ \frac{k_{z3}}{\varepsilon_3} + \frac{k_{z2}}{\varepsilon_2} \right] & e^{-k_{z2}a} \left[ \frac{k_{z3}}{\varepsilon_3} - \frac{k_{z2}}{\varepsilon_2} \right] \end{pmatrix} \begin{pmatrix} H_{y2}^+ \\ H_{y2}^- \end{pmatrix} = \begin{pmatrix} 0 \\ 0 \end{pmatrix} \quad (3.70)$$

To obtain the nonzero solutions of this system of equations the determinant of the matrix must be zero. The dispersion relation for a thin layer reads

$$e^{-2k_{z2}a} = \frac{\left( \frac{k_{z1}}{\varepsilon_1} + \frac{k_{z2}}{\varepsilon_2} \right) \left( \frac{k_{z3}}{\varepsilon_3} + \frac{k_{z2}}{\varepsilon_2} \right)}{\left( \frac{k_{z1}}{\varepsilon_1} - \frac{k_{z2}}{\varepsilon_2} \right) \left( \frac{k_{z3}}{\varepsilon_3} - \frac{k_{z2}}{\varepsilon_2} \right)}. \quad (3.71)$$

One checks that for  $a \rightarrow \infty$  the exponential  $e^{-2k_{z2}a} \rightarrow 0$ , in this case eq. (3.71) reduces to eq. (3.51) i.e. it corresponds to the dispersion relation for a one-interface system.

- **The first and last layers are identical**

When the first and last layer are identical, equation (3.71) simplifies to

$$e^{-2k_{z2}a} = \left[ \frac{\left( \frac{k_{z1}}{\varepsilon_1} + \frac{k_{z2}}{\varepsilon_2} \right)}{\left( \frac{k_{z1}}{\varepsilon_1} - \frac{k_{z2}}{\varepsilon_2} \right)} \right]^2.$$

This equation has two roots

$$e^{-k_{z2}a} = \pm \frac{\left( \frac{k_{z1}}{\varepsilon_1} + \frac{k_{z2}}{\varepsilon_2} \right)}{\left( \frac{k_{z1}}{\varepsilon_1} - \frac{k_{z2}}{\varepsilon_2} \right)}. \quad (3.72)$$

rearranging the equation above we obtain

$$\frac{k_{z1}}{\varepsilon_1} \Big/ \frac{k_{z2}}{\varepsilon_2} = -\frac{e^{-k_{z2}a} \pm 1}{e^{-k_{z2}a} \mp 1} = \begin{cases} -\frac{e^{-k_{z2}a/2} + e^{k_{z2}a/2}}{e^{-k_{z2}a/2} - e^{k_{z2}a/2}} = \coth(k_{z2}a/2) \\ -\frac{e^{-k_{z2}a/2} - e^{k_{z2}a/2}}{e^{-k_{z2}a/2} + e^{k_{z2}a/2}} = \tanh(k_{z2}a/2) \end{cases} \quad (3.73)$$

The dispersion relation can be split into a pair of equations:

$$\begin{aligned} \frac{k_{z1}}{\varepsilon_1} \Big/ \frac{k_{z2}}{\varepsilon_2} &= \coth(k_{z2}a/2) & \Rightarrow H_{z2}^+ &= -H_{z2}^- \\ \frac{k_{z1}}{\varepsilon_1} \Big/ \frac{k_{z2}}{\varepsilon_2} &= \tanh(k_{z2}a/2) & \Rightarrow H_{z2}^+ &= H_{z2}^- \end{aligned} \quad (3.74)$$

For a thick metal film a bound mode propagates independently at each interface. When the thickness is reduced these modes couple forming two TM polarized bound modes. The first and second lines of eq. (3.74) above describe modes of odd (antisymmetric) and even (symmetric) nature. Maier [15] used the dispersion relation of eq. (3.74) to investigate the properties of the coupled SPP modes in IMI (insulator-metal-insulator) and MIM (metal-insulator-metal) structures.

### 3.3.3 Dispersion of surface plasmons polaritons (SPP) for an n layer geometry

The preceding sections have described the direct dispersion  $\omega(k)$  of the bulk eq. (3.15), surface plasmon polaritons at a single interface eq. (3.53) and an implicit dispersion relation eq. (3.72) for a three-layer system. For n layers such an expression is difficult to obtain since an implicit system of n equations similar to eq. (3.70) must be solved. Numerically one can calculate an observable, for example the reflectance  $\mathfrak{R}$  or the transmittance  $\mathfrak{T}$  as a function of  $\omega$  and  $k_x$ . Then the maxima of this observable as a function of  $\omega$  and  $k_x$  will give a dispersion curve. To obtain the dispersion curve for the  $n \geq 3$  system, Barnes [81; 84; 85] calculated the dispersion of the power dissipated by a fictitious oscillating dipole placed in a dielectric layer inside a stack of thin films. In the present work I will calculate the dispersion using: i) the transmitted intensity of an oscillating dipole located above the first interface; ii) the reflectance; iii) the transmittance of a stack of thin films.

## 3.4 Conclusion

In this chapter we have reviewed the different type of plasmons. The bulk plasmon in a solid occurs at frequencies corresponding to a zero in the permittivity ( $\text{Re}[\varepsilon(\omega)]=0$ ). The surface plasmon polaritons (SPP) are bound and the surface plasmon (SP) resonance corresponds to the limit at large wave vector  $k_x$  of an SPP mode ( $\text{SP} = \lim_{k_x \rightarrow \infty} [\text{SPP}]$ ).

The second section discusses the Decartes-Snell law at a dielectric-dielectric interface and its extension to a dielectric-metal interface. Using the real part of the dielectric function one finds a band gap between the SPP and bulk plasmon dispersion curves. Whereas using the complex refractive index of the metal the band gap disappears (figure 3.8).

Finally we have analytically derived a direct eq. (3.53) and an implicit eq. (3.72) for the dispersion relation for one and two interfaces systems. The dispersion curve of a multilayer stack, such as the one presented in chapter 5, will be calculated numerically for an observable (reflectance or transmitted flux) as a function of  $\omega$  and  $k_x$ .

# Chapter 4

## Experimental set-ups for measuring plasmon properties

Consider an air-metal interface as discussed in chapter 3. Figure 4.1 displays the dispersion curves of the SPP (green line) and light line (blue line). One notices that for a given frequency  $\omega$  the SPP wave vector  $k_\rho$  is always larger than the wave vector of light in free space i.e.  $k_{SPP} > k_{air}$ . Since these wave vectors do not match, this means that for a planar interface, an SPP cannot be directly excited by light propagating in free space.

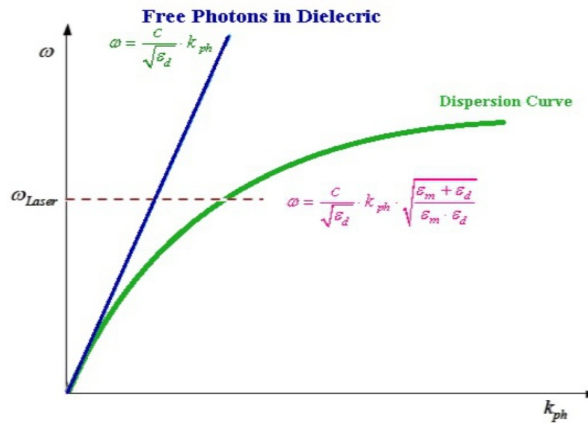


Figure 4.1: Dispersion curve of the SPP at a dielectric-metal interface (green curve), and the free-space light line (blue line) (taken from Hosseini *et al.* [86]).

The only way to excite the SPP is by increasing the wave vector component of the exciting light over its free-space value. For the source at infinity one can increase the wave vector component by using a cover layer having a refractive index greater than the substrate (see e.g. figure 4.2) and measuring the reflected light.

Below I will describe a few representative experimental set-ups where SPPs can be excited.

The experimental apparatuses can be classified using:

1. The excitation: the excitation can be performed by light either by a source located at infinity or a local source;
2. The excitation can also be performed by electrons, tunneling electrons from an STM tip or high energy electrons using a scanning electron microscope (SEM).
3. The measurement: the observables measured in an experiment correspond either to the reflection or to the transmission of the flux intensity.

In the present chapter I will use a classification based on the measurement method and the associated observable.

## 4.1 Measuring the reflected light

### 4.1.1 Plane wave source using a prism

Using far field excitation, Otto [32] and Kretschmann and Raether [34] have presented set-ups using a prism coupler permitting the excitation of an SPP mode. In both configurations discussed below the excitation of an SPP will appear as a minimum in the reflected flux or reflectance (the experiment is called attenuated total reflection (ATR)). The reflectance minimum is a consequence of missing light which has been converted into an SPP wave.

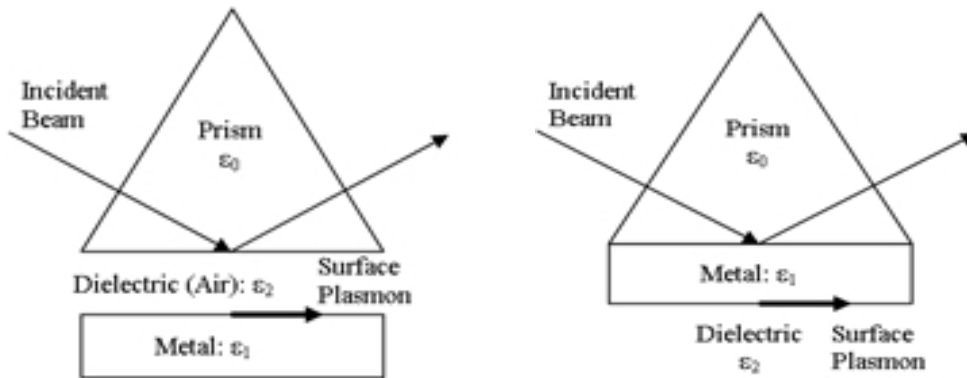


Figure 4.2: Otto [32] and Kretschmann-Raether [34] experimental set-ups using prisms (from Wikipedia) respectively left and right graphs. Left graph is an  $I_1I_2M$  stack with  $\epsilon_0 > \epsilon_2$ . In the right graph the stack is  $I_1MI_2$  with  $\epsilon_0 > \epsilon_1$ .

In the Otto configuration [32] illustrated in the left graph of figure 4.2, the prism is separated from the metal by a thin air gap (insulator-insulator-metal  $I_1I_2M$  configuration). The light

incident from the prism side at an angle beyond the angle of total internal reflection ( $\theta_i > \theta_c^i$ ) generates an evanescent wave which in turn excites the SPP at the air/metal interface if the air layer is thin enough. When the gap width is larger than the penetration depth in air (see the definition of the penetration depth for evanescent waves eq. (3.29) and SPP modes eq. (3.60)) the SPP can no longer be efficiently excited and the SPP dip vanishes. The Otto configuration proved to be experimentally inconvenient because of the challenge of controlling the air layer of the tiny prism-metal gap.

Kretschmann and Raether [34], proposed an alternative excitation set-up that solved the problem of the Otto configuration. In their set-up, sketched in the right hand side of figure 4.2, a thin metallic film is deposited on top of a prism. As in the Otto configuration the plane wave incident from the glass side of the prism, generates an evanescent wave. This evanescent wave penetrates through the metal layer and excites the SPPs at the metal/air interface. This is an  $I_1MI_2$  (insulator-metal-insulator) configuration where the amplitude of the reflectance dip depends on the metal thickness. If the metal layer thickness is larger than the penetration and the skin depths then the reflectance dip vanishes.

In both the Otto [32] and Kretschmann and Raether [34] configurations an angular scan (in  $\theta_i$  or  $k_\rho$ ) is necessary at each laser frequency.

### 4.1.2 Focused laser beam

SPP excitation with a focused laser beam was initiated by Kano *et al.* [37] using an oil immersion objective lens. The laser beam incident from the glass side is focused at the interface between the glass substrate and the metallic film. For an objective with a numerical aperture larger than the wave vector projection  $k_{SPP}$  of the SPP mode, a single measurement (all  $\theta_i$  or  $k_\rho$ ) gives the entire reflectance including its SPP mode dip at a particular wavelength. Note that one can not excite the SPP if the numerical aperture is smaller than  $k_{SPP}$ . The experimental set-up is sketched in Figure 4.3 and corresponds to a Kretschmann-Raether  $I_1MI_2$  configuration.

This set-up was used by Kano and Knoll [88] to measure the thickness of a thin film deposited onto a metal. It has also been used in measurements of the local refractive index map of a sample with a resolution better than  $1.5 \mu\text{m}$  [87].

Zhan [89] use a radially polarized beam generating a zero order Bessel beam which is non dispersive.

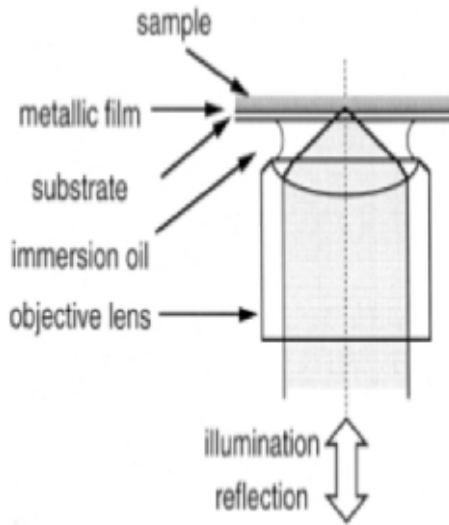


Figure 4.3: Kano and Knoll [87] optical arrangement exciting the SPP using a focused laser beam.

## 4.2 Measuring the transmitted light. Leakage radiation microscopy

The above experimental set-ups all measure the reflected flux or the reflectance. Now an experimental set-up for a transmission measurement will be presented. Raether [14] defined a transmission measurement as radiation damping, whereas more recently Hecht [38], Drezet *et al.*[90] and Hoheneau *et al.*[91] called these measurements leakage radiation (LR) microscopy. For a metal film deposited on a glass film, one can excite its SPP mode using the light of a near field scanning optical microscope (NSOM), a focused laser beam, the light incident on a rough surface or on a surface with defects or with deposited nanostructures. In such an experiment the sample is excited from the air side and one detects in transmission (glass medium) the flux using an oil immersion objective. This set-up corresponds to the so called leakage radiation microscopy (LR) occurring at a specific angle  $\theta_{LR}$ . Then the SPP wave vector reads

$$\text{Re}[k_{SPP}] = n_{glass}k_0 \sin \theta_{LR}$$

Recall that the metal (silver or gold) has to be sufficiently thin, so that the SPP evanescent field of the first interface extends through the metal into the transparent substrate medium (glass).

### 4.2.1 Near field scanning optical microscope (NSOM)

Consider a sample (air-metal-glass) which is excited using the evanescent field of a near field scanning optical microscope (NSOM). In NSOM the light source is usually a laser focused into an optical fiber whose aperture has a diameter smaller than the excitation wavelength,

resulting in an evanescent field (or near-field). The excitation may also be a quantum emitter coupled to the NSOM tip [92; 93]. Using an NSOM tip located above the gold and silver films to excite the SPPs, Hecht *et. al* [38] collected the transmitted light using an oil immersion objective. The experimental set-up presented in figure 4.4 sketches an NSOM illuminating the

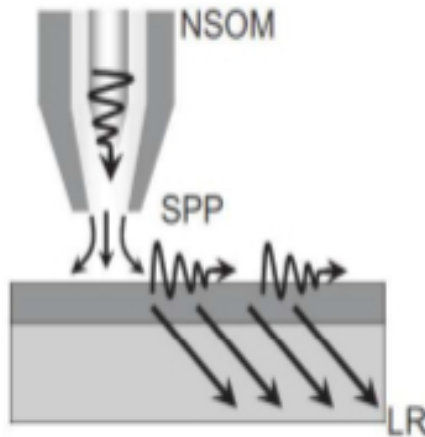


Figure 4.4: Principle of an experiment generating SPP leakage radiation (LR) collected in transmission using an oil immersion objective. The structure is excited using an NSOM. From Drezet *et al.* [90, figure 8]

surface of a metallic film in the near field. The excitation is localized near the surface and acts as a source exciting the SPPs. The evanescent field issuing from the NSOM consists of large wave vectors allowing phase matched excitation of SPPs. Due to the lateral positioning of the NSOM, SPPs can be excited at different locations on the metal surface. SPPs propagating from the illumination spot can be conveniently imaged by collecting the leakage radiation of the substrate. The SPP radiation is emitted at an angle  $\theta_{SPP}$ . In the Fourier space the angular distribution of the transmitted radiation appears as a thin ring of radius  $\theta_{SPP}$ .

### 4.2.2 Rough thin films and illumination of a defect

Raether [14] has extensively studied the SPP excitation of rough surfaces. Figure 4.5 displays the experimental arrangement of the SPP leakage radiation excited by light scattered by the roughness of a film surface. This film roughness produces the amount of the momentum necessary to match the SPP dispersion relation.

Drezet *et. al*[90] analyzed the interaction between the SPP and defects or plasmonic nano-devices by using leakage radiation microscopy. The optical leakage radiation microscopy set-up is sketched in figure 4.6. The laser beam is focused on a defect on a gold film itself deposited on a glass substrate. The defects are much smaller than the SPP wavelength and to a first approximation they can be considered as point-like dipole emitters. Scattering the light by a nanostructure gives rise to evanescent waves supplying the right amount of momentum necessary for generating an SPP wave. In both cases the leakage radiation emitted through the glass substrate is collected again by an oil immersion objective. Light is subsequently refocused on

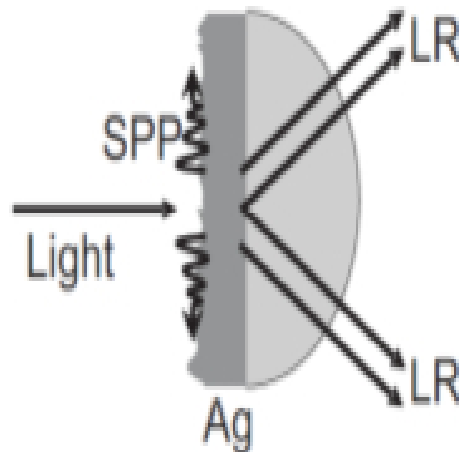


Figure 4.5: Observing an SPP mode excited on a rough film. This roughness produces the amount of momentum necessary to match the SPP dispersion relation 4.1. The leakage radiation is collected in the far field through a glass substrate using a photographic plate. From Drezet *et al.* [90, figure 5].

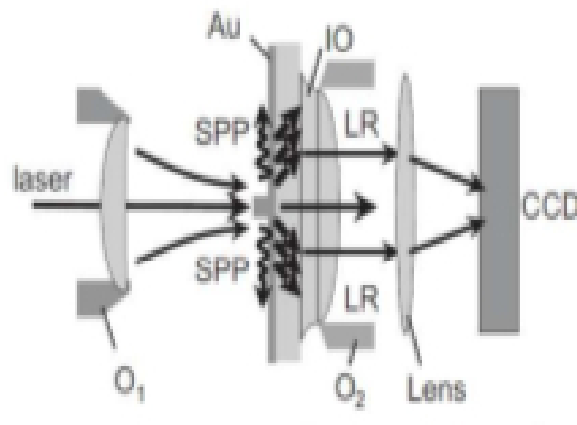


Figure 4.6: Observing SPP leakage radiation (LR) excited on a surface thanks to defects or nanostructures. The leakage radiation is collected in the far field through a glass substrate and imaged using a CCD camera. From Drezet *et al.* [90, figure 5].

a charge coupled device (CCD) camera. Finally the leakage radiation can be imaged in both Fourier and coordinate spaces.

## 4.3 Excitation by electrons

### 4.3.1 Scanning tunneling microscope (STM)

In the experimental set-ups presented above light has been used as the excitation source. For a scanning tunneling microscope (STM) the excitation source is the inelastic tunnel current between the tip and the sample. The advantages of this experiment are:

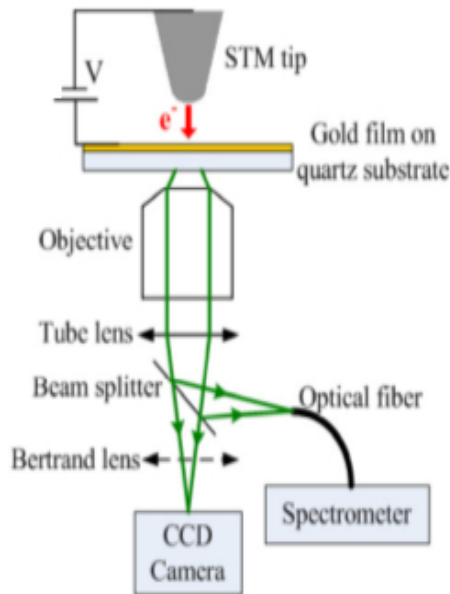


Figure 4.7: An STM tip combined with an inverted optical microscope. Photon emission is detected in transmission using a CCD camera. Either the image plane or the Fourier plane is recorded by removing or adding extra lens in front of the CCD camera respectively. From Wang *et al.* [39].

1. the tunneling electron follows the shortest path perpendicular to the interface. During the inelastic tunneling the inelastic electrons lose all or part of their energy, energy which may be used to excite plasmons
2. an important difference between the STM and optical excitation is that a whole range of radiation frequencies  $\nu$ , with  $h\nu < eV$  ( $E = h\nu$  is the energy of the electrons), may be produced in a single STM experiment. To excite an SPP in a standard optical experiment one must scan the angular frequency  $\omega$ .

In most of the early STM experiments (see e.g. [94–97]) the photon emission was detected on the air side of the noble metal film, i.e. on the same side as the STM tip. In this case, no light from propagating SPPs may be detected as explained in section 4.1. The detected light is only from localized surface plasmons.

Wang *et. al* [39] and Bharadwaj *et. al* [59] excite an SPP mode of an air-gold-glass thin film stack on the cover layer (air) side using the inelastic electrons of an STM. The light intensity is collected in transmission in a higher refractive index medium where the transmitted intensity is measured using the leakage radiation microscopy techniques discussed above. Figure 4.7 displays such a leakage radiation experimental set-up, an STM combined with an inverted optical microscope. The sample is  $I_1MI_2$  with  $I_1$  air and  $I_2$  glass and the photon emission is detected through the sample using a cooled CCD camera. In such an experiment the image plane or the Fourier plane is recorded by removing or adding an extra lens in front of the CCD camera. As expected the leakage radiation occurs at a specific angle  $\theta_{LR} > \theta_c$ , where  $\theta_c$  is the critical angle at which total internal reflection occurs for a glass-air interface.

### 4.3.2 Scanning electron microscope

SPPs may also be excited by high energy electrons, for example, in a scanning electron microscope (SEM). This type of excitation was first studied by Ritchie [5] using an high energy electron gun. A point charge moving in vacuum is accompanied by an electromagnetic field which is regarded as an evanescent source of radiation which permits exploring large wave vector value that lie outside the light cone. Consequently the fast electrons generate SPPs when passing near a metal surface [40]. The SPP excitation by high energy electrons can be probed by studying the energy loss of the electrons (electron energy loss spectroscopy) or by detecting the optical radiation that is subsequently emitted by the material. Polman *et al.* [41]

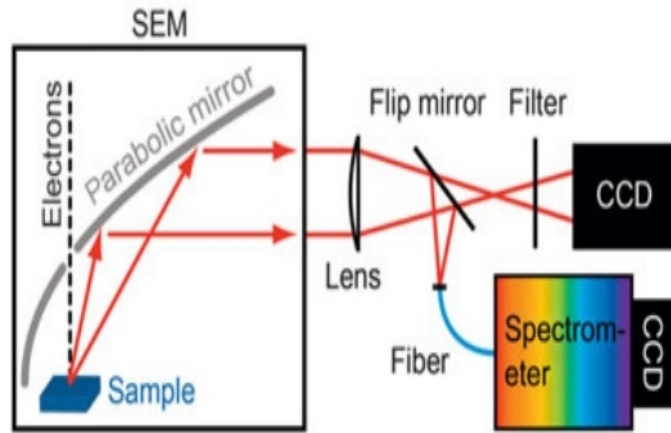


Figure 4.8: Schematic overview of the setup showing the different detection schemes: a spectrometer for 2D cathodoluminescence (CL) imaging spectroscopy and a charge-coupled device (CCD) imaging detector for angle-resolved measurements (taken from [41, figure 1]).

used an electron beam in an SEM as a direct excitation source for polarizable materials, and they collected the emitted radiation using an angle-resolved cathodoluminescence imaging spectroscopy. Using angle-resolved detection, they have been able to deduce the nature of localized modes and the dispersion of propagating modes in plasmonic structures. Polman *et al.* [41] demonstrate the use of this technique for the excitation of SPP on single metal nanoparticles.

## 4.4 Conclusion

In this chapter different experimental set-ups were discussed that permit the excitation of the SPP mode of a thin film stack. These set-ups are classified on the basis of the measurement method in reflection or in transmission. In our group Shuiyan Cao, Elizabeth Boer-Duchemin and Eric Le Moal have performed experiments on a six layer thin film stack using the STM experimental set-up presented above in section 4.3.1 and in figure 4.7. Their experimental results will be compared to our modeling in chapter 6. This bibliographic study permits us to understand the existing experimental techniques used to study the SPP of a thin film stack.

# Chapter 5

## Modeling: source at infinity and local source of excitation

This chapter presents the modeling of the excitation of an n-layer thin film stack excited either by a laser source located at infinity (i.e. a plane wave) or by a local source of electrons or photons located a few nanometers above the surface. This local source can be an STM, a NSOM or a radiating molecule.

### 5.1 Excitation source at infinity (ESI)

In this section, I will model the excitation of a thin film stack by a source of light at infinity. The observables, namely reflectance ( $\mathcal{R}$ ) and transmittance ( $\mathcal{T}$ ) measured in an experiment, correspond either to reflection or to transmission of the incident light. Below I will explain in detail the model of a thin film stack consisting of n layers bounded by two semi infinite layers the superstrate (air) and the substrate (glass).

#### 5.1.1 Fresnel coefficients in a one interface system

The reflectance  $\mathcal{R}$  and the transmittance  $\mathcal{T}$  are the observables measured when a plane wave source of light is used. The incident, reflected and transmitted flux crossing a unit area normal to the wave vector  $\mathbf{k}$  (in isotropic media the Poynting vector  $\vec{S}$  is parallel to  $\mathbf{k}$ ) read

$$S^{(i)} \cos \theta_i \quad S^{(r)} \cos \theta_r \quad S^{(t)} \cos \theta_t$$

The reflected flux or the reflectance  $\mathcal{R}$  is the ratio of the reflected and the incident components of Poynting vector  $\vec{S}$

$$\mathcal{R} = \frac{S^{(r)} \cos \theta_r}{S^{(i)} \cos \theta_i}. \quad (5.1)$$

The transmittance is the ratio of the transmitted flux over the incident flux

$$\mathcal{T} = \frac{S^{(t)} \cos \theta_t}{S^{(i)} \cos \theta_i}, \quad (5.2)$$

where, in the particular case of  $p$  polarization and homogeneous media, the Poynting vector reads

$$\vec{S} = \vec{E} \times \vec{H}^* = \sqrt{\frac{\varepsilon_0 \varepsilon}{\mu_0 \mu}} \vec{E} \cdot \vec{E}^* \vec{k} = \sqrt{\frac{\varepsilon_0 \varepsilon}{\mu_0 \mu}} \vec{k} (E_x E_x^* + E_z E_z^*) = \sqrt{\frac{\varepsilon_0 \varepsilon}{\mu_0 \mu}} \vec{k} E^2, \quad (5.3)$$

Below I will write the reflectance  $\mathcal{R}$  and transmittance  $\mathcal{T}$  in terms of the Fresnel reflection  $r$  and the transmission  $t$  coefficients. At an interface one defines these coefficients as the ratio of the reflected  $E_r$  and transmitted electric field  $E_t$  over the incident one  $E_i$  (see Born and Wolf [12], Jackson [68] and Kliever [98]). These fields have a generic form

$$\vec{E}(\vec{r}, t) = \vec{E}_0 \exp(i \vec{k} \cdot \vec{r} - i \omega t) \quad (5.4)$$

For the two polarizations,  $p$ /transverse magnetic or  $s$ /transverse electric, the boundary conditions of the tangential fields at an interface located at  $z=0$  read:

- For  $p$ /TM or transverse magnetic polarization, the **tangential electric and magnetic field** boundary conditions can be written as

$$\left. \begin{array}{l} \text{electric} \\ \text{magnetic} \end{array} \right\} \begin{array}{l} \cos \theta_i (\vec{E}_0^i - \vec{E}_0^r) - \cos \theta_t \vec{E}_0^t = 0 \\ \sqrt{\frac{\varepsilon_i}{\mu_i}} (\vec{E}_0^i + \vec{E}_0^r) - \sqrt{\frac{\varepsilon_r}{\mu_r}} \vec{E}_0^t = 0 \end{array} \quad (5.5)$$

- For  $s$ /TE or transverse electric polarization, the **tangential electric and magnetic field** boundary conditions can be written as

$$\left. \begin{array}{l} \text{electric} \\ \text{magnetic} \end{array} \right\} \begin{array}{l} \vec{E}_0^i + \vec{E}_0^r - \vec{E}_0^t = 0 \\ \sqrt{\frac{\varepsilon_i}{\mu_i}} (\vec{E}_0^i - \vec{E}_0^r) \cos \theta_i - \sqrt{\frac{\varepsilon_t}{\mu_t}} \vec{E}_0^t \cos \theta_t = 0 \end{array} \quad (5.6)$$

In the literature, the Fresnel coefficients are defined in two ways:

1. Born and Wolf [12, section 1.5 and 13.4] define the reflection and the transmission coef-

ficients by eliminating  $E_t$  and  $E_r$  from the above equations:

$$(TE) \begin{cases} r_{ij}^{(s)} = \frac{E_0^{(r)}}{E_0^{(i)}} = \frac{n_i \cos \theta_i - n_j \cos \theta_j}{n_i \cos \theta_i + n_j \cos \theta_j} = \frac{N_i - N_j}{N_i + N_j} = \frac{k_{iz} - k_{jz}}{k_{iz} + k_{jz}} \\ t_{ij}^{(s)} = \frac{E_0^{(t)}}{E_0^{(i)}} = \frac{2 n_i \cos \theta_i}{n_i \cos \theta_i + n_t \cos \theta_t} = \frac{2 N_i}{N_i + N_j} = \frac{2 k_{iz}}{k_{iz} + k_{jz}} \end{cases} \quad (5.7)$$

$$(TM) \begin{cases} r_{ij}^{(p)} = \frac{E_0^{(r)}}{E_0^{(i)}} = \frac{n_j \cos \theta_i - n_i \cos \theta_j}{n_j \cos \theta_i + n_i \cos \theta_j} = \frac{\varepsilon_j N_i - \varepsilon_i N_j}{\varepsilon_j N_i + \varepsilon_i N_j} = \frac{\varepsilon_j k_{iz} - \varepsilon_i k_{jz}}{\varepsilon_i k_{iz} + \varepsilon_j k_{jz}} \\ t_{ij}^{(p)} = \frac{E_0^{(t)}}{E_0^{(i)}} = \frac{2 n_i \cos \theta_i}{n_j \cos \theta_i + n_i \cos \theta_j} = \frac{2 n_i n_j N_i}{\varepsilon_j N_i + \varepsilon_i N_j} = \frac{2 n_i n_j k_{iz}}{\varepsilon_j k_{iz} + \varepsilon_i k_{jz}} \end{cases} \quad (5.8)$$

$$r_{ij} = -r_{ji} \quad t_{ij} t_{ji} = 1 - r_{ij}^2 \quad \mathcal{R}^{(s,p)} = r_{ij}^{(s,p)} (r_{ij}^{(s,p)})^* \quad (5.9)$$

$$\mathcal{T}^{(s,p)} = \frac{n_i^* n_j N_j^*}{n_i n_j^* N_i^*} t_{ij}^{(s,p)} (t_{ij}^{(s,p)})^* = \frac{4 \varepsilon_j N_i \varepsilon_i^* N_j^*}{(\varepsilon_i N_j + \varepsilon_j N_i)(\varepsilon_i^* N_j^* + \varepsilon_j^* N_i^*)}. \quad (5.10)$$

Bethune [58, appendix] uses a similar formulation where

$$r_{ij}^{\text{Born-Wolf}} = -r_{ij}^{\text{Bethune}} \quad t_{ij}^{\text{Born-Wolf}} = t_{ij}^{\text{Bethune}}$$

Using this formalism, the reflectance and the transmittance for the  $s$  and  $p$  polarizations read

$$\begin{aligned} \text{Reflectance} & \quad \mathcal{R}^{s,p} = r^{s,p} \cdot (r^{s,p})^* \\ \text{Transmittance} & \quad \mathcal{T}^{s,p} = \frac{n_i^* n_j N_j^*}{n_i n_j^* N_i^*} t^{s,p} \cdot (t^{s,p})^* \end{aligned} \quad (5.11)$$

where

$$N_j = n_j \cos \theta_j = [n_j^2 - n_1^2 \sin^2 \theta_1]^{1/2} \quad (5.12)$$

Note that if the material functions are real, eq. (5.11) reads as

$$\text{Transmittance} \quad \mathcal{T}^{s,p} = \frac{N_j}{N_i} t^{s,p} \cdot (t^{s,p})^* \quad (5.13)$$

2. Raether [14, appendix] uses a different definition for the transmitted Fresnel coefficient  $t=1+r$ . For TE polarization the Born and Wolf [12, section 1.5 and 13.4] and Raether[14,

appendix] definitions are equivalent whereas for TM polarization  $\vartheta^p$  is different:

$$t_{ij}^{(p)} = 1 + r_{ij}^{(p)} = \frac{2\varepsilon_j N_i}{\varepsilon_j N_i + \varepsilon_i N_j} = \frac{2\varepsilon_j k_{iz}}{\varepsilon_j k_{iz} + \varepsilon_i k_{jz}} \quad (5.14)$$

$$r_{ij} = -r_{ji} \quad t_{ij} = 1 + r_{ij} \quad (5.15)$$

$$\mathcal{R}^{(s,p)} = r_{ij}^{(s,p)} (r_{ij}^{(s,p)})^* \quad (5.16)$$

$$\mathcal{T}^{(s,p)} = \frac{\varepsilon_i^* N_j^*}{\varepsilon_j^* N_i^*} t_{ij}^{(s,p)} (t_{ij}^{(s,p)})^* = \frac{4\varepsilon_j N_i \varepsilon_i^* N_j^*}{(\varepsilon_i N_j + \varepsilon_j N_i)(\varepsilon_i^* N_j^* + \varepsilon_j^* N_i^*)}. \quad (5.17)$$

In this formalism, the reflectance and the transmittance of  $s$  and  $p$  polarization read:

$$\begin{aligned} \text{Reflectance} & \quad \mathcal{R}^{s,p} = r^{s,p} \cdot (r^{s,p})^* \\ \text{Transmittance} & \quad \mathcal{T}^{s,p} = \frac{\varepsilon_i^* N_j^*}{\varepsilon_j^* N_i^*} t^{s,p} \cdot (t^{s,p})^* \end{aligned} \quad (5.18)$$

For real material functions, the transmittance  $\mathcal{T}$  reads as

$$\text{Transmittance} \quad \mathcal{T}^{s,p} = \frac{\varepsilon_i N_j}{\varepsilon_j N_i} t^{s,p} \cdot (t^{s,p})^* \quad (5.19)$$

Smith *et al.* [44, Appendix] use a formulation derived from the one of Raether [14, appendix]

$$r_{ij}^{\text{Raether}} = r_{ij}^{\text{Born-Wolf}} = -r_{ij}^{\text{Smith-et-al}} = -r_{ij}^{\text{Bethune}} \quad t_{ij}^{\text{Raether}} = t_{ji}^{\text{Smith-et-al}}$$

These equations are derived for a single interface. A fundamental question must be asked: How do these Fresnel coefficients change in the presence of a thin film stack composed of several interfaces?

### 5.1.2 Fresnel coefficients in a thin film stack

Figure 5.1 presents a multilayer thin film stack including the multiple reflections and refractions of the light at the interfaces. An algorithm should take into account these multiple events that are otherwise absent in a single interface system. To obtain the Fresnel coefficients for a thin film stack, three types of models have been developed.

- i) **Characteristic matrix algorithm** implemented by Born and Wolf [12, chapter 1]. This model solves the Helmholtz wave equation for no charges and no currents. The solution is written as a product of standing and traveling fields in  $z$  and  $x$  coordinates respectively. When solving the wave equation the traveling field in  $x$  is eliminated and one is left with first order differential equations for the standing waves in  $z$ . The solution of these equations gives a characteristic matrix of the stack and finally the reflection and transmission coefficients of the entire stack. The final electric field is a product of standing

in  $z$  and traveling in  $x$  directions waves. In the classical theory of light the electric and magnetic fields having the appropriate boundary condition must be expressed in the plane wave form. Therefore, finally, the Born and Wolf mixed fields must be converted into a plane wave form. Compared to the recent implementation using plane waves only, the Born and Wolf model is cumbersome and we will not use it below.

- ii) **Transfer matrix algorithm** of Abèles [99] as implemented by Bethune[58] (see also Potter [13]). The electric field is written in a traveling wave basis. At an interface one uses the boundary conditions of the field expressed in equations (5.5) and (5.6). For the propagation in the medium one uses plane waves  $\exp(\pm ik_z z)$ . Namely the electric field eq. (5.4) is now composed of forward (+) and backward (-) components of fields in the layer  $j$

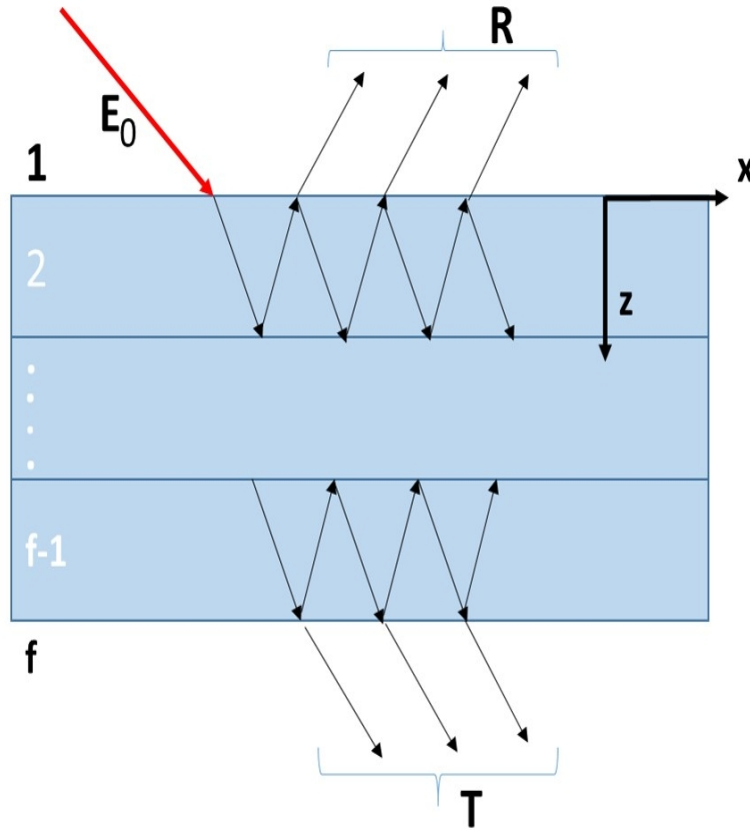


Figure 5.1: Multilayer thin film stack where the first and the last semi infinite layers are called the cover layer (1) and the substrate (f). The reflection R and transmission T are represented. Note that no reflexion occurs in the substrate f.

$$\vec{E}_j^\pm(\vec{r}, t) = \vec{\mathcal{E}}_j^\pm \exp(\pm ik_z z) \exp(ik_\rho x - i\omega t). \quad (5.20)$$

Snell's law for the continuity of  $k_{\parallel}$  or  $k_\rho$  at the interface, is

$$\frac{\sin \theta_j}{\sin \theta_{j+1}} = \frac{n_{j+1}}{n_j} \quad k_\rho = k_{j\rho} \quad \forall j. \quad (5.21)$$

and the photon wave vector satisfies

$$k_j^2 = k_0^2 \varepsilon_j = k_\rho^2 + k_{jz}^2 = k_0^2 (\sin^2 \theta_j + N_j) \quad (5.22)$$

where below we will use the notation

$$N_j = \frac{k_{jz}}{k_0} = n_j \cos \theta_j = [n_j^2 - n_1^2 \sin^2 \theta_1]^{1/2} \quad (5.23)$$

Note that the last form of  $N_j$  is used above the critical angle when  $\cos \theta_j$  is undefined. For a lossy medium we use the convention that  $\text{Im}(N_j) > 0$  (see footnote 1).

The Bethune[58] algorithm for layered media requires two steps:

- First consider an interface  $ij$  between the media  $i$  and  $j$ . One requires the continuity (eqs. (5.5) and (5.6)) of the tangential components of the electric ( $E_x$  for "p",  $E_y$  for "s") and magnetic fields at that interface. The relationship between the amplitudes of the electric fields  $E_i^\pm$  and  $E_j^\pm$  is written in a matrix form

$$\begin{pmatrix} E_i^+ \\ E_i^- \end{pmatrix} = M_{ij} \begin{pmatrix} E_j^+ \\ E_j^- \end{pmatrix} \quad (5.24)$$

where  $M_{ij}$  is the transfer matrix at the interface  $ij$

$$M_{ij} = \frac{1}{t_{ij}} \begin{pmatrix} 1 & r_{ij} \\ r_{ij} & 1 \end{pmatrix}$$

and  $r_{ij}$  and  $t_{ij}$  are respectively the reflection and the transmission coefficients at the  $ij$  interface given in equations 5.7 and 5.8 above using the Born and Wolf formulation (see subsection 5.1.1).

- second, one can calculate the propagation in an homogeneous medium  $j$ , using the propagating matrix  $\Phi_j$

$$E_j(z_j + d_j) = \Phi_j E_j(z_j) = \begin{pmatrix} \phi_j & 0 \\ 0 & \bar{\phi}_j \end{pmatrix} E_j(z_j). \quad (5.25)$$

Here  $\phi_j = \exp(iN_j k_0 d_j)$ , with  $z_j$  and  $d_j$  defining the position and the thickness in the  $j$ -th layer and  $\bar{\phi}$ , the complex conjugate.

For  $f$  layers one multiplies the products of such matrices (the transfer matrix at the interface  $M_{ij}$  and the propagation matrix  $\phi_j$  in medium  $j$ ) to obtain the total transfer matrix  $T(\omega)$ . Precisely one starts from the interface 2 1 and proceeds to the last interface  $f$  ( $f-1$ ):

$$T(\omega) = M_{f(f-1)} \Phi_{f-1} \dots \Phi_2 M_{21}. \quad (5.26)$$

Note that 1 and  $f$  are the cover layer and the substrate layers respectively (see figure 5.1).

Using the transfer matrix  $T$  the electric field in the substrate layer  $f$  reads

$$\begin{pmatrix} E_f^+ \\ E_f^- \end{pmatrix} = \begin{pmatrix} T_{11} & T_{12} \\ T_{21} & T_{22} \end{pmatrix} \begin{pmatrix} 1 \\ r \end{pmatrix} E_1 \quad (5.27)$$

where  $r$  is the total reflection coefficient. In the substrate layer reflection is absent and one has

$$E_f^- = 0 = T_{21} + T_{22}r \quad (5.28)$$

and one extracts the reflection coefficient  $r$

$$r = \frac{E_1^-}{E_1^+} = \frac{-T_{21}}{T_{22}} \quad (5.29)$$

The transmission coefficient is defined as the ratio of the final  $E_f^+$  over the initial  $E_1^+$  amplitudes. Since the amplitude  $E_1^+ = E_0 = 1$  one obtains

$$t = \frac{E_f^+}{E_1^+} = T_{11} + r T_{12} = T_{11} - \frac{T_{12}T_{21}}{T_{22}} \quad (5.30)$$

The reflectance  $\mathcal{R}$  and the transmittance  $\mathcal{T}$  are calculated using eqs. (5.11) above.

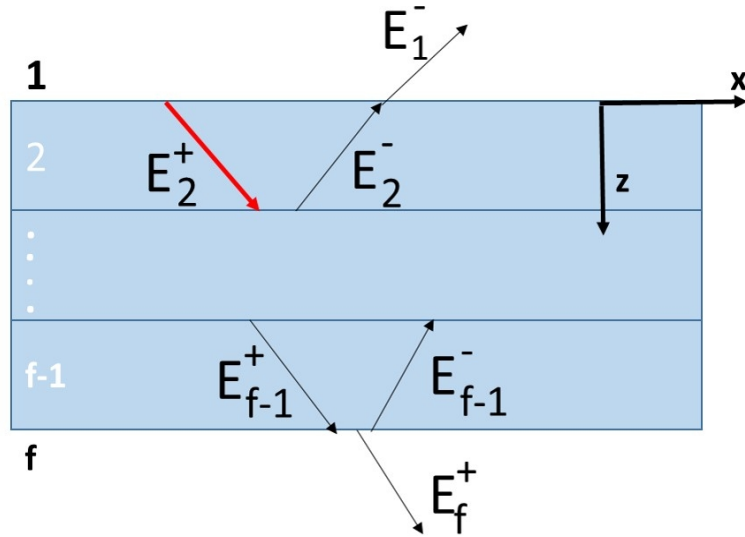


Figure 5.2: Geometry and excitation in a non-absorbing thin film of a thin-film stack. The arrows correspond to the direct (+) and reflected (-) electric field (Based on figure 1 of Smith *et al.*[44]).

iii) Iterative algorithm implemented by Smith *et al.* [44, Appendix].

Contrary to the Bethune formalism [58] where the light is incident from medium 1, in the Smith *et al.* [44, Appendix] formalism the photon source is located in the second layer

(see figure 5.2). The forward and backward electric fields at the interfaces read

$$\begin{array}{ll}
 \textit{initialization} & E_2^+ = 1 & E_2^- = (r_{2f} \exp[ik_{2z} d_2]) E_2^+ \\
 & E_1^+ = 0 & E_1^- = (r_{2f} \exp[2ik_{2z} d_2] + 1) E_2^+ \\
 & \dots & \dots \\
 \textit{propagation} & E_j^+ = \frac{t_{j-1,j} \exp[ik_{j-1,z} d_{j-1}] E_{j-1}^+}{1 + r_{j-1,j} r_{j,f} \exp[2ik_{jz} d_j]} & E_j^- = r_{jf} \exp[ik_{jz} d_j] E_j^+ \\
 & \dots & \dots \\
 & & E_{f-1}^- = r_{(f-1)f} \exp[ik_{(f-1)z} d_{f-1}] E_{f-1}^+ \\
 \textit{end} & E_f^+ = t_{f-1,f} \exp[ik_{f-1,z} d_{f-1}] E_{f-1}^+ & E_f^- = 0.
 \end{array} \tag{5.31}$$

where the reflection coefficient  $r_{j,j+1}$  and the transmission  $t_{j,j+1}$  coefficients for contiguous layers are calculated using equations (5.7) and (5.14) above. The total reflection coefficient for a multilayer system in the Smith *et al.* [44, Appendix] formalism reads

$$r_{jn}^{s,p} = \frac{r_{j,j+1}^{s,p} + r_{j+1,f}^{s,p} \exp[2ik_{j+1,z} d_{j+1}]}{1 + r_{j,j+1}^{s,p} r_{j+1,f}^{s,p} \exp[2ik_{j+1,z} d_{j+1}]} \quad \forall j \in [1, n-2]$$

As in equations (5.7) and (5.14) the transmitted coefficient is given by  $t_{jn}^{s,p} = 1 + r_{jn}^{s,p}$ , the reflectance is calculated using eq. (5.18).

In this section I have presented the Bethune formulation giving the reflectance and transmittance associated with the photon excitation of a thin film stack by a source at infinity. We have also presented the Raether-Smith implementation because we have used it to study the behavior of the electric field  $E$  as a function of the penetration coordinate  $z$  (see the analysis of this work in chapter 7, section 7.1.4). In the rest of this work we will exclusively use Bethune's transfer matrix algorithm. In the next section I will model the excitation of a thin film stack by a point source located a few nanometers above the surface, and calculate the emitted light measured in transmission.

## 5.2 Excitation by a local source

In this section I will first discuss the relation between the tunneling electrons of an STM and the model of oscillating dipole (OD) then detail this model.

### 5.2.1 From tunneling electrons of an STM to the oscillating dipole (OD) model

Uehara *et al.* [100] have discussed the steps leading from a model calculating the inelastic emission of the STM tunneling electrons to the replacement of the inelastic current by an oscillating dipole directly generating light (see figure 5.3).

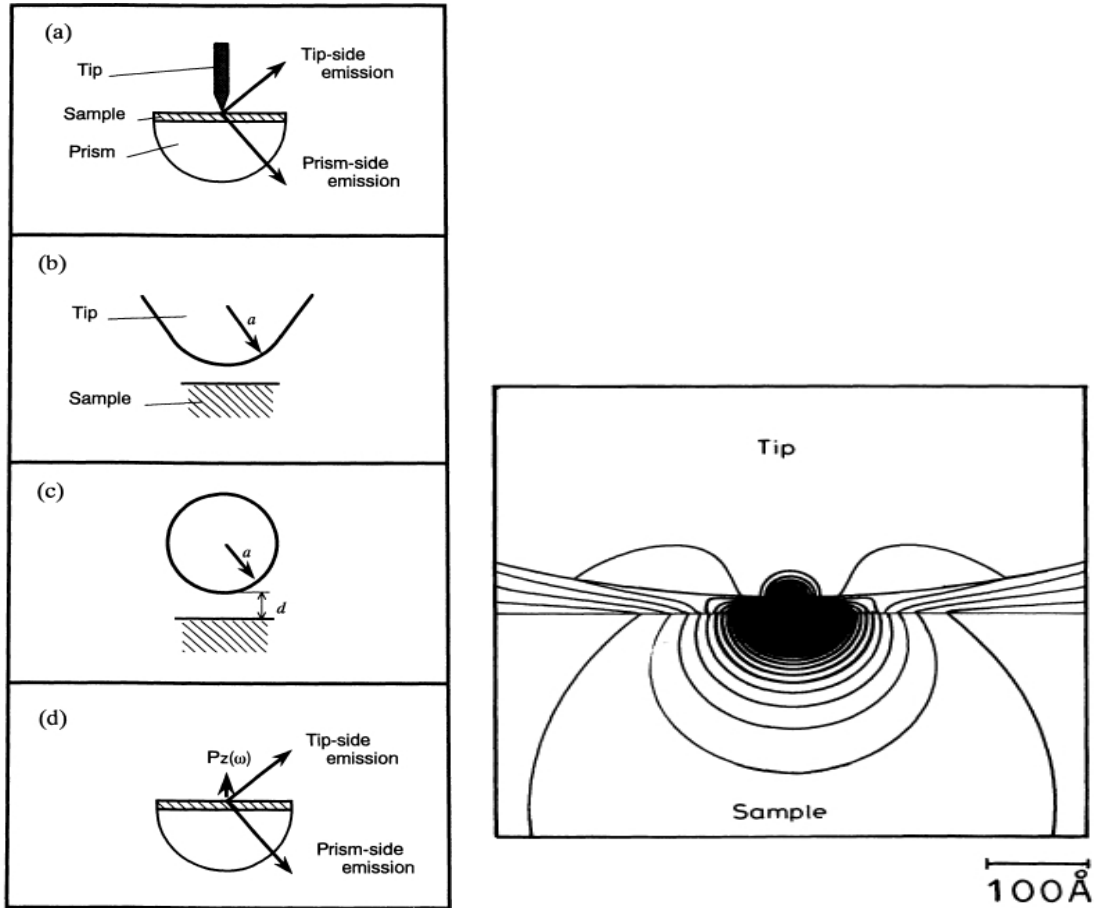


Figure 5.3: left graph: (a) the geometry of the STM-sample system and the emission: towards the vacuum "tip-side emission" and towards the sample "prism-side emission"; (b) Expanded picture of the region around the tip-sample gap; (c) The tip is modeled as a sphere and the sample is modeled as a semi infinite substrate with a flat surface. The distance  $d$  is the tip-sample separation; (d) The gap-sample structure and the tunneling current are replaced by an effective dipole  $P_z(\omega)$ . Right graph: the calculated equipotential curves of the electric field (taken from Uehara *et al.* [100]).

Consider a metal film deposited on a glass substrate. The sample is considered having an IMI structure with a metal film bounded by the cover layer (air) and the substrate (glass). An STM tip is located close to the sample (see graph (a) left column of figure 5.3). The power

spectrum of the STM tunneling current is decreasing linearly with frequency

$$\langle I^2 \rangle = \frac{1}{2\pi} e \cdot I \left( 1 - \frac{\hbar\omega}{eV_0} \right) \quad (5.32)$$

where  $V_0$  is the bias voltage and  $I$  is the DC current [100].

From the fluctuations of the current flux the intensity of the radiation is obtained by solving Maxwell equations. One focuses on the region in the vicinity of the tip and the sample surface presented in graph (b) left column in figure 5.3. Since the tunneling current decays exponentially with the tunneling distance this current, localized between the tip and the sample surface below, is sensitive to this local region only.

Uehara *et al.* model the tip as a sphere and the sample as a flat surface with a semi infinite extent (see graph (c) left column of figure 5.3). Since tunneling occurs in a very small region of the tip, the STM sphere radius is of an order of a few Angstroms ( $1 \text{ \AA} = 0.1 \text{ nm}$ ). To calculate the radiation intensity, one introduces an effective dipole  $P_z(\omega)$  which equivalently generates the electromagnetic field (see graph (d) left column of figure 5.3).

Figure 5.3 right graph displays the electric field induced by the tunneling current spreading over a wider region. But the main part of this field is confined in a region much smaller than the size of the tip and the wavelength of the visible light. This tangential region is about a hundred of Angstroms in size.

From this qualitative explanation one concludes that the inelastic tunneling current of an STM can be modeled, as we did in the present work, as an oscillating dipole with only the normal surface component ( $z$  in our case). The calculation of the oscillating dipole field, its penetration in the sample and the transmitted electromagnetic flux is done in the framework of Lukosz and Kunz [18], Novotny[20], Drezet and Genet [23], and Arnoldus and Foley [61] models discussed in the next section.

### 5.3 Oscillating dipole model (OD) in the momentum space

The system studied in this section is presented in Figure 5.4. A stack of thin films (e.g. air-Au-SiO<sub>2</sub>-Au-Ti-glass) is excited by inelastic tunneling electrons (the localized source is located about 1 nm from the surface). In the experiment we want to model, the light transmitted through the substrate of the thin film stack is collected by an inverted optical microscope.

Gimzewski *et al.* [101] discovered that the inelastic tunneling electrons excite the localized gap plasmon localized modes of a tip-sample junction. These gap plasmons excite the SPPs of a gold-air interface. If the Au film is thin enough ( $\lesssim 70 \text{ nm}$ ) then the evanescent field of the SPPs can "leak" into the next layer of higher refractive index and give rise to the emission of photons. The smaller the distance the higher the tunnel current thus the vast majority of the current passes vertically between the tip and the sample. Therefore, the oscillating dipole representing

the tunnel current is taken to be vertical. Several models of the light emission under the STM tip have been presented in the literature. Here we mention the models of Lukosz and Kunz [18], Novotny[20], Drezet and Genet [23], and Arnoldus and Foley [61]. Following these authors we approximate the excited gap plasmons by an oscillating dipole which radiates. The model, called the oscillating dipole model (OD) uses the formulation of Novotny[20] and Bhardwaj *et al.* [59]. We have also programmed the Drezet and Genet [23] model which gives similar results. Bhardwaj *et al.* [59] and Drezet and Genet [23] implement their models for a three-layer, two interface system. Since the derived expression contains the transmitted coefficients of the entire stack, the final transmitted flux (eq. (5.48) below) implicitly depends on the number of layers. Our contribution is the implementation of a method calculating this transmitted flux for an **arbitrary** number of layers.

Let us return to figure 5.4 presenting the geometry of the multilayer system where the oscillating dipole is located at a height  $h$  above the surface. The OD model expresses the light

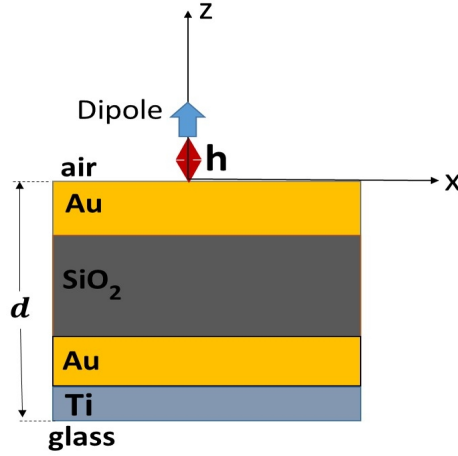


Figure 5.4: Six layer thin film stack excited by an oscillating dipole located at a height  $h$  above the first interface, where  $d$  is the total thickness of the stack.

emission by an oscillating dipole in terms of the Hertz auxiliary vectors  $\vec{\Pi}$ . If the substrate and the layers are described by linear, homogeneous and isotropic material functions then the electromagnetic field can be derived from two scalar functions, in fact two components of the Hertz vector  $\vec{\Pi} = (\Pi_x, 0, \Pi_z)$ . In the time-harmonic approximation (with the convention  $\exp(-i\omega t)$ ) the electric and magnetic fields in terms of Hertz vectors  $\vec{\Pi}$  read

$$\vec{E} = (k^2 + \vec{\nabla} \cdot \vec{\nabla}) \vec{\Pi} \quad \vec{H} = -i\omega \epsilon_0 \epsilon \vec{\nabla} \times \vec{\Pi} \quad (5.33)$$

For a layer  $j$  the Hertz vector  $\vec{\Pi}$  is calculated by solving the vector Helmholtz wave equation

$$(\nabla^2 + k_j^2) \vec{\Pi}(\vec{r}) = 0, \quad k_j = (\omega/c) \sqrt{\epsilon_j \mu_j} \quad j \in [1, n] \quad (5.34)$$

The basis functions satisfying this wave equation are a product of a Bessel function  $J_n$  of order  $n$  and an exponential. In cylindrical coordinates one has

$$J_n(k_\rho \rho) \exp(ik_z z + in\varphi), \quad (5.35)$$

where  $(\rho, \varphi, z)$  are the position coordinates and  $k_\rho$  and  $k_z$  are the components of the wave vector  $\vec{k}$  parallel and perpendicular to the interface. The solution of the Helmholtz equation in terms of a scalar free-space Green's function  $G_0(\vec{r}, \vec{r}')$  (see Novotny [102, chapter 2]) and a current density  $\vec{j}(r)$  reads

$$\vec{\Pi}(\vec{r}) = \frac{i}{\omega \varepsilon_0 \varepsilon} \int_V dV' \vec{j}(\vec{r}') G_0(\vec{r}, \vec{r}'). \quad (5.36)$$

For an oscillating dipole of momentum  $\vec{p}_0$  located at  $\vec{r} = h$  (see figure 5.4) the current density is  $\vec{j}(\vec{r}') = -i\omega \vec{p}_0 \delta(\vec{r}' - h)$ . In this case the Green's function  $G_0$  is written as a spherical wave. Then one rewrites eq. (5.36)

$$\vec{\Pi}(\vec{r}) = \frac{\vec{p}_0}{4\pi \varepsilon_0 \varepsilon} \frac{\exp(ik|\vec{r} - h|)}{|\vec{r} - h|} \quad (5.37)$$

Using the Sommerfeld identity expansion we can write the spherical wave as a superposition of plane waves in cylindrical coordinates

$$\begin{aligned} \frac{\exp(ikR_0)}{R_0} &= i \int_0^\infty dk_\rho \frac{k_\rho}{k_z} J_0(k_\rho \rho) \exp(ik_z|z - h|) \\ &\propto \sum_{\theta=0}^{\theta_c} \text{plane wave thin film}(\varepsilon_1/\dots/\varepsilon_n) + \sum_{\theta_c}^{90} \text{plane wave thin film}(\varepsilon_n/\dots/\varepsilon_1) \\ &\propto \sum_{\theta=0}^{\theta_c} \text{propagating} + \sum_{\theta_c}^{90} \text{evanescent} \end{aligned} \quad (5.38)$$

where  $R_0 = [\rho + (z - h)]^{1/2}$ , and  $J_0$  is again a Bessel function. Note that the expression in cylindrical coordinates permits a simple separation of the two terms. Arnoldus and Foley [61] use spherical coordinates. In order that eq. (5.38) be convergent, one requires  $\text{Im}(k_z) > 0$  which corresponds to  $\tilde{n} = n + i\kappa$  (see footnote 1).

The Sommerfeld expansion of a spherical wave is a mathematical tool. It contains two contributions: one propagating from the source (in our case the oscillating dipole in air) and one propagating from the substrate (opposite direction, glass medium). In these two cases the wave vector projection does not span the same domain,  $k_\rho^{air} \in [0, 1] k_0$  and  $k_\rho^{glass} \in [1, 1.52] k_0$ . The metrics of these projections are different and below we will use  $k_\rho^{glass}$  associated to the angle  $\theta^{glass}$  of the  $\varepsilon_n > \varepsilon_1$  medium. One can make the following comments on the above two terms of eq. (5.38) in the simplest case of dielectric media

1.  $\sum_{\theta=0}^{\theta_c}$  **propagating**: corresponds to an allowed/propagating wave. Propagating from the upper layer (air) to the lower layer (glass) with  $\theta_{air} \in [0, 90^\circ]$  and  $\theta_{glass} \in [0, \theta_c]$ , where  $\theta_c$  is the critical angle

$$\theta_c = \arcsin \frac{n_{air}}{n_{glass}} \quad (5.39)$$

where  $n_{air}$  and  $n_{glass}$  are the refractive indices. The wave vector projections  $k_\rho$ ,  $k_{z\,air}$  and

$k_{z\ glass}$  are real (see also the definition (5.22) and (5.23))

$$k_\rho = k_0 n_{air} \sin \theta \quad k_{z\ air} = \sqrt{(k_0 n_{air})^2 - k_\rho^2} \quad k_{z\ glass} = \sqrt{(k_0 n_{glass})^2 - k_\rho^2}. \quad (5.40)$$

2.  $\sum_{\theta_c}^{90}$  **evanescent**: corresponds to a forbidden or an evanescent wave. The light propagates from the lower layer (glass) to the upper layer (air) with an incident angle  $\theta_{glass}$  beyond the critical angle  $\theta_c$  ( $\theta_{glass} \in [\theta_c, 90^\circ]$ ). In this case the wave vector  $k_\rho$  and  $k_{z\ glass}$  are real while  $k_{z\ air}$  is purely imaginary

$$k_\rho = k_0 n_{glass} \sin \theta \quad k_{z\ glass} = \sqrt{(k_0 n_{glass})^2 - k_\rho^2} \quad k_{z\ air} = i \sqrt{k_\rho^2 - (k_0 n_{air})^2}. \quad (5.41)$$

Since in the evanescent region  $k_{z\ air}$  is purely imaginary, the exponent  $i k_{z\ air} |z - h|$  in eq. (5.38) is real, meaning that perpendicular to the interface the light is evanescent. Figure 5.5 presents the variation of  $k_{z\ air}$  and  $k_{z\ glass}$  as a function of the normalized in-plane wave vector  $k_\rho/k_0$  using eqs. (5.40) and (5.41). As explained above  $k_{z\ air}$  is purely real or purely imaginary respectively in the propagating ( $k_\rho/k_0$  within 1) and the evanescent ( $k_\rho/k_0$  beyond 1) domains whereas  $k_{z\ glass}$  is real everywhere.

With a complex refractive index,  $k_z$  becomes complex. Such a case seldomly appears in practice since the discussion above concerns the superstrate (first layer, air) and the substrate (last layer, glass). The other layers of the thin film stack can be of different material nature, this will not change the above discussion.

$$k_z = k_z^r + i k_z^i. \quad (5.42)$$

Each thin film of our stack presented in figure (5.4) is expanded in terms of the basis functions

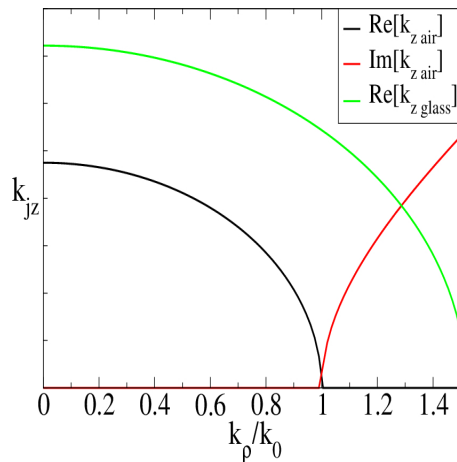


Figure 5.5: Variation of  $k_{z\ air}$  and  $k_{z\ glass}$  as a function of the normalized in-plane wave vector  $k_\rho/k_0$  using eqs. (5.40) and (5.41) at the wavelength  $\lambda_0=700$  nm.

eq.(5.35). The different expansions must satisfy the boundary conditions at the interfaces. The

corresponding Hertz vectors  $\vec{\Pi}$  can be derived from eqs. (5.33) using the boundary conditions at the interfaces, which requires  $k^2(\partial\Pi_x/\partial z)$ ,  $k^2\Pi_x$ ,  $\nabla\cdot\vec{\Pi}$ , and  $k^2\Pi_z$ . Since the field of a vertical dipole is rotationally symmetric, the Hertz vector  $\vec{\Pi}$  has only one component  $\vec{\Pi} = (0, 0, \Pi_z)$ .

Experimentally the intensity distribution of the emitted photons in the back focal plane of the collection objective is imaged. This corresponds to a calculation of the in-plane vectors of momentum/Fourier space. In more precise terms, the use of cylindrical coordinates allows one to treat the penetrating  $z$  and in-plane  $\rho$  and  $\varphi$  coordinates. The coordinates that will be involved in the Fourier transform correspond to the couple  $(\rho, \varphi) \Leftrightarrow (k_\rho, k_\varphi)$ . The  $z$  coordinate remains unchanged throughout these transformations. Moreover, in the present model we assume no  $\varphi \Leftrightarrow k_\varphi$  dependence in the observables and therefore this coordinate will be withdrawn from the expressions below.

Following the above discussion, we first calculate the in-plane electric field in the substrate  $\mathcal{E}(k_\rho, z, \omega)$  in momentum space. It is a function of the in-plane momentum distribution of the transmitted photons written in terms of the transmission coefficient  $t^{(p)}$  calculated using Bethune's algorithm (see section 5.1.2). Based on the Novotny formulation [20], Bharadwaj *et al.* [59] calculated the in-plane electric field  $\mathcal{E}_\rho$  in cylindrical coordinates

$$\mathcal{E}_\rho(k_\rho, z, \omega) = \frac{i}{8\pi^2\varepsilon_0} \frac{k_0 k_\rho t^{(p)}(k_\rho, z)}{k_{z\text{air}}} \exp[\{i[k_{z\text{air}}h - k_{z\text{glass}}(z+d)]\}], \quad (5.43)$$

where again  $h$  is the position of the dipole above the gold surface and  $d$  is the thickness of the system (both are displayed in figure 5.4) and  $k_0 = \omega/c$  is the vacuum wave vector. The electric field of eq. (5.43) is used to calculate the transmitted flux or Poynting vector through the thin film stack. Using the time harmonic Faraday-Maxwell equation for the magnetic field one has in coordinate space

$$\begin{aligned} \vec{S} &= \vec{E} \times \vec{H}^* & i\omega\mu_0\mu\vec{H} &= \vec{\nabla} \times \vec{E} \\ \vec{S} &= \frac{1}{i\omega\mu_0\mu} \vec{E} \times (\vec{\nabla} \times \vec{E}^*) \end{aligned}$$

In momentum/Fourier space one writes

$$\begin{aligned} \vec{S} &= \vec{\mathcal{E}} \times \vec{\mathcal{H}}^* & \omega\mu_0\mu\vec{\mathcal{H}} &= \vec{k} \times \vec{\mathcal{E}} \\ \omega\mu_0\mu\vec{S} &= \vec{\mathcal{E}} \times (\vec{k} \times \vec{\mathcal{E}}^*) = (\vec{\mathcal{E}} \cdot \vec{\mathcal{E}}^*)\vec{k}^* - (\vec{\mathcal{E}} \cdot \vec{k}^*)\vec{\mathcal{E}}^* = (\vec{\mathcal{E}} \cdot \vec{\mathcal{E}}^*)\vec{k}^* \end{aligned} \quad (5.44)$$

where, since the two vectors  $\vec{k}$  and  $\vec{\mathcal{E}}$  are orthogonal for homogeneous media,  $(\vec{\mathcal{E}} \cdot \vec{k})\vec{\mathcal{E}}^*$  in the second line of the expressions above is zero.

One is interested in the transmitted flux or Poynting vector  $\mathcal{S}^\downarrow$  in the last medium of the multilayer (or substrate)

$$\mathcal{S}^\downarrow(k_\rho, z, \omega) = \vec{S}(k_\rho, z, \omega) \cdot \vec{n}_z = \frac{\vec{\mathcal{E}}(k_\rho, z, \omega) \cdot \vec{\mathcal{E}}^*(\vec{k}_\rho, z, \omega) k_{fz}^*}{\omega\mu_0\mu}, \quad (5.45)$$

where  $\vec{n}_z$  is the unit vector perpendicular to the interface of the stack of thin films. Normalizing the Poynting vector eq. (5.45) to the incident Poynting vector  $S_0$ , one obtains the intensity of the transmitted light

$$I^\downarrow(k_\rho, z, \omega) = \frac{\mathcal{S}_\rho^\downarrow(k_\rho, z, \omega)}{S_0} = \frac{k_{fz}^*}{S_0 \omega \mu_0 \mu} \mathcal{E}_{k_\rho}(k_\rho, z, \omega) \mathcal{E}_{k_\rho}^*(k_\rho, z, \omega); \quad (5.46)$$

where  $S_0$  reads

$$S_0 = \frac{p_{0z}^2 \omega}{12\pi^2 \varepsilon_0} k_1^5 \quad [S_0] = \frac{Q^2 L^2 T^{-1}}{Q^2 T^2 / (M L^3)} L^{-5} = \frac{M}{T^3} \quad (5.47)$$

where  $p_{0z}$  is the dipole moment of the oscillating dipole and  $k_1$  is the wave vector in medium 1. As in the spherical wave expansion, the transmitted flux in the lowest medium  $I_f^\downarrow$  can be decomposed into two contributions  $I_{allowed}^\downarrow$  and  $I_{forbidden}^\downarrow$ , which are respectively the power radiated into the forward direction **within** (allowed light) and **beyond** (forbidden light) the critical angle  $\theta_c$  defined in this last medium. Therefore the intensity of the transmitted light  $I^\downarrow(k_\rho, z, \omega)$  presents two forms

$$\left\{ \begin{array}{l} I_{allowed}^\downarrow = \frac{k_0^2 k_{z\ glass}^*}{S_0 \omega \mu_0 \mu} \frac{k_\rho^2 |t^{(p)}(k_\rho, z)|^2}{k_{z\ air}^2} \quad k_\rho \in [0, k_0 n_{air}] \\ I_{forbidden}^\downarrow = \frac{k_0^2 k_{z\ glass}^*}{S_0 \omega \mu_0 \mu} \frac{k_\rho^2 |t^{(p)}(k_\rho, z)|^2}{k_{z\ air}^2} \exp(-2 k_{z\ air}^i h) \quad k_\rho \in [k_0 n_{air}, k_0 n_{glass}] \end{array} \right. , \quad (5.48)$$

where  $k_{z\ air}^i$  is the imaginary part of the wave vector projection  $k_{z\ air}$ ,  $t^{(p)}(k_\rho, z)$  is the transmission coefficient of thin film stack of thickness  $d$ . Note that the complete information about the layered system is contained in the transmission coefficient  $t^{(p)}$  calculated using eq. (5.30) of section 5.1.2 above. Since  $k_{z\ air}^i$  is positive, the power flux of the evanescent waves decays exponentially with the inverse of the height  $h$  of the dipole above the interface. The height  $h$  of the dipole above the first interface permits a modulation of the origin of the transmitted light. If the height  $h$  is large the emitted flux originates from propagating waves  $I_{allowed}$  only, since  $\exp(-2 k_{z\ air}^i h)$  reduces the evanescent contribution to almost zero. If the height is small then there is a significant contribution of the evanescent term. The originality of our model is that we can treat a problem of an arbitrary number of layers.

### 5.3.1 Oscillating dipole (OD) transmitted flux in coordinate space

To obtain the flux  $S_\rho^\downarrow(\rho, z)$  in real space  $\{\vec{\rho}, z\}$  one must separately inverse Fourier transform the electric field  $\mathcal{E}_\rho$  and the product  $k_{fz} \cdot \mathcal{E}_\rho$

$$\vec{E}_\rho(\vec{\rho}, z) = \frac{1}{\sqrt{2\pi}} \int d\vec{k}_\rho \vec{\mathcal{E}}_\rho(\vec{k}_\rho, z) e^{(i\vec{k}_\rho \cdot \vec{\rho})} \quad \frac{d\vec{E}_\rho(\vec{\rho}, z)}{dz} = \frac{1}{\sqrt{2\pi}} \int d\vec{k}_\rho k_{fz} \cdot \vec{\mathcal{E}}_\rho(k_\rho, z) e^{(i\vec{k}_\rho \cdot \vec{\rho})}, \quad (5.49)$$

Using eq. (5.44) the field and its derivative are combined to obtain the equivalent of eqs. (5.45) and (5.46) of the Poynting vector and of the flux intensity in coordinate space

$$S_\rho^\downarrow(\rho, z) = \frac{1}{\omega \mu_0 \mu} E_\rho(\rho, z) \cdot \frac{dE_\rho^*(\rho, z)}{dz} \quad I(\rho, z) = \frac{1}{S_0 \omega \mu_0 \mu} E_\rho(\rho, z) \cdot \frac{dE_\rho^*(\rho, z)}{dz}. \quad (5.50)$$

We would like to point out that the coordinate  $z$  is a spectator coordinate. It is never used in a Fourier transform.

## 5.4 Conclusion

This chapter presented the excitation by a source at infinity (ESI) model and a local excitation using an oscillating dipole (OD) model of a multilayer ( $n > 3$ ) thin film stack. In the ESI model the light is analyzed in reflection and transmission using respectively the reflectance and transmittance. In the OD model, derived in refs. [18; 20; 23], we used the Sommerfeld expansion expressing the spherical waves generated by the dipole in terms of plane waves in **cylindrical** coordinates. Both models ESI and OD require calculations using a plane wave formalism. The transfert matrix algorithm of Abès as implemented by Bethune [58], an algorithm taking into account multiple reflexions, is used to obtain the reflexion and transmission Fresnel coefficients. The ESI and OD models have been implemented in a Mathematica notebook, the results and the comparison with the experiment are presented in the next chapter.

# Chapter 6

## Comparative study of the SPP-like and of the wave guide like (WG-like) modes of the three and six-layer thin film stacks

This chapter presents the calculations of observables when a thin film stack is excited by a source at infinity or a local source of light or electrons. As explained in chapter 5 we used models where the source is at infinity (ESI, section 5.1 of the preceding chapter) and a local source of excitation where the inelastic tunneling electrons of the STM are represented by a vertical oscillating dipole (OD, section 5.3 of the preceding chapter). The results are presented for three (air-Au-glass) and six-layer (air-Au-SiO<sub>2</sub>-Au-Ti-glass) thin film stacks. For the six layer stack, the two gold layers have identical thicknesses.

For the ESI model, the observables are the reflectance and the transmittance, whereas using the OD model one studies the transmitted flux intensity. Sections 6.2.1, 6.2.2 and 6.4.1 below which discuss the ESI and the OD models begin by exploring the observables as a function of the thicknesses of the Au and SiO<sub>2</sub> layers respectively  $d_{Au}$  and  $d_{SiO_2}$ . Then one discusses the dispersion curves and finally the comparison of the model calculations with the experiment. The last part of this chapter presents the transmitted flux intensity calculation in coordinate space using the OD model.

### 6.1 Material functions

In this section I will compare the Palik compilation and Johnson and Christy [103] data for the refractive index of the gold layer. The metal refractive index reads

$$n_{metal} = n + i\kappa$$

where  $n$  and  $\kappa$  are the real and the imaginary parts of the refractive index. Figure 6.1 displays the real and imaginary parts of the refractive index as a function of the wavelength  $\lambda$ . Based on figure 6.1, the imaginary part of the refractive index is smooth for the Johnson and Christy data [103] whereas the Palik compilation [104] displays a plateau between 570-670 nm. This plateau can change the results in the region between 570 nm and 670 nm. The real part of the data in discussion are very similar. More recent data of Yakubovsky *et al.* [105] and Olmon *et al.* [106] reproduce the Johnson and Christy results. We conclude that the Palik data presents a problem between 570-670 nm and we will use the Johnson and Christy data in the following.

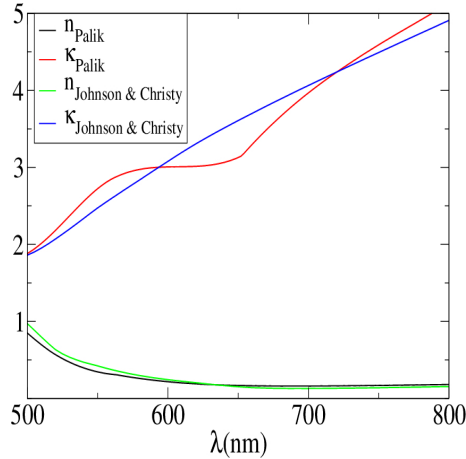


Figure 6.1: Comparison between the refractive index of gold as a function of the wavelength  $\lambda$ , using the data of Palik and Johnson and Christy.

## 6.2 Excitation by a source at infinity (ESI): Reflectance and transmittance

Recall that a thin film stack (see chapter 2) is composed of a number of layers where the first, called the cover layer, and the last, called the substrate, are semi infinite. In the ESI model discussed in this section, the thin film stack is excited by a plane wave incident from the glass medium, and the normalized reflected flux or reflectance is calculated (see figure 6.2). One also calculates the transmittance. In the next two sections we will vary the geometrical parameters of the thin film in search of the appropriate geometrical parameters for the experimental measurements.

glass-Ti(3 nm)-Au( $d_{Au}$ )-SiO<sub>2</sub>( $d_{SiO_2}$ )-Au( $d_{Au}$ )-air

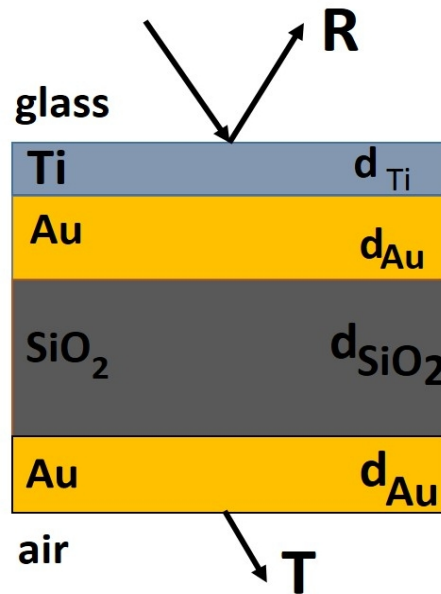


Figure 6.2: The six layer thin film stack used in the calculations.

### 6.2.1 Au thickness variation

In this section the gold thickness of the three and the six-layer thin film stack is varied while the SiO<sub>2</sub> thickness is 70, 310 or 410 nm.

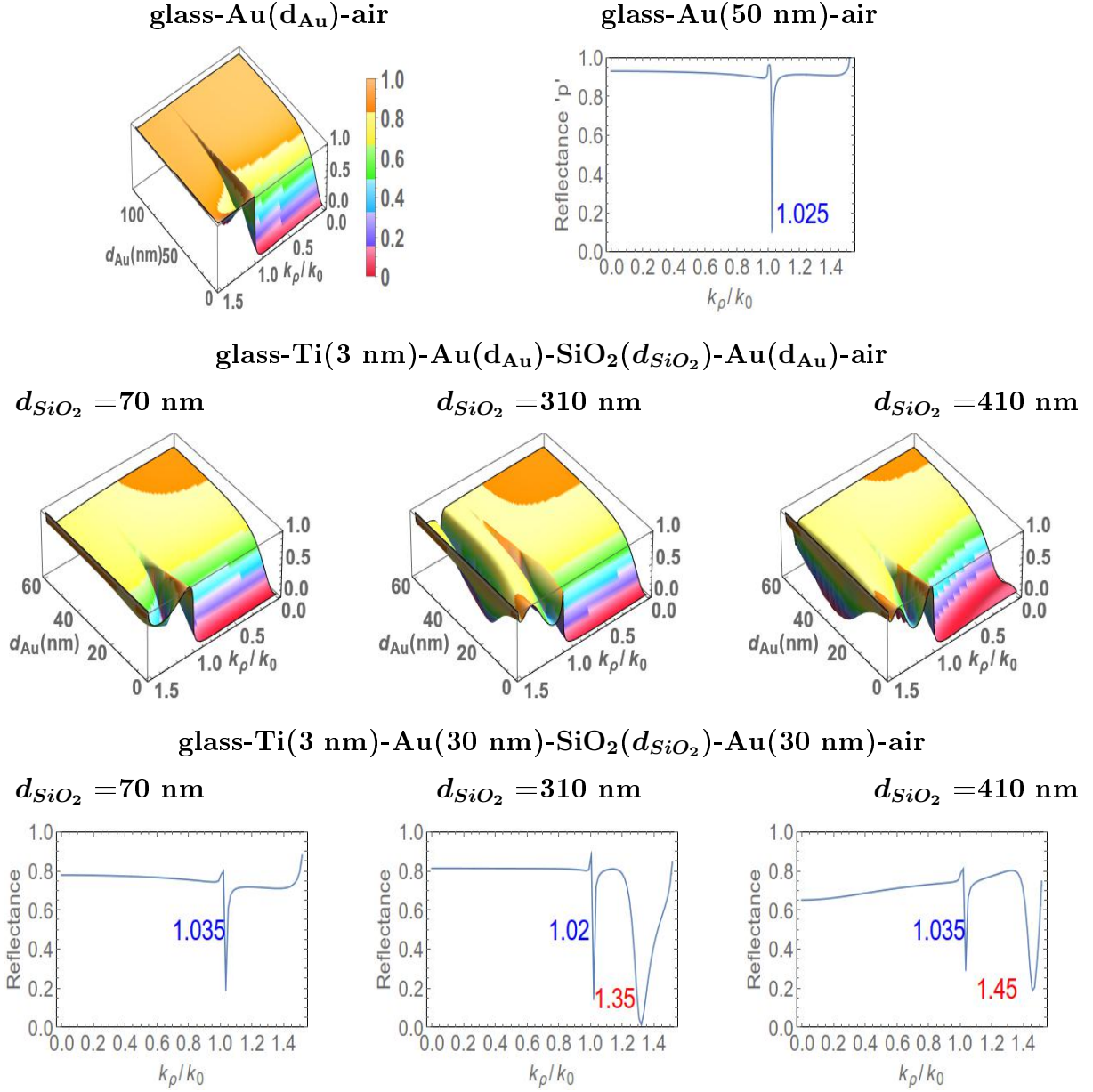


Figure 6.3: Reflectance as a function of the Au layer thickness  $d_{Au}$  and of the normalized in-plane wave vector  $k_{\rho}/k_0$  for incident  $p$  polarized light  $\lambda = 750$  nm. The first row presents the data for the three-layer stack as a 3D plot (left), and as a 2D plot (right) for  $d_{Au} = 50$  nm. The second row left, middle and right graphs display the reflectance of the six-layer stack with  $d_{SiO_2} = 70$  nm,  $d_{SiO_2} = 310$  nm and  $d_{SiO_2} = 410$  nm respectively. The third row displays 2D cuts for an experimental thickness  $d_{Au} = 30$  nm of the 3D plots of the second row.

Figure 6.3 displays a 3D graph of the reflectance  $\mathcal{R}$  as a function of the gold thickness  $d_{Au}$  and the normalized in-plane wave vector  $k_{\rho}/k_0$  at the wavelength of  $\lambda = 750$  nm. This figure also presents 2D graphs of the reflectance as a function of  $k_{\rho}/k_0$  of a three-layer stack with  $d_{Au} = 50$  nm (first row, right graph). Since the energy of the incident light is transferred to the SPP bound mode and is not reflected, the SPP mode appears as a dip in the reflectance [34]. The associated experimental method is discussed in chapter 4. In the three-layer stack (first row

in figure 6.3) the dip in the evanescent region appears at  $k_\rho/k_0 \cong 1.025$  for  $d_{Au}(nm) \in [10, 90]$  and it corresponds to an SPP mode (see for example Bharadwaj *et al.*[59], Wang *et al.* [39] and Marty *et al.* [60]).

First of all the difference between the three-layer  $d_{Au}^{three}(nm) \in [10, 90]$  and six-layer  $d_{Au}^{six}(nm) \in [10, 50]$  stacks originates from the presence of two gold thin films in the six-layer stack. For a six-layer stack, three different thicknesses of  $d_{SiO_2}$  are explored, 70, 310 and 410 nm, first, second and third column in figure 6.3. In these graphs the reflectance has a significant dip at  $k_\rho/k_0 = 1.035, 1.02$  and  $1.035$  for  $d_{Au}(nm) \in [10, 50]$ . Since the dip has a normalized in-plane wave vector close to the one of the SPP for three-layer, this mode possibly has an SPP character and will be called an SPP-like mode.

At large  $SiO_2$  thicknesses our six-layer structure can support guided modes in the  $SiO_2$  layer (see the discussion of this assignment of this mode in section 6.4.4). For the thicknesses  $d_{SiO_2} = 310$  and  $410$  nm a second dip is present possibly having this wave guide nature and it will be designated as a wave guide like (WG-like) mode. It corresponds to a larger normalized in-plane wave vector  $k_\rho/k_0 = 1.35$  and  $1.45$  respectively for  $d_{SiO_2} = 310$  and  $410$  nm. Note also that for  $d_{SiO_2} = 310$  nm (figure 6.3 third row, second column) the normalized wave vector dip of the SPP-like mode is shifted down to  $1.02$  being possibly repelled by the presence at  $k_\rho/k_0 = 1.35$  of a WG-like mode.

Based on the above discussion, a three-layer experimental sample is prepared with  $d_{Au}^{three} = 50$  nm and a six layer is prepared with  $d_{Au}^{six} = 30$  nm. These samples correspond to a significant dip in the reflectance (figure 6.3 third row). The WG-like mode appears only in the six-layer stack and the conditions of its appearance as a function of  $SiO_2$  thickness are explored next.

### 6.2.2 $SiO_2$ thickness variation in a six-layer stack

The results of the preceding section let us select the Au layer thickness of the six-layer stack. Figure 6.4 displays the reflectance for  $\lambda = 750$  nm as a function of the  $SiO_2$  thickness  $d_{SiO_2}$  and the normalized in-plane wave vector  $k_\rho/k_0$  for  $d_{Au} = 15$  (left graph) and  $30$  nm (right graph). Figure 6.5 presents 2D cuts of the 3D graphs in figure 6.4, at  $k_\rho/k_0 = 0.5, 1.02, 1.04$  and  $1.35$  for both  $d_{Au} = 15$  nm and  $d_{Au} = 30$  nm. These normalized in-plane wave vectors  $k_\rho/k_0$  are chosen in order to present the reflectance as a function of  $SiO_2$  thickness in the propagating, close to 1 and evanescent regions. In the propagating region  $k_\rho/k_0 \in [0, 1]$  (see figure 6.4 and figure 6.5 first column) the graphs display clear periodic behavior, with a period of about 280 nm.

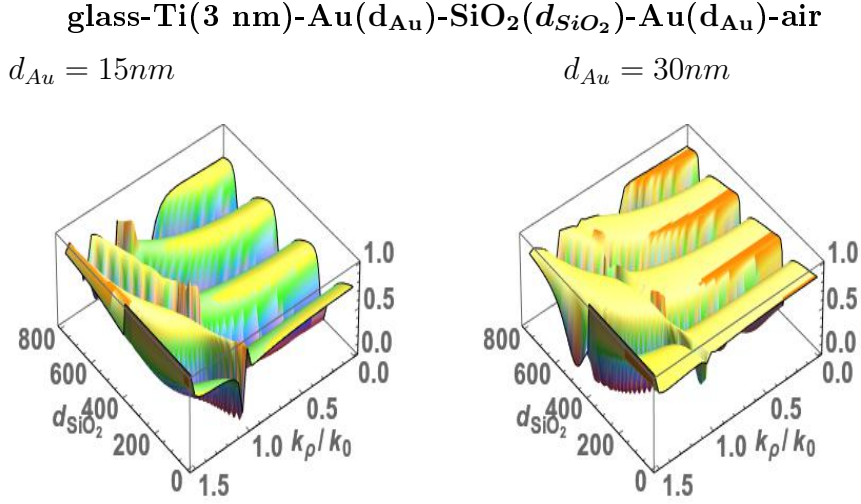


Figure 6.4: The reflectance of incident  $p$  polarized light of  $\lambda = 750$  nm as a function of  $d_{SiO_2}$  and the normalized in-plane wave vector  $k_\rho/k_0$ . Left graph  $d_{Au}=15$  nm, right graph  $d_{Au}=30$  nm.

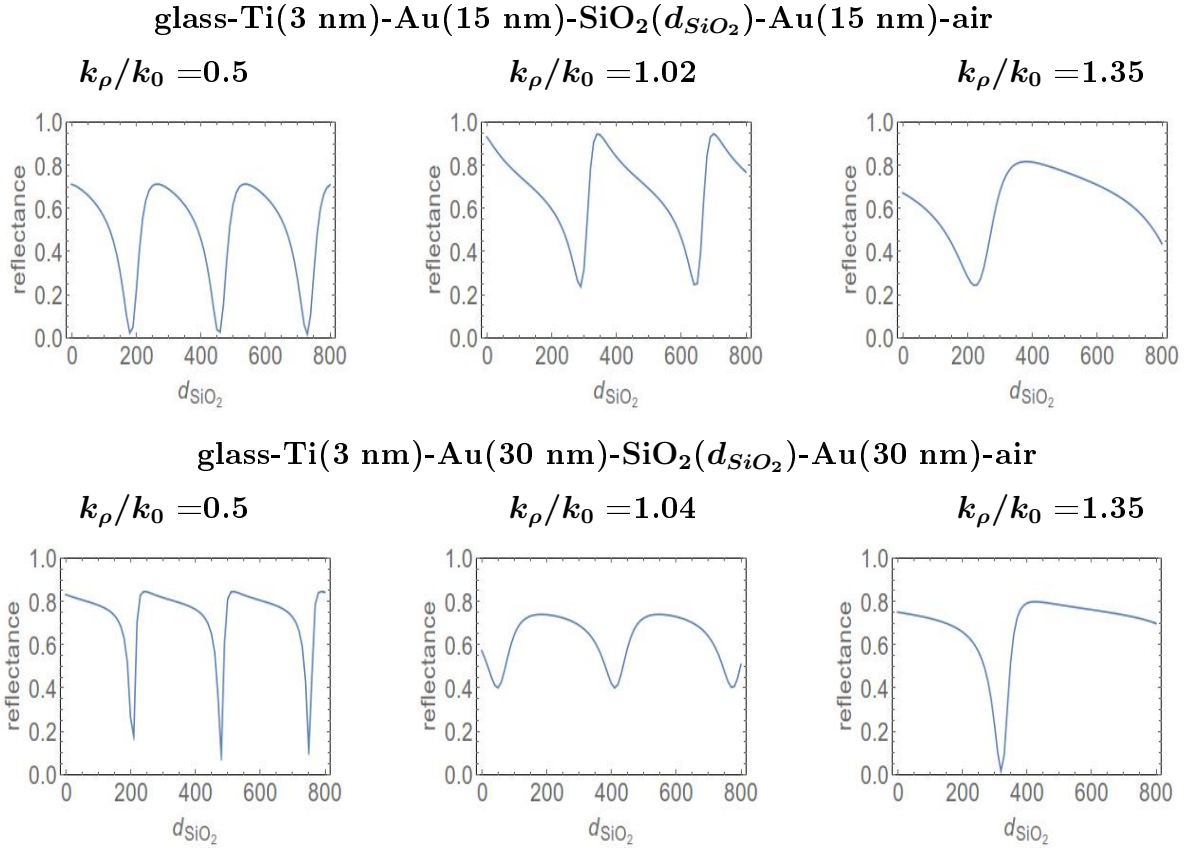


Figure 6.5: The reflectance of  $p$  polarized light at  $\lambda = 750$  nm as a function of the SiO<sub>2</sub> thickness  $d_{SiO_2}$ . At fixed normalized in-plane wave vector  $k_\rho/k_0$  the first row glass-Au(15nm)-SiO<sub>2</sub>( $d_{SiO_2}$ )-Au(15nm)-Ti(3nm)-air at  $k_\rho/k_0 = 0.5, 1.02,$  and  $1.35$ , and the second row glass-Au(30nm)-SiO<sub>2</sub>( $d_{SiO_2}$ )-Au(30nm)-Ti(3nm)-air at  $k_\rho/k_0 = 0.5, 1.04,$  and  $1.35$  are presented in the first, second and third columns respectively.

The first column of figure 6.5 presents a cross-section at  $k_\rho/k_0=0.5$  in the allowed region with a clear periodicity as mentioned above and deep minima in the reflectance. The maxima and minima collected in table 6.1 are not very different.

Table 6.1: Reflectance amplitude for  $d_{Au}=15$  and 30 nm at  $k_\rho/k_0=0.5, 1.02, 1.04$  and 1.35.

$k_\rho/k_0$	0.5		1.02 / 1.04		1.35	
$d_{Au}$	15 nm	30 nm	15 nm	30 nm	15 nm	30 nm
$\mathcal{R}_{min}$	$\sim 0$	0.1	0.28	0.42	0.22	$\sim 0$
$\mathcal{R}_{max}$	0.75	0.85	0.95	0.8	0.8	0.8

The second column of figure 6.5 displays the results at  $k_\rho/k_0=1.02$  and 1.04 respectively for  $d_{Au}=15$  and 30 nm. These particular normalized in-plane wave vectors corresponding to a shallower reflectance minimum, are probably due to the interaction between the SPP and WG-like modes. The minima are deeper for  $d_{Au}=15$  nm than for  $d_{Au}=30$  nm (see table 6.1) indicating that the transmission due to the evanescent wave is stronger for thinner layers of gold (see figure 6.3 of the preceding section).

How can one understand the periodic behavior of the reflectance at  $k_\rho/k_0 < 1$  and the relation between thickness and the wavelength? Born and Wolf [12, chapter 1] demonstrate this periodic behavior for a glass-SiO<sub>2</sub>-air dielectric stack. The Fresnel coefficient  $r_{13}$  of this stack reads

$$r_{13} = \frac{r_{12} + r_{23} \exp(2i\beta)}{1 + r_{12} r_{23} \exp(2i\beta)},$$

with

$$\beta = \frac{2\pi}{\lambda} n_2 \cos \theta_2 h$$

where  $h$  is the thickness of SiO<sub>2</sub> layer. The corresponding reflectance  $\mathcal{R}_{13}$  is

$$\mathcal{R}_{13} = r_{13} r_{13}^* = \frac{r_{12}^2 + r_{23}^2 + r_{12} r_{23} \cos(2\beta)}{1 + r_{12}^2 r_{23}^2 + 2 r_{12} r_{23} \cos(2\beta)}. \quad (6.1)$$

The reflectance  $\mathcal{R}_{13}$  is unchanged when replacing  $\beta$  by  $\beta + \pi$

$$\begin{aligned} \beta + \pi &= \frac{2\pi}{\lambda} n_2 \cos \theta_2 h + \pi = \frac{2\pi}{\lambda} n_2 \cos \theta_2 \left( h + \frac{\lambda}{2 n_2 \cos \theta_2} \right) = \frac{2\pi}{\lambda} n_2 \cos \theta_2 (h + \Delta h) \\ \Delta h &= \frac{\lambda}{2 n_2 \cos \theta_2} = \frac{\lambda}{2 \sqrt{n_2^2 - (k_\rho/k_0)^2}} \end{aligned} \quad (6.2)$$

Born and Wolf [12] conclude that the reflectance of a dielectric film is periodic with a period of  $\Delta h$ .

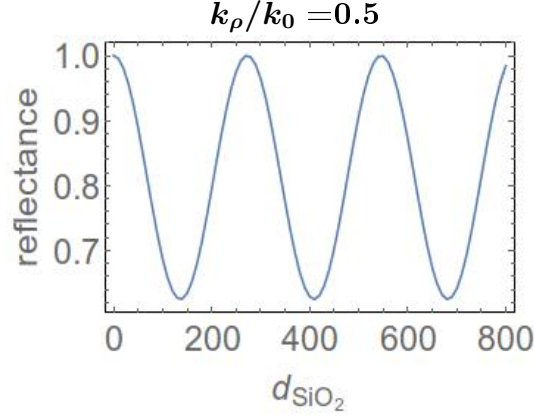


Figure 6.6: Reflectance at  $\lambda=750$  nm of a  $\text{SiO}_2$  film bounded by glass and air, as a function of the  $\text{SiO}_2$  thickness  $d_{\text{SiO}_2}$ .

At  $\lambda=750$  nm and  $k_\rho/k_0=0.5$ , figure 6.6 displays the reflectance of glass- $\text{SiO}_2$ -air stack, as a function of  $\text{SiO}_2$  thickness  $d_{\text{SiO}_2}$ . With this WG model, supporting only the WG-like modes,  $\Delta h=278$  nm compared with  $\Delta h=280$  nm measured in the graphs of the first column of figure 6.5. We conclude that what we are observing at  $k_\rho/k_0=0.5$  (figure 6.5 first column) is a WG-like mode. In the evanescent region for  $k_\rho/k_0 \in [1, 1.52]$  the periodicity with  $d_{\text{SiO}_2}$  is less obvious and partly disappears (see figure 6.4 and the second and third columns of figure 6.5) and there is a change in the slope of the reflectance furrow of the WG-like mode.

### 6.2.3 Reflectance of three and six-layer thin film stacks as a function of $\lambda$ and $k_\rho/k_0$

In the preceding two sections we have presented the results of the calculation of the reflectance at the wavelength  $\lambda=750$  nm. Here I want to explore the wavelength dependence of the reflectance for the thicknesses of  $d_{\text{Au}}$  and  $d_{\text{SiO}_2}$  found above. Figure 6.7 presents the reflectance as a function of the wavelength  $\lambda$  and the normalized in-plane wave vector  $k_\rho/k_0$  for a three (first row) and six-layer (second row) stack where the left, middle and right graphs correspond to  $d_{\text{SiO}_2} = 190, 310$  and  $410$  nm respectively. For the three-layer case, the SPP mode appears at  $k_\rho/k_0 = 1.025$  (see figure 6.3 above, first row right graph) and the normalized in-plane wave vector is nearly invariant with the wavelength ( $\Delta k_\rho/k_0 = 0.06$ ). For the six-layer stack, the dip corresponding to the SPP-like mode appears in the evanescent region and again this dip is nearly invariant with the wavelength. For the chosen thicknesses of  $\text{SiO}_2$  the WG-like mode appears at different  $\lambda$  and varies with  $k_\rho/k_0$  in both the propagating and evanescent regions. In the evanescent region this picture is not clear due to the simultaneous presence of the SPP-like and WG-like modes. At  $k_\rho/k_0=1.5$  the WG-like mode starts at  $\lambda=680, 850$  and  $1050$  nm for  $d_{\text{SiO}_2}=190, 310$  and  $410$  nm respectively. From this, one can conclude that with increasing  $\text{SiO}_2$  thickness, the appearance of the region of the WG-like mode is displaced to larger wavelengths. Precisely

these graphs display an avoided crossing (anti-crossing) discussed in relation with the density plot graphs figure 6.9.

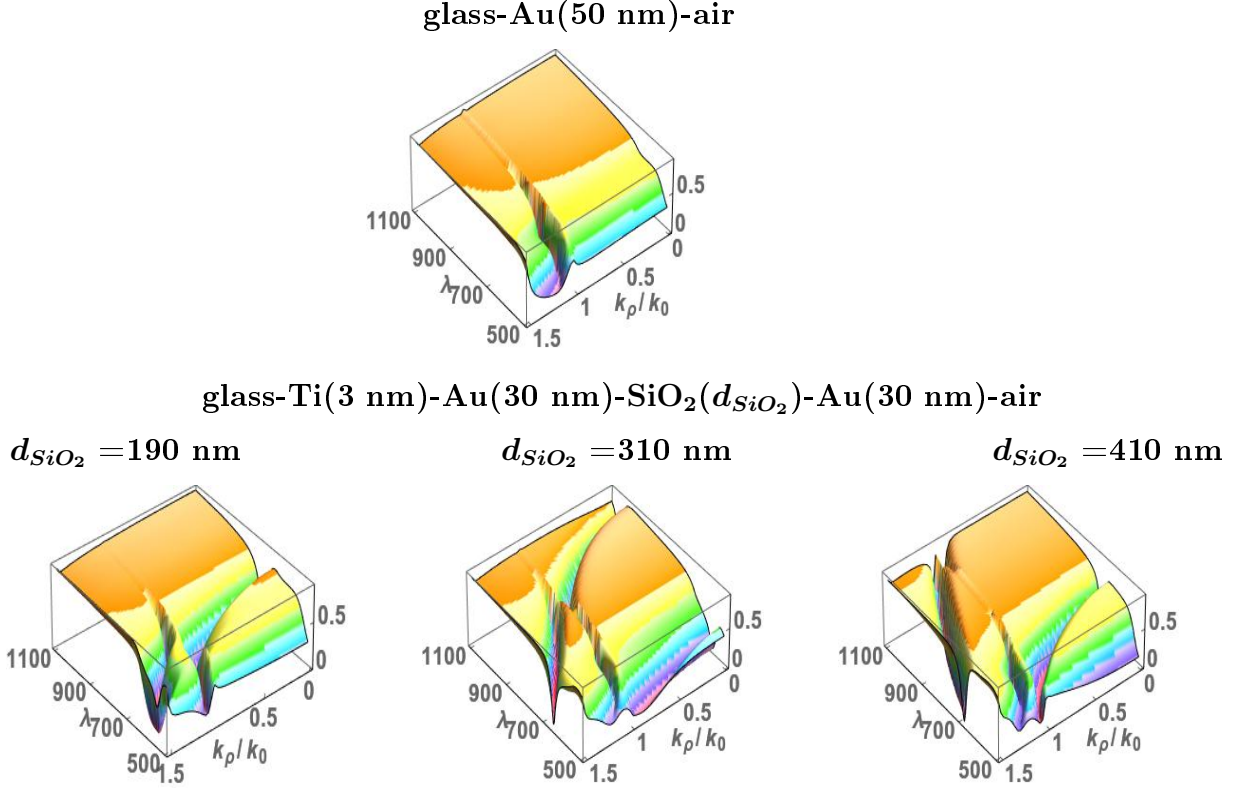


Figure 6.7: The reflectance of  $p$  polarized light as a function of the wavelength  $\lambda$  and of the normalized in-plane wave vector  $k_\rho/k_0$ . The first row presents the three-layer stack glass-Au(50nm)-air. The second row left, middle and right graphs display the reflectance of a six-layer stack glass-Au(30nm)-SiO<sub>2</sub>( $d_{SiO_2}$ )-Au(30nm)-Ti(3nm)-air with  $d_{SiO_2} = 190, 310$  and  $410$  nm respectively.

Columns  $\lambda=680, 750$  and  $850$  nm of figure 6.8 present the detailed graphical study of the reflectance as a function of the normalized in-plane wave vector  $k_\rho/k_0$  of a six-layer stack with  $d_{SiO_2}=190, 310$  and  $410$  nm in the first, second and third rows respectively. We discard  $d_{SiO_2}=70$  nm since the WG-like mode is absent (see section 6.2.2).

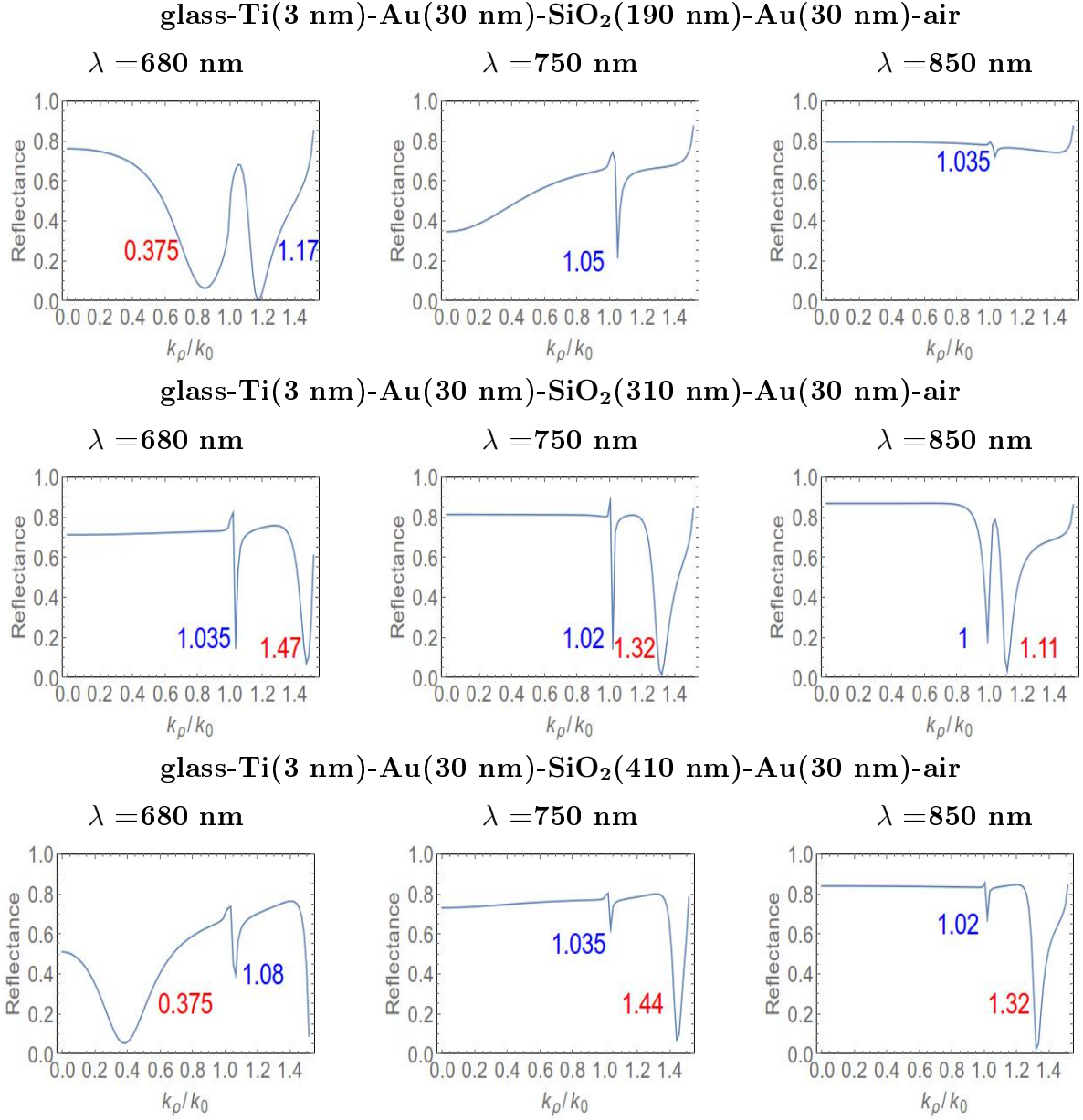


Figure 6.8: The reflectance of  $p$  polarized light as a function of the normalized in-plane wave vector  $k_\rho/k_0$ . A row corresponds to a particular thickness  $d_{\text{SiO}_2}=190, 310$  and  $410$  nm of the glass-Au-SiO<sub>2</sub>-Au-Ti-air thin film stack. A column corresponds to a particular wavelength  $\lambda=680, 750$  and  $850$  nm.

In these graphs the dip appearing just above  $k_\rho/k_0=1$  corresponds to an SPP-like mode usually with a low mixing of the WG-like mode (see next chapter for more details). Sometimes the SPP-like mode is enlarged and shifted (see figure 6.8 SiO<sub>2</sub>=190,  $\lambda=680$  nm) corresponding to a larger mixing between the SPP-like and WG-like mode. The other dips appearing in the propagating (see previous section) and in the evanescent regions (see the rest of the chapter) are mainly of the WG-like mode type. From figures 6.7 and 6.8, and the discussion of the preceding two sections, one concludes that the SPP-like mode position in  $k_\rho/k_0$  is nearly invariant with the wavelength except in the domain of the interaction with the WG-like mode. It is the wide

variation of the WG-like  $k_\rho/k_0$  position of the reflectance dip function of the wavelength that permits the interaction and the avoided crossing (anti-crossing) with the SPP-like mode.

#### 6.2.4 Dispersion of the reflectance for $s$ and $p$ polarizations

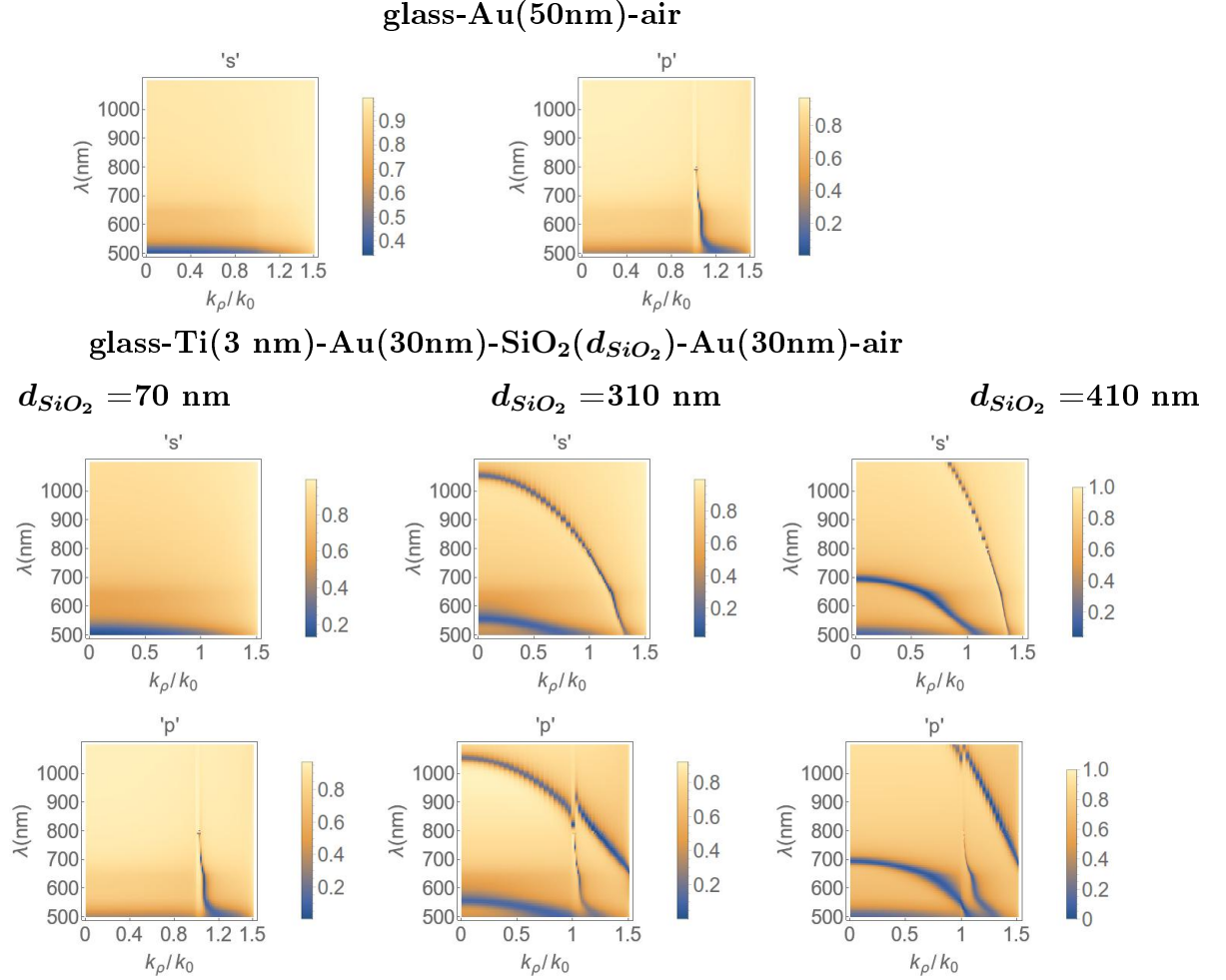


Figure 6.9: Reflectance dispersion of a thin film stack illuminated with  $s$  and  $p$  polarized light. The first row presents the three-layer stack glass-Au(50 nm)-air results, left,  $s$  and right  $p$  polarizations. The second and third rows present the  $s$  and  $p$  polarization laser excitation of a six-layer glass-Ti(3 nm)-Au(30nm)-SiO<sub>2</sub>( $d_{SiO_2}$ )-Au(30nm)-air stack. The columns of the second and third rows correspond from left to right to  $d_{SiO_2}=70$ , 310 and 410 nm.

Figure 6.9 presents density plots (in the form of a 3D graph where the third component is presented as color scale) of the dispersion curve of the reflectance for illumination with  $s$  and  $p$  polarized light. The first row displays the three-layer stack excited by  $s$  and  $p$  polarized light. For  $s$  polarized light no apparent SPP mode is visible, since the SPP can not be excited (see chapter 3). Therefore, the dip in the  $p$  polarization reflectance (first line, right graph) corresponds to the SPP mode (see discussion in section 6.2.1).

The second and third rows present the six-layer stack excited again by  $s$  and  $p$  polarized light respectively. The last two rows of the figure correspond to  $d_{\text{SiO}_2}=70, 310$  and  $410$  nm, in the left, middle, and right columns. The  $p$  polarized reflectance, displayed as a density plot in the last row of figure 6.9 for  $d_{\text{SiO}_2}=310$  and  $410$  nm, has already been presented as 3D plots in figure 6.7 and as 2D plots in figure 6.8. In the second row of figure 6.9 the  $s$  polarized reflectance does not sustain SPP modes. Therefore, the dip in the  $s$  polarization reflectance appearing for  $d_{\text{SiO}_2}>200$  nm can only be attributed to a WG-like mode. The comparison of the features obtained using  $s$  and  $p$  polarized light validates our assignment of the non SPP mode to the WG-like one. The SPP-like modes appear in the  $p$  polarization whereas the WG-like modes appear in both  $s$  and  $p$  polarizations.

As discussed at the end of section 6.4.4 below and in the next chapter the WG-like mode is located in the  $\text{SiO}_2$  dielectric and its characteristics depend mainly on the dielectric thickness. Contrary to SPP-like mode which appears only in the evanescent region, no condition is imposed on the light polarization or on the region of appearance of the WG-like mode.

For  $p$  polarized light in the evanescent region there is an avoided crossing between the SPP-like and WG-like modes simultaneously present. Their avoided crossing (anti-crossing) appears at  $\lambda=900$  and  $1100$  nm respectively for  $d_{\text{SiO}_2}=310$  and  $410$  nm. One can conclude that with increasing  $\text{SiO}_2$  thickness the avoided crossing is displaced to larger wavelengths.

### 6.2.5 Reflectance: comparison with the experiment

In our group at ISMO Shuiyan Cao, Eric Le Moal and Elizabeth Boer-Duchemin have performed experiments equivalent to our calculations at a particular wavelength. In the experiment a linearly polarized He-Ne laser is used and the light is incident from below the substrate at a wavelength of  $633$  nm. The laser is focused on the sample using an oil immersion objective. The reflected light beam is collected using the same objective. Note that in the experiment they measure the reflected intensity which is not normalized. Figure 6.10 presents a cut at  $\lambda = 633$  nm in the 3D plots of figure 6.7 and in our density plots figure 6.9 along with the experimental results.

glass-Au(50nm)-air

 glass-Ti(3 nm)-Au (30nm)-SiO<sub>2</sub>( $d_{SiO_2}$ )-Au(30nm)-air

 $d_{SiO_2} = 70$  nm

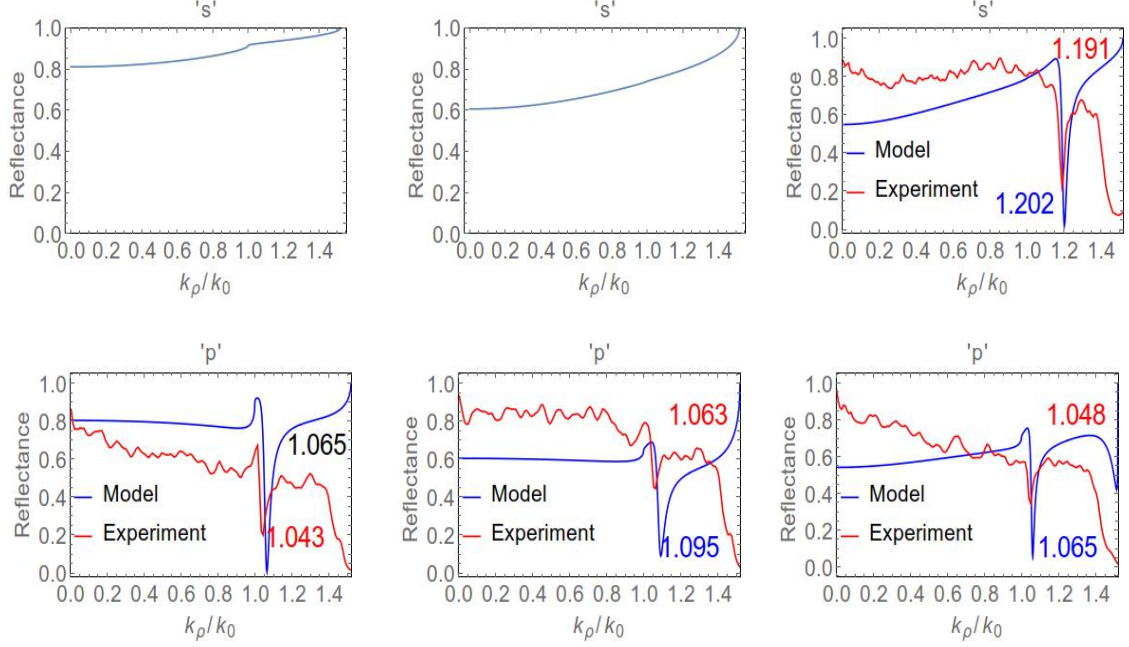
 $d_{SiO_2} = 310$  nm


Figure 6.10: Model and experimental reflectance at  $\lambda=633$  nm where the first and the second rows correspond to  $s$  and  $p$  polarization respectively. The first, second and third columns present the data for a three-layer and a two six-layer stack with  $d_{SiO_2}=70$  nm and  $d_{SiO_2}=310$  nm respectively.

Table 6.2: Comparison between the model and the experiment normalized in-plane wave vector  $k_\rho/k_0$  of the SPP-like and WG-like modes at  $\lambda=633$  nm.

type	polarization	three layer	six layer		
			$d_{SiO_2}=70$ nm	$d_{SiO_2}=310$ nm	
		$k_{SPP}/k_0$	$k_{SPP}/k_0$	$k_{SPP-like}/k_0$	$k_{WG-like}/k_0$
experiment	$s$	-	-	-	1.191
model	$s$	-	-	-	1.202
experiment	$p$	1.043	1.063	1.048	-
model	$p$	1.065	1.095	1.065	1.5

Table 6.2 shows that the  $k_\rho/k_0$  position of the SPP-like and WG-like modes simulated in our calculations and measured in the experiment are close to each other ( $\Delta k_\rho/k_0 = \pm 0.02$ ). At the studied wavelength  $\lambda=633$  nm, the WG-like reflectance dip appears at about  $k_\rho/k_0=1.2$  and  $1.5$  for  $s$  and  $p$  polarization respectively. Figure 6.9 above has already presented the position of

these modes. As for  $\lambda=633$  nm discussed above the WG-like mode appears at both polarizations but for different normalized in-plane wave vectors  $k_\rho/k_0$ .

### 6.2.6 Transmittance

Previously we have discussed the reflectance, let us now look at transmittance. Figure 6.11 displays the real (first line) and imaginary (second line) components of the transmittance at  $\lambda=750$  nm as a function of the SiO<sub>2</sub> thickness  $d_{SiO_2}$  and the normalized in-plane wave vector  $k_\rho/k_0$  for  $d_{Au} = 15$  (left column) and 30 nm (right column <sup>1</sup>).

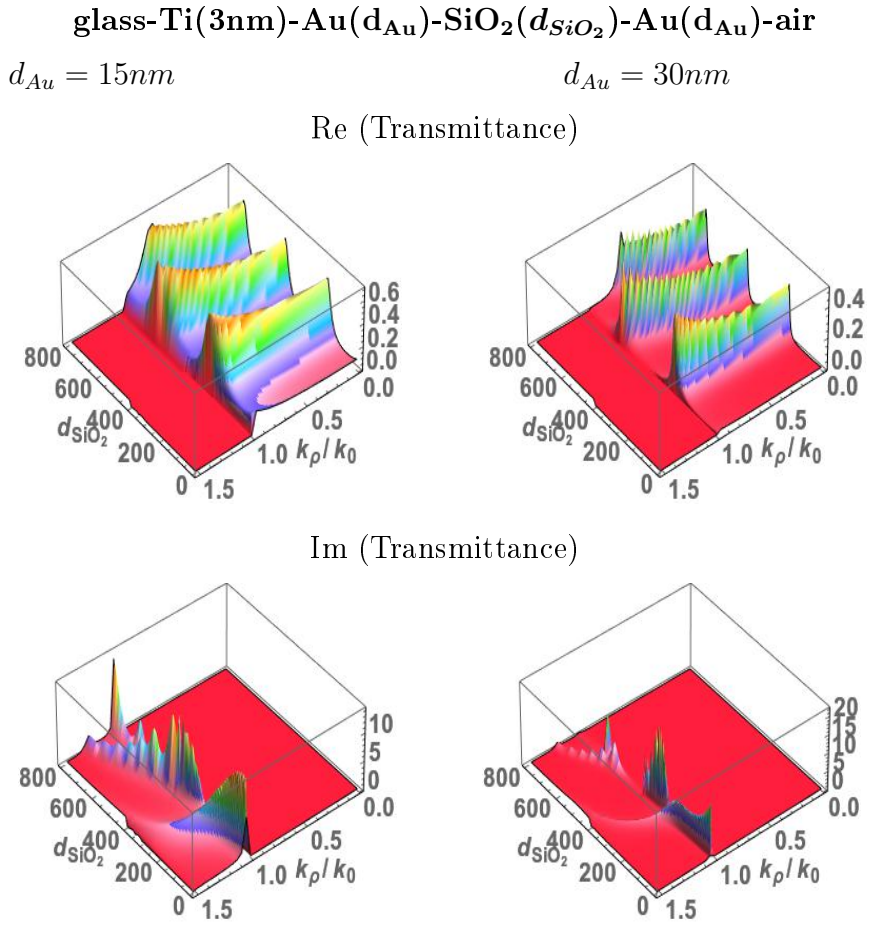


Figure 6.11: The real (first line) and imaginary (second line) components of the transmittance of incident  $p$  polarized light of  $\lambda = 750$  nm as a function of  $d_{SiO_2}$  and the normalized in-plane wave vector  $k_\rho/k_0$ . Left column  $d_{Au}=15$  nm, right column  $d_{Au}=30$  nm.

As expected, in this figure the real part of the transmittance maxima correspond to the reflectance minima in figure 6.4. Therefore the real part of the transmittance presents the same

<sup>1</sup>The oscillations in the graphs are due to the mesh used for the normalized in-plane wave vector in the calculations.

periodicity as the real part of the reflectance but with inverse amplitude. The imaginary part corresponds to the evanescent region of the reflectance. We can conclude that these observables (transmittance and reflectance) are as it should be complementary.

Next we explain the behavior of the transmittance  $\mathcal{T}$ . As discussed in chapter 5 for real refractive indices for the cover layer and the substrate  $n_{air}$  and  $n_{glass}$  the transmittance reads

$$\mathcal{T}^{s,p}(k_\rho, \omega) = \frac{N_{glass}}{N_{air}} |t^{s,p}(k_\rho, \omega)|^2 \quad (6.3)$$

where  $N_{glass} = k_{z,glass}/k_0 = n_{glass} \cos \theta_{glass}$  and  $N_{air} = k_{z,air}/k_0 = n_{air} \cos \theta_{air}$ .  $N_{glass}$  is real for all  $k_\rho/k_0 \in [0, 1.52]$  whereas  $N_{air}$  is real for  $k_\rho/k_0 \in [0, 1]$  and is purely imaginary beyond 1 (see figure 5.5 and our discussion of the evanescent waves in chapter 3). In the above expression  $t^{s,p}$  is the transmission coefficient of the entire thin film stack given in eq. (5.30) in the Bethune [58] formalism.

Figure 6.12 presents the real (first row) and imaginary (second row) components of the transmittance and the factor  $N_{glass}/N_{air}$  of eq. (6.3) (third row), as a function of the wavelength  $\lambda$  and the normalized in-plane wave vector  $k_\rho/k_0$ . The first, second and third columns correspond to a three-layer and two six-layer stacks with  $d_{SiO_2} = 190$  nm and  $d_{SiO_2} = 310$  nm respectively. The real part of  $\mathcal{T}$  is non zero in the propagating region ( $k_\rho/k_0 \leq 1$ , first row of the figure) whereas its imaginary part is non zero in the evanescent region ( $k_\rho/k_0 > 1$ , second row of the figure). The ratio  $N_{glass}/N_{air}$  behaves like  $N_{air}$ , namely real in the propagating region and imaginary in the evanescent region. A deeper understanding of the transmission observables will be acquired in section 6.4.2 below where we will compare the present transmittance with the intensity of the transmitted flux generated by a local source.

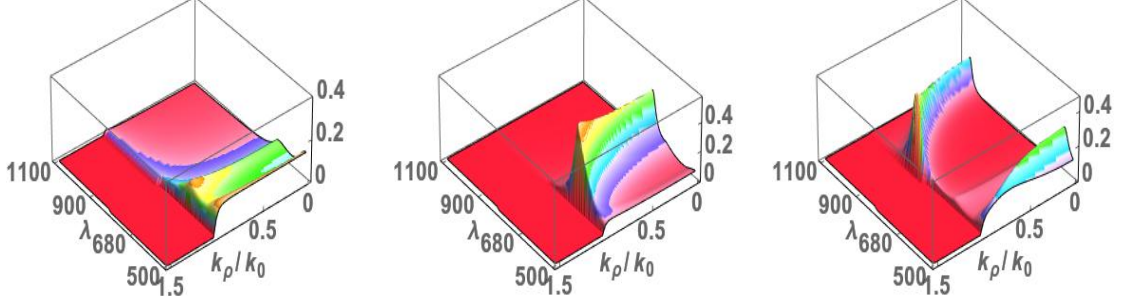
glass-Au(50nm)-air

 glass-Ti(3 nm)-Au(30nm)-SiO<sub>2</sub>( $d_{SiO_2}$ )-Au(30nm)-air

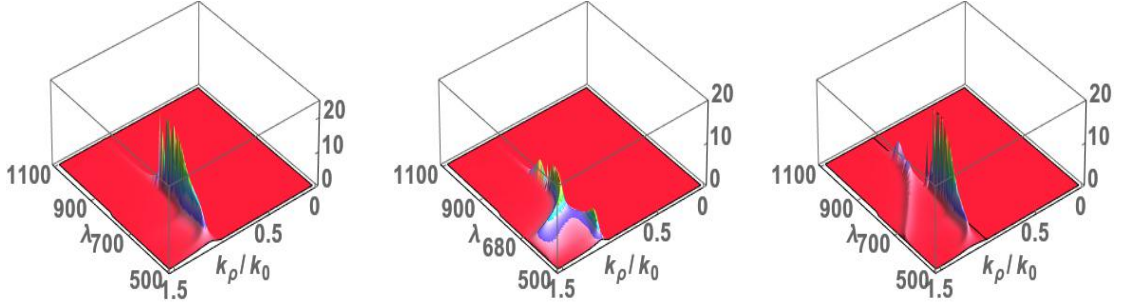
 $d_{SiO_2} = 190$  nm

 $d_{SiO_2} = 310$  nm

Re(Transmittance)



Im(Transmittance)


 Re( $N_{glass}/N_{air}$ )

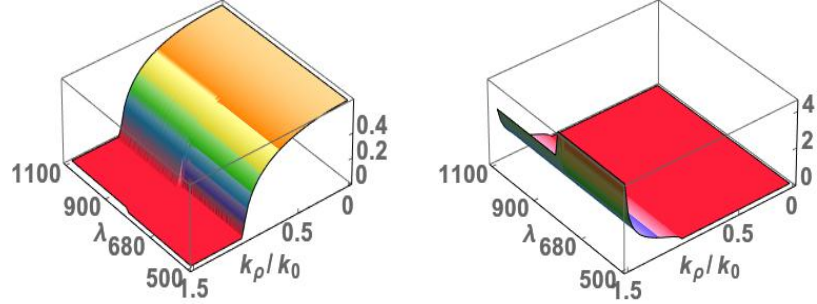
 Im( $N_{glass}/N_{air}$ )


Figure 6.12: The real (first row) and the imaginary (second row) components of the transmittance as a function of  $\lambda$  and  $k_\rho/k_0$ . The third row presents the same dependence of the real (left) and imaginary (right) parts of the multiplicative factor  $N_{glass}/N_{air}$  of eq. (6.3). The first, second and third columns of the first two rows correspond to a three-layer and six-layer stack respectively with  $d_{SiO_2} = 190$  nm and  $d_{SiO_2} = 310$  nm.

Let us now consider an  $n$ -layer sample with an air cover layer and a glass substrate. In an experiment one measures the real part of the transmittance  $\text{Re}(\mathcal{T})$  therefore in the far field the evanescent region cannot be studied, since the factor  $N_{glass}/N_{air}$  of eq. (6.3) is purely imaginary and consequently the transmittance is purely imaginary too. However, one would be able to measure a non zero transmittance in the air evanescent region in a  $(n+1)$ -layer stack. Namely

the  $n$ -th semi infinite air layer becomes a part of the stack and the  $(n+1)$  substrate semi infinite layer is the glass. The thickness of the air layer must be smaller than the light penetration depth.

## 6.3 Conclusion for the excitation by a source at infinity (ESI) calculations

In the preceding sections I have presented the results of the calculations obtained using the ESI model giving the reflectance and the transmittance of a three and six-layer thin film stack. The incident plane wave light has been considered for both the  $s$  and  $p$  linear polarizations. The three-layer stack, widely studied in the literature [39; 59; 91], has been presented as a reference and used for comparison with the present six-layer stack results.

The first part of section 6.2 concentrates on how the variation of the thicknesses of the thin film stack affect the results. In the three-layer stack one can vary the thickness of the gold. Our six-layer stack is glass-Ti-Au- $(d_{Au})$ -SiO<sub>2</sub> $(d_{SiO_2})$ - Au- $(d_{Au})$ -air with an identical thickness of the two gold layers. The transmission is weak in a sufficiently thick gold layer, while the confinement is weak for a thin gold layer. We have shown that for  $d_{Au}^{three}(nm) \in [10, 90]$  and  $d_{Au}^{six}(nm) \in [10, 50]$ , respectively for the three and six-layer stacks, the observables are significant. In fact this corresponds to the same thickness since in the six-layer stack we use two thin gold films of equal thickness. In agreement with the experimental samples for the rest of our calculations we have fixed  $d_{Au}^{three}=50$  nm and  $d_{Au}^{six}=30$  nm. The introduction of a dielectric (SiO<sub>2</sub>) between two gold thin films in a six-layer thin film stack gives rise to a second mode possibly of a wave guide (WG-like) type. This mode appears for values of  $d_{SiO_2}$  slightly above 190 nm and it is periodic with the  $d_{SiO_2}$  thickness and couples with the SPP-like mode, therefore one can not indicate its optimal thickness (see next chapter for more details). But, depending on the goal one can select a particular thickness of  $d_{SiO_2}$ .

The SPP-like and the WG-like modes behave differently. The SPP-like mode appears only for  $p$  polarized incident light in the evanescent region ( $k_\rho/k_0 > 1$ ) and its dispersion is nearly independent of the wavelength. The WG-like mode appears for both polarizations  $s$  and  $p$  at different normalized in-plane wave vectors (see section 6.2.5) in the propagating and in the evanescent regions. It strongly dispersive with wavelength ( $\lambda/(k_\rho/k_0)$ ), and it is periodic with SiO<sub>2</sub> thickness.

In section 6.2.5 we have compared our calculations with the experiments performed at ISMO by Shuiyan Cao, Eric Le Moal and Elizabeth Boer-Duchemin. At  $\lambda=633$  nm the experimental and theoretical results are in good agreement ( $\Delta k_\rho/k_0 = \pm 0.02$ ).

## 6.4 Local source excitation using the oscillating dipole model (OD): Transmitted flux intensity in momentum space

In this and the following sections I will present the calculations of the transmitted flux intensity of a three (air-Au-glass) and a six (air-Au-SiO<sub>2</sub>-Au-Ti-glass) layer thin film stack. In the STM experiment the inelastic tunneling electrons excite the optical and the plasmonic modes of the thin film layer stack and the transmitted flux is measured. Here I will use the oscillating dipole model (OD) presented in chapter 5. The inelastic tunneling electrons of an STM are modeled as a vertical oscillating dipole emitting light and located a few nanometers above the first interface in the air layer.

In the experiment the transmitted flux intensity is measured from the substrate using an optical immersion microscope. For an air-gold-glass three-layer thin film stack Bharadwaj *et al.* [59] and Wang *et al.* [39] measured the transmitted flux intensity and identified an SPP mode in the evanescent region have a normalized in-plane wave vector close to 1.

### 6.4.1 Transmitted flux intensity as a function of layer thickness in the three and six-layer thin film stacks

In this section we will study the variation of the transmitted flux intensity as a function of the gold thickness for an air-Au-glass and an air-Au-SiO<sub>2</sub>-Au-Ti-glass thin film stack. We also study this transmitted flux as a function of  $d_{SiO_2}$  thickness in the six-layer stack. The geometry of the problem is presented in figure 6.13

air-Au( $d_{Au}$ )-SiO<sub>2</sub>( $d_{SiO_2}$ )-Au( $d_{Au}$ )-Ti(3 nm)-glass

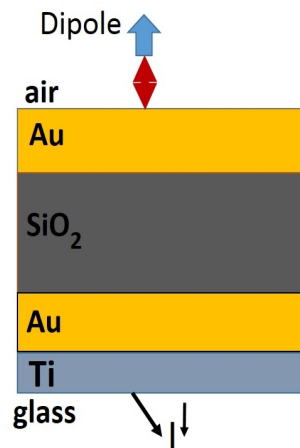


Figure 6.13: The six layer thin film stack used in the calculation of the transmitted flux intensity  $I^\downarrow$ .

Figure 6.14 displays 3D graphs of the transmitted flux as a function of the thickness  $d_{Au}$  and

the normalized in-plane wave vector  $k_\rho/k_0$  at  $\lambda = 750$  nm. Complementary to the reflectance as seen in section 6.2, for the transmitted flux a mode appears as a maximum. In the three (first row) and six-layer stack with  $d_{SiO_2}=70$  nm (second row left graph) the maxima in the evanescent region at  $k_\rho/k_0=1.02$  (three layer) and  $k_\rho/k_0=1.05$  (six layer) correspond to an SPP mode, since these  $k_\rho/k_0$  are close to the one founded by Bharadwaj *et al.*[59], Wang *et al.* [39] and Marty *et al.* [60].

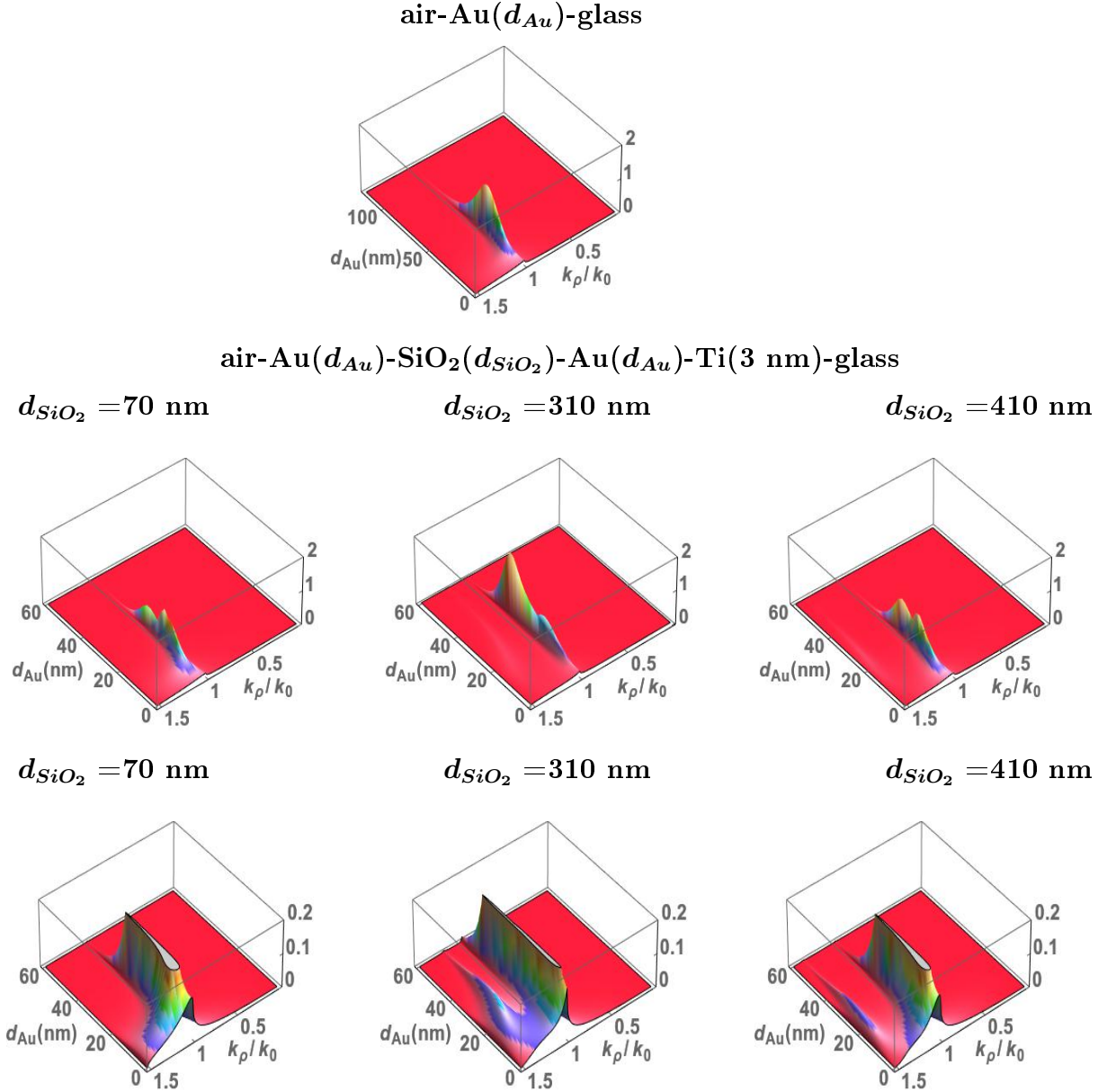


Figure 6.14: The transmitted flux intensity at  $\lambda = 750$  nm as a function of the normalized in-plane wave vector  $k_\rho/k_0$  and the gold thickness  $d_{Au}$ . The first row displays a three-layer stack air-Au( $d_{Au}$ )-glass. The second row left, middle and right graphs display the transmitted flux intensity of a six-layer stack air-Au( $d_{Au}$ )-SiO<sub>2</sub>( $d_{SiO_2}$ )-Au( $d_{Au}$ )-Ti(3nm)-glass with  $d_{SiO_2} = 70, 310$  and  $410$  nm respectively. In the third row, the z-scale has been decreased showing the presence of the weaker WG-like mode.

For the thicknesses  $d_{SiO_2}=310$  and  $410$  nm (in third row, the z-scale has been decreased) the second maximum assigned to a WG-like mode corresponds to a large normalized in-plane wave vector  $k_\rho/k_0 \in [1.3, 1.5]$  and  $d_{Au}(nm) \in [10, 50]$ . The larger the thickness of  $d_{SiO_2}$ , the larger the normalized in-plane wave vector of the WG-like mode (see figure 6.14 third line, second and third columns). From now on we will consider that the mode appearing close to  $k_\rho/k_0=1$  is an SPP-like mode and the one that appears for larger normalized wave vectors is a WG-like mode. Our assignment will be confirmed in the following sections.

Let us now turn to the study of the transmitted flux as a function of the thickness of the SiO<sub>2</sub> layer. Figure 6.15 displays the transmitted flux at the wavelength of  $\lambda=750$  nm as a function of SiO<sub>2</sub> thickness  $d_{SiO_2}$  and the normalized in-plane wave vector  $k_\rho/k_0$  (first row). For  $d_{Au}=15$  nm (left column) and  $30$  nm (right column) a zoom of the ordinate is also shown to highlight the presence of a weaker second mode (second row). Recall that (see section 6.2.2) in the propagating region  $k_\rho/k_0 \in [0, 1]$  the reflectance is periodic in  $d_{SiO_2}$  (see figures 6.4 and 6.5 above). However, no  $d_{SiO_2}$  periodicity can be observed for this transmitted flux in the propagating region since the light is incident from the air and the WG-like mode is very weak (see the explanation in the next section).

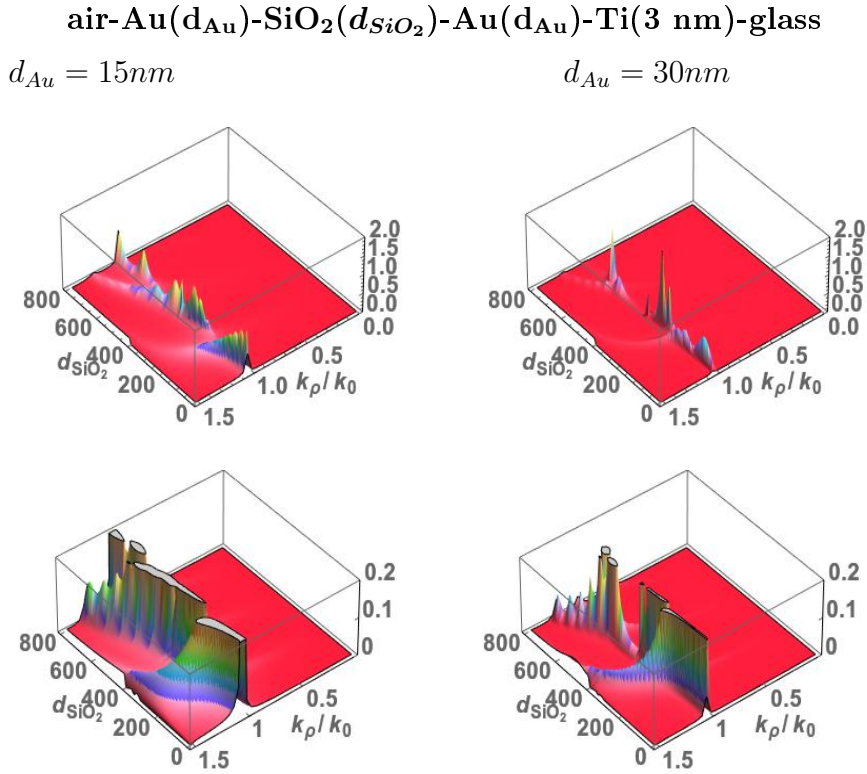


Figure 6.15: The transmitted flux intensity at  $\lambda = 750$  nm as a function of  $d_{SiO_2}$  and the normalized in-plane wave vector  $k_\rho/k_0$ . The first row: left graph  $d_{Au}=15$  nm and right graph  $d_{Au}=30$  nm. The second row : a zoom of the ordinate of the first row graphs showing the presence of a weaker second mode.

Contrary to the reflectance discussed in section 6.2 above, figure 6.14 and 6.15 do not display avoided crossing (anti-crossing). Instead, at high  $k_\rho/k_0$ , the SPP-like and the WG-like modes

seem to merge together at about  $k_\rho/k_0 \approx 1$ . The merging takes place at a different wavelength depending on the  $\text{SiO}_2$  thickness. A clearer picture can be obtained if one considers this  $d_{\text{SiO}_2}$  variation at particular wavelengths. Figure 6.16 presents the density plots of the transmitted flux intensity of an air-Au(30nm)- $\text{SiO}_2(d(\text{nm}))$ -Au(30nm)-Ti(3nm)-glass stack as a function of  $d_{\text{SiO}_2}$  and the normalized in-plane wave vector  $k_\rho/k_0$ , at  $\lambda=680, 750$  and  $850$  nm in the left, middle and right graphs respectively. Over the entire range of the  $\text{SiO}_2$  thickness  $d_{\text{SiO}_2}$ , the SPP-like mode appears at  $k_\rho/k_0 \approx 1$  and the WG-like mode at  $k_\rho/k_0 > 1.20$ . For  $\lambda=680, 750$  and  $850$  nm the wave guide mode starts at  $d_{\text{SiO}_2}=200, 250$  and  $300$  nm respectively. As explained in section 6.4.4 below, the thickness of the  $\text{SiO}_2$  layer at which the WG-like mode appears is related to the light wavelength (see eq. (2.3) below), namely the thinner  $d_{\text{SiO}_2}$ , the shorter the wavelength at which the WG-like mode appears.

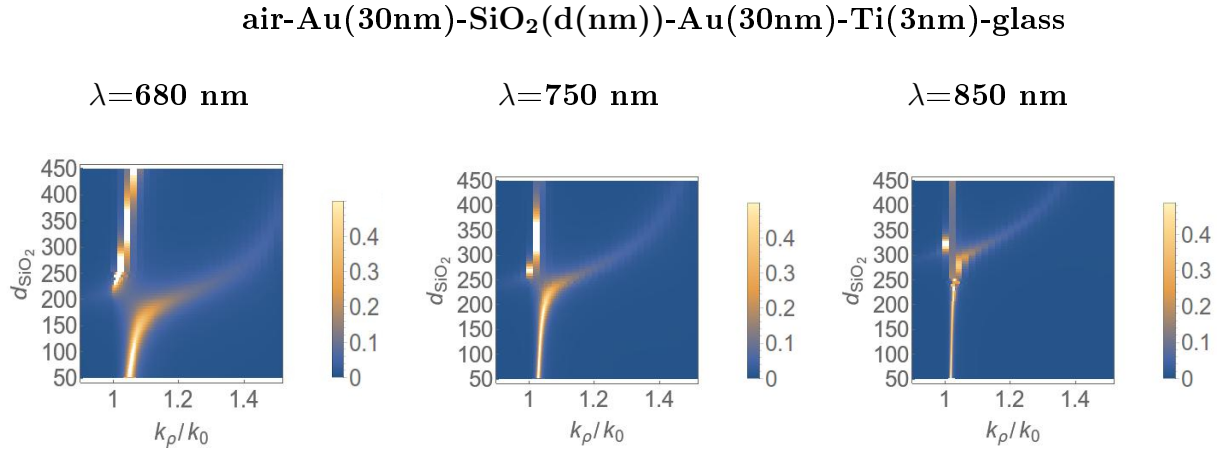


Figure 6.16: Density plots of the transmitted flux intensity of an air-Au(30nm)- $\text{SiO}_2(d(\text{nm}))$ -Au(30nm)-Ti(3nm)-glass stack as a function of  $\text{SiO}_2$  thickness  $d_{\text{SiO}_2}$  and the normalized in-plane wave vector  $k_\rho/k_0$  at  $\lambda=680, 750$  and  $850$  nm respectively in the left, middle and right graphs.

#### 6.4.2 Comparison between the transmitted flux for the light sources located at infinity and close to the surface.

In this section we will show that the transmittance of a source located at infinity (see section 6.2.6) and the transmitted flux of a local source are complementary. The transmittance is presented in eq. (6.3). Recall the transmitted flux intensity  $I^\downarrow$  of a local source given in equation (5.46) of chapter 5 (see the meaning of the notations there)

$$\left\{ \begin{array}{l} I_{allowed}^\downarrow = \frac{k_0^2 k_z^* \text{glass} k_\rho^2 |t_{air}^{(p)}(k_\rho, z)|^2}{S_0 \omega \mu_0 \mu} \frac{1}{k_z^2 \text{air}} \quad k_\rho \in [0, k_0 n_{air}] \\ I_{forbidden}^\downarrow = \frac{k_0^2 k_z^* \text{glass} k_\rho^2 |t_{glass}^{(p)}(k_\rho, z)|^2}{S_0 \omega \mu_0 \mu} \exp(-2 k_z^i \text{air} h) \quad k_\rho \in [k_0 n_{air}, k_0 n_{glass}] \end{array} \right. , \quad (6.4)$$

$$I^\downarrow(k_\rho, z, \omega) = F_I |t(k_\rho, z)|^2$$

where the factor  $F_I$  reads

$$F_I = \frac{k_0^2 k_{z\text{glass}}^*}{S_0 \omega \mu_0 \mu} \frac{k_\rho^2}{k_{z\text{air}}^2} \exp(-2 k_{z\text{air}}^i h). \quad (6.5)$$

Here  $t(k_\rho, z)$  is the Fresnel transmission coefficient of the entire layer.

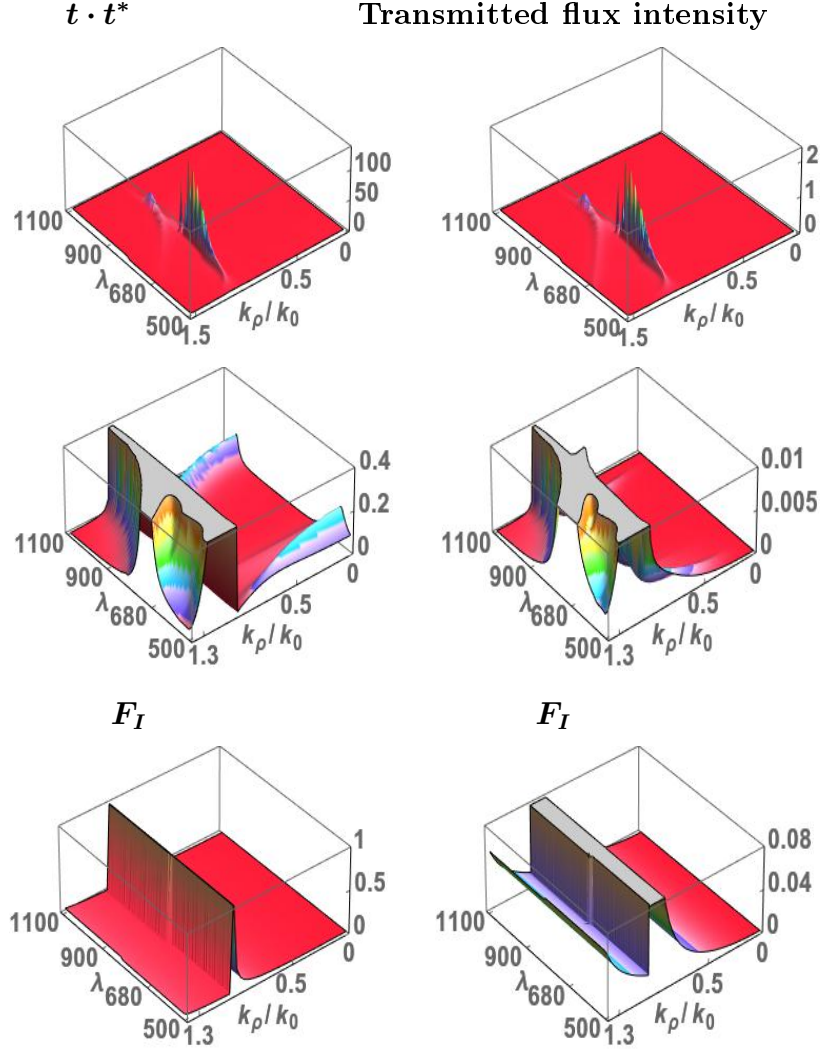


Figure 6.17: First row presents the square of Fresnel transmitted coefficients  $t \cdot t^*$  (left graph) and the transmitted flux intensity eq. (6.4) (right graph) as a function of the wavelength  $\lambda$  and the normalized in-plane wave vector  $k_\rho/k_0$  for a six-layer stack with  $d_{SiO_2}=310$  nm. Second row is a zoom of the first row. The third row left graph displays the transmitted flux factor  $F_I$  eq. (6.5) and the right graph is a zoom of the left graph

Both the transmittance (eq. (6.3)) and the transmitted flux eq. (6.4) are written as a product of a numerical factor and a dynamical contribution in terms of Fresnel coefficients. First let us compare the factors  $N_{\text{glass}}/N_{\text{air}}$  (eq. (6.3) and figure 6.12 third row) and  $F_I$  (eq.

(6.5) and figure 6.17 third row). The coefficient  $N_{glass}/N_{air}$  is real and purely imaginary in the propagating and the evanescent regions respectively. The coefficient  $F_I$  is always real with a large amplitude in the evanescent region.

The comparison between the transmittance  $\mathcal{T}^p(k_\rho, \omega)$  (eq. (6.3)) and the transmitted flux  $I^\downarrow$  can really be performed only in the evanescent region. Precisely in the propagating region the Fresnel transmission coefficients  $|t|^2$  in eq. (6.3) correspond to the excitation from glass whereas these coefficients in the transmitted flux intensity (eq.(6.4) first line) corresponds to the excitation from air. Moreover in the propagating region the Fresnel transmission coefficients in air  $|t_{air}|^2$  used for the transmitted flux are significantly weaker (left graph, second line of figure 6.17) than these same coefficients in glass (figure 6.12 first line, right graph). In the evanescent region the transmittance  $\mathcal{T}^p(k_\rho, \omega)$  is imaginary because  $N_{glass}/N_{air}$  is imaginary and therefore can not be measured. Whereas the transmitted flux  $I^\downarrow$  is real and can be measured. The transmitted flux is very weak in the propagating region since both  $|t_{air}|^2$  and  $F_I$  are weak.

### 6.4.3 Dispersion of the transmitted flux intensity

Let me now explore the dispersion of the three and six-layer thin film stack at fixed  $d_{SiO_2}$ . The reflectance dispersion curves of a source at infinity for the three and six-layer thin film stacks have been presented in figure 6.9 above. Now for a local source of excitation figure 6.18 presents the transmitted flux intensity function of the wavelength  $\lambda$  and the normalized in-plane wave vector  $k_\rho/k_0$  for three-layer (first row) and six-layer stacks (second, third and fourth row) left, middle and right graphs for  $d_{SiO_2}=190, 310$  and  $410$  nm. For the three and six-layer stacks a mode appearing just above  $k_\rho/k_0=1$  that is nearly invariant with the wavelength is present and is temporarily assigned to SPP-like mode. For  $k_\rho/k_0 \in [1.1, 1.5]$  in the ranges  $\lambda(nm) \in [650, 850]$  and  $\lambda(nm) \in [700, 1000]$ , for  $d_{SiO_2} = 310$  and  $410$  nm respectively, one identifies a WG-like mode. Increasing the SiO<sub>2</sub> thickness shifts the WG-like mode to larger wavelengths. Comparing the transmitted flux intensity (figure 6.18) with the reflectance (figure 6.9) dispersion curves one finds that in the evanescent region ( $k_\rho/k_0 > 1$ ) the same modes are observed. Following the discussion of preceding section, for the transmitted flux intensity in the propagating region the WG-like mode is very weak.

When looking at the dispersion in figure 6.18 (see also figure 6.15) one is astonished since at about  $k_\rho/k_0=1$  the SPP-like and WG-like modes merge in a single feature. This is in contradiction with the findings of the first part of this chapter discussing the excitation source at infinity where a clear but very weak avoided crossing (anti-crossing) is observed in the reflectance (see figure 6.4, 6.7 and 6.9). In the preceding section we have shown that, in the propagating region, the transmitted flux amplitude originates from air and it is very weak. Therefore the avoided crossing is still present in the transmitted flux amplitude of the OD model but is practically suppressed by the weakness of  $|t_{air}|^2$  and of the factor  $F_I$  (see figure 6.17 above).

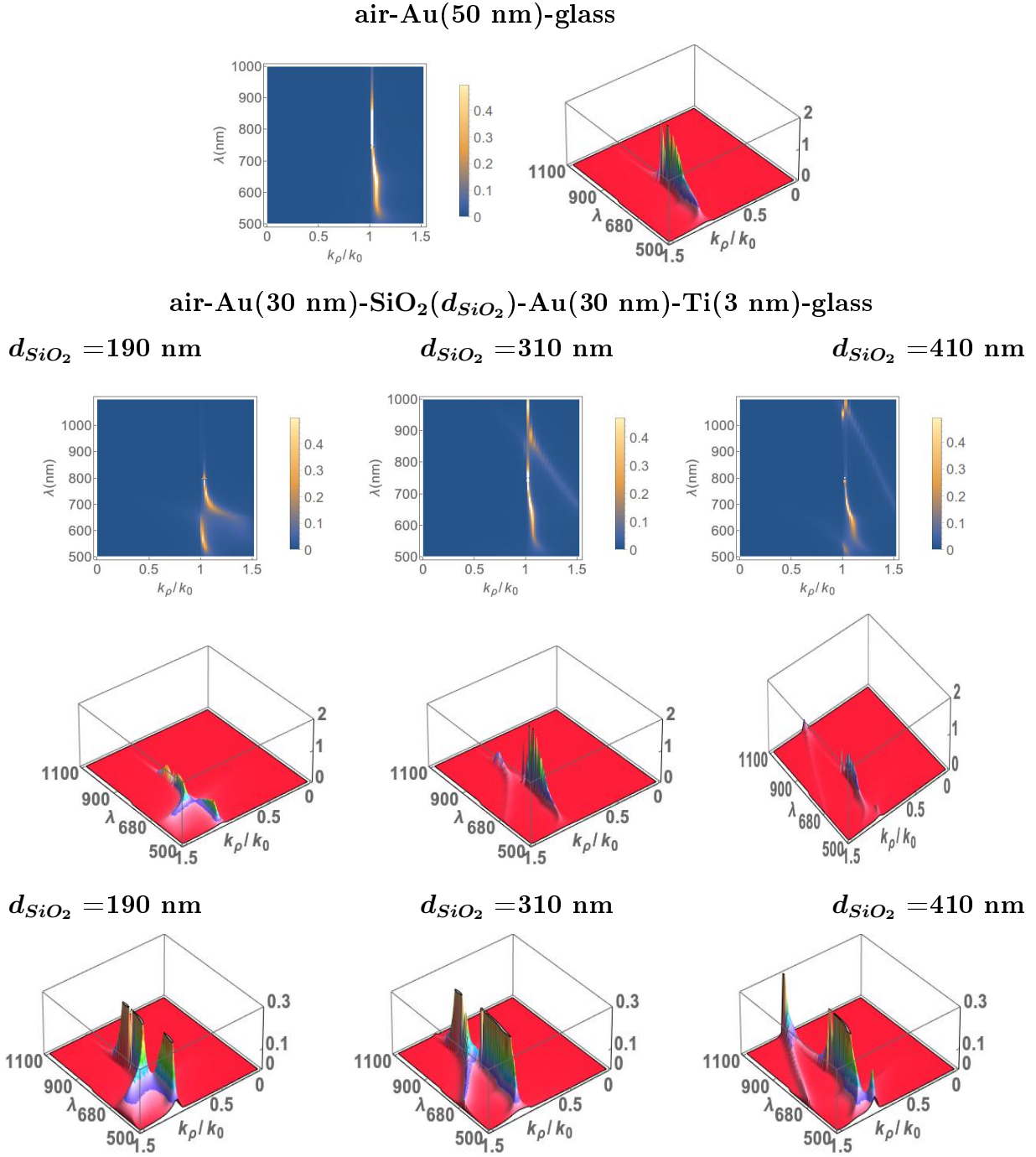


Figure 6.18: The transmitted flux intensity as a function of the wavelength  $\lambda$  and the normalized in-plane wave vector  $k_\rho/k_0$ . The first row presents the three-layer stack air-Au( $d_{Au}$ )-glass, and for the six-layer stack in the second (density plot) and third (3D graphs) rows. Left, middle and right graphs display the transmitted flux intensity of a six-layer stack air-Au(30 nm)-SiO<sub>2</sub>( $d_{SiO_2}$ )-Au(30 nm)-Ti(3nm)-glass for  $d_{SiO_2} = 190, 310$  and  $410$  nm respectively. The fourth row is a zoom of the ordinate of the 3D plot of the third row displaying the weaker WG-like mode.

We compare again the reflectance (figures 6.7 and 6.9) and the transmitted flux amplitude

$I^\downarrow$  dispersion (figure 6.18). One sees that the amplitude of SPP-like modes are similar whereas the WG-like mode in transmission is much weaker than in reflexion. A possible explanation is related to the wave guide nature of this mode. For the reflectance the WG-like dip sums up the losses due to the absorption in the metal and the field trapped in the  $SiO_2$  wave guide giving rise to a deep minimum. The transmitted flux intensity is weaker than the absorption in reflectance since a part of the flux remains trapped in  $SiO_2$ .

#### 6.4.4 Model and experimental dispersion of a six-layer thin film stack

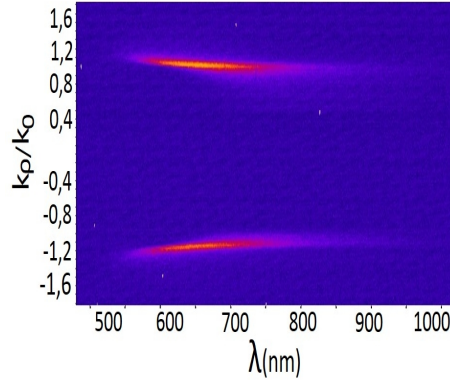
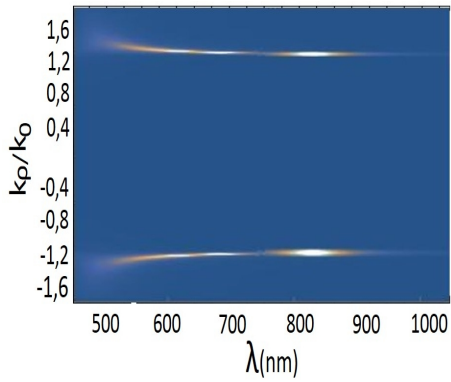
In this section I compare our results with the experiments performed in our group by Shuiyan Cao, Eric Le Moal and Elizabeth Boer-Duchemin. Figure 6.19 exhibits the transmitted flux intensity dispersion of a six-layer stack calculated using our OD model (left graphs, see also figure 6.18 presenting standard density plots) and measured in the experiment (right graphs) for three samples with  $d_{SiO_2} = 70, 190,$  and  $310$  nm first, second and third line in the figure. The calculated and experimentally measured dispersions are in good agreement. The feature appearing just above  $k_\rho/k_0=1$  is assigned to an SPP-like mode whereas for  $d_{SiO_2} = 190$  and  $310$  nm respectively in the region  $\lambda(nm) \in [600, 650]$  and  $\lambda(nm) \in [650, 850]$  a second feature is assigned to the presence of the WG-like mode.

air-Au(30nm)-SiO<sub>2</sub>( $d_{SiO_2}$ )-Au(30nm)-Ti(3 nm)-glass

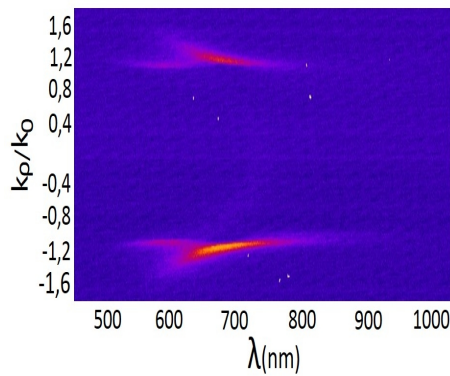
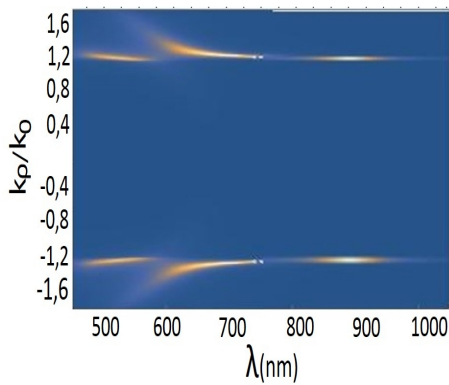
$d_{SiO_2}=70$  nm

Model

Experiment



$d_{SiO_2}=190$  nm



$d_{SiO_2}=310$  nm

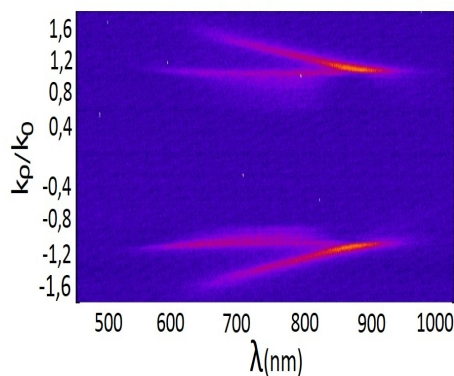
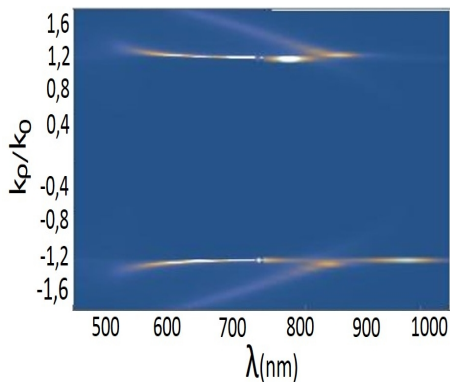


Figure 6.19: Dispersion density plot (rotated by 90° relative to the standard representation see figure 6.18 and 6.16) of the transmitted flux intensity. First column presents the OD model, second column the experimental results of our group.

A precise comparison between our model and the experiment is made using cross sections in

the dispersion density plots of the three and six-layer stack data presented in figure 6.18. Figure 6.20 displays the selected transmitted flux as a function of the normalized in-plane wave vector  $k_\rho/k_0$ . The left, middle and right columns correspond to the three and the six-layer stacks with  $d_{SiO_2}=70$  and 310 nm respectively. For  $\lambda=700$  and 900 nm and in both the three and six-layer stacks with  $d_{SiO_2}=70$  nm the maxima correspond to an SPP-like mode. For the six-layer stack with  $d_{SiO_2}=310$  nm, a supplementary mode, assigned to the WG-like mode, appears only for  $\lambda = 700$  nm. These figures 6.19 and 6.20 confirm the agreement between the OD model and the experiment.

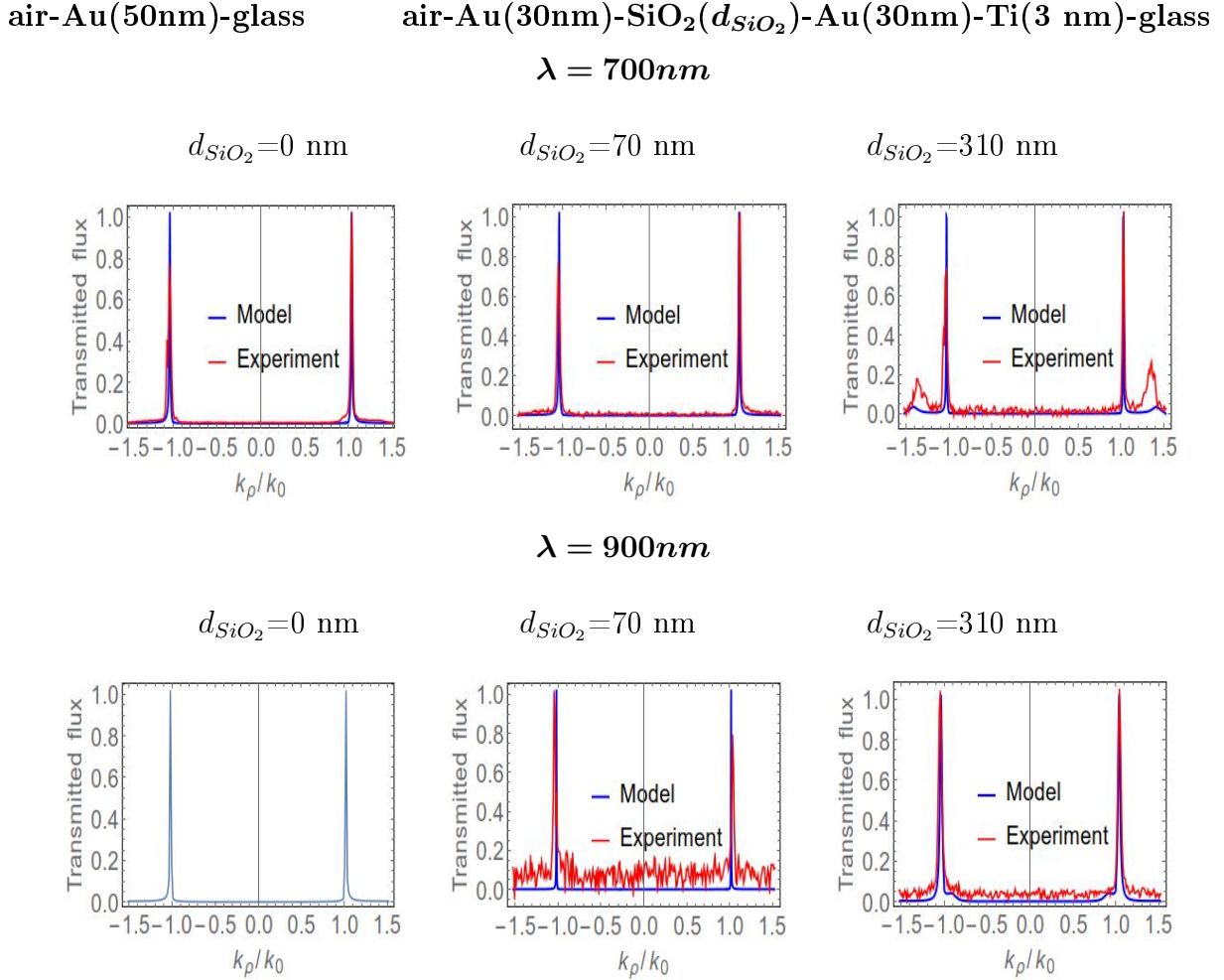


Figure 6.20: Transmitted flux intensity at  $\lambda=700$  nm (first row) and 900 nm (second row) respectively for a three-layer (left) and a six-layer stack with  $d_{SiO_2}=70$  nm (middle) and  $d_{SiO_2}=310$  nm (right) graphs as a function of the normalized in-plane wave vector  $k_\rho/k_0$ .

A detailed analysis of the wavelength of the six-layer stack for  $d_{SiO_2}=190$  and 310 nm as a function of  $k_\rho/k_0$  is presented in figures 6.21 and 6.22. For  $d_{SiO_2}=190$  nm (figure 6.21) the mode assigned to the WG-like appears at  $\lambda=625$  and  $\lambda=655$  nm. At  $\lambda=655$  nm its normalized in-plane wave vector is closer to that of the SPP-like mode. One can infer that increasing the wavelength further leads to a decrease the normalized in-plane wave vector corresponding to WG-like mode and that beyond  $\lambda=684$  nm it mixes with the SPP-like before merging with it.

air-Au(30 nm)-SiO<sub>2</sub>(190 nm)-Au(30 nm)-Ti(3 nm)-glass

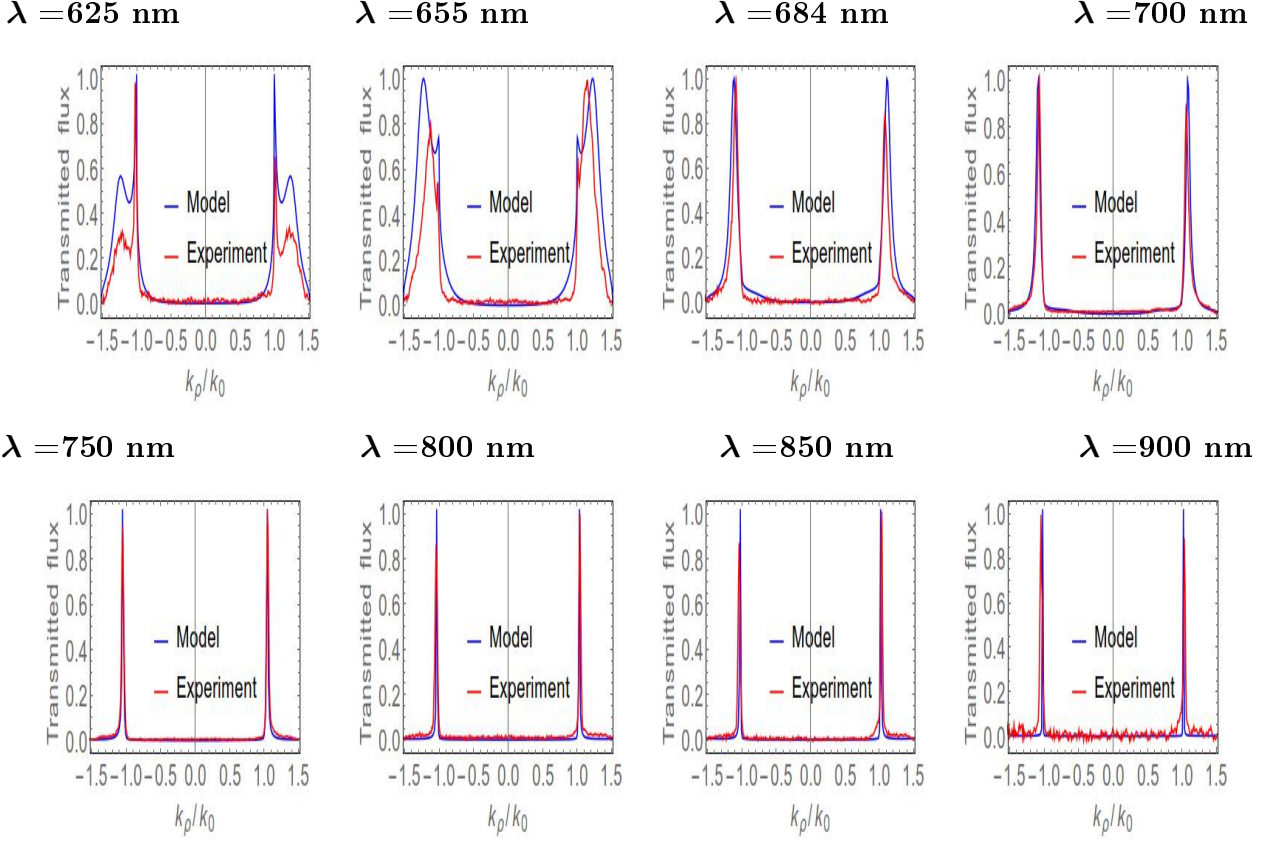


Figure 6.21: Transmitted flux as a function of  $k_\rho/k_0$  of an air-Au(30 nm)-SiO<sub>2</sub>(190 nm)-Au(30 nm)-Ti(3 nm)-glass stack at different wavelengths  $\lambda$ .

For  $d_{\text{SiO}_2}=310$  nm (figure 6.22), the WG-like mode first appears at longer wavelengths. At  $\lambda=625$  nm in the experiment the WG-like mode appears at  $k_\rho/k_0=1.47$ , whereas, using our OD model the WG-like mode is shifted to  $k_\rho/k_0=1.5$ . Then between  $\lambda=700$  nm and 850 nm the agreement with the experiment is fair and at 900 nm the WG-like mode merges with the SPP-like mode. Section 6.4.3 above explains this behavior by the weakness of the amplitude of the WG-like in the propagating region.

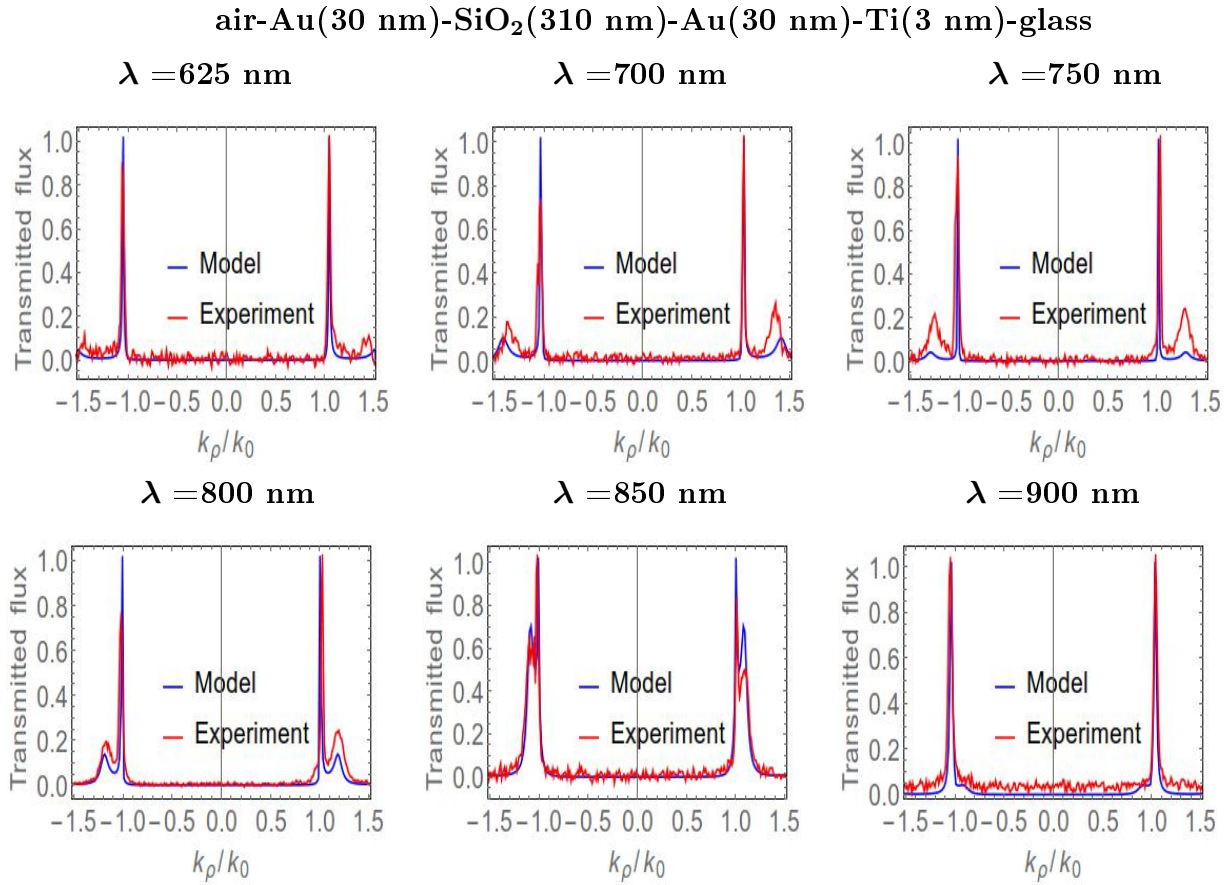


Figure 6.22: Transmitted flux as a function of  $k_\rho/k_0$  for an air-Au(30 nm)-SiO<sub>2</sub>(310 nm)-Au(30 nm)-Ti(3 nm)-glass stack at different wavelengths  $\lambda$ .

Figure 6.23 presents an analysis of the nature of the modes displayed in the dispersion graphs in figures 6.18 and 6.19. The upper row of figure 6.23 presents the dispersion curve of a mode appearing at large  $k_\rho/k_0$ . This mode is calculated using our OD model (black line in figure 6.23), and compared with the experiment (red line in figure 6.23) performed in our group. To help identification of this hypothetical WG modes we also use a simplified WG model corresponding to a stationary wave solution of the electric field in a box (see e.g. Saleh and Teich [66, section 7.2]) presented in detail in chapter 2.

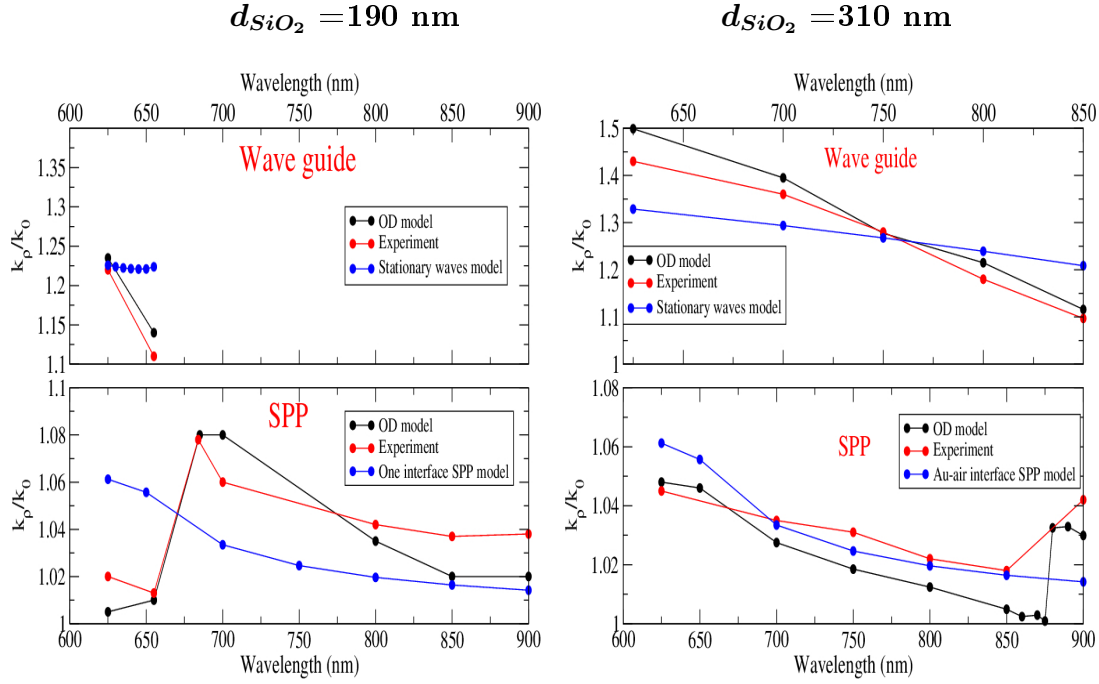


Figure 6.23: The dispersion curve of the WG-like (upper row) and SPP-like (lower row) modes for a six-layer stack air-Au-SiO<sub>2</sub>-Au-Ti-glass for  $d_{SiO_2}=190$  nm (left column) and  $d_{SiO_2}=310$  nm (right column). In the upper row, showing the WG-like mode, the results of a simple standing wave model using eq. (2.3) of chapter 2 are also displayed (see text). In the lower row displaying the SPP-like mode, an Au-air single interface dispersion model is also presented.

The OD model and the experimental results all appear in the range  $k_\rho/k_0 \in [1.2, 1.4]$  for both thickness  $d_{SiO_2}=190$  and 310 nm. In the preceding section many indications of the nature of this mode have been given (it is periodic with SiO<sub>2</sub> thickness (section 6.2.2), strongly varies with  $k_\rho/k_0$ ), from which it can be concluded that this mode corresponds to WG.

The upper row of figure 6.23 displays the WG mode calculated using the OD model (black), experiment (red) and simplified model (blue) results using eq. (2.3) of chapter 2. The OD model and the experiment are close. In disagreement with the OD model and the experiment, the simplified model gives an almost constant normalized in-plane wave vector  $k_\rho/k_0$ . The difference between the simplified model and the OD model and the experiment is probably due to the merge between SPP-like and the WG-like modes at  $\lambda=650$  and 850 nm respectively for  $d_{SiO_2}=190$  and 310 nm.

The lower row of figure 6.23 presents an SPP-like mode calculated using our OD model and measured in the experiment. In chapter 7 we will show that the amplitude of the SPP-like electric field in a six-layer stack air-Au-SiO<sub>2</sub>(310 nm)-Au-Ti-glass is located at the Au-air interface. Therefore, one can model the SPP-like dispersion, presented in the second row of figure 6.23, by a single interface SPP-like dispersion expression derived in chapter 3, eq. (3.53):

$$k_{SPP} = \frac{\omega}{c} \sqrt{\frac{\varepsilon_{air}\varepsilon_{Au}}{\varepsilon_{air} + \varepsilon_{Au}}}$$

The right graph, in second line of figure 6.23 presents the results of the two models, one interface SPP and OD, and the experiment and are in good agreement except for above about  $\lambda=875$  nm where the WG mode merges with the SPP mode. In the left graph of the second line of figure 6.23, the agreement between the one interface SPP model on one side and the experiment and OD model on the other side presented in the left graph second line of figure 6.23 is not so good. Again this discrepancy is related to the merge of the SPP-like and the WG-like modes between  $\lambda = 650 - 700$  nm.

In summary, using simple models in this section the SPP-like can be assigned to the SPP and the WG-like mode can be assigned to the WG mode except in the region where the WG merges with the SPP mode.

## 6.5 Local excitation: transmitted flux intensity in coordinate space

This section presents the transmitted flux intensity in the coordinate space obtained as an inverse Fourier transform (IFT) of the OD model calculations in the momentum space. Note that the IFT transforms  $\vec{k}_\rho \longleftrightarrow \vec{\rho}$  coordinate, the coordinate  $z$  remaining unchanged. These results are compared with the experimental measurements of Shuiyan Cao, Eric Le Moal and Elizabeth Boer-Duchemin of our group at ISMO.

### 6.5.1 Transmitted flux intensity in the coordinate space from the inverse Fourier transform of the fields. Padding the Fourier space

The transmitted flux intensity in coordinate space is obtained from an inverse Fourier transform (IFT) of the electromagnetic fields

$$\vec{E}_\rho(\vec{\rho}, z) = \frac{1}{\sqrt{2\pi}} \int d\vec{k}_\rho \vec{\mathcal{E}}_\rho(\vec{k}_\rho, z) e^{i\vec{k}_\rho \cdot \vec{\rho}} \quad \frac{d\vec{E}_\rho(\vec{\rho}, z)}{dz} = \frac{1}{\sqrt{2\pi}} \int d\vec{k}_\rho k_{nz} \cdot \vec{\mathcal{E}}_\rho(k_\rho, z) e^{i\vec{k}_\rho \cdot \vec{\rho}},$$

where formally the integral is written over the vector  $\vec{k}_\rho$  but a field having cylindrical symmetry has no  $k_\phi$  dependence and consequently the IFT is one dimensional in  $k_\rho$ . Note that the coordinate  $z$  does not participate in the IFT. The transmitted flux amplitude is a product of

the above electric field and its derivative

$$I(\rho, z) = \frac{1}{S_0 \omega \mu_0 \mu} \vec{E}_\rho(\rho, z) \cdot \frac{d\vec{E}_\rho^*(\rho, z)}{dz}.$$

Calculating using this algorithm ensures a zero amplitude of the transmitted flux intensity in coordinate space at the coordinate origin.

In momentum space, the physical domain of the normalized in-plane wave vector  $k_\rho/k_0$  is  $[0, 1.52]$ . The mesh  $dk_\rho$  is related to the mesh  $d\rho$  in position space by the relation

$$d\rho = \frac{2\pi}{m * dk_\rho}$$

where  $m$  is the number of points in the dual spaces. The inverse proportionality between  $d\rho$  and  $dk_\rho$  handicaps the resolution of features in one of the spaces, the coordinate space in the present case. If one simply extends the momentum space beyond its physical domain  $k_\rho/k_0 \in [0, 1.52]$  (glass medium) one will generate new features absent from the experiment. Instead in order to diminish the coordinate space mesh one can pad the momentum space beyond the end of the physical domain with zeros. This padding with zeros diminishes the step size in the position space, but does not add new features in the momentum or coordinate spaces.

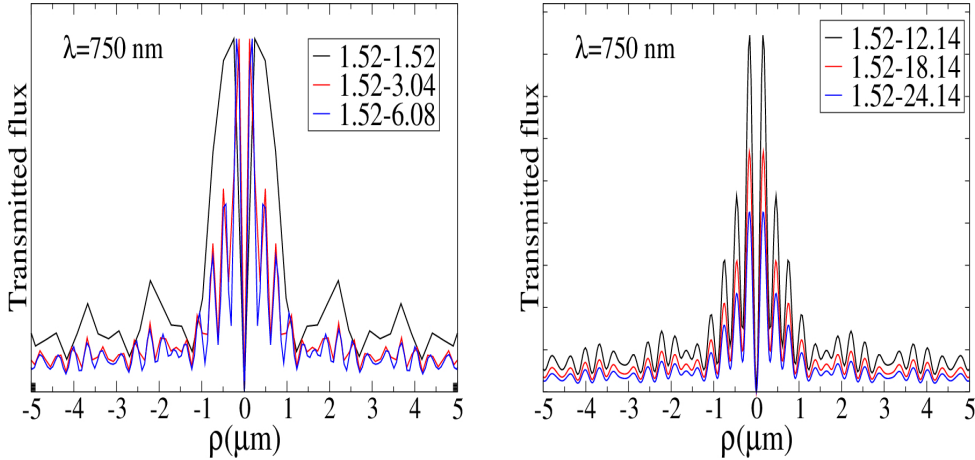


Figure 6.24: Influence of padding in the momentum space on the transmitted flux in coordinate space. Physical momentum space  $k_\rho/k_0 \in [0, 1.52]$  padded to  $(k_\rho/k_0)_{max} = 1.52, 3.04$  and  $6.08$  (left graph) and to  $(k_\rho/k_0)_{max} = 12.14, 18.14,$  and  $24.14$  (right graph) for a three-layer thin film stack.

In order to understand the influence of the padding on the resolution, figure 6.24 presents the transmitted flux of a three-layer thin film stack. The physical momentum space  $k_\rho/k_0 \in [0, 1.52]$  is padded to  $(k_\rho/k_0)_{max} = 1.52, 3.04$  and  $6.08$  (left graph) and to  $(k_\rho/k_0)_{max} = 12.14, 18.14$  and  $24.14$  (right graph). One definitely sees that the padding resolves the fringes in coordinate space. Without padding, i.e. left graph figure 6.24 1.52-1.52, the actual fringes are hidden by fringes with much larger spacing. Henceforth, in the calculations presented below we will use

the padding  $(k_\rho/k_0)_{max}=24.14$ .

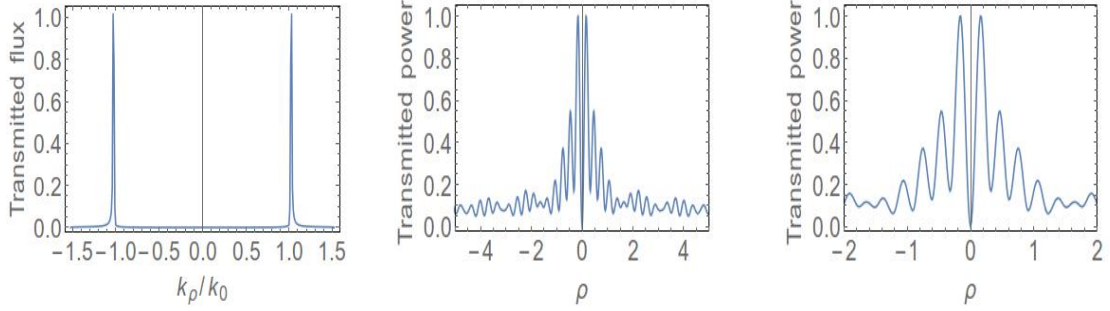
### 6.5.2 Comparison and interpretation of three and six layers stack in the coordinate space at a single wavelength

Using the algorithm of section 6.5.1 here I will calculate the transmitted flux intensity through a stack as observed in coordinate space. Figure 6.25 presents the momentum space (first column) and the coordinate space (second and third column zoom) for three (first row) and six (second row) thin films stacks at  $\lambda=750\text{nm}$ . For simplicity we start by discussing the three layer stack presented in the first row of the figure. In the momentum space (first row, first column) the three layer SPP mode has a very narrow width and it is located just above  $k_\rho/k_0 = 1$ . The narrow width of the peaks in momentum space leads to fringes of large period in coordinate space (see the first row, second and third columns in the figure) since the momentum and coordinate spaces are reciprocal spaces. Similarly, the larger the separation of the two peaks of the mode in momentum space, the smaller the period of the resulting fringes in coordinate space, in agreement with Fourier theory (see shifting properties of the Fourier transform given for example in Messiah [107, vol.1 , appendix A, table] or Press *et al.* [108]). Thus two fringe periodicities are seen as expected, one arising from the width of the peaks, the other from their separation (see any book on Fourier transform).

Section 6.4 (see particularly figures 6.20, 6.21 and 6.22) above presented the transmitted flux intensity in the Fourier space after excitation of a six-layer stack by a local source. The second row, first column graph in figure 6.25 reproduces the six-layers stack transmitted flux intensity in the momentum space at  $\lambda = 750\text{nm}$  displaying a second WG-type mode of larger width and lower intensity located at  $k_\rho/k_0 > 1.1$ . Compared to the three layer stack the first maximum appears at larger  $|\rho|$ . In the coordinate space (see 6.25 second row second and third column) the wide periodicity fringes have a larger period and their amplitude is also greater. But qualitatively this six layers results in the coordinate space is similar to the three layer one.

In summary for the six layer stack in the coordinate space one identifies the origin of the fringes but one is unable to establish a clear one to one correspondence between the features in the momentum and in the coordinate spaces. To better understand the results in the coordinate space, the next section will present 3D graphs of the transmitted flux intensity of a six layer stack as a function of the wavelength and the coordinate  $\rho$  parallel to interfaces.

**Air-Au(50nm)-glass**



**Air-Au(30 nm)-SiO<sub>2</sub>(310 nm)-Au(30 nm)-Ti(3 nm)-glass**

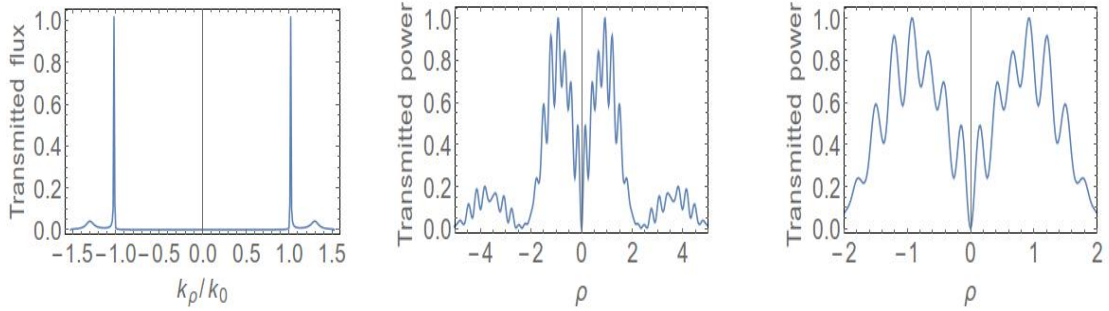
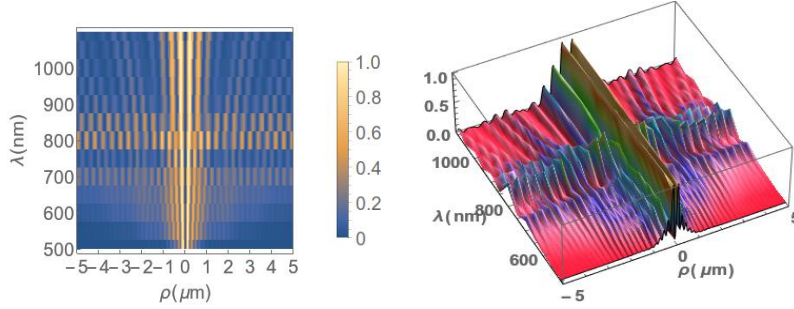


Figure 6.25: Three and six thin film stacks in momentum and coordinate space at wavelength  $\lambda = 750$  nm. The first column presents the transmitted flux intensity in the momentum space as a function of  $k_\rho/k_0$ . The second and third columns display the transmitted flux in the coordinate space using a padding of 24.14, for the three and the six-layer thin film stacks, first and the second rows respectively. Note that we conserve the notation  $k_\rho/k_0$  formally defined only for a positive axis instead of using the exact Cartesian coordinates notation  $k_x/k_0$ .

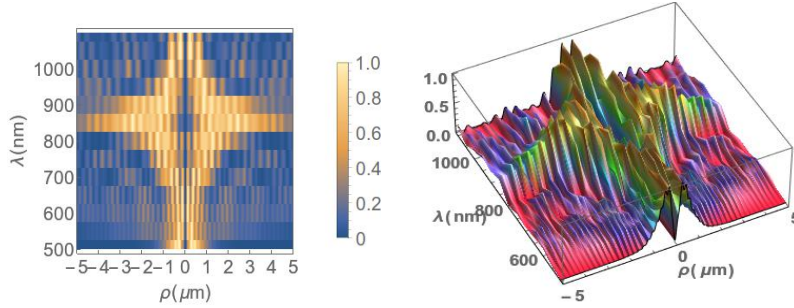
**6.5.3 3D-coordinate space transmitted flux of the stacks function of the wavelength and the in-plane coordinate**

Figure 6.26 presents density plots (left column) and 3D graphs (right column) of the transmitted flux in the coordinate space as a function of the in plane coordinate  $\rho(\mu m)$  and the wavelength  $\lambda(\text{nm})$  for the six layer thin film stack for  $d_{SiO_2}=70, 310$  and  $410$  nm, first, second and third row respectively.

$$d_{SiO_2}=70 \text{ nm}$$



$$d_{SiO_2}=310 \text{ nm}$$



$$d_{SiO_2}=410 \text{ nm}$$

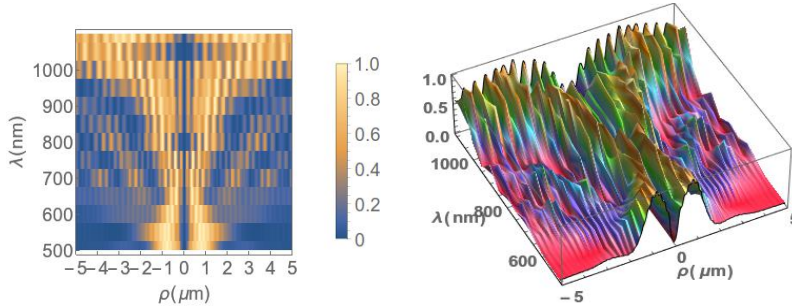


Figure 6.26: Transmitted flux intensity in the coordinate space for  $p$  polarized light for a six-layer thin film stack as a function of the spatial coordinate  $\rho(\mu m)$  and the wavelength  $\lambda$  using a padding of 24.14 in the IFT. The rows correspond to  $d_{SiO_2}=70, 310$  and  $410$  nm and the left and right columns present density plots and 3D graphs.

For  $d_{SiO_2}=70$  nm in the six layer stack (first line in figure 6.26) the results are similar to those for a three layer stack presented at  $\lambda=750$  nm as a 2D graph in the first line of figure 6.25. Namely the result is symmetrical relative to the coordinate origin with  $I(\rho = 0) = 0$ . Large large periodicity fringes ( $\Lambda_l$ ) related to the width of the SPP mode in momentum space are also seen. On top of this periodicity there are narrow periodicity fringes ( $\Lambda_s$ ) which arise from the separation of the two SPP peaks in momentum space. This picture holds everywhere except

around  $\lambda=800$  nm where the transmitted flux intensity is relatively large for large values of  $\rho$ . The density plot (first line left graph) resemble to a cross with the narrow periodicity fringes having a smaller period at low wavelengths. In agreement with the analysis in the momentum space, the WG mode is absent for this small  $d_{SiO_2}$  thickness.

For  $d_{SiO_2}=310$  nm the presence of the WG mode changes the overall visual aspect of the 3D graphs. The density plot (second line left graph in the figure) is now a kind of rhombus instead of the cross seen for  $d_{SiO_2}=70$  nm. The region of high intensity far from the coordinate origin has now shifted to about 850 nm and it is slightly extended up to and beyond 850 nm. The period of the narrow period fringes ( $\Lambda_s$ ) is larger here than for  $d_{SiO_2}=70$  nm and as above it increases with the increasing wavelength.

Finally the results of  $d_{SiO_2}=410$  nm and of  $d_{SiO_2}=310$  nm thickness are similar. The region of high intensity results is displaced beyond  $\lambda=1000$  nm and, because the definition domain of the ordinated in the density plot, here one can only see the lower part of the rhombus.

In summary the 3D graphs in the coordinate space, presented in figure 6.26 show that the coordinate space results are very sensitive to small changes in the position and width of the peaks in momentum space. In particular, these results vary significantly when an SPP-WG avoided crossing occurs.

To investigate the fringe periodicity in greater detail, below I present cross sections of the 3D graphs of figure 6.26 at  $\lambda=680$  and 850 nm in Fourier and the coordinate spaces. For the three and six-layer stacks with  $d_{SiO_2}=70$  nm, in Fourier space only a SPP-like mode is observed (see figures 6.27 and 6.28 first row, left graph and second row, left graph). In coordinate space one observes large periodicity fringes ( $\Lambda_l$ ) corresponding to the width of the SPP mode in the momentum space (figures 6.27 and 6.28 first row right graph and third row left graph; see also figure 6.25 first row, second column at  $\lambda=750$  nm). The small periodicity fringes are due to the separation of the SPP peaks in momentum space.

For  $d_{SiO_2}=310$  and 410 nm, in Fourier space a mode exists at large  $k_\rho/k_0$  which we have assigned to a WG-like mode (see figures 6.27 and 6.28 second row, middle and right graph). In momentum space (second line second and third graphs in figures) the SPP mode appears at about  $k_\rho/k_0 \approx 1$  whereas the WG-like mode changes from  $k_\rho/k_0 \approx 1.5$  at  $\lambda=680$  nm to a value of  $k_\rho/k_0 \approx 1.2$  for  $d_{SiO_2}=310$  nm and a value of  $k_\rho/k_0 \approx 1.4$  for  $d_{SiO_2}=410$  nm. This behavior is related to the avoided/anti crossing between the SPP and WG modes already discussed when studying the reflectance using the ESI model (see section 6.2 above). Remember that near the avoided/anti crossing the two modes are mixed each mode having both SPP and WG character. When comparing  $\lambda=680$  nm (see the third line second graph of figure 6.27 and  $\lambda=850$  nm (see the third line second graph of figure 6.28) for  $d_{SiO_2}=310$  nm in the coordinate space one sees a dramatic change in the periodicity of the fringes of larger period. To have a better representation of the periodicity of the wide fringes, the last line of figure 6.28 presents graphs with wider abscissa. In summary the coordinate space results show greater sensitivity to the avoided crossing of and the interaction between the SPP and WG-like modes than the momentum space ones.

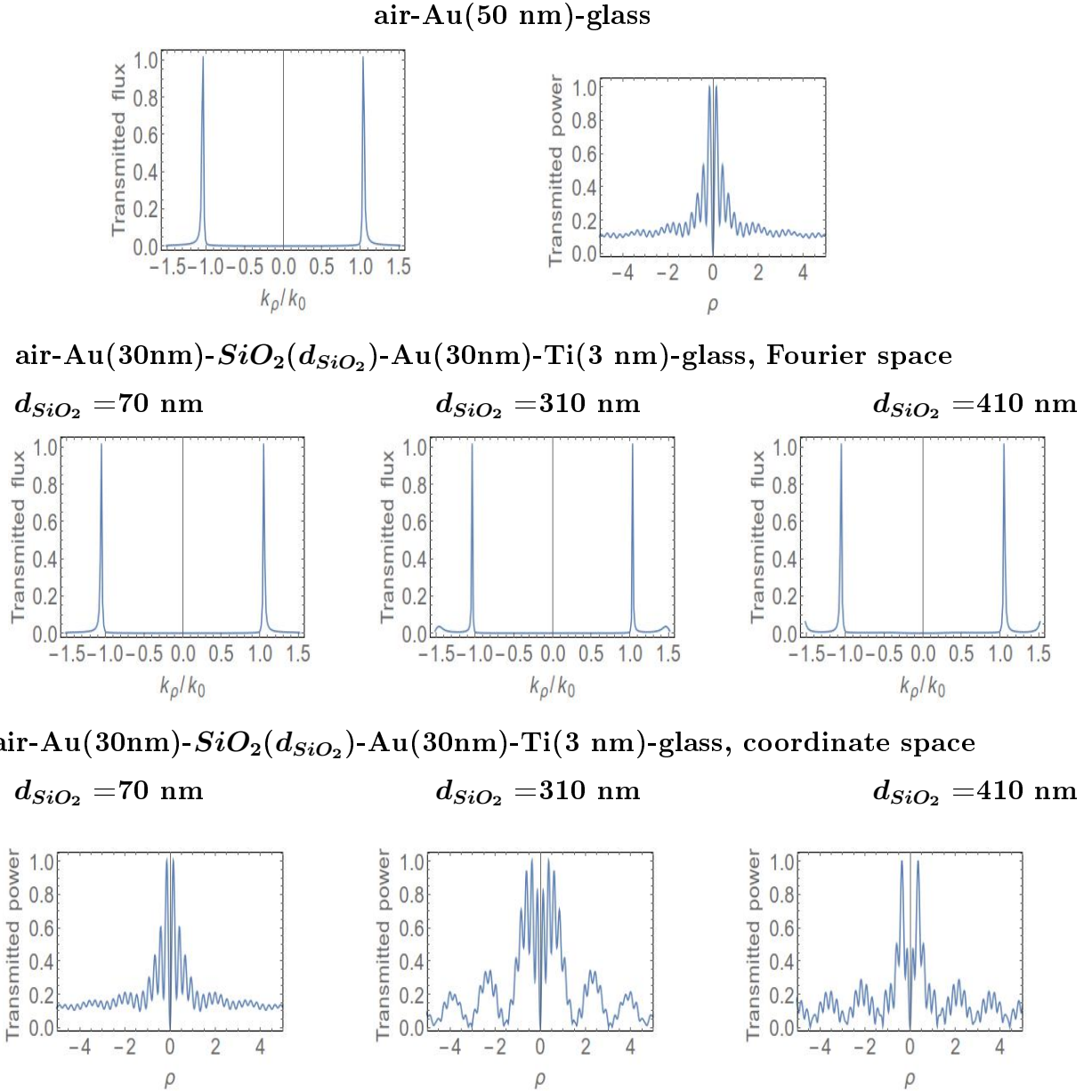


Figure 6.27: Transmitted flux intensity in momentum and coordinate spaces at the wavelength  $\lambda=680$  nm. The first row displays the results of the three-layer stack in momentum and coordinate spaces. The second and third rows show the results of the six layer stack in the momentum and coordinate spaces. The first, second and third columns of the second and third rows correspond to  $d_{SiO_2} = 70, 310$  and  $410$  nm. In momentum space, the padding is taken to be 24.14.

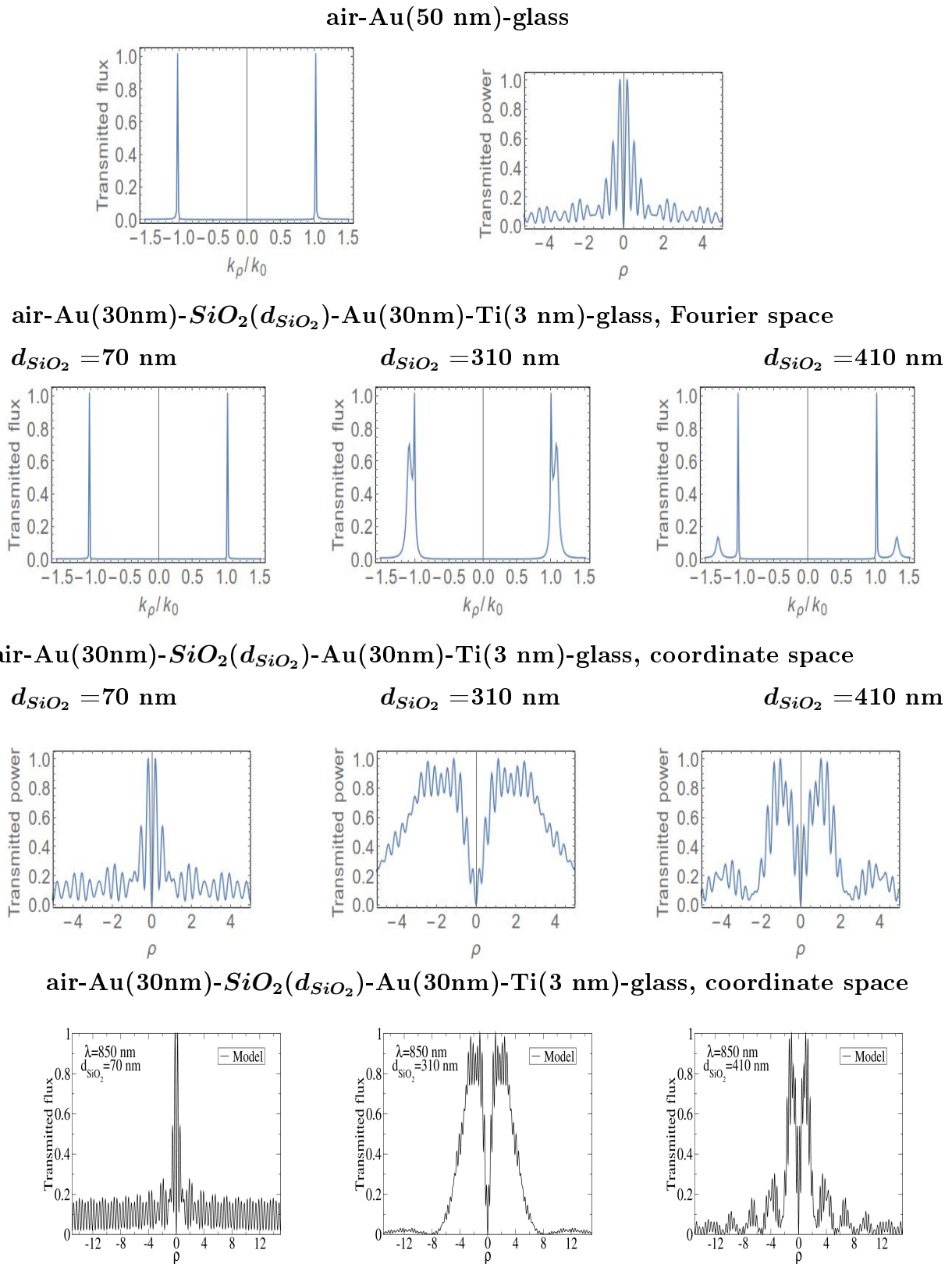


Figure 6.28: Transmitted flux intensity at wavelength  $\lambda=850$  nm. The last row in the figure is the coordinate space results with extended abscissa. Same explanation as in figure 6.27.

Figure 6.9 of section 6.2.4 above compared in the momentum space the reflectance for  $s$  and  $p$  polarized light showing that, as deduced theoretically, the SPP mode is absent for  $s$  polarization. Figure 6.29 presents the transmitted flux intensity of a six layer thin film stack of  $s$  polarized light as a function of the spatial coordinate  $\rho(\mu m)$  and the wavelength  $\lambda(nm)$  for  $d_{SiO_2}=310$  nm. The density plot corresponding to the excitation by  $s$  polarized light (left graph of figure 6.29) clearly displaying fringes of wide periodicity. The 3D graph (middle graph of figure 6.29) displays a very weak narrow periodicity oscillations on top of the large periodicity fringe, oscillations originating from the separation of the two peaks in momentum space. The right graph of figure 6.29 presents a cross section of the 3D graph at 800 nm showing that this feature is extremely large. At other wavelengths the 3D graph display between  $\lambda=500$  and  $\lambda=600$  nm and above  $\lambda=1100$  nm a much narrower width.

In summary the transmitted flux intensity of  $s$  (figure 6.29) and  $p$  (figure 6.26) polarized incident light display very different results. Namely for  $s$  polarization only WG modes can be excited whereas for  $p$  polarization WG and SPP modes excitation and their interaction can be identified. The coordinate space results are highly sensitive to the WG-SPP interaction showing results that rapidly change near the avoided/anti crossing between these modes. The comparison between  $s$  and  $p$  polarized incident light give a new element for the assignment of the WG mode.

$$d_{SiO_2}=310 \text{ nm}$$

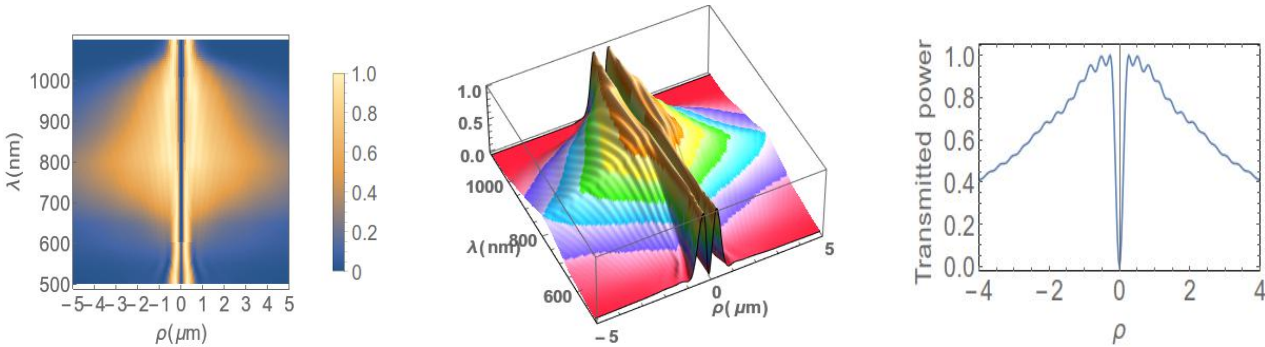


Figure 6.29: Transmitted flux intensity in coordinate space (i.e., as a function of the  $\rho(\mu m)$ ) and the wavelength  $\lambda$  from a six-layer thin film stack ( $d_{SiO_2}=310$  nm) illuminated with  $s$  polarized light (padding 24.14 in the IFT). The right graph presents a cross section at  $\lambda=800$  nm.

The numerical values of the narrow ( $\Lambda_s$ ) and wide ( $\Lambda_l$ ) periodicity fringes are summarized in table 6.3. The narrow periodicity fringes  $\Lambda_s$  are the same in all graphs and their spacing is related to the separation of the two peaks in momentum space  $k_\rho^{SPP}$  and  $k_\rho^{WG}$ . The large periodicity fringes are related to the width of the mode in the momentum space. Near the avoided/anti crossing the mixing between SPP and WG mode is large and  $\Lambda_l$  varies rapidly with the wavelength.

Table 6.3: Narrow ( $\Lambda_s$ ) and wide ( $\Lambda_l$ ) fringes periodicities.

Structure	$d_{SiO_2}$	Periodicities	$\lambda=680$ nm	$\lambda=850$ nm
Three layer	0	$\Lambda_s$	0.29	0.42
		$\Lambda_l$	1.55	1.55
Six layer	70	$\Lambda_s$	0.3	0.39
		$\Lambda_l$	1.29	1.69
Six layer	310	$\Lambda_s$	0.29	0.37
		$\Lambda_l$	1.8	9.1
Six layer	410	$\Lambda_s$	0.29	0.37
		$\Lambda_l$	1.3	3.27

#### 6.5.4 Comparison of the coordinate-space experimental results with the model calculation for dipole-illuminated stacks

Figure 6.30 displays a comparison of our calculations in coordinate space with experiments performed in our group. The left, middle and right graphs correspond to  $d_{SiO_2}=70$ , 190 and 310 nm respectively. For the six-layer stack with  $d_{SiO_2}=70$  nm or the three-layer stack, figure 6.30 left graph, the model and the experiment are relatively close to each other displaying narrow periodicity fringes at  $\Lambda_s^{model}=0.2573$  and  $\Lambda_s^{exp}=0.318$  respectively. At large values of the coordinate  $\rho$  the experimental intensity drops faster than for the OD model. For the six layer stack at  $\lambda=625$  nm with  $d_{SiO_2}=190$  nm (middle graph in the figure) as well as at  $\lambda=800$  nm with  $d_{SiO_2}=310$  nm (right graph in the figure), the experiment and the model calculations disagree. The OD model presents narrow and wide periodicity fringes whereas the experimental results do not display this structure. This disagreement can possibly be justified by the sensitivity of the coordinate space calculations to the differences in the position, width and the intensity of the WG mode in the OD calculations and in the experiment. Namely at  $\lambda=625$  nm for the thickness of  $d_{SiO_2}=190$  nm (figure 6.21, top left graph) the relative amplitude of the SPP and WG modes in the momentum space is different in the experiment and simulations. Also at  $\lambda=800$  nm for the thickness of  $d_{SiO_2}=310$  nm (figure 6.22, second row first column) the relative amplitude and the position of the SPP and WG modes in the momentum space are also different. We conclude that these differences can be at the origin of the different experimental and theoretical results in the coordinate space.

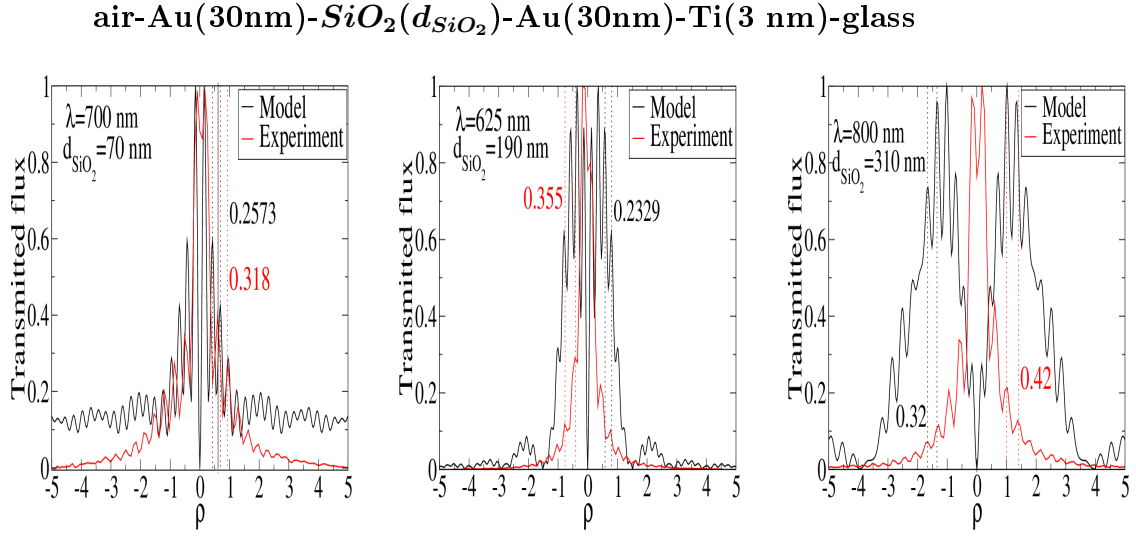


Figure 6.30: Transmitted flux intensity in coordinate space using a padding of 24.14 compared to the experiment of Shuiyan Cao, Eric Le Moal and Elizabeth Boer-Duchemin. The first, second and third graphs correspond to  $d_{SiO_2} = 70$ ,  $d_{SiO_2} = 190$  and  $d_{SiO_2} = 310$  nm respectively.

## 6.6 Conclusion of the local excitation OD model calculations

In the second part of this chapter (sections 6.4 and 6.5) I have presented the results of our calculations using a local source of excitation giving the transmitted flux of the three and the six-layer thin film stacks in both Fourier and coordinate spaces. In these calculations the inelastic tunneling electrons of an STM exciting the sample have been represented by a vertical oscillating dipole using the oscillating dipole model (OD).

As in the first part of this chapter using the ESI model we have varied the thickness of  $d_{Au}$  and  $d_{SiO_2}$  of the three and six-layer stacks. The gold thickness corresponding to a significant observable intensity is the same as ESI calculation namely:  $d_{three}(nm) \in [10, 90]$ ,  $d_{six}(nm) \in [10, 50]$  and  $d_{WG} > 190$  nm.

Section 6.4.2 discusses the comparison between the transmittance of the excitation for a source at infinity (ESI model section 6.2.6) and the transmitted flux intensity of an excitation from a local source. These transmitted observables are governed by a prefactor times the square from the transmission Fresnel coefficients. Our analysis shows that the transmittance of the ESI model and the transmitted flux of the OD model give complementary information. Namely the transmittance contains the prefactor  $N_{glass}/N_{air}$  which is imaginary in the evanescent region and no transmittance can be measured (see figure 6.12). For our six-layer stack the transmitted Fresnel coefficients (calculated for air-Au-SiO<sub>2</sub>-Au-TiO<sub>2</sub>-glass) are very weak and no visible transmitted flux intensity is measured in the propagating region (see figure 6.17). In summary one measures non zero transmittance for the ESI model in the propagating region

and a non-zero transmitted flux intensity of the OD model in the evanescent region.

For a source located at infinity (section 6.2 of this chapter) the dispersion displays an avoided crossing (anti-crossing) between SPP and WG modes (see figure 6.9 for the p polarization case). Ditlbacher *et al.* [56] study the avoided crossing (anti-crossing) obtained from a thin film stack similar to ours modeling the avoided crossing using two non interacting and one interacting physical system. In our thin film stack, the experiment and the OD model display an SPP and WG mode which merge into a single feature at the limit of the evanescent region. We explain this particular behavior by a very weak (invisible) amplitude of the WG mode in the propagating region (see section 6.4) and a weak avoided crossing with a very small separation between the curves.

In momentum space (section 6.4.4) our OD model calculations compare favorably with the experimental results of Shuiyan Cao, Elizabeth Boer-Duchemin and Eric Le Moal.

Section 6.5 presented the transmitted flux amplitude in coordinate space displaying a structure having a form of fringes. The wide periodicity fringes ( $\Lambda_l$ ) correspond to the SPP and WG width in the momentum space whereas the narrow periodicity fringes ( $\Lambda_s$ ) are related to the separation of the two peaks in momentum space. The interplay of four periodicities of the SPP and WG modes contribute to the rapid change of the coordinate space results as a function of wavelength near the SPP-WG avoided crossing. For a three-layer stack our calculations compare favorably with the experimental measurement obtained by the experimental group at ISMO. For the six-layer stack, near the avoided crossing between SPP and WG modes in momentum space the experimental and theoretical results are different. The origin of this discrepancy is probably due to differences in the position, width and relative amplitudes of SPP and WG-like modes in the experiment and theory.

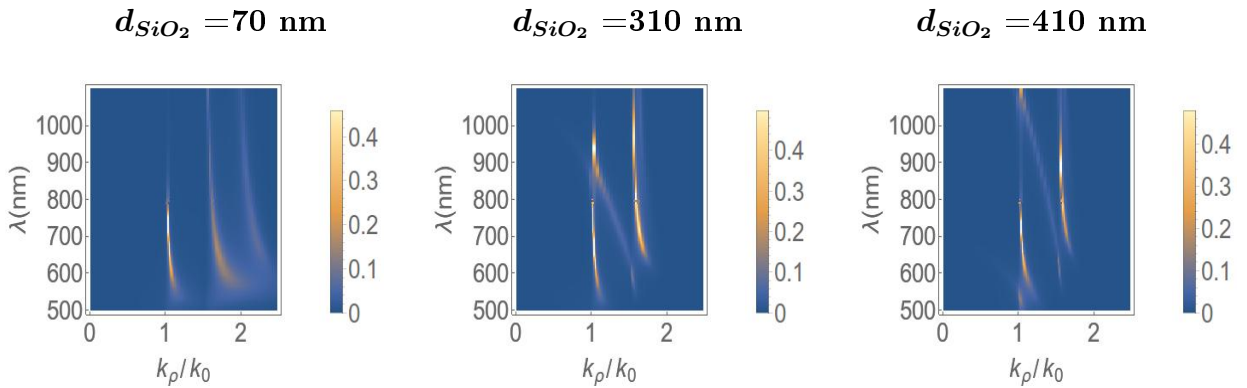


Figure 6.31: Transmitted flux intensity dispersion density plot of a six-layer stack air-Au(30nm)-SiO<sub>2</sub>( $d_{SiO_2}$ )-Au(30nm)-Ti(3 nm)-glass from left to right for  $d_{SiO_2} = 70$  nm,  $d_{SiO_2} = 310$  nm and  $d_{SiO_2} = 410$  nm respectively. Note the extended scale of the abscissa

Finally let us look beyond the experimental constraints as did for example Smith *et al.* [44]. The oscillating dipole can generate plane waves with normalized wave vectors larger than the substrate index of refraction, here 1.52 of the glass. Since the numerical aperture used in the

experiment work is  $NA=1.49$ , in the present chapter we have restricted our analysis to the wave vector grid  $k_\rho/k_0 \in [0, 1.5]$ . As possible future work, in the following we briefly explore the normalized in-plane wave vector in an extended domain, for example  $k_\rho/k_0 \in [0, 2.5]$ . Figure 6.31 displays the dispersion density plot of the transmitted flux intensity of the six-layer stack (from left to right with  $d_{SiO_2} = 70$  nm,  $d_{SiO_2} = 310$  nm and  $d_{SiO_2} = 410$  nm respectively). For an  $SiO_2$  thickness of  $d_{SiO_2} = 70$  nm we find three modes 1.08, 1.82 and 2.17. The  $SiO_2$  thickness is too small to sustain a WG mode, therefore these modes are all of SPP type. For the two other samples with  $d_{SiO_2} = 310$  and  $d_{SiO_2} = 410$  nm a WG mode appears between the SPP mode at 1.08 and the one at 1.8. This mode is recognizable since it varies significantly with  $k_\rho/k_0$ . Experimentally one can obtain large effective refractive indices by replacing the glass substrate by a medium with a larger refractive index. But one must also have an objective lens permitting a measurement with large normalized in-plane wave vectors.

# Chapter 7

## Characterization of the SPP and WG modes of the three and six-layer thin film stacks

### 7.1 Electric field profile mode assignment

In chapter 6 we have presented our results of the observables when a thin film stack is excited by a source at infinity or a local source of light. The dispersion curve have been studied for the three and six-layer thin film stacks. In three-layer stack we have recognize an SPP mode in the evanescent region, whereas for the six-layer stack two modes are observed in the evanescent region corresponding to an SPP-like mode ( $k_\rho/k_0 \simeq 1$ ) and WG-like mode ( $k_\rho/k_0 > 1$ ).

This chapter presents the characterization of the nature of the excited modes using the representation of their electric field as a function of the penetration coordinate  $z$  (perpendicular to the interfaces). Relative to the Fourier transform  $(\rho, \phi) \Leftrightarrow (k_\rho, k_\phi)$  presented in the preceding chapter this  $z$  coordinate is a spectator i.e. it is never Fourier transformed.

The electric field profile  $\vec{E}_n(\vec{r}, \omega_n)$  of the exciting light is a powerful tool for the spatial localization of this field helping in the identification of the nature of the modes. The local density is defined in the solid state physics for electrons and recently the development of the local probe instruments based on light like for example the SNOM it has been also defined and calculated for photons (see refs. [84; 109; 110])

$$\rho(\vec{r}, \omega) = \sum_n \delta(k^2 - k_n^2) |\vec{E}_n(\vec{r}, \omega_n)|^2$$

The expression above shows that the local density of the photonic states and the photon field profile are closely related.

### 7.1.1 Electric field as a function of the penetration coordinate

The two methods discussed in chapter 5, section 5.1.2, in relation to the excitation by a source at infinity (ESI) model and the Fresnel coefficients of a thin film stack give the electric field as a function of the penetration coordinate:

- **Transfer matrix formalism of Bethune [58]:**

$$\begin{aligned}
 \begin{pmatrix} E_1^+ \\ E_1^- \end{pmatrix} &= \begin{pmatrix} 1 \\ r_{1f} \end{pmatrix} E_0 \\
 \begin{pmatrix} E_2^+ \\ E_2^- \end{pmatrix} &= \begin{pmatrix} e^{ik_{2z}(z-z_1)} & 0 \\ 0 & e^{-ik_{2z}(z-z_1)} \end{pmatrix} M_{21} \begin{pmatrix} E_1^+ \\ E_1^- \end{pmatrix} & z \in [z_1, z_2] \\
 \dots & & \dots \\
 \begin{pmatrix} E_j^+ \\ E_j^- \end{pmatrix} &= \begin{pmatrix} e^{ik_{jz}(z-z_{j-1})} & 0 \\ 0 & e^{-ik_{jz}(z-z_{j-1})} \end{pmatrix} M_{j(j-1)} \Phi_{j-1} \begin{pmatrix} E_{j-1}^+ \\ E_{j-1}^- \end{pmatrix} & z \in [z_{j-1}, z_j] \\
 \begin{pmatrix} E_f^+ \\ E_f^- \end{pmatrix} &= \begin{pmatrix} e^{ik_{fz}(z-z_{f-1})} & 0 \\ 0 & e^{-ik_{fz}(z-z_{f-1})} \end{pmatrix} M_{f(f-1)} \Phi_{f-1} \begin{pmatrix} E_{f-1}^+ \\ E_{f-1}^- \end{pmatrix} & z \in [z_{f-1}, z_f].
 \end{aligned} \tag{7.1}$$

where  $f$  is the number of layers and  $j$  is the running layer. Note that  $E_f^- = 0$  since no light can be reflected in the last layer.  $M_{ij}$  (eq. (5.24), chapter 5) and  $\Phi_j$  (eq. (5.25), chapter 5) are the transfer and the propagation matrices, respectively, and  $r_{1f}$  is the total reflection coefficient calculated using the Bethune formalism [58]. In this chapter we are calculating the electric field as a sum  $E_j(z) = E_j^+(z) + E_j^-(z)$ . This field can be a vector or its components.

- **Iterative algorithm of Smith *et al.*[44]:**

For  $p$  polarization the electric field as a function of the penetration coordinate reads

$$\begin{aligned}
 E_1(z) &= E_1^- \exp[-ik_{1z}(z)] (1, 0, k_x/k_{1z}) & z \leq 0 \\
 \dots & & \dots \\
 E_j(z) &= E_j^+ \exp[+ik_{jz}(z - z_{j-1})] (1, 0, -k_x/k_{jz}) \\
 &\quad + E_j^- \exp[-ik_{jz}(z - z_j)] (1, 0, k_x/k_{jz}) & z_{j-1} \leq z \leq z_j \\
 \dots & & \dots \\
 E_f(z) &= E_f^+ \exp[+ik_{fz}(z - z_{f-1})] (1, 0, -k_x/k_{fz}) & z_{f-1} \leq z.
 \end{aligned} \tag{7.2}$$

where again  $f$  is the number of layers and  $j$  is the an intermediate layer.  $E_j^+$  and  $E_j^-$  are the transmitted and reflected electric fields, respectively (chapter 5, eq. (5.31)). The formulation of the  $s$  polarization is slightly different and the reader may consult the appendix of Smith *et al.* [44] for the relevant expressions.

### 7.1.2 Characterization of the modes

Considering a metal-insulator-metal (MIM) structure, one can detect an SPP mode propagating at each interface. If the insulator is thick, the evanescent waves do not transverse it and these SPP are independent from each other. When the insulator becomes thin enough to allow non zero evanescent waves at the other interface, coupling takes place and symmetric and an antisymmetric SPP modes occur. The antisymmetric SPP mode has a large propagation length and this mode is called a long range SPP (LRSP) [111]. For a three-layer system, Smith *et al.* [44] classified these modes on the basis of the symmetry properties of the electric field. To characterize the mode in our more complicated six-layer system, we use the mean electric field in the layer j

$$\vec{E} = E_x \vec{i}_x + E_z \vec{i}_z \quad (7.3)$$

$$\bar{E}_x^j = \frac{\int E_x^j(z) dz}{d_j}; \quad \bar{E}_z^j = \frac{\int E_z^j(z) dz}{d_j}; \quad \bar{E}^j = \frac{\int \sqrt{(E_x^j(z))^2 + (E_z^j(z))^2} dz}{d_j},$$

where  $d_j$  is the thickness of the layer j. If the mean electric field amplitude in the metal is large, then the light absorption is significant and the SPP mode decays rapidly, one has a short range SRSP. Otherwise for the SPP mode the electric field has its main amplitude in insulator/dielectric and can propagate over long distances i.e. it is called LRSP.

### 7.1.3 Validation of the E(z) algorithm

Using the two methods presented above we have calculated the modulus  $|E|$  of the electric field reproducing the results of Smith *et al.*[44], Refki *et al.* [57] and Choudhury *et al.* [49].

As an example in figure 7.1 we compare our results (right column) with those of Refki *et al.* [57] (left column) for a glass-Ag-Poly(methyl methacrylate) (PMMA)-Ag-air thin film stack (a comparison with Smith *et al.*[44] results is given in appendix). Refki *et al.* [57] show that an angular scan of the attenuated total reflexion (ATR) of such MIM sample exhibits a sharp dip around  $42.56^\circ$  and a broad dip around  $53.1^\circ$ . These authors calculate the modulus of the electric field as a function of the penetration coordinate  $z$  at the mentioned two angles and at an intermediate angle of  $46.0^\circ$ . The good agreement between Refki *et al.* [57] (figure 7.1, left column) and our modeling (figure 7.1, right column) validates our algorithm calculating the electric field as a function of the penetration coordinate. The agreement is qualitative only since, compared to the paper we use a different set of material functions.

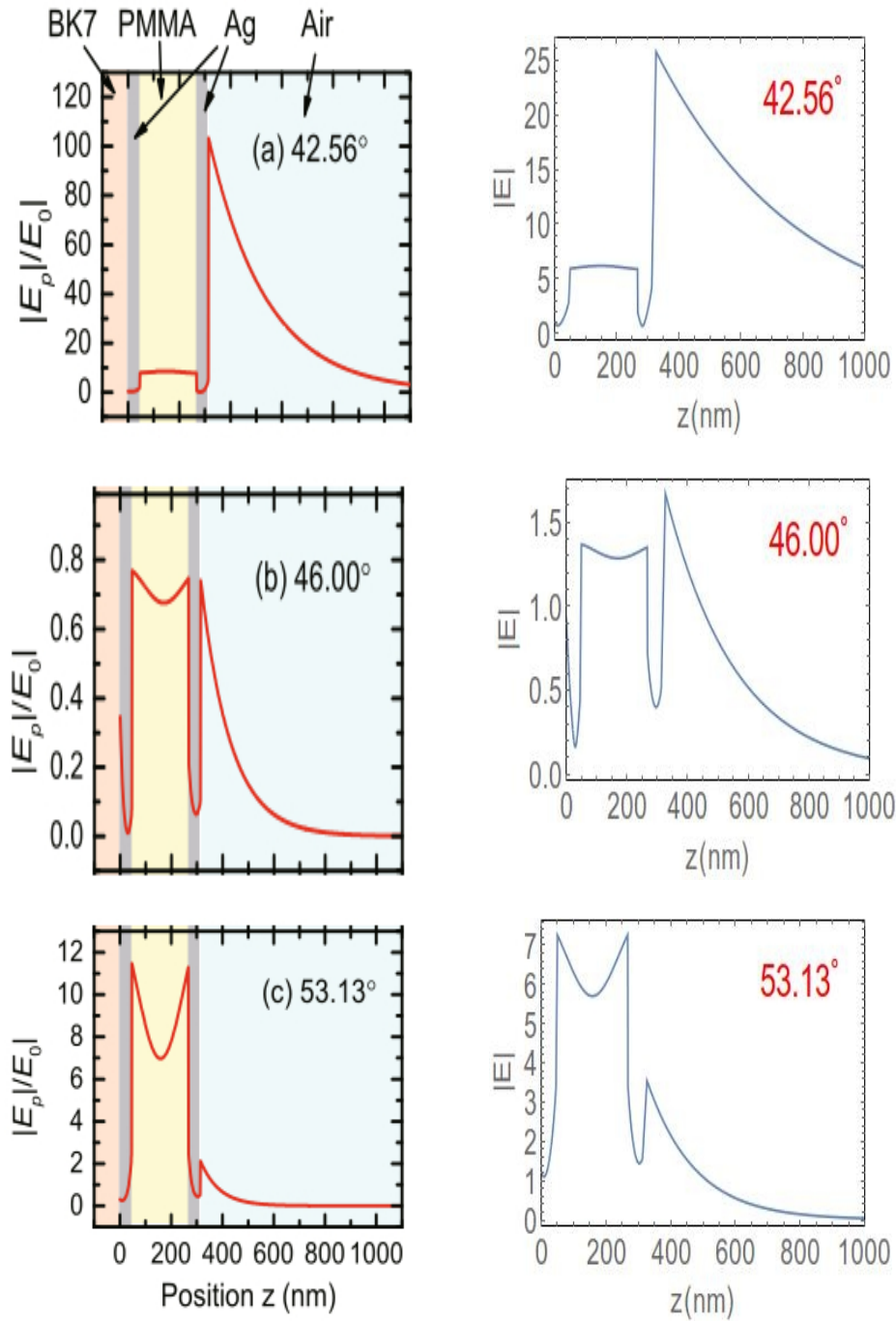


Figure 7.1: Modulus of the electric field as a function of the penetration coordinate  $z$  at  $\lambda=632.8$  nm for a glass-Ag(47 nm)-PMMA (221.5 nm)-Ag(47 nm)-air structure. Left column Refki *et al.*[57] calculation, right column our results.

### 7.1.4 Modulus of the total electric field as a function of the penetration coordinate ( $z$ ), $d_{Au}$ and $d_{SiO_2}$

Before characterizing the modes let us present the amplitude of the electric field as a function of the two thickness parameters of the six-layer system  $d_{Au}$  and  $d_{SiO_2}$ . Such a presentation will lead us to understand the variation of the location of the modes in gold and  $SiO_2$ . Figure 7.2 displays the electric field as a function of the gold thickness  $d_{Au}$  and the penetration coordinate  $z$  at  $\lambda=680, 750$  and  $850$  nm in the left, middle and right columns respectively. The wavelength  $\lambda=680$  nm corresponds to the location of the reflectance dip of the WG mode at  $k_\rho/k_0=1.5$  (figure 6.7, second line middle graph) and the wavelength  $\lambda=850$  nm to the SPP-WG interaction region at  $k_\rho/k_0 \simeq 1$ .

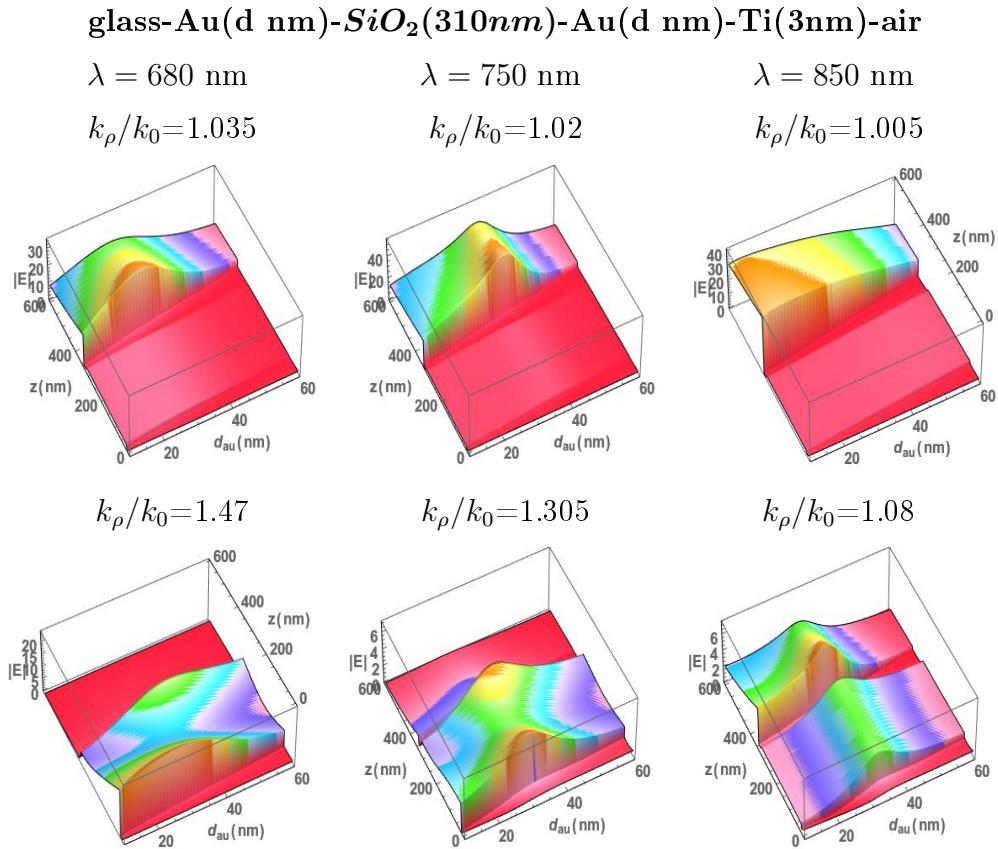


Figure 7.2: Electric field as a function of the  $z$  coordinate and gold thickness for  $p$  polarized light at  $\lambda = 680, 750$  and  $850$  nm are presented in the left, middle and right columns respectively. The first and second rows correspond to close to 1 and large normalized wave vectors respectively. Note that  $z=0$  corresponds to the glass-Au interface.

Recall that in chapter 6 we have proposed that the mode with  $k_\rho/k_0$  close to 1 is an SPP mode and the one with large  $k_\rho/k_0$  is a WG mode. The first row of the figure presents the electric field corresponding to the SPP mode at  $k_\rho/k_0=1.035, 1.02$  and  $1.005$  for  $\lambda=680, 750$  and  $850$  nm respectively, whereas the second row displays the WG mode at  $k_\rho/k_0=1.47, 1.305$  and  $1.08$ . In agreement with our results in the preceding chapter (sections 6.4.1 and 6.2.1) for both SPP

and WG modes, the electric field has a significant amplitude in the range  $d_{Au}(nm) \in [10, 50]$ . The electric field associated with the SPP mode is always confined to the gold-air interface. The electric field of the WG mode (second row in the figure) is confined in the SiO<sub>2</sub> layer  $z(nm)[d_{Au}, 310 + d_{Au}]$ . For  $\lambda=850$  nm (second row, right graph) the electric field profile is significant in both SiO<sub>2</sub> and at the gold-air interface, corresponding to the region where the SPP-WG mixing in the field can be significant.

Next for a fixed  $d_{Au} = 30$  nm the variation of the modulus  $|E|$  as a function of the thickness  $d_{SiO_2}$  and the penetration coordinate  $z$  is presented in figure 7.3 second and fourth lines. The left, the middle and right columns correspond to  $\lambda=680, 750$  and  $850$  nm (the choice of  $\lambda$  is explained when we have presented figure 7.2). The first and third lines display respectively the value of  $k_\rho/k_0$  at the maximum of the SPP mode (first line) and WG mode (third line) as a function of  $d_{SiO_2}$ . The corresponding electric field is presented in the second and the fourth rows of the figure. Analyzing these graphs one understands the SPP and WG modes can not be completely separated. In these 2D graphs (first and third row in the figure) the discontinuity at  $d_{SiO_2}=200, 250$  and  $300$  nm respectively in the left, middle and right graphs corresponds to the appearance of the WG mode. The second row in the figure displays the 3D graphs of the SPP mode as a function of  $d_{SiO_2}$  and shows, as in figure 7.2, that the SPP is located at the Au-air interface.

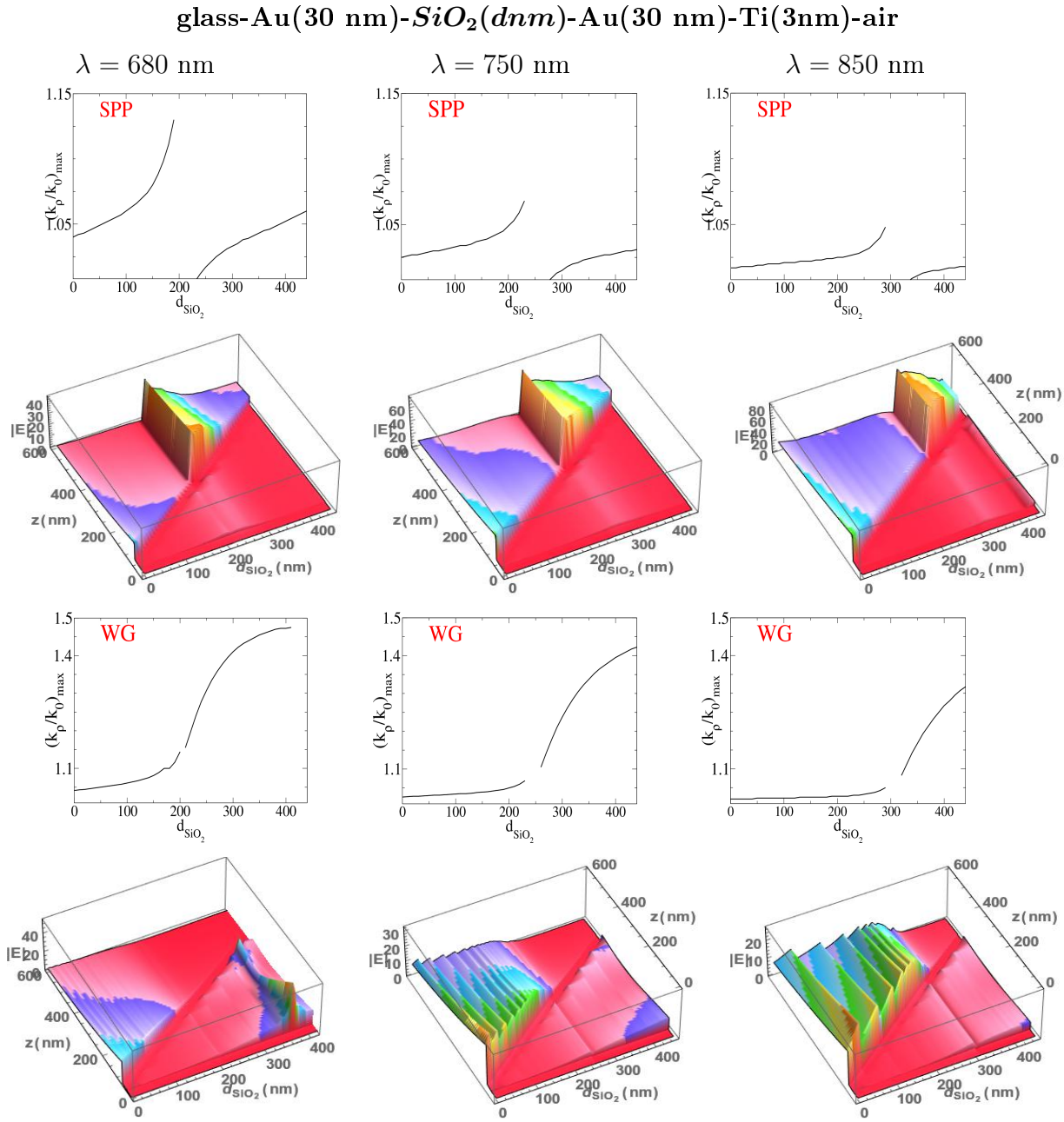


Figure 7.3: The SPP and WG modes excited by  $p$  polarized light at  $\lambda = 680, 750$  and  $850$  nm are shown in the left, middle and right columns respectively. The first and the third rows display the position of the maxima of SPP and WG modes as a function of  $d_{SiO_2}$ . The second and fourth rows present the modulus of the electric field as a function of the  $z$  coordinate and the silica thickness  $d_{SiO_2}$ . Note that  $z=0$  corresponds to the glass-Au interface.

In the figure, the back triangle corresponds mainly to the SPP mode and the "wall" at about  $d_{SiO_2}=200, 250$  and  $300$  nm respectively in left, middle and right graphs corresponds to the appearance of the WG mode. Interestingly enough the appearance of the WG mode gives rise to a sudden rise of the  $|E|$  in the SPP mode. The electric field of the WG mode as a function of the penetration coordinate  $z$  and  $d_{SiO_2}$  at  $\lambda=680$  nm is presented in the first column of figure

7.3. The front "triangle" is the WG mode. The back "triangle" corresponds to the SPP mode which is present as long as the WG mode is absent. The second and third columns in figure 7.3 can be analyzed in a similar way where the WG mode appears at  $d_{SiO_2}=250$  and 300 nm.

In summary figure 7.3 confirms the location of  $|E|$  for the SPP at the Au-air interface and for the WG mode in the  $SiO_2$ . The presence of the WG mode gives rise to a jump in  $|E|$ .

### 7.1.5 Total electric field modulus as a function of the wavelength $\lambda$ and the penetration coordinate $z$

Next we study the  $|E|$  as a function of  $\lambda$  and of course the penetration coordinate  $z$ . For  $d_{Au}=30$  nm and  $d_{SiO_2}=70, 310$  and 410 nm, recall that in the dispersion curves presented in chapter 6 the peak position ( $k_\rho/k_0$ ) of the modes depends on the wavelength  $\lambda$ .

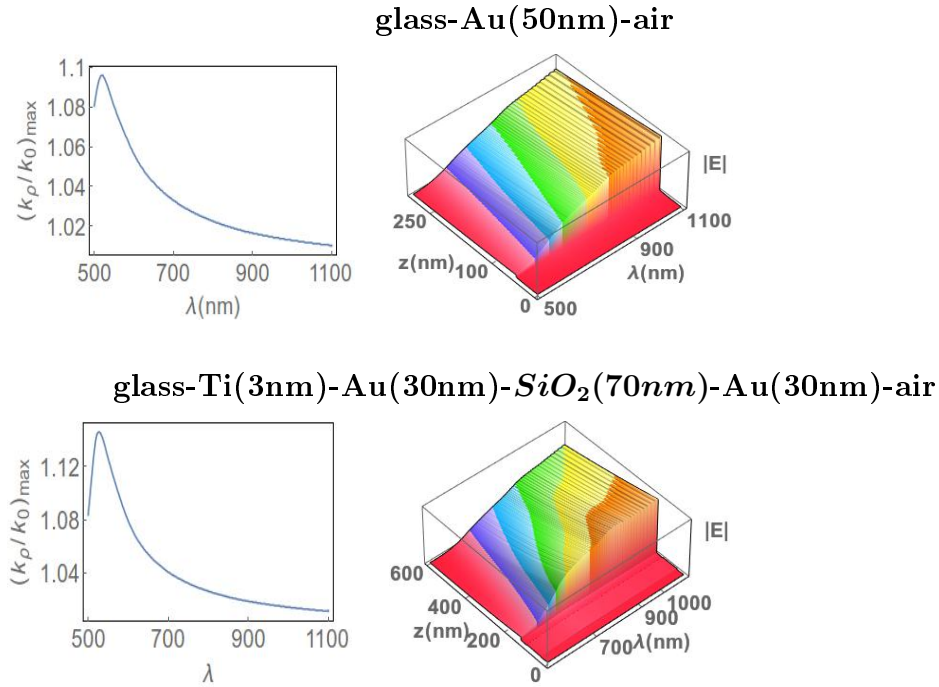


Figure 7.4: The electric field modulus  $|E|$  represented as a function of the penetration coordinate  $z$  and of the wavelength  $\lambda$  (right column) for a three (first row) and a six (second row) thin film stack. The left column graphs display the correspondence between  $\lambda$  and  $(k_\rho/k_0)_{max}$  at the maximum of the SPP mode. The right column graphs display the electric field modulus of the SPP mode as a function of the wavelength  $\lambda$  and the penetration coordinate  $z$ . Recall that  $z=0$  corresponds to the glass-Au interface.

The left column graph of figure 7.4 displays the SPP mode peak position as a function of the wavelength  $\lambda$  for three and six-layer thin film stacks with  $d_{SiO_2}=70$  nm. Each wave vector projection  $k_\rho/k_0$  of the SPP-like mode maximum in the left column of the figure corresponds a

specific wavelength  $\lambda$ . The total electric field modulus  $|E|$  of this maximum is presented in the right column of figure 7.4 as a 3D graph as a function of the wavelength  $\lambda$  and the penetration coordinate  $z$ . The three and six-layer 3D graphs display a similar behavior showing that the electric field is localized at the Au-air interface. The thickness of the  $\text{SiO}_2$  layer is too small to sustain the WG modes.

For a six-layer thin film stack with larger  $\text{SiO}_2$  thickness two modes appear (see chapter 6).

**glass-Ti(3nm)-Au(30nm)- $\text{SiO}_2(d_{\text{SiO}_2}\text{nm})$ -Au(30nm)-air**

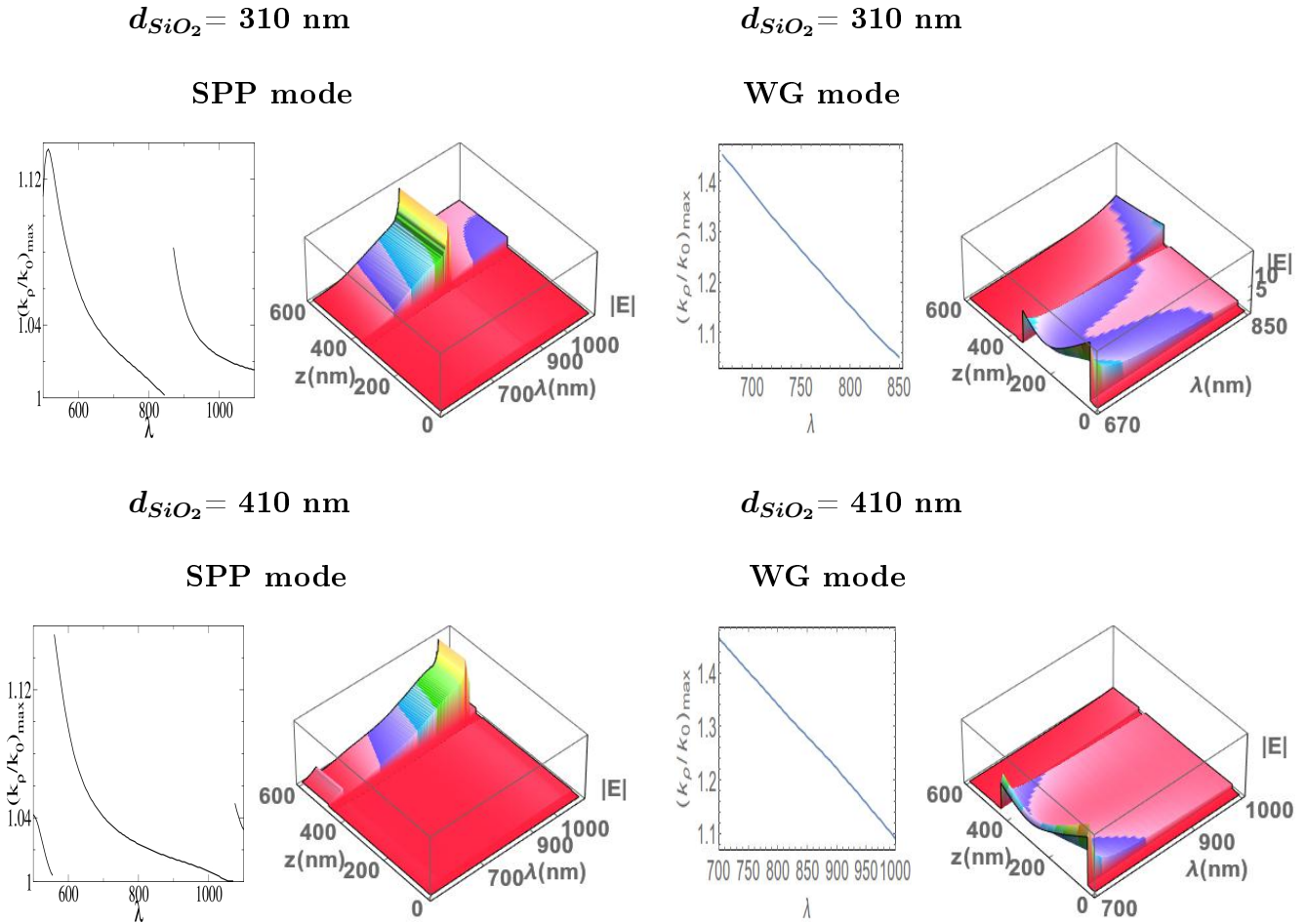


Figure 7.5: Six-layer stack electric field modulus  $|E|$  as a function of the penetration coordinate  $z$  and the wavelength  $\lambda$  (second and fourth columns). The first and third columns present the mode maxima in  $k_\rho/k_0$  as a function of the wavelength  $\lambda$ . The first two columns correspond to the SPP and the last two columns to the WG modes. In the first and the second rows one uses  $d_{\text{SiO}_2}=310 \text{ nm}$  and  $d_{\text{SiO}_2}=410 \text{ nm}$  respectively. Recall that  $z=0$  corresponds to the glass-Au interface.

The first and third columns of figure 7.5 present the position  $(k_\rho/k_0)_{max}$  as a function of  $\lambda$  for the SPP and WG modes respectively. The discontinuities in the maxima of the SPP mode presented in the first column graphs are of the same nature as the ones found and discussed

in figure 7.3, namely the appearance of the WG mode and its interaction with the SPP mode. For  $d_{SiO_2}=410$  nm there are two discontinuities probably partly related to the periodicity of the field with  $d_{SiO_2}$ . The second and fourth columns of figure 7.5 display the 3D graph of  $|E|$  as a function of the penetration coordinate  $z$  and wavelength  $\lambda$ . The SPP mode (figure 7.5 second column) is located at the air-gold interface. The "wall" at about  $\lambda=850$  nm for  $d_{SiO_2}=310$  nm and  $\lambda=850$  nm for  $d_{SiO_2}=410$  nm is due to the presence of the WG.

The third and fourth columns of figure 7.5 present the WG mode. For this mode the normalized in-plane wave vector is continuous. Since the WG mode appears only in the range  $\lambda(\text{nm}) \in [650, 850]$  for  $d_{SiO_2}=310$  nm and  $\lambda(\text{nm}) \in [700, 1000]$  for  $d_{SiO_2}=410$  nm (see dispersion curves presented in figure 6.9 and 6.18 in previous chapter), the third column displays the position  $(k_p/k_0)_{max}$  in these region only. The corresponding electric field (fourth column figure 7.5) is confined in the  $SiO_2$  layer. At  $\lambda \simeq 850$  nm one identifies a significant electric field at the Au-air interface except when the SPP and WG modes are close in momentum space and the separation is difficult.

A deeper characterization of the modes is made using the modulus of the projected electric field  $|E_x|$ ,  $|E_z|$ , the total electric field modulus  $|E|$  and the mean field of a layer given in eq.(7.3) above. For this detailed analysis we have chosen a cut in the 3D graphs of figures 7.4 and 7.5 at  $\lambda=750$  nm. For a three layer stack, the left, middle and right graphs of figure 7.6 present the modulus of the x and z projections  $|E_x|$  and  $|E_z|$ , and the modulus  $|E|$  as a function of the penetration coordinate  $z$  respectively. Figure 7.6 and the mean electric field presented in table 7.1, locate this mode ( $k_p/k_0=1.02$  for  $\lambda=750$  nm) at the Au-air interface and in air. Since the electric field is located mainly in air ( $\bar{E}^{air} \gg \bar{E}^{Au}$ ) the SPP at an Au-air interface has long range SPP (LRSP) character

**glass-Au(50nm)-air**

$k_p/k_0=1.02, \lambda=750$  nm

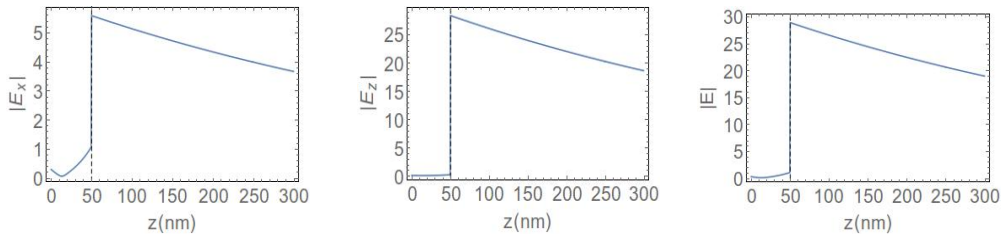


Figure 7.6: Electric field as a function of the  $z$  coordinate,  $|E_x|$  left,  $|E_z|$  middle and  $|E|$  right for air-Au(50 nm)-glass system. The origin of the coordinates  $z=0$  is at the glass-Au interface.

Table 7.1: Character of the plasmonic resonances of the glass-Au(50 nm)-air system at  $\lambda=750$  nm. Note that  $\bar{E}^j$  is the mean field in the layer defined in eq. (7.3)

$k_\rho/k_0$	$\bar{E}^{Au}$	$\bar{E}^{Air}$	localisation	Character
1.035	0.8208	23.616	Au/air	LRSP

For a six-layer stack at 750 nm with  $d_{SiO_2}=70$  nm, the SPP mode appears at  $k_\rho/k_0=1.05$ . Figure 7.7 and the mean field presented in table 7.2 show that this mode is again located at the Au-air interface (see figure 7.6) as was observed for the three-layer stack. This mode also has LRSP character since the electric field is mainly located in air ( $\bar{E}^{air} \gg \bar{E}^{Au}$ ).

**glass-Ti(3nm)-Au(30nm)-SiO<sub>2</sub>(70nm)-Au(30nm)-air**

**$k_\rho/k_0=1.05$ ,  $\lambda=750$  nm**

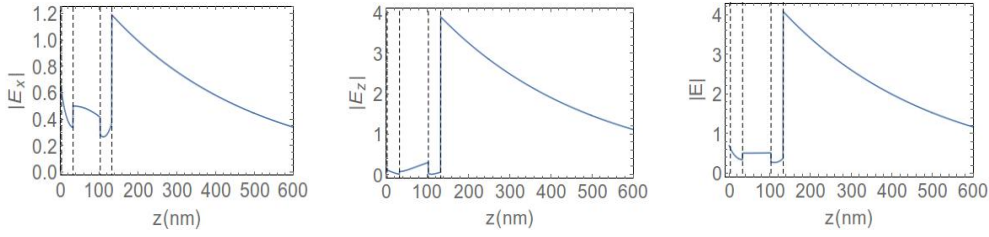


Figure 7.7: Electric field of a six-layer glass-Ti(3nm)-Au(30nm)-SiO<sub>2</sub>(70nm)-Au(30nm)-air system as a function of the  $z$  coordinate,  $|E_x|$  left,  $|E_z|$  middle and  $|E|$  right.

Table 7.2: Character of the plasmonic resonances of a six-layer system (glass-Ti(3nm)-Au(30nm)-SiO<sub>2</sub>(70nm)-Au(30nm)-air) at  $\lambda=750$  nm

$d_{SiO_2}$	$k_x/k_0$	$\bar{E}^{Ti}$	$\bar{E}^{Au}$	$\bar{E}^{SiO_2}$	$\bar{E}^{Au}$	$\bar{E}^{Air}$	localisation	Character
70nm	1.05	0.6674	0.4295	0.5059	0.292379	2.325	Au/air	LRSP

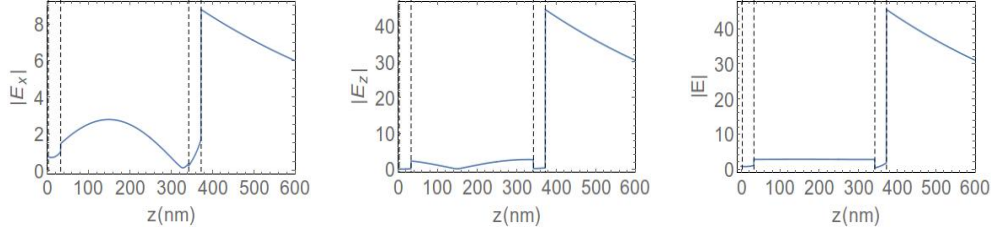
Finally figures 7.8 and 7.8 show the results for the glass-Ti(3nm)-Au(30nm)-SiO<sub>2</sub>(310nm)-Au(30nm)-air system at 750 nm (first line) and 850 nm (second line) where two modes have been identified :

1.  $\lambda=750$  : an SPP-like mode at  $k_\rho/k_0=1.02$  and a WG-like mode at  $k_\rho/k_0=1.305$
2.  $\lambda=850$  : an SPP-like mode at  $k_\rho/k_0=1.005$  and a WG-like mode at  $k_\rho/k_0=1.08$ .

From these graphs and table 7.3 and 7.4, giving the mean electric field in a layer we deduce that the SPP mode is localized at the Au-air interface and in air and has a LRSP character.

**glass-Ti(3nm)-Au(30nm)-SiO<sub>2</sub>(310nm)-Au(30nm)-air , SPP-like mode**

$$k_\rho/k_0=1.02, \lambda=750 \text{ nm}$$



$$k_\rho/k_0=1.005, \lambda=850 \text{ nm}$$

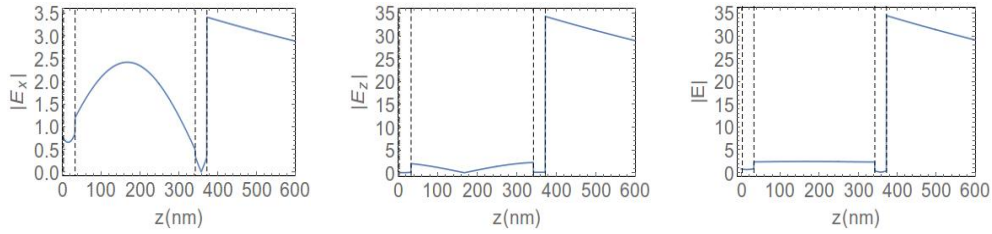
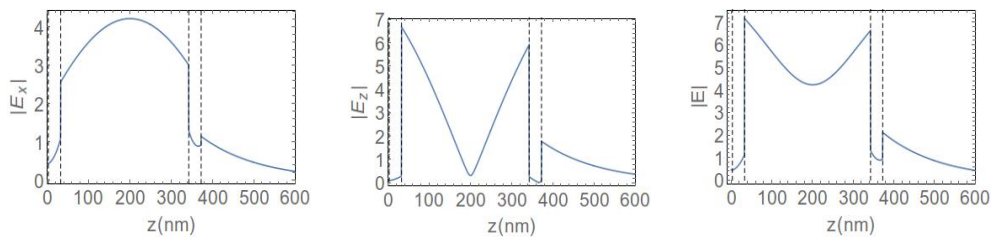


Figure 7.8: The electric field as a function of the  $z$  coordinate ( $z=0$  at glass-Au interface),  $|E_x|$  left,  $|E_z|$  middle and  $|E|$  right for a six-layer stack glass-Ti(3nm)-Au(30 nm)-SiO<sub>2</sub>(310 nm)-Au(30 nm)-air system. The polarization is  $p$  and the wavelengths are 750 (first row) and 850 nm (second row). The in-plane wave vector  $k_\rho/k_0$  corresponds to an SPP mode.

**glass-Ti(3nm)-Au(30nm)-SiO<sub>2</sub>(310nm)-Au(30nm)-air , WG-like mode**

$$k_\rho/k_0=1.305, \lambda=750 \text{ nm}$$



$$k_\rho/k_0=1.08, \lambda=850 \text{ nm}$$

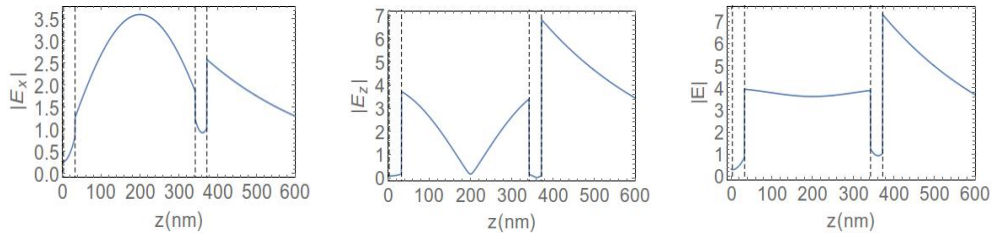


Figure 7.9: The electric field as a function of the  $z$  coordinate ( $z=0$  at glass-Au interface),  $|E_x|$  left,  $|E_z|$  middle and  $|E|$  right for a six-layer stack air-Au(30 nm)-SiO<sub>2</sub>(310 nm)-Au(30 nm)-Ti(3nm)-glass system. Same characteristics as in figure 7.8.

Table 7.3: The character of the plasmonic modes of a multi layer system (glass-Ti(3nm)-Au(30 nm)-SiO<sub>2</sub>(310 nm)-Au(30 nm)-air) at  $\lambda=750$  nm, The first line in the table refers to figure 7.8, the second line to figure 7.9.

$d_{SiO_2}$	$k_x/k_0$	$\bar{E}^{Ti}$	$\bar{E}^{Au}$	$\bar{E}^{SiO_2}$	$\bar{E}^{Au}$	$\bar{E}^{Air}$	localisation	Character
310 nm	1.02	0.77582	0.7905	2.7556	0.9174	37.7621	Au/air	LRSP
310 nm	1.305	0.4544	0.6947	5.31406	1.0002	1.05729	SiO <sub>2</sub>	WG

Table 7.4: The character of the plasmonic modes of a multi layer system (glass-Ti(3nm)-Au(30 nm)-SiO<sub>2</sub>(310 nm)-Au(30 nm)-air) at  $\lambda=850$  nm, The first line in the table refers to figure 7.8, the second line to figure 7.9.

$d_{SiO_2}$	$k_x/k_0$	$\bar{E}^{Ti}$	$\bar{E}^{Au}$	$\bar{E}^{SiO_2}$	$\bar{E}^{Au}$	$\bar{E}^{Air}$	localisation	Character
310 nm	1.005	0.7834	0.7076	2.377	0.1993	31.7062	Au/air	LRSP
310 nm	1.08	0.31006	0.4769	3.729	1.0041	5.298	SiO <sub>2</sub>	WG

## 7.2 Conclusion

This chapter presented the location of the electric field in the three and six-layer thin film stacks. The electric field corresponding to the SPP is located at the Au-air interface, whereas the WG mode is located in the SiO<sub>2</sub>. For a six-layer thin film stack at  $k_x/k_0=1.08$  with  $d_{SiO_2}=310$  nm and  $\lambda=850$  nm one identifies an avoided crossing between SPP and WG modes, where at the crossing the electric field has a mixed SPP-WG character. We have seen also that all the modes in a six-layer thin film stack have LRSP or WG character, probably due to the coupling between the SPP and WG modes. In the literature (see e.g. Smith *et al.*[44], Refki *et al.* [57]) such a case of weak coupling and mixing of modes is not common. The presented electric field profile permits calculate a local density of photonic modes, and thus can be applied to calculate the emission rates of quantum emitters in the vicinity of a multilayer system, and thus of the variations of lifetime and quantum efficiency of radiative emission.

# Chapter 8

## Conclusion

This work has presented a study of the surface plasmon polariton (SPP) and wave guide (WG) modes of three and six-layer thin film stacks separated by flat structureless interfaces. The thin film stacks were composed of air-Au-glass and air-Au-SiO<sub>2</sub>-Au-Ti-glass thin films respectively. A majority of the recent studies of SPP modes concentrate on their properties in nano objects, samples with cavities, antennas, wires and ordered arrays of nano objects. Our choice of the thin film stack which are 2D periodic samples was dictated by the simplicity of the theoretical models to be implemented and of the relative facility of the interpretation of the results. We think that one can use our thin film stack results as a benchmark when studying systems of lower dimension or having particular geometric forms. By themselves these thin film stacks are of interest in the study of the propagation properties along the interfaces related to wave guides and optical fibers.

The theoretical models I used to calculate the observables in the present work are based on the Fresnel theory at flat interfaces and plane wave propagation in the thin film layers as detailed in chapter 5. These models are simple and they require the continuity of the field at the interface. The excitation source can be either a source of light located at infinity or a local source. The inelastic tunneling electrons from an STM tip were modeled as a vertical oscillating dipole located just above the surface.

At a given wavelength  $\lambda$  and a particular interface where the refractive indices are  $n_{top} > n_{bottom}$  the wave vector domain is divided into two regions: propagating and evanescent (see chapter 5 section 5.3). The SPPs manifest themselves in the evanescent region by a significant mean electric field at and near the interfaces. An SPP mode appears as a dip in the reflectance of a source located at infinity and as a maximum in the transmitted flux in the case of excitation by a local vertical oscillating dipole. For the six layer thin film stack when the SiO<sub>2</sub> thickness is larger than 190 nm a second mode of wave guide (WG) type is present. In a particular wavelength domain the SPP and the WG modes repel each other giving rise to an avoided crossing (also known as anti-crossing, chapter 6) which for the samples studied here is weak.

The transmittance of a source at infinity and the transmitted flux of a local source have

---

significant intensity in the propagating and the evanescent regions respectively and therefore are complementary whereas the reflectance covers the entire propagating and evanescent regions of the wave vector range.

The three layer stack has a single thickness parameter to be varied  $d_{Au}^{three}$ . The transmission is weak in a sufficiently thick gold layer while the confinement is weak for thin gold layer. The two thin film thicknesses of the gold are taken to be equal, the six layer thin film stack presents two thickness to be varied  $d_{Au}^{six}$  and  $d_{SiO_2}$ . Two sections of chapter 6 study in detail the influence of these thicknesses on the observables: the reflectance of a source located at infinity (section 6.2) and the transmitted flux of a local source excitation (section 6.4). The thickness domains where the observables are significant are:  $d_{Au}^{three} \in [10, 90]$  for the three and  $d_{Au}^{six} \in [10, 50]$  nm for the six layer stacks. Since the six layer stack has two identical gold films these results are equivalent. For a six layer stack the observables are periodic with the  $d_{SiO_2}$  thickness and this is easily seen in the propagating domain (see figure 6.5) since a single WG mode is present. In the evanescent region the SPP-WG avoided crossing partly destroys this picture. This oscillatory behavior defines several optimal values of  $d_{SiO_2}$ , thicknesses which can be narrowed by analyzing the evanescent domain.

The study of the electric field as a function of the spatial coordinate presented in chapter 7 allows us to characterize the nature of the modes. For a three layer stack with two interfaces and a six layer stack with five interfaces significant electric field exists in one or several interfaces or inside a thin film. From these results we can clearly assign the observed modes to either SPP or wave guide modes.

The most interesting region to be studied is the avoided crossing (anti-crossing) between the SPP and WG modes. In figure 6.18 it seems that close to the border of the evanescent region the SPP and WG merge together. In fact the merging region corresponds to an avoided crossing since: i) there is no continuation of the WG dispersion curve in the propagating region since the Fresnel transmission coefficients are weak giving rise to a weak transmitted flux intensity; ii) the interaction between SPP and WG is weak and the avoided crossing is unimportant since the SPP mode is mainly located at the air-Au interface and the WG mode is located in the SiO<sub>2</sub>.

We have compared our calculations to experimental work performed in our group by Shuyian Cao, Elizabeth Boer-Duchemin and Eric le Moal. Before performing these experiments, a preliminary study was done in order to choose the Au and SiO<sub>2</sub> thicknesses. The choice of the gold and silica layer thicknesses is guided by two requirements: high amplitude of the observable and wide wavelength dependence of the in-plane wave vector  $k_\rho$ . For the optimal  $d_{Au} = 30$  nm and  $d_{SiO_2} > 190$  nm corresponding to the appearance of WG mode, both the reflectance and the transmitted flux intensity of the experimental and the theoretical results are in a good agreement (see section 6.2 and 6.4). A clear disagreement between the simulations and the experimental results is found for the six-layer thin film stack in coordinate space. I think that this disagreement is related to slight experiment-model misfit of the domain of the SPP-WG avoided crossing (anticrossing). This is so since the closest position of the SPP-WG avoided crossing corresponds to an absence of the wide spaced fringes in coordinate space (see section 6.5).

During our calculations we also went beyond the effective refractive index of 1.52 of the glass (see chapter 6, section 6.6). At about  $k_\rho/k_0=2.17$  a new rather intense SPP mode appears. It would be interesting to find an experimental set-up allowing to study this new mode.

In summary, the present work concentrates on the detailed study of surface plasmon polariton (SPP) and wave guide (WG) modes appearing in a six-layer stack. We gave the range of the thicknesses where the observables are significant and discussed in detail the dispersion curves and the interaction and the avoided crossing (anti-crossing) between the SPP and the WG modes. These results are obtained in momentum space. We also in-plane Fourier transform these calculations and obtain supplementary information about the SPP and WG modes in coordinate space. Using the electric field as a function of the penetration coordinate we were able to characterize these modes.

As mentioned above, the present model is based on Fresnel equations at the interface and plane wave propagation in the medium. Since the material functions change suddenly the electric field derivative will not be continuous. Chapter 2 already described the surface and quantum well (QW) state and compare these electronic modes with the photonic wave guide (WG) modes largely discussed in this thesis. In that chapter I showed that the surface states can be calculated if the electronic potential is continuous and sustains a shallower potential well (see detail in figure 8.1). Any of the models cited in the introduction can be used (e.g. VPED model of Raseev [31]). Such calculations may solve the few discrepancies between the present model and the experiment, for example the results for the six-layer stack in coordinate space.

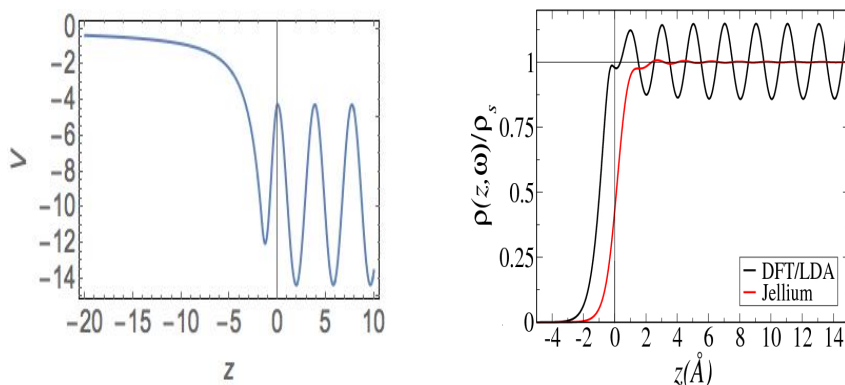


Figure 8.1: DFT-LDA model potential (left graph) and the corresponding electron density and the jellium electron density (right graph) of aluminum [31].

One can also study the SPP-WG avoided crossing (anticrossing) found in the present system or in other systems. From the literature I have selected two examples of interest:

- **Fano line shapes arising from the coupling between surface plasmon polariton and wave guide modes.** Analyzing the discrete-continuum interaction in atomic physics, Fano analytically formalized a particular type of line shape of the spectral lines. This type of spectral feature has been found and discussed in the spectra of many different

---

kinds of plasmonic samples (see e.g. ref. [112]). Recently Hayashi *et al.* [113; 114] have shown that a thin film stack of dielectric-plasmonic metal-dielectric<sub>1</sub>-dielectric<sub>2</sub>-dielectric<sub>3</sub> with the condition  $Re[\varepsilon_{dielectric_2}] < Re[\varepsilon_{dielectric_3}]$  can present very narrow features having the Fano shape profile. The interpretation of these authors is that this Fano feature corresponds to the interaction of a bright SPP mode (metal-dielectric) and a dark WG mode (dielectric<sub>1</sub>-dielectric<sub>2</sub>). In the present work our six layer stack is of a different type and our SPP-WG interaction gives rise to less localized features having a Lorentzian shape. But our model is able to calculate these very interesting Fano shape features in the spectra;

- **Strong coupling between Tamm plasmon polaritons (TPP) and the two dimensional semiconductor excitons.** Kaliteevski and co-workers [115] have shown that the confinement of the optical field can occur at the interface between a distributed Bragg reflector (DBR) and 2D metallic layer (see also Hu *et al.* [116]). The confinement arises, on one side, from the metal's negative dielectric constant, and on the other side, from the DBR's stop band (see ref. [117]). The confined light can interact with the Tamm surface state giving rise to Tamm plasmon polaritons (TPP). In contrast to conventional surface plasmons, TPPs can be excited by direct optical excitation.

The developed programs can be used as such for a calculation of any number of layers of a stack of dielectrics or dielectrics and metals in the propagating and evanescent regions. For example one can consider a multilayer thin film dielectric stack studied among others by Ndiaye, Zerrad and Amra *et al.* [118–120]. Here no surface plasmon polariton modes appear but for a TE polarization in the evanescent region large absorptance (1-(reflectance+transmittance)) corresponding to a large enhancement of the field can take place. Ndiaye *et al.*[118] use a source of light located at infinity, a source which does not permit a non-zero transmitted flux in the evanescent region (see the comparison of the transmittance and transmitted flux in chapter 6 section 6.4.2). Our model permits the study in transmission of such stacks excited by a local source (see chapter 6) and it would be interesting to model such multilayer dielectric stacks.

As we mentioned above, the inelastic tunneling current of an STM tip is modeled as a vertical oscillating dipole. Our OD model can easily be extended to a horizontal or an arbitrary dipole orientation (see e.g. Novotny [20]). The arbitrarily oriented dipole transmitted flux intensity is an incoherent linear combination of the horizontal (combination of  $s$  and  $p$  polarizations) and the vertical ( $p$  polarization only) intensities. An arbitrarily oriented dipole can model a molecule adsorbed on a surface which emits electromagnetic radiation (see e.g. Chance *et al.* [48]).

One would think that the thin film stack separated by flat surfaces is of academic interest only. As discussed in detail in the introduction, devices based on surface plasmon polaritons are used in physics, chemistry and biology (see e.g. Berini [1] and Homola [50]).

# Bibliography

- [1] P. Berini. Long-range surface plasmons polaritons. *Adv. Optics Photonics*, 1:484–588, 2009.
- [2] E. N. Economou. Surface plasmons in thin films. *Phys. Rev.*, 182:539–554, Jun 1969.
- [3] D. Bohm and D. Pines. *Phys. Rev.*, 92:609, 1953.
- [4] D. Pines. *Phys. Rev.*, 92:626, 1953.
- [5] R. H. Ritchie. Plasma losses by fast electrons in thin films. *Phys. Rev.*, 106:874–881, 1957.
- [6] R. H. Ritchie. Surface plasmons in solids. *Surf.Sci.*, 34:1–19, 1973.
- [7] R. A. Ferrell. Surface plasma oscillations of a degenerate electron gas. *Phys. Rev.*, 111:1214, 1958.
- [8] R. H. Ritchie. Photon excitation of surface plasmons. *Surf. Sci.*, 4:497–499, 1965.
- [9] S. Franzen. Surface plasmon polaritons and screened plasma absorption in indium tin oxide compared to silver and gold. *J. Phys. Chem.*, 112:6027–6032, 2008.
- [10] J M Pitarke, V M Silkin, E V Chulkov, and P M Echenique. Theory of surface plasmons and surface-plasmon polaritons. *Reports on Progress in Physics*, 70(1):1, 2007.
- [11] Abdellatif Akjouj, Gaëtan Lévêque, Sabine Szunerits, Yan Pennec, Bahram Djafari-Rouhani, Rabah Boukherroub, and Leonard Dobrzyński. Nanometal plasmon polaritons. *Surf. Sci. Reports*, 68:1–67, 2013.
- [12] M. Born and E. Wolf. *Principle of Optics (sixth edition)*. Pergamon Press, Oxford, 1980.
- [13] R. E. Potter. Basics parameters for measuring optical properties. In E. Palik, editor, *Handbook of optical constants of solids*, volume I, chapter 2, pages 11–34. Academic Press Inc., Orlando, USA, 1985.
- [14] H. Raether. *Surface plasmons on smooth and rough surfaces and on gratings*. Springer-Verlag, Berlin, 1988.
- [15] S. A. Maier. *Plasmonics: Fundamentals and applications*. Springer, New York, 2007.

- [16] D. Sarid and W. A. Challener. *Modern introduction to surface plasmons*. Cambridge University Press, 2010.
- [17] H. T. M. C. M. Baltar, K. Drozdowicz-Tomsia, and E. M. Goldys. *Propagating surface plasmons and dispersion relations for nanoscale multilayer metallic-dielectric films*. InTech, 2012.
- [18] W. Lukosz and R. E. Kunz. Light emission by electric and magnetic dipoles close to a planar interface. I. Total radiated power. *J. Opt. Soc. Am.*, 67:1607–1615, 1977.
- [19] W. Lukosz and R.E. Kunz. Light emission by magnetic and electric dipoles close to a plane dielectric interface. II. Radiation patterns of perpendicular oriented dipoles. *J. Opt. Soc. Am.*, 67:1615–1619, 1977.
- [20] L. Novotny. Allowed and forbidden light in near-field optics. I. A single dipolar source. *J. Am. Opt. Soc. A*, 14:91–104, 1997.
- [21] B. Hecht and L. Novotny. *Principles of Nano-Optics*. Cambridge University Press, 2006.
- [22] H.F. Arnoldus and J.T. Foley. Spatial separation of the traveling and evanescent parts of dipole radiation. *Optics Letters*, 28(15):1299–1301, 2003.
- [23] A. Drezet and C. Genet. Imaging surface plasmons: From leaky waves to far-field radiation. *Phys. Rev. Lett*, 110:213901, 2013.
- [24] B.T. Draine. The discrete-dipole approximation and its application to interstellar graphite grains. *Astrophysical J.*, 333:848–872, 1988.
- [25] B. T. Draine and P. J. Flatau. Fast near field calculations in the discrete dipole approximation for regular rectilinear grids. *Optics Express*, 20:1247–1252, 2012.
- [26] B. T. Draine and P. J. Flatau. User Guide for the Discrete Dipole Approximation Code DDSCAT 7.2, May 2012.
- [27] R. Lazzari and Simonsen I. GRANFILM: a software for calculating thin-layer dielectric properties and fresnel coefficients. *Thin Solid Films*, 419:124–136, 2002.
- [28] Kane S. Yee. Numerical solution of initial boundary value problem involving Maxwell’s equations in isotropic media. *IEEE Trans. Antennas Propag.*, AP-14(3):302–307, 1966.
- [29] A. Taflove and S.C. Hagness. *Computational Electrodynamics*. Artech House, Boston, London, 2005.
- [30] A. F. Oskooin, D. Roundy, M. Ibanescu, P. Bermel, J. D. Joannopoulos, and S. G. Johnson. MEEP: A flexible free-software package for electromagnetic simulations by the FDTD method. *Computer Phys. Comm.*, 181:687–715, 2010.
- [31] G. Raşeev. Laser fields at flat interfaces: I. Vector potential. *European Phys. J.*, D66:179, 2012.
- [32] A. Otto. Excitation of nonradiative surface plasma waves in silver by the method of frustrated total reflection. *Z. Phys*, 216:398–410, 1968.

- [33] Andreas Otto. Excitation by light of  $\omega_+$  and  $\omega_-$  surface plasma waves in thin metal layers. *Z. Phys*, 219:227–233, 1969.
- [34] E. Kretschmann and H. Raether. *Z. Naturforsch*, 23a:2135, 1968.
- [35] E. Kretschmann. *Z. Phys*, 241:313, 1971.
- [36] D Barchiesi and A. Otto. Excitations of surface plasmon polaritons by attenuated total reflection, revisited. *Il Nuovo Cimento*, 36:173–209, 2013.
- [37] H. Kano, S. Mizuguchi, and S. Kawata. Excitation of surface-plasmon polaritons by a focused laser beam. *J.Opt. Soc. Am. B*, 15:1381–1386, 1998.
- [38] B. Hecht, H. Bielefeldt, L. Novotny, Y. Inouye, and D. Pohl. *Phys. Rev. Lett*, 77:1889, 1996.
- [39] T. Wang, E. Boer-Duchemin, Y. Zhang, G. Comtet, and G. Dujardin. Excitation of propagating surface plasmons with a scanning tunnelling microscope. *Nanotechnology*, 22:175201, 2011.
- [40] F. J. García de Abajo. Optical excitations in electron microscopy. *Rev. Mod. Phys.*, 82:209–275, Feb 2010.
- [41] T. Coenen, B. Brenny, E.J. Vesseur, and A. Polman. Cathodoluminescence microscopy: Optical imaging and spectroscopy with deep-subwavelength resolution. *Materials Research Society*, 40:359–365, 2015.
- [42] J Fahrenfort. Attenuated total reflection: A new principle for the production of useful infra-red reflection spectra of organic compounds. *Spectrochimica Acta*, 17:698–709, 1961.
- [43] A. Drezet, A. Hohenau, D. Koller, Stepanov; A., H. Ditlbacher, B. Steinberger, F.R. Aussenegg, and J. R. Leitner, A. Krenn. Leakage radiation microscopy of surface plasmon polaritons. *Material Science and Engineering B*, 149:220–229, 2008.
- [44] L Smith, C. Taylor, R. Hooper, and L. Barnes. Field profiles of coupled surface plasmon-polaritons. *Modern Optics*, 55:2929–2943, 2008.
- [45] Hikaru Saito, Kyoko Namura, Motofumi Suzuki, and Hiroki Kurata. Dispersion relations for coupled surface plasmon-polariton modes excited in multilayer structures. *Microscopy*, 63:85–93, 2013.
- [46] Hongyan Yang, Jianqing Li, and Gongli Xiao. Significantly increased surface plasmon polariton mode excitation using a multilayer insulation structure in a metal-insulator-metal plasmonic waveguide. *Appl. Opt.*, 53(17):3642–3646, Jun 2014.
- [47] Shinji Hayashi, Akimichi Maekawa, Suk Chan Kim, and Minoru Fujii. Mechanism of enhanced light emission from an emitting layer embedded in metal-insulator-metal structures. *Phys. Rev. B*, 82:035441, Jul 2010.
- [48] A. Chance, R. Prock and R. Silbey. Molecular fluorescence and energy transfer near interfaces. *Advance in Chemical Physics*, 37, 1978.

- [49] S. Choudhury, R. Badugu, and R. Lakowicz. Directing fluorescence with plasmonic and photonic structures. *Accounts of Chemical Research*, 48:2171–2180, 2015.
- [50] Jiří Homola. Surface plasmon resonance sensors for detection of chemical and biological species. *Chemical Reviews*, 108(2):462–493, 2008.
- [51] K. Matsubara, S. Kawata, and S. Minami. A compact surface plasmon resonance sensor for measurement of water in process. *Appl. Spectrosc.*, 42(8):1375–1379, Nov 1988.
- [52] L. M. Zhang and D. Uttamchandani. Optical chemical sensing employing surface plasmon resonance. *Electron. Lett*, 24:1469, 1988.
- [53] Claes Nylander, Bo Liedberg, and Tommy Lind. Gas detection by means of surface plasmon resonance. *Sensors and Actuators*, 3:79 – 88, 1982.
- [54] J.M. Brockman, B.P. Nelson, and R.M. Corn. Surface plasmon resonance imaging measurements of ultrathin organic films. *Annu. Rev. Phys. Chem*, 51:41, 2000.
- [55] Jie. En. Li Tzu-Hsiang Lan, Yi. Kuan. Chung and Chung-Hao Tien. Plasmonic rainbow rings induced by white radial polarization. *Optics Letters*, 37:1205–1207, 2012.
- [56] H. Ditlbacher, N. Galler, D.M. Koller, A. Hohenau, A. Leitner, F.R. Aussenegg, and J.R. Krenn. Coupling dielectric waveguide modes to surface plasmon polaritons. *Opt. Express*, 16(14):10455–10464, Jul 2008.
- [57] S. Refki, S. Hayashi, A. Rahmouni, and D.V. Nesterenko. Anticrossing behavior of surface plasmon polariton dispersions in metal-insulator-metal structures. *Plasmonics*, 11:433–440, 2016.
- [58] D. S. Bethune. Optical harmonic generation and mixing in multilayer media: analysis using optical transfer matrix techniques. *J. Opt. Soc. Am. B*, 6:910–916, 1989.
- [59] P. Bharadwaj, A. Bouhelier, and L. Novotny. Electrical excitation of surface plasmons. *Phys.Rev.Lett.*, 106:226802, 2011.
- [60] R. Marty, C. Girard, A. Arbouet, and G. Colas des Francs. Near-field coupling of a point-like dipolar source with a thin metallic film: Implication for stm plasmon excitations. *Chem.Phys.lett*, 532:100–105, 2012.
- [61] H. Arnoldus and J. Foley. Transmission of dipole radiation through interfaces and the phenomenon of anti-critical angles. *J. Opt. Soc*, 21:1109–1117, 2004.
- [62] A. Zangwill. *Physics at surfaces*. Cambridge University Press., Cambridge, 1988.
- [63] P.M. Echenique and J.B. Pendry. *J. Phys. C*, 11:2065, 1978. no pdf.
- [64] N. V. Smith. Phase analysis of image states and surface states associated with nearly-free-electron band gaps. *Phys. Rev. B*, 32(6):3549–3555, Sep 1985.
- [65] F. Forster, E. Gergert, A. Nuber, H. Bentmann, Li Huang, X. G. Gong, Z. Zhang, and F. Reinert. Electronic localization of quantum-well states in ag/au(111) metallic heterostructures. *Phys. Rev. B*, 84:075412, Aug 2011.

- [66] M. Teich B. Saleh. *Fundamental of photonics*. Wiley Series of Pure and Applied Physics, Jhon Wiley and Sons, Inc, New York, 1991.
- [67] C. Kittel. *Introduction to solid state physics*. John Wiley and Sons, Inc., New York, 1996.
- [68] J. D. Jackson. *Classical Electrodynamics (3-rd Edition)*. John Wiley & Sons, New York, 1998.
- [69] F. Wooten. *Optical properties of solids*. Academic Press Inc., New York, 1972.
- [70] N. W. Ashcroft and N. D. Mermin. *Solid state physics*. Thomson Learning, Stamford, USA, 1976.
- [71] G. V. Chester. The Boltzmann equation for inhomogeneous electric fields. *Proc.Phys. Soc.*, 81:938–948, 1963.
- [72] K. L. Kliever and Ronald Fuchs. Anomalous skin effect for specular electron scattering and optical experiments at non-normal angles of incidence. *Phys. Rev.*, 172(3):607–624, Aug 1968.
- [73] Prof. Robert and P. Lucht. Drude model for dielectric constant of metals. *Purdue University*.
- [74] W.L. Barnes, A. Dereux, and T.W. Ebbesen. Surface plasmons in subwavelength optics. *Nature*, 424:824–830, 2003.
- [75] F. de Fornel. *Les Ondes évanescentes en optique et optoélectronique*. Eyrolles, Paris, 1998.
- [76] C. Nicols R. Bell, K. Armstrong and R. Bradley. Generalized laws of refraction and reflection. *J. Opt. Soc. America*, 59:187–189, 1969.
- [77] M. Dupertuis, B. Acklin, and M. Proctor. Generalization of complex Snell-Descarts and Fresnel laws. *J. Opt. Soc. Am. A*, 11:1159–1166, 1994.
- [78] M. Dupertuis, B. Acklin, and M. Proctor. Generalized energy balance and reciprocity relations for thin-film optics. *J. Opt. Soc. Am. A*, 11:1167–1174, 1994.
- [79] S. Kovalenko. Descarts-Snell law of refraction with absorpion. *Semicond. Phys*, 4:214–218, 2001.
- [80] J. Chang, J. Walker, and K. Hopcraft. Ray tracing in absorbing media. *J. Quantative Spectr. Radiative Transfer*, 96:327–341, 2005.
- [81] W. Barnes. Electromagnetic crystal for surface plasmon polaritons and the extraction for light from emissive devices. *J. Lightwave Technology*, 17:2170–2182, 1999.
- [82] W. L. Barnes. Surface plasmon-polaritons length scales: a route to sub-wavelength optics. *J. Optics A: Pure and Applied Optics*, 8, 2006.
- [83] Z. Lide. Z. Junxi and X. Wei. Surface plasmon polaritons: physics and applications. *J. of Physics D: Applied Physics*, 11:113001, 2012.

- [84] C. Weeber J.-C. Chicane C. David T. Dereux A. Peyrade D. Colas des Francs, G. Girard. Optical analogy to electronic quantum corrals. *Phys. Rev. Lett*, 45:661–699, 2001.
- [85] J. A. E. Wasey and L. Barnes. Efficiency of spontaneous emission from planar microcavities. *Modern Optics*, 47:725–741, 2000.
- [86] S. Hosseini, A. Reza, and M. Maarof. *Application of Surface Plasmon Resonance Based on a Metal Nanoparticle*. InTech, Rijeka, 2012.
- [87] H. Kano and W. Knoll. A scanning microscope employing localized surface-plasmon-polaritons as a sensing probe. *Optics Communications*, 182:11–15, 2000.
- [88] H. Kano and W. Knoll. Locally excited surface-plasmon-polaritons for thickness measurement of lbc films. *Opt. Communication*, 153:235–239, 1998.
- [89] Q. Zhan. Evanescent bessel beam generation via surface plasmon resonance excitation by a radially polarized beam. *Opt. Lett*, 31:1726–1728, 2006.
- [90] D. Koller A. Stepanov-H. Ditlbacher B. Steinberger F. R. Aussenegg A. Leitner A. Drezet, A. Hoheneau and J.R. Krenn. Leakage radiation microscopy of surface plasmon polaritons. *Phy. Opt*, 2010.
- [91] A. Hohenau, J. R. Krenn, A. Drezet, O. Mollet, S. Huant, C. Genet, B. Stein, and T. W. Ebbesen. Surface plasmon leakage radiation microscopy at the diffraction limit. *Opt. Soc. Am*, 19:25749–25762, 2011.
- [92] A. Cuche, O. Mollet, A. Drezet, and S. Huant. Deterministic quantum plasmonics. *Nano Lett*, 17:19969–19980, 2009.
- [93] S. Huant J. Roch-F. Treussart Y. Sonnefraud O. Faklaris A. Cuche, A. Drezet. Near-field optical microscopy with a nanodiamond-based single-photon tip. *Opt. Express*, 10:4566–4570, 2010.
- [94] J. Mitra M. Boyle and P. Dawson. The tip-sample water bridge and light emission from scanning tunnelling microscopy. *Nanotechnology*, 20:335202, 2009.
- [95] P. Dawson D. G. Walmsley, T. S. Tan. Light emission from gold and silver thin films in a scanning tunneling microscope: role of contamination and interpretation of grain structure in photon maps. *Surf. Sci*, 572:497–520, 2004.
- [96] P. Dawson and M. Boyle. Light emission from scanning tunneling microscope on polycrystalline au films-what is happening at the single- grain level? *J. Opt. A: Pure Appl. Opt*, 8:S219, 2007.
- [97] G. Rumbles-M. Al-Jassim M. Romero, J. van de Lagemaat. Plasmon excitation in scanning tunneling microscopy: simultaneous imaging of modes with different localizations coupled at the tip. *Appl. Phys. Lett*, 90:193109, 2007.
- [98] K. L. Kliewer. Electromagnetic effects at metal surfaces. a nonlocal view. *Surf. Sci*, 101:57–83, 1980.

- [99] F. Abèles. Recherches sur la propagation des ondes electromagnetiques sinusoidales dans le milieux stratifies: application aux couches minces. *Ann.Phys*, 5:598, 1950.
- [100] Yoichi Uehara, Yuichi Kimura, Sukekatsu Ushioda, and Koichiro Takeuchi. Theory of visible light emission from scanning tunneling microscope. *Japanese Journal of Applied Physics*, 31(8R):2465, 1992.
- [101] J. K. Gimzewski, J. K. Sass, R. R. Schlitter, and J Schott. Enhanced photon emission in scanning tunnelling microscopy. *Europhys.Lett*, 8:435–440, 1989.
- [102] L. Novotny and B. Hecht. *Principles of Nano-Optics*. Cambridge University Press, Cambridge, England, 2006.
- [103] P. B. Johnson and R. W. Christy. Optical constants of the noble metals. *Phys. Rev. B*, 6:4370–4379, Dec 1972.
- [104] E. D. Palik. *Handbook of optical constants of solids*. Academic Press Inc., Orlando, 1985.
- [105] Dmitry I. Yakubovsky, Aleksey V. Arsenin, Yury V. Stebunov, Dmitry Yu. Fedyanin, and Valentyn S. Volkov. Optical constants and structural properties of thin gold films. *Opt. Express*, 25(21):25574–25587, Oct 2017.
- [106] Robert L. Olmon, Brian Slovick, Timothy W. Johnson, David Shelton, Sang-Hyun Oh, Glenn D. Boreman, and Markus B. Raschke. Optical dielectric function of gold. *Phys. Rev. B*, 86:235147, Dec 2012.
- [107] A. Messiah. *Quantum Mechanics*. North-Holland Publishing Company, Amsterdam, 1961.
- [108] W. H. Press, S. A. Teukolsky, W. T. Vetterling, and B. P. Flannery. *Numerical Recipes in Fortran 77. The art of scientific computing*. Cambridge University Press, Cambridge(internet version), 1992.
- [109] L. Barnes. Fluorescence near interfaces: the role of photonic mode density. *Modern Optics*, 86:4950–4953, 2000.
- [110] M. Stéphan O. Garcia de Abajo F. J. Tencé M. Henrard L. Taverna D. Pastoriza-Santos I. Liz-Marzan L. M. Colliex C. Nelayah, J. Kociak. Mapping surface plasmons on a single metallic nanoparticle. *Nature Physics* 3, 348, 2007.
- [111] Shinji Hayashi and Takayuki Okamoto. Plasmonics: visit the past to know the future. *Journal of Physics D: Applied Physics*, 45(43):433001, 2012.
- [112] B. Luk'yanchuk, N. I. Zheludev, S. A. Maier, N. J. Halas, P. Nordlander, H. Giessen, and C. T. Chong. The Fano resonance in plasmonic nanostructures and metamaterials. *Nature Materials*, 9:707, 2010.
- [113] S. Hayashi, D. V. Nesterenko, A. Rahmouni, and Z. Sekkat. Observation of Fano line shapes arising from coupling between surface plasmon polariton and waveguide modes. *Applied Physics Letters*, 108(5):051101, 2016.

- [114] S. Hayashi, D. V. Nesterenko, and Z. Sekkat. Fano resonance and plasmon-induced transparency in waveguide-coupled surface plasmon resonance sensors. *Applied Physics Express*, 8:022201, 2015.
- [115] M. Kaliteevski, I. Iorsh, S. Brand, R. A. Abram, J. M. Chamberlain, A. V. Kavokin, and I. A. Shelykh. Tamm plasmon-polaritons: Possible electromagnetic states at the interface of a metal and a dielectric Bragg mirror. *Phys. Rev. B*, 76:165415, Oct 2007.
- [116] Tao Hu, Yafeng Wang, Lin Wu, Long Zhang, Yuwei Shan, Jian Lu, Jun Wang, Song Luo, Zhe Zhang, Liming Liao, Shiwei Wu, Xuechu Shen, and Zhanghai Chen. Strong coupling between Tamm plasmon polariton and two dimensional semiconductor excitons. *Applied Physics Letters*, 110(5):051101, 2017.
- [117] O. Gazzano, S. Michaelis de Vasconcellos, K. Gauthron, C. Symonds, J. Bloch, P. Voisin, J. Bellessa, A. Lemaître, and P. Senellart. Evidence for confined Tamm plasmon modes under metallic microdisks and application to the control of spontaneous optical emission. *Phys. Rev. Lett.*, 107:247402, Dec 2011.
- [118] Cesaire Ndiaye, Fabien Lemarchand, Myriam Zerrad, Dominique Ausserré, and Claude Amra. Optimal design for 100% absorption and maximum field enhancement in thin-film multilayers at resonances under total reflection. *Appl. Opt.*, 50:C382–C387, 2011.
- [119] C. Ndiaye, M. Zerrad, A. L. Lereu, R. Roche, Ph. Dumas, F. Lemarchand, and C. Amra. Giant optical field enhancement in multi-dielectric stacks by photon scanning tunneling microscopy. *Appl. Phys. Lett.*, 103:131102, 2013.
- [120] Aude L. Lereu, Myriam Zerrad, Cesaire Ndiaye, Fabien Lemarchand, and Claude Amra. Scattering losses in multielectric structures designed for giant optical field enhancement. *Appl. Opt.*, 53:A412–A416, 2014.

# Appendix A

## Electric field profile

Here we will compare our results with those of Smith *et al.* [44] for a IMI (insulator-metal-insulator) and a MIM (metal-insulator-metal) thin film stack.

Smith *et al.* studied the light emitted by an oscillating dipole placed in the second layer at 50 nm from the interface. They presented the instantaneous electric field at a particular wavelength  $\lambda$  and wave vector  $k_\rho$  as a function of the penetration coordinate  $z$ . Figure A.1 presents a silver-air interface (left column) and a silver thin film of 50 nm in air (right column). At  $\lambda=600$  nm for air-Ag interface an SPP mode appears at  $k_\rho = 1.039 k_0$ , whereas for air-Ag-air structure two modes appear at  $k_\rho = 1.0225 k_0$  ( $SPP_1$ ) and  $k_\rho = 1.0644 k_0$  ( $SPP_2$ ). For an MIM, Ag-air-Ag in the present case (figure A.2) they identify three modes at  $k_\rho = 0.515 k_0$ ,  $0.6162 k_0$  and  $1.0992 k_0$  respectively labeled  $TE_0$ ,  $TM_0$  and  $TM_{-1}$ .

The second line of figures A.1 and A.2 present the instantaneous electric field as a function of the penetration coordinate  $z$  results of Smith *et al.*[44, figure 6] for the IMI and MIM structure respectively. The third line in each figure displays our results. The comparison of the two last rows in figures A.1 and A.2 show fair agreement.

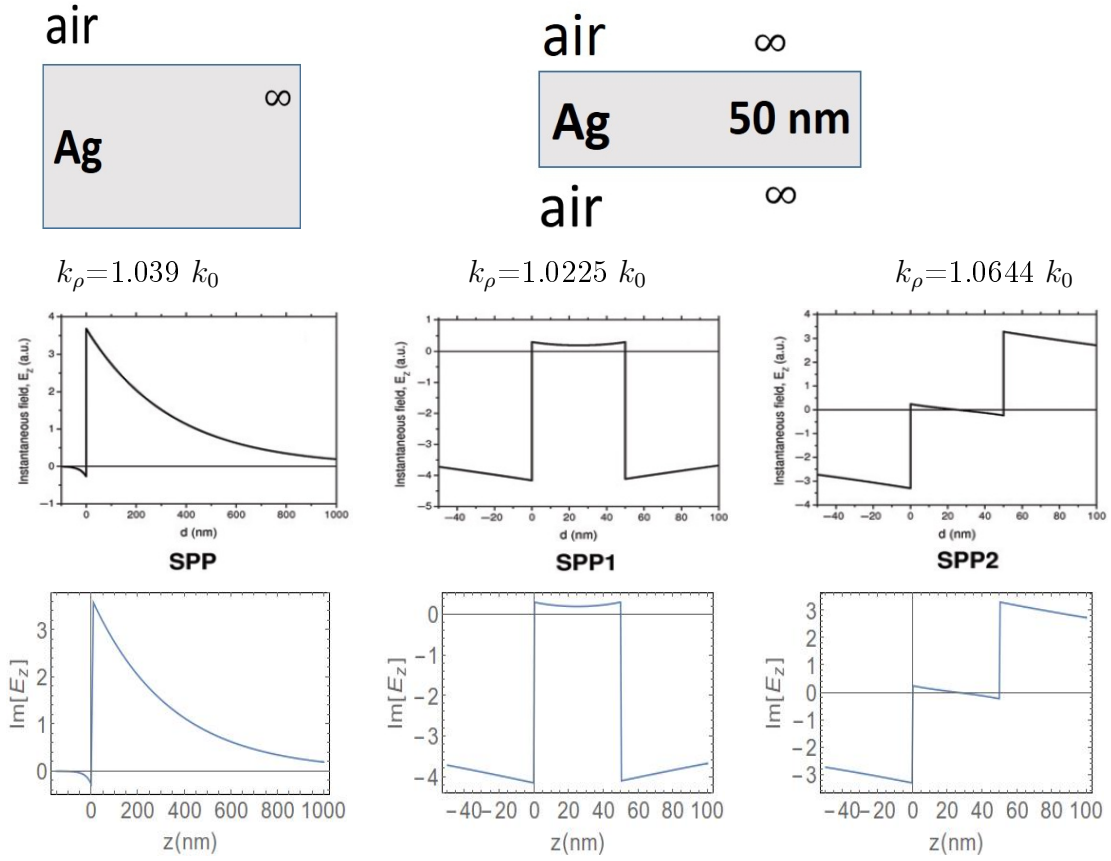


Figure A.1: Instantaneous field for  $\lambda=600$  nm of the SPP mode of a single metal-air interface (left column) and of a thin metallic film (air-metal (50 nm)-air, IMI structure) respectively middle and right columns. The relative permittivity of the metal (silver) was taken as  $-13.8+0.59i$ . The in-plane wave vector for a single interface SPP mode is  $1.039 k_0$ , and for the IMI stack  $1.0225 k_0$  (middle column) and  $1.0644$  (right column). The second and third row present Smith *et al.* [44, figure 3, second row] and our calculations.

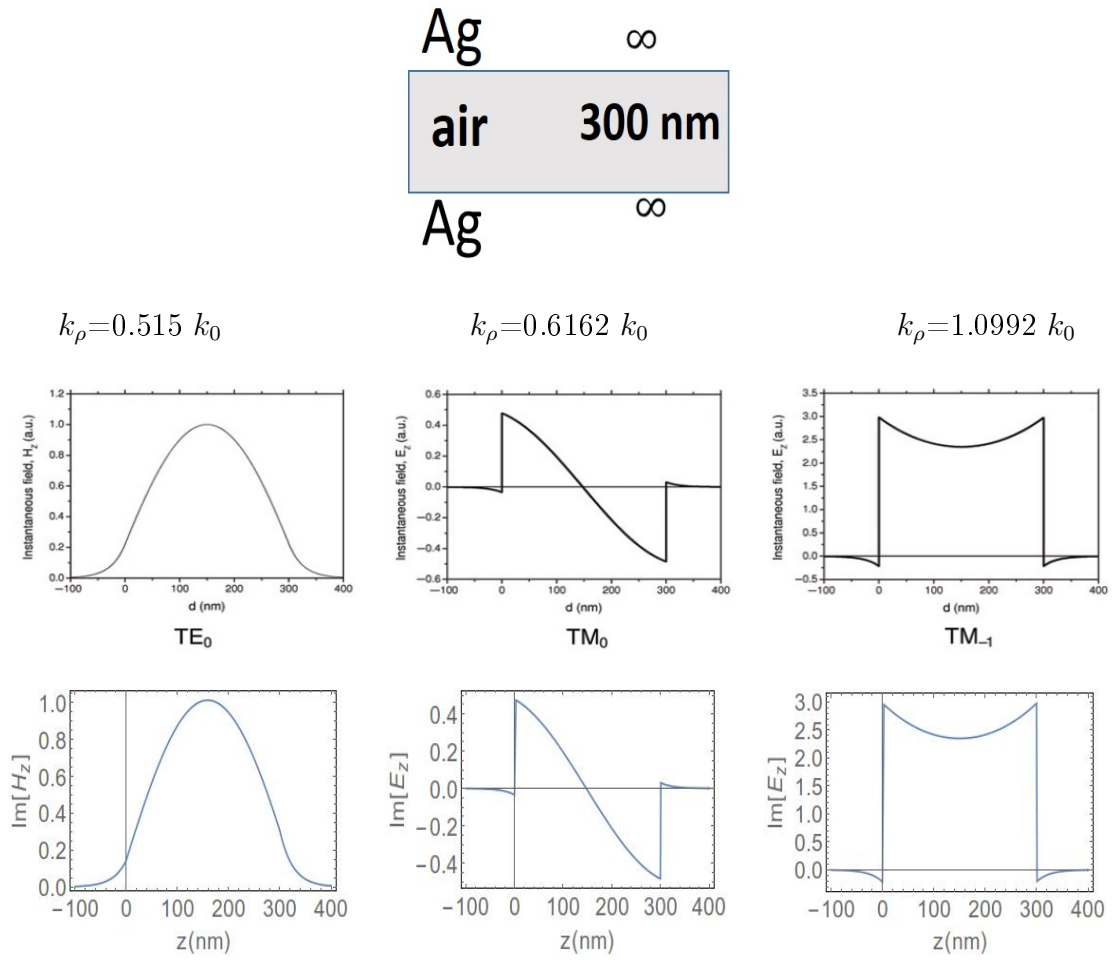


Figure A.2: Instantaneous field at  $\lambda=600$  nm of the  $TE_0$  for  $k_\rho/k_0=0.515$  (first column),  $TM_0$  for  $k_\rho/k_0=0.6162$  (second column), and  $TM_{-1}$  for  $k_\rho/k_0=1.0992$  (third column) these modes are associated with a metal-clad air cavity. The top and bottom rows show, respectively, Smith *et al.* [44, figure 6, second row] and our calculations.

# Résumé

Dans ce travail, nous étudions les propriétés optiques d'un système multicouche MIM (air-Au-SiO<sub>2</sub>-Au-Ti-verre) et les modes plasmoniques (plasmon polariton de surface, surface plasmon polaritons (SPP)) et photonique (guide d'onde, wave guide (WG)). Un tel système est utilisé dans des biocapteurs pour détecter des espèces biologiques et chimiques ainsi que pour contrôler l'émission de la fluorescence des molécules adsorbées. Dans la littérature il a été démontré qu'un système multicouche peut être utilisé pour améliorer la sensibilité des capteurs SPR en offrant une grande dépendance de la résonance angulaire du plasmon de surface. Cette propriété est due à la présence des modes plasmoniques (SPP) et photoniques (WG).

Notre modèle combine la continuité des champs électromagnétique à l'interface avec la propagation des ondes planes dans les couches minces et tient compte des réflexions multiples. L'échantillon est excité i) soit par une source à l'infini (ESI); ii) soit par une source locale situé à quelques nanomètres de la surface. Dans ce dernier cas dans l'échantillon est excité par une source d'électrons tunnel inélastiques provenant d'un microscope à effet tunnel (STM). Notre modèle remplace le courant tunnel inélastique par une dipôle oscillant vertical. En utilisant ces modèles, nous avons calculé les flux réfléchis (reflectance) et transmis (transmittance) d'une source de lumière à l'infini (ESI) et le flux transmis de l'excitation locale par dipôle oscillant, oscillating dipole (OD). La reflectance, transmittance et le flux transmis montrent des modes plasmoniques (surface plasmon polaritons (SPP)) et photoniques (wave guide (WG)). Les modes SPP et WG se comportent différemment. Le mode SPP n'apparaît que pour la lumière incidente polarisée  $p$  dans la région évanescente ( $k_\rho/k_0 > 1$ ) et sa dispersion est presque indépendante de la longueur d'onde. Le mode WG apparaît pour les deux polarisations  $s$  et  $p$  dans les régions propagatives et dans les régions évanescentes. Ce mode WG est fortement dispersif avec la longueur d'onde ( $\lambda / (k_\rho/k_0)$ ), et il est périodique avec une épaisseur de SiO<sub>2</sub>. A des longueurs et vecteurs d'onde particuliers les courbes de dispersion des SPP et WG présentent un croisement évité. La dispersion du flux transmis d'une excitation locale OD cache partiellement le croisement évité car l'amplitude de mode WG est très faible dans la partie propagative.

Le choix des épaisseurs d'or (Au) et de silice (SiO<sub>2</sub>) doit satisfaire à deux contraintes: une amplitude importante des observables et une large dépendance en longueurs d'onde du vecteur d'onde dans le plan  $k_\rho$ . Pour l'or nous avons trouvé que les observables ont des amplitudes importantes à  $d_{Au}^{trois} \in [10, 90]$  pour l'empilement de trois couches et  $d_{Au}^{six} \in [10, 50]$  nm pour celui de six couches. Dans le modèle ESI l'amplitude de la reflectance est périodique avec  $d_{SiO_2}$  et ceci se voit particulièrement bien dans la région propagative ( $k_\rho < 1$ ). Les modes de guide d'onde apparaissent pour  $d_{SiO_2} > 190$  nm.

---

Les calculs décrits ci-dessus ont été effectués dans l'espace de moments. Les calculs dans l'espace des coordonnées obtenus par transformée de Fourier sont très sensibles aux détails de l'interaction entre les modes SPP et WG particulièrement autour du croisement évité entre ces deux modes. Cette sensibilité permet une analyse fine de ce croisement évité en fonction de l'épaisseur de  $\text{SiO}_2$ .

Afin de caractériser la localisation du champ dans l'empilement et déterminer la nature d'un mode, nous avons calculé le champ électrique fonction de la coordonnée de pénétration de l'empilement  $z$ . Nous avons trouvé que pour le mode SPP le champ est localisé à l'interface Au-air et dans l'air, tandis que le champ électrique du guide d'onde est confiné dans la couche  $\text{SiO}_2$ . Dans la région du croisement évité le champ électrique est mixte ayant un caractère plasmonique (SPP) et photonique (WG). Aussi nous avons trouvé que tous les modes sont des modes longue portée se propageant sur une distance de l'ordre d'une dizaine de nanomètres. Cette longueur de propagation est probablement due au couplage SPP-WG.

Nos résultats théoriques présentés dans ce travail sont en bon accord avec les résultats des études expérimentales menées dans notre groupe.

**Titre :** Modes dans un Empilement de Six Couches Minces : Plasmons Polaritons de Surface et Guides d'Onde

**Mots clés :** Plasmons Polaritons de Surface, Guides d'Onde, Dipole Oscillant, Empilement des Couches Minces.

**Résumé :** Dans cette thèse, nous étudions les propriétés optiques d'un système multicouche (air-Au-SiO<sub>2</sub>-Au-Ti-verre). Les interfaces sont planes et la modélisation est réalisée en utilisant les coefficients de Fresnel à l'interface et la propagation d'ondes planes dans les couches. Deux modèles sont utilisés où l'échantillon est : i) excité par une source à l'infini (ESI) ; ii) excité par une source locale. Dans l'expérience que nous avons modélisée l'empilement est excité par les électrons tunnel inélastiques dans un microscope à effet tunnel (STM).

Dans le modèle, le courant tunnel inélastique est remplacé par un dipôle oscillant vertical. En utilisant ces modèles, nous avons calculé les flux réfléchis (reflectance) et transmis (transmittance) d'une source de lumière à l'infini et le flux transmis de l'excitation locale. La reflectance, transmittance et le flux transmis montrent des modes plasmoniques (plasmon polariton de surface (SPP)) et photoniques (guide d'onde (WG)). A des longueurs d'onde particulières, les courbes de dispersion des SPP et WG présentent un croisement évité. Le choix des épaisseurs d'or (Au) et de silice (SiO<sub>2</sub>) a deux contraintes : Une amplitude importante des observables et une large dépendance en longueurs d'onde du vecteur d'onde dans le plan  $k_{\rho}$ . Nous étudions aussi l'influence des

épaisseurs sur les observables. Nous avons trouvé que les observables ont des amplitudes importantes à  $d_{\text{Au}}^{\text{trois}}(\text{nm}) \in [10,90]$  pour l'empilement de trois couches et  $d_{\text{Au}}^{\text{six}}(\text{nm}) \in [10,50]$  pour celui de six couches. Les modes de guide d'onde apparaissent pour  $d_{\text{SiO}_2} > 190 \text{ nm}$ .

Afin de caractériser la localisation du champ dans l'empilement et déterminer la nature du mode, nous avons calculé le champ électrique en fonction de la coordonnée de pénétration  $z$ . Nous avons trouvé que pour le mode SPP le champ est localisé à l'interface Au-air, tandis que le champ électrique du guide d'onde est confiné dans la couche SiO<sub>2</sub>.

Les résultats théoriques présentés sont en bon accord avec les résultats des études expérimentales menées dans notre groupe.

**Title:** Surface Plasmon Polariton and Wave Guide Modes in a Six Layer Thin Film Stack

**Keywords:** Surface Plasmon Polariton, Wave Guide, Oscillating Dipole, Thin Film Stack

**Abstract:** In this thesis, we investigate the optical properties of a six-layer stack (air-Au-SiO<sub>2</sub>-Au-Ti-glass). The interface is flat, and the modeling is performed using elementary Fresnel expressions at the interface and plane wave propagation in the layers. Two models are used where the sample is: i) excited by a source at infinity (excitation by source at infinity (ISE)); ii) excited by a local source. In the experiments we are modeling this source consists of the inelastic tunneling electrons from a scanning tunneling microscope (STM).

In our modeling this source is replaced by a vertical oscillating dipole. Using these two models one calculates the reflected (reflectance) and the transmitted (transmittance) flux from a source at infinity and the transmitted flux of a local source. Surface plasmon polariton (SPP) and wave guide (WG) modes may be identified in the reflectance, transmittance and transmitted flux. In a particular wavelength domain, the SPP and WG repel each other giving rise to an avoided crossing.

The choice of the gold (Au) and silica (SiO<sub>2</sub>) thicknesses of the six-layer stack is guided by two requirements: high amplitude of the observable and wide wavelength dependence of the in-plane wave vector  $k_p$ . We also study the influence of the gold and silica thicknesses on the observables. We find that the observables are significant for  $d_{Au}^{trois}(\text{nm}) \in [10,90]$  for the three and

$d_{Au}^{six}(\text{nm}) \in [10,50]$  for six layer stacks and this predictive study guided the choice of the experimental sample thicknesses. The wave guide mode appears for  $d_{SiO_2} > 190$  nm.

The electric field as a function of the penetration coordinate  $z$  is calculated in order to characterize the location of the field in the stack and to assign the nature of the modes. We observe that for the SPP the electric field is confined at the Au-air interface whereas, the electric fields corresponding to the WG mode are confined inside SiO<sub>2</sub> layer.

Our calculations presented in this work are in good agreement with the experimental measurements performed in our group.

